Dipl.-Ing. Maria Gombotz, BSc.

Ion Dynamics and Electrochemical Properties of Energy Materials

Dissertation
zur Erlangung des akademischen Grades
Doktorin der technischen Wissenschaften (Dr. techn.)

eingereicht an der
Technischen Universität Graz

Betreuer
Univ.-Prof. Dr. Martin Wilkening
Institut für die Chemische Technologie von Materialien

Graz, März 2021

Meinen Eltern.

Es ist eine gefährliche Sache, Frodo, aus deiner Tür hinauszugehen.
Du betrittst die Straße, und wenn du nicht auf deine Füße aufpasst,
kann man nicht wissen, wohin sie dich tragen.
Bilbo, Der Herr der Ringe

Statutory Declaration

I declare that I have authored this thesis independently, that I have not used other than the declared sources / resources, and that I have explicitly indicated all material which has been quoted either literally or by content from the used sources. The text document uploaded to TUGRAZonline is identical to the present doctoral thesis.

Eidesstaatliche Erklärung

Ich erkläre an Eides statt, dass ich die vorliegende Arbeit selbstständig verfasst, andere als die angegebenen Quellen/Hilfsmittel nicht benutzt, und die den benutzten Quellen wörtlich und inhaltlich entnommenen Stellen als solche kenntlich gemacht habe. Das in TUGRAZonline hochgeladene Textdokument ist mit der vorliegenden Dissertation identisch.

Graz, _____ _____

Date, Datum Signature, Unterschrift

Abstract

The constant advancement of existing and the development of new, more sustainable battery systems are of significant social, economical and ecological importance nowadays. Researcher worldwide focus on the development of Li-ion batteries (LIB) with solid electrolytes, due to its manifold benefits such as a higher energy density. For the design of highly conductive, stable solid electrolytes, a deep understanding of fundamental diffusion processes in solids is indispensable. Therefore, the center of attention of the first part of this thesis is to describe and understand ion dynamics in different solid systems, with Li^+, H^+, Ag^+ and F^- being the mobile species.

In the first study presented here, two aspects of the solid electrolyte Li_3YBr_6 were studied in detail, namely an occurring phase transition and the influence of nanostructuring on Li^+ conductivity. It was found that a change of the Li sublattice at approximately 0°C comes along with an increase of conductivity for microcrystalline Li_3YBr_6. Even though this increase is either missing or less obvious for nanocrystalline Li_3YBr_6, the conductivity of the mechanosynthesized sample is only slightly lower. This fact would suggest that the nanostructured form could indeed serve as sustainable alternative to replace microcrystalline Li_3YBr_6. However, an electronic conductivity being slightly too high for the direct use as electrolyte, characterises the nanocrystalline form.

Furthermore, here the so far unknown lithiumhalogenide $Li[In_xLi_y]Br_4$ was synthesised and reviewed for its suitability as solid electrolyte. The study included the structure determination via X-ray powder diffraction, alongside with a detailed investigation of the conductivity. The moderate conductivity found at room temperature would allow an implementation of this electrolyte in cells operated at higher temperatures. The electronic conductivity, however, turned out to be not sufficiently low, bearing the risk of self discharge processes.

Fundamental research about ion dynamics in the mixed ion conductor LiF in combination with the isolator TiO_2 was carried out hereinafter. In such ion conductor | isolator systems, diffusion paths form at the interface between the two phases, enhancing the conductivity of poorly conducting LiF. Often space charge zones are responsible for this increase. Impedance spectroscopy showed that the highest conductivity is reached if 40vol% TiO_2 are added to LiF. Li^+ was identified by variable-temperature ^7Li and ^{19}F NMR measurements to be the dominant mobile species.

Another examined material class are lithium garnets, which are considered as promising electrolytes. These materials, however, enclosed as problematic in the course of time, as already traces of water and oxygen can trigger degradation. Here, a detailed understanding of the reactions such as the ongoing exchange of Li^+ by H^+ is of importance to design counter measures. Therefore, this exchange and the accompanying effects were examined in the garnet $Li_{6.4}La_3ZrTaO_{12}$, which served as a model system for this investigation. The

incorporation of H^+ without changing its structure, was examined by neutron diffraction. The impact of H^+ on Li^+ dynamics was investigated by means of both, impedance spectroscopy and ^{7}Li NMR measurements. The latter indicates only a minor effect of H^+ incorporation on Li ion dynamics. ^{1}H NMR measurements revealed relatively fast proton dynamics with jump rates comparable to those of ^{7}Li.

An exceptional case of diffusion in solids is represented by movements of ions in layered, 2D systems, as, for example, the commercial cathode material $LiCoO_2$. Model systems with unambiguous evidence of 2D diffusion are scare - this is why the 2D F^--conductor $RbSn_2F_5$ was synthesised and characterised in detail. Impedance spectroscopy helped to identify macroscopic dynamics and the activation energies characterising long-range ion transport. The data obtained was compared to results from NMR, whereby here only 2D spectral density functions provided plausible findings being in line with results from impedance spectroscopy and, hence, being a prove for 2D F^- dynamics in $RbSn_2F_5$.

Another cation conductor investigated within this thesis is Ag_3SI, which is already know for a long time due to its 'superionic' properties. Here, Ag^+ conductivities of up to 38 mS cm^{-1} at room temperature were obtained for the metastable, quenched α^*-phase. The main focus was laid on the stability of α^*-Ag_3SI, studied by holding the sample at different temperatures while measuring the conductivity to track the transformation back to β-Ag_3SI. It turned out that it takes ca. 28 h at 60° to obtain again β-Ag_3SI, highlighting the unstable character of the α^*-phase at elevated temperatures.

The second, smaller part of the thesis is concerned with a new, relatively unexplored battery system relying on F^- ions. Here, the in prototypes routinely used solid electrolyte $La_{0.9}Ba_{0.1}F_{2.9}$ was examined for the first time with regard to its electrochemical stability against metal electrodes. Cyclic voltammetry revealed that the high reactivity of fluorine bearing substances results in instabilities, which could hinder the realisation of top performing cells.

Kurzfassung

Die Weiterentwicklung bestehender und die Entwicklung neuer, nachhaltigerer Batteriesysteme ist in klimainstabilen Zeiten von großer gesellschaftlicher und umwelttechnischer Relevanz. ForscherInnen weltweit legen daher ihren Fokus auf die Entwicklung von Li-Ionen Batterien (LIB) mit Festkörperelektrolyten, da sich zahlreiche Vorteile wie z.B. eine höhere Energiedichte erhofft werden. Um leitfähigere, stabilere Festkörperelektrolyte zu entwickeln ist es nötig, ein tiefes Verständnis bezüglich grundlegender Diffusionsprozesse in Festkörpern zu erlangen. Deswegen liegt der Hauptaugenmerk im ersten Teil der Arbeit auf Ionendynamik in verschiedenen, festen Systemen, in denen Li^+, H^+, Ag^+ und F^- die mobilen Spezies sind.

In der ersten Studie wurden zwei Aspekte des festen Elektrolyten Li_3YBr_6 im Detail studiert, nämlich ein stattfindender Phasenübergang und der Einfluss von Nanostrukturierung auf die Li^+-Leitfähigkeit. Die Untersuchung ergab, dass mit der Änderung im Li-Untergitter bei ca. 0 °C ein Leitfähigkeitsanstieg in mikrokristallinem Li_3YBr_6 einhergeht. Obwohl dieser Anstieg für nanokristallines Li_3YBr_6 nicht oder nur schwach zu sehen ist, ist die Leitfähigkeit nur marginal geringer. Daher könnte man davon ausgehen, dass sich nanostrukturiertes Li_3YBr_6 als nachhaltige Alternative von getemperten Li_3YBr_6 eignet. Jedoch ist diese Probe durch eine leicht zu hohe elektronische Leitfähigkeit charakterisiert, um direkt für den Einsatz als Elektrolyt geeignet zu sein.

Im weiteren Verlauf der Arbeit wurde das bisher wenig bekannte Lithiumhalogenid $Li[In_xLi_y]Br_4$ synthetisiert und auf seine Eignung als Festkörperelektrolyt hin überprüft. Die Studie beinhaltet die Strukturaufklärung mit Röntgenbeugung und eine detaillierte Untersuchung der Leitfähigkeit. Bei Raumtemperatur würde die bestimmte, moderate Leitfähigkeit die Anwendung als Elektrolyt nur in Zellen, welche bei höheren Temperaturen betrieben werden, erlauben. Die elektronische Leitfähigkeit ist zudem nicht ausreichend gering, um langsame Selbstentladungsprozesse vollständig unterdrücken zu können, was Diffusionsbarrieren zwischen Elektrolyt und Elektrode unumgänglich machen würde.

Ein weiteres Forschungsthema befasst sich mit der Ionendynamik in LiF in Kombination mit dem Isolator TiO_2. In solchen Systemen bilden sich an der Grenzfläche zwischen Ionenleiter und Isolator schnelle Diffusionspfade aus, welche die Leitfähigkeit von langsamen Leitern, wie LiF, erhöhen. Oftmals sind Raumladungszonen für diesen Anstieg verantwortlich. Mittels Impedanzspektroskopie wurde die höchste Leitfähigkeit für das System mit 40vol% TiO_2 gefunden. Die hauptsächlich mobile Spezies Li^+ wurde mittels NMR Messungen identifiziert.

Des Weiteren wurden Lithiumgranate, welche schon seit Längerem als vielversprechende Kandidaten für den Einsatz als Festkörperelektrolyte angesehen werden, untersucht. Diese Klasse von Materialien entpuppte sich jedoch im Laufe der Zeit als problematisch, da

bereits kleinste Mengen an Sauerstoff und Wasser zur Degradation führen. Dieser Austausch und die damit einhergehenden Auswirkungen auf die Li^+ Dynamik wurden im Granat $Li_{6.4}La_3ZrTaO_{12}$ untersucht. Die Einlagerung von H^+ in der Struktur wurde mittels Neutronenbeugung nachgewiesen. Es zeigte sich, dass H^+ nur einen geringen Einfluss auf die Li^+-Dynamik hat, was mittels Impedanz- und NMR Spektroskopie nachgewiesen wurde. Auch die mikroskopische Diffusion von H^+ wurde mittels NMR Messungen charakterisiert, wobei Linien Messungen eine nicht unwesentliche H^+ Translationsdynamik aufzeigen.

Einen Sonderfall von Diffusion in Festkörpern stellt die 2-dimensionale Bewegung von Ionen in Schichtstrukturen, wie z.B. in dem kommerziellen Kathodenmaterial $LiCoO_2$, dar. Modelsysteme, in denen eindeutige Beweise für 2D Diffusion zu finden sind, sind rar, weswegen der 2D-F^--Leiter $RbSn_2F_5$ synthetisiert und charakterisiert wurde. Die makroskopische Ionendynamik wurde mittels Impedanzspektroskopie untersucht, um Aktivierungsenergien, welche diese Prozesse charakterisieren, zu bestimmen. Die erhaltenen Daten wurden mit den Ergebnissen der NMR-Relaxationsmessungen verglichen. Diese Messergebnisse liefern nur dann ein plausibles Bild, im Einklang mit den makroskopischen Aktivierungsenergien, wenn eine Spektraldichtefunktion passend für 2D-Materialien für die Auswertung herangezogen wurde.

Einen weiteren untersuchten Kationenleiter stellt Ag_3SI dar, welcher bereits sehr lange aufgrund seiner hohen Leitfähigkeit bekannt ist. In dieser Arbeit wurden Ag^+-Leitfähigkeiten von bis zu 38 mS cm^{-1} bei Raumtemperatur mit der metastabilen, gequenchten α^*-Phase erreicht. Der Fokus wurde hier auf die Stabilität dieser Phase gelegt, welche durch das Halten der Probe auf verschiedenen Temperaturen und gleichzeitigem Verfolgen der Leitfähigkeiten studiert wurde. Dadurch konnte die Umwandlung der α^*-Phase in die weniger leitfähigere β-Phase verfolgt werden. Nach ca. 28 h bei 60° wandelt sich α^*-Phase in die weniger leitfähige β-Phase um, was den instabilen Charakter der α^*-Phase offensichtlich macht.

Der zweite, kleinere Teil der Arbeit beschäftigt sich mit dem neuen, noch sehr unerforschten Batteriesystem, welches auf Fluorid-Ionen basiert. $La_{0.9}Ba_{0.1}F_{2.9}$, der standardmäßig verwendete Festkörperelektrolyt in Prototypzellen, wurde erstmals mittels Cyclovoltammetrie bezüglich seiner elektrochemischen Stabilität in Kombination mit Metallelektroden untersucht. Es konnte gezeigt werden, dass die hohe Reaktivität von Fluor Instabilitäten zur Folge hat, welche für die Realisierung leistungsfähiger Zellen von großem Nachteil sein können.

Contents

Statutory Declaration I
Abstract III
Kurzfassung V

1 Introduction **1**
Outline of the Thesis 3

2 Structural Characterization by X-Ray Diffraction **5**
2.1 General Aspects 5
2.2 Crystal Units 6
2.3 Generation of X-rays 8
2.4 Interaction of X-rays with Matter 9
2.5 Diffraction Methods 10
2.6 Data Evaluation 11

3 Ion Dynamics in Crystalline Solids **15**
3.1 Diffusion in Solids 15
3.1.1 Defects in Solids 16
3.1.2 Diffusion Mechanisms 18
3.1.3 Direct and Indirect Methods to Determine the Diffusion Coefficient 19
3.2 Nanocrystalline Solids and Mechanochemistry 21
3.3 Impedance Spectroscopy - Revealing Ion Dynamics on the Macroscopic Length Scale 24
3.3.1 Principles and Device Set-up 24
3.3.2 Important Variables and Interpretation of the Results 26
3.4 Solid State Nuclear Magnetic Resonance - Revealing Ion Dynamics on the Microscopic Length Scale 32
3.4.1 Physical Background 32
3.4.2 Measurement Principles 36
3.4.3 Relaxation 36
3.4.4 Interpretation of the Results 39
3.4.5 Magic Angle Spinning NMR 40
3.4.6 Device Set-up 41

Publications in peer reviewed journals and unpublished manuscripts **42**
P1 - Fast Li Ion Dynamics in the Mechanosynthesized Nanostructured Form of the Solid Electrolyte Li_3YBr_6 . . . 47
P2 - Lithium-Ion Transport in Nanocrystalline Spinel-type $Li[In_xLi_y]Br_4$ as Seen by Conductivity Spectroscopy and NMR . . . 67
D1 - Enhanced Ion Dynamics by Interface Engineering in the Dispersed Ionic Conductor $LiF:TiO_2$ . . . 81
M1 - Degradation of Single-Crystalline $Li_{6.4}La_3ZrTaO_{12}$ in Humidity: A Nuclear Magnetic Resonance and Neutron Diffraction Study . . . 91
P3 - Spatial confinement - Rapid 2D F^- diffusion in micro- and nanocrystalline $RbSn_2F_5$ . . . 107
D2 - Temperature stability of the metastable, superionic Ag^+ conductor α^*-Ag_3SI 125

4 Fluorine-ion Batteries **135**
4.1 State of the Art . . . 135
4.2 Working Principle . . . 136
4.3 Electrodes used . . . 136
4.4 Side Reactions within Solid Systems . . . 138
4.5 Electrolytes used . . . 139
4.5.1 Solid Electrolytes . . . 139
4.5.2 Liquid Electrolytes . . . 139
4.6 Conclusion . . . 140

Publications in peer reviewed journals **147**
P4 - Fluoride Ion Batteries: On the Electrochemical Stability of Nanocrystalline $La_{0.9}Ba_{0.1}F_{2.9}$ Against Metal Electrodes . . . 149

5 Conclusion **165**

A Experimental **167**

B Bibliography **171**

C Publications **183**
C.1 Publications in Peer Reviewed Journals . . . 183
C.2 Oral Presentations . . . 184
C.3 Posters . . . 184

D Acknowledgement **185**

1 Introduction

Pigments of tea distributing homogeneously in water, fragrances spread in air or the propagation of carbon into steel - diffusion of ions and atoms in different media accompanies humans everyday. Also in Lithium-ion batteries (LIB), on which high hopes are resting due to the needed reorientation in the energy sector, diffusion plays a major role, as ions need to diffuse through the electrolyte from one electrode to another to supply electric energy. Being fast in liquid electrolytes, the movement of Li^+ in solid electrolytes occurs usually way slower due to the restricted place and many other factors ions are facing in condensed matter. Fast ion dynamics in solid electrolytes are, however, needed for the development of competitive all-solid-state batteries. Here, fundamental and applied science plays a capitol role to push this research further.

During this thesis first and foremost fundamental research was conducted to study ion dynamics in different systems partly serving as model compounds inspired by applications. Not only the movement of Li^+, but also of F^-, Ag^+ and H^+ was investigated with various spectroscopic methods. X-ray powder diffraction or neutron diffraction helped study the structure, while translational ion dynamics on different length scales were probed by impedance and Nuclear Magnetic Resonance (NMR) spectroscopy. Complementary methods include thermal analysis, Secondary Electron Microscopy (SEM), polarisation measurements or Cyclic Voltammetry (CV).

In the following, the main questions, which were to be answered during the thesis, are enlisted alongside with a short statement on the strategy.

How does a present phase transition influence ion dynamics in the solid electrolyte Li_3YBr_6? And, is nanocrystalline Li_3YBr_6 a sustainable alternative to microcrystalline Li_3YBr_6 annealed at high temperatures?

Li_3YBr_6 was already successfully tested by Asano et al. [1] as solid electrolyte in a Lithium-ion battery prototype. A phase transition at around 0°C, as seen in impedance spectroscopy data, however, needed to be further investigated, as a fluctuation in conductivity in this temperature range could impede its application in future all-solid-state batteries. The phase transition was investigated by thermal analysis (DSC) and changes in conductivity and ion dynamics were revealed by impedance as well as NMR measurements. Recent temperature variable neutron diffraction measurements [2] helped us to resolve structural changes between the two present phases. Furthermore, a nanocrystalline

sample was received after just one hour of milling and tested whether it could serve as sustainable alternative to annealed Li_3YBr_6.

Is the so far unknown lithium ion conductor $Li[In_xLi_y]Br_4$ a suitable material to be employed as solid electrolyte in LIB?

During this thesis the Li-ion conductor $Li[In_xLi_y]Br_4$ was synthesised via a mechanochemical route. As always in the case of an unknown material, the structural characterisation was the starting point. Here, ^{6}Li, ^{79}Br MAS NMR was employed to underpin the obtained x-ray data. The relation of ionic to electronic conductivity plays a leading role if it comes to determine the suitability of a material to serve as an electrolyte. Therefore, impedance spectroscopy together with polarisation experiments were applied, followed by a detailed analysis of ion dynamics through ^{7}Li NMR spectroscopy.

Are ion dynamics in LiF enhanced if a certain amount of the insulator TiO_2 is added?

Different vol% of TiO_2 were added to the poor ionic conductor LiF by planetary milling to see whether the introduction of ion conductor | insulator interfaces enhances the conductivity. While impedance spectroscopy was used to probe long-range ion dynamics, NMR helped identify the main charge carrier, Li^+ or F^-.

Does the incorporation of H^+ upon degradation in the garnet material $Li_{6.4}La_3ZrTaO_{12}$ change the Li^+ dynamics and/or structure?

The degradation of the garnet material $Li_{6.4}La_3ZrTaO_{12}$ upon contact with O_2 and H_2O was investigated to see whether structural changes occur. Such changes were studied by neutron diffraction experiments. The influence of H^+ incorporation on Li^+ dynamics was examined again by impedance and NMR spectroscopy. Interestingly, while Li^+ dynamics remain almost unchanged, at least if bulk properties are considered, fast H^+ motions were revealed by ^{1}H NMR line measurements.

Can evidence be found with the aid of NMR and impedance spectroscopy that 2D F^- motion occurs in $RbSn_2F_5$?

The layered F^- ion conductor $RbSn_2F_5$ was synthesised in the nano- and microcrystalline form to investigate if explicit evidence can be found that restricted 2D motion occurs in this material. Impedance as well as NMR spectroscopy was used to shed light on both micro- and macroscopic diffusion. Indeed, a detailed analysis of the data, recorded over a broad dynamic range, provided strong evidence for 2D motion of F^- in $RbSn_2F_5$.

Under which conditions does the highly conductive α^* form of Ag_3SI transform into the β-phase?

β-Ag_3SI was synthesised through a conventional solid-state synthesis. At temperatures above 235°C, a phase transformation to the superionic α-phase occurs, which can be quenched to obtain the metastable α^*-phase, which exhibits higher conductivities than the β-phase. To answer the question under which conditions the quenched phase is stable, conductivity measurements at 30°C and 60°C were performed for 140 h and 48 h, respectively, followed by XRD measurements.

Is $La_{0.9}Ba_{0.1}F_{2.9}$ electrochemically stable in combination with the most widely used electrode materials?

$La_{0.9}Ba_{0.1}F_{2.9}$, widely applied as solid electrolyte in 1^{st} generation Fluorine-ion batteries (FIB), was tested for the first time for its electrochemical stability in combination with different electrode materials (Pt, Ag, Au, Ni, Cu). Cyclic Voltammetry using a two electrode set-up was applied alongside with optical and electron microscopy to investigate any degradation reactions.

Outline of the Thesis

Chapter 2 of this thesis deals with the theoretical background of the structural characterisation by X-ray diffraction. Chapter 3 introduces basics about diffusion in solids, the synthesis of nanocrystalline, metastable materials via mechanochemistry and the two main characterisation techniques, impedance spectroscopy and Nuclear Magnetic Resonance spectroscopy. Thereafter publications, manuscripts and manuscript drafts, which can be assigned to the topic of ion dynamics in solids are presented. The second topic of this thesis, Fluorine-ion batteries (FIB), is covered in chapter 4. An overview about the state of the art, used materials and downsides of FIB are given, before the according publication is presented.

2 Structural Characterization by X-Ray Diffraction

Outline

Mechanochemical syntheses of known (*e.g.* Li_3YBr_6) and so far unknown (*e.g.* $Li[In_xLi_y]Br_4$) crystalline materials came always along with structural characterisation via X-ray powder diffraction (XRPD). Information about the crystal lattice, phase purity and the crystallite size were retrieved thereby.

Even though this characterization technique is a simple routine measurement, the theoretical background and the measurement possibilities are manifold. This section, therefore, gives a fundamental understanding of important aspects of crystals, the diffraction of x-rays, different methods and the instrumentation needed. The data evaluation will be discussed, covering topics like phase and line broadening analysis.

2.1 General Aspects

The determination of the crystal structure is not only important if completely new materials are characterised, but also if already known crystals are modified to adjust certain characteristics. Here, direct and indirect methods are used to uncover different crystal properties. Transmission electron microscopy (TEM) and scanning probe microscopy (SPM) belong to the group of direct methods, where electrons with high energies (up to 300 keV) are accelerated towards the sample and get diffracted, making crystal structures directly visible. Both techniques are limited to either extremely thin samples (below 100 nm) or to the sole exploration of the sample surface [3]. Direct methods are therefore neither suited as routine measurements, nor to acquire information about larger crystallites or periodic structures.

X-ray (Powder) Diffraction (XR(P)D) represents the most prominent indirect method. The understanding of crystals and their classification forms the basis for XRD and is therefore discussed before methodical details are considered.

2.2 Crystal Units

A crucial prerequisite for XRD is a periodic structure, as present in crystals. Amorphous materials, like glasses, with absent long-range order are invisible in x-ray diffraction experiments.

Perfect or ideal crystals can be described by an infinite repetition of identical structural units in all three dimensions. These units are composed of the lattice itself, represented by a periodic arrangement of points, and the basis, consisting of single or multiple ions or atoms, respectively [3]. To describe a crystal entirely, the unit cell is used, which is defined as *"the smallest repeating unit which shows the full symmetry of the crystal structure" [4]*, meaning that all information needed to describe a crystal is comprised in this cell. This is, however, only valid for ideal crystals, which exist hypothetically at 0 K [4]. In real crystals the situation at hand is more complex, as various kind of defects (discussed in detail in subsec. 3.1.1) are present.

Crystals can be classified by their symmetry, which means that certain geometrical operations can be applied to transfer the crystal again into itself. Such procedures are called symmetry operations, while the according geometric object is called a symmetry element. The symmetry element is characterised by the fact that it remains unchanged during the operation. For example, if a rotation (= operation) about an axis occurs, the axis remains fixed and represents a symmetry element.

Here, it is already possible to make a first distinction; The point group includes operations with at least one stationary point, the translation group operations without stationary points. The symmetry operations of the point group include five symmetry elements (*e.g.* inversion or rotation around an axis), whereby usually more than one of these symmetry elements exit in a crystal [3, 4]. On the basis of this, the so-called group theory leads to a total of 32 possible crystal classes [3]. If translational symmetry operations are included too, a total of 230 space groups can be deduced. Every existing crystal can be described by one of those [4].

A further important point is that in order to be able to classify crystals in a more straightforward way, seven adapted coordinate systems are used. These are called crystal systems, see table 2.1, namely cubic, tetragonal, orthorhombic, hexagonal, trigonal, monoclinic and triclinic. And the combination of each system with a lattice type (primitive (P), body-centered (I), face-centered (F) or base-centered (C) basis), results in the fourteen Bravais lattices [4].

Within a certain crystal system the unit cells are characterised by the lattice parameters, namely the length and angles between the axes. The lattice constants a, b and c mark the length of the axes, usually given in Å, the angles are denoted by α, β and γ.

Table 2.1: Overview of the seven crystal systems and the fourteen Bravais lattices [3, 5, 6]

Crystal system	**Unit cell shape - axis length**	**Unit cell shape - axis angles**	**Bravais lattice**
Cubic	a = b = c	$\alpha = \beta = \gamma = 90°$	P, F, I
Tetragonal	a = b ≠ c	$\alpha = \beta = \gamma = 90°$	P, I
Orthorhombic	a ≠ b ≠ c	$\alpha = \beta = \gamma = 90°$	P, I, C, F
Hexagonal	a = b ≠ c	$\alpha = \beta = 90°$ $\gamma = 120°$	P
Trigonal	a = b = c	$\alpha = \beta = \gamma < 120°$ $\neq 90°$	P
Monoclinic	a ≠ b ≠ c	$\alpha = \gamma = 90° \neq \beta$	P, C
Triclinic	a ≠ b ≠ c	$\alpha \neq \beta \neq \gamma \neq 90°$	P

Highly symmetric crystal systems, like cubic cells, exhibit fixed axis lengths ($a = b = c$) and solely 90° angles between the axes. The situation at hand is completely different in crystal systems with lower symmetry, where neither the axes lengths nor the angles have a fixed value. The requirements the crystals have to exhibit to belong to a certain class, are listed in table 2.1.

Apart from lattice parameters, also lattice planes describe crystals and are crucial when talking about x-ray diffraction. They are defined as planes inside the crystal, which are occupied with lattice points [3]. In order to be able to define planes accurately, the interceptions with the axes of the unit cells are determined in the first step. For example, see figure 2.1 (a), where the lattice plane is coloured in yellow. This plane has its intercept with the a-axis at $\frac{1}{2}$ of the unit cell and is parallel to the b and c-axis, hence intersecting with these axes by definition at ∞. By taking the reciprocal of these three numbers ($\frac{1}{2}$, ∞, ∞), the Miller indices *(hkl)* are determined; (200). Figure 2.1 (b) shows another example of a plane with the indices (101). If planes are parallel to each other, one speaks of a plane family, which is depicted in figure 2.1 (c). [3] The distance between planes of a family is called the interplanar distance or d-spacing (d_{hkl}) [7] and will be of significant importance, as soon as x-ray diffraction comes into play.

The relation between the Miller indices *(hkl)*, the lattice parameters a, b and c and the interplanar spacing d_{hkl} is given by equation (2.1) for orthogonal crystal classes.

$$\frac{1}{d_{hkl}} = \sqrt{\frac{h^2}{a^2} + \frac{k^2}{b^2} + \frac{l^2}{c^2}} \tag{2.1}$$

The according equation for non-orthogonal classes like triclinic crystals, is much more complicated due to the deviation of the angles from 90° and can be found elsewhere [3].

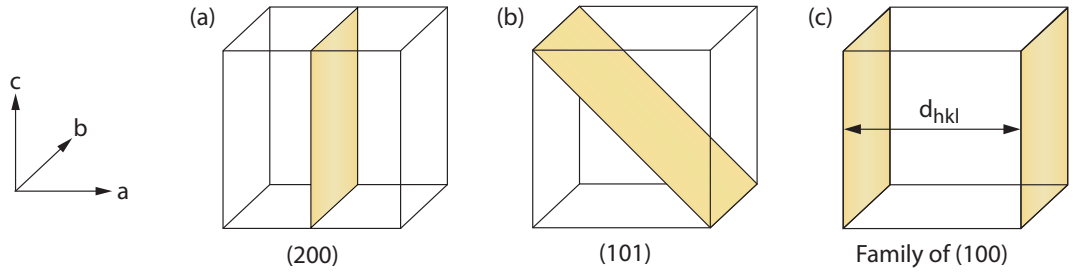

Fig. 2.1: Visualisation of crystallographic planes in a cubic lattice. Depicted are examples of planes with the Miller indices **(a)** (200) and **(b)** (101). **(c)** Showing a family of planes with the Miller indices (100) and the interplanar distance d_{hkl} between them. Adapted from reference [4, 7].

2.3 Generation of X-rays

The determination of the stated parameters is possible by conducting x-ray diffraction experiments [3–5]. Here, in the most commonly used diffractometers, x-rays are generated in x-ray tubes, where electrons are emitted from a tungsten filament. These electrons get accelerated towards a metal target fixed on the anode, by applying a high voltage difference (around 20-40 kV). This process is outlined in figure 2.2 (a). When these high energetic electrons hit the target, they are slowed down, hence loosing energy. This energy is converted into x-rays, generating continuous bremsstrahlung, also called white radiation. Apart from this kind of radiation, characteristic, sharp x-ray lines with a defined energy are observed too, being dependent on the kind of metal used as target. As a large fraction of energy from the accelerated electrons is converted into heat, the anode has to be cooled continuously.

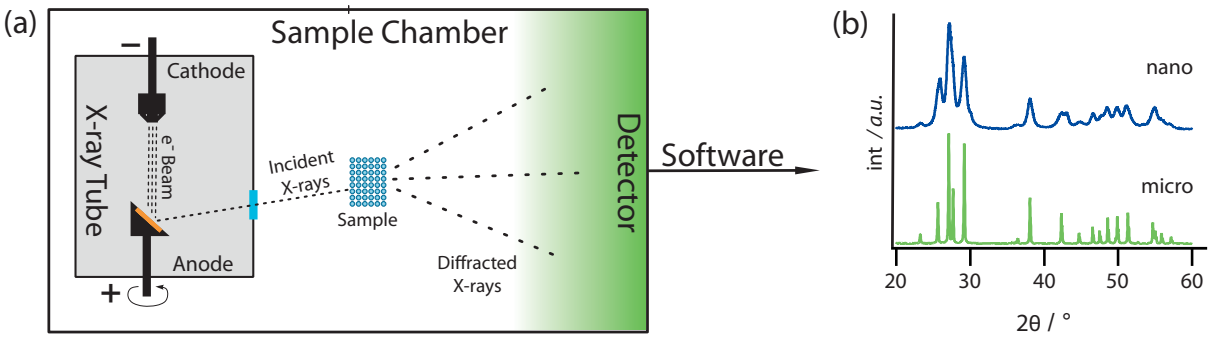

Fig. 2.2: **(a)** Outline of a (powder) diffractometer consisting of a x-ray tube (cathode, anode with target in yellow and Be window in blue), the sample and a detector. Adapted from reference [4]. **(b)** The resulting X-ray powder diffraction pattern of micro- (lower part in green) and nanocrystalline PbF_2 (upper part in blue).

The characteristic x-ray lines arise from the fact that electrons hit the atoms, kicking out electrons from inner shells (*e.g.* K / L / M - shells). These electron holes are then filled up with electrons from outer shells, releasing excess energy as x-rays. The resulting x-ray lines are characteristic for each element, as the transition energy from one shell to the other has a specific value. Therefore different lines occur in a characteristic x-ray spectrum, as several transitions are possible. Predominately, α (2p to 1s) and β (3p to 1s) transitions can be distinguished, with the former having higher energy [4]. In commercial diffractometers Cu anodes are common and here, $K_{\alpha 1}$ radiation is used for experiments with a characteristic wavelength of 1.541 Å. The denotion α_1 refers to the fact that two spin states are possible for the 2p electron, hence, also two slightly different energies are observable for the transition. After the generation, it is important to filter the rays to finally obtain only K_α x-rays *e.g.* (consisting in this case of $K_{\alpha 1}$ and $K_{\alpha 2}$). Mainly two techniques are used here; metal foils or crystal monochromators. After the generation and the filtering of x-rays inside the high-vacuum tube, they permeate a Beryllium window, before interacting with the sample. Beryllium is suited as window material, as it allows x-rays to pass, due to its low atomic number and, hence, its low scattering cross section. [5,8]

2.4 Interaction of X-rays with Matter

After passing through the Be window, the x-rays enter the sample chamber inside the diffractometer, see figure 2.2 (a). The x-rays propagate as waves with a certain wavelength, which is defined as the distance between the wave peaks. Finally hiting the sample, they get reflected, interact with a conservation of energy, or by either losing all (=absorption) or a fraction of its energy. If there is a loss of energy, one speaks of incoherent scattering, also called inelastic or Compton scattering, and the phase relationship to the incident x-ray gets lost. This incoherent scattering is besides bremsstrahlung a major source for background radiation in diffraction experiments. If, however, the phase relationship between incident and scattered x-ray is preserved, the x-ray changes direction, while no energy is lost. Only such coherent x-rays are useful in diffraction experiments. [3–5]

W. L. Bragg was a pioneer in the field of x-ray diffraction and introduced a simple, yet not totally correct model to visualise the scattering process. Within this model, x-rays get "reflected" by imagined, crystallographic planes defined by Miller indices. As depicted in figure 2.3 the x-rays 1 and 2, with a defined wavelength λ, strike the planes with an angle θ, before they get either reflected by the plane or, as most of the x-rays, penetrate it. [3, 5]

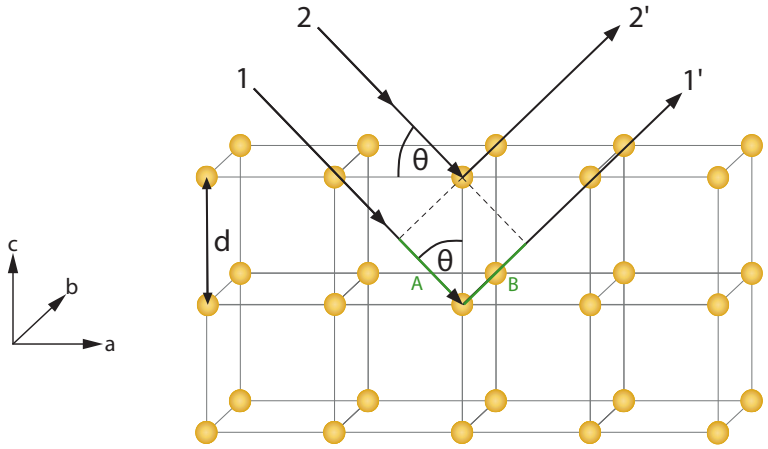

Fig. 2.3: Schematic drawing of a pair of x-rays, marked as 1 and 2, hitting the crystal in a certain angle θ and undergoing coherent scattering. Adapted from reference [4, 5]

If two x-rays, which are in phase to each other, get "reflected" on a plane of atoms separated by the interplanar distance d, they leave the crystal, as discussed, either in or out of phase. The beams are only in phase after diffraction, hence leading to constructive interference, if the additional way **AB** beam 1 has to pass, is a multiple integer n of λ. The distance here can be described by $2d{\cdot}\sin\theta$ leading finally to Bragg's equation 2.2 [3–5]:

$$n \cdot \lambda = 2 \cdot d \cdot \sin\theta \tag{2.2}$$

Bragg's law is, however, only satisfied if the wavelength $\lambda \leq 2d$, illustrating that the wavelength of the used x-rays has to be in the order of the observed lattice parameters ($\sim$Å) [3]. The shortcoming of the model, introduced by Bragg is that x-rays are not "reflected" by planes, but get diffracted or scattered by atoms. Only in rare cases the imagined reflecting planes do correspond to the layers of atoms, which diffract and scatter [4]. The implementation of the reciprocal space, the Ewald sphere *etc.* give a detailed description of the processes occurring during diffraction, which can be found elsewhere [3–5].

2.5 Diffraction Methods

The experimental set-up of diffraction experiments strongly depends on the kind of sample - single crystal or powder - and the fact, if the wavelength λ is variable or fixed. The main three methods, namely the Laue, rotating crystal and Debye-Scherrer method, will be covered in the following [3, 4].

Laue Method

The Laue method, the oldest of all techniques presented, features several limitations, as for example, it can be only used for single crystals. For this method, polychromatic x-rays (λ variable) get diffracted on a crystal, mounted in a fixed position. The x-rays then hit the detector plate, which is mounted behind the crystal and create a point pattern, where each point represents defined plane surfaces. Bragg's law is satisfied due to the fact that for each plane surface there is a suited wavelength within the used continuous x-ray spectrum.

The use of polychromatic x-rays make the data evaluation more complicated and hence time consuming, as superimposition of reflexes occurs and these reflexes can not be assigned to a certain wavelength. Compared to other techniques, it is possible to track fast processes as the measurement time is reduced.

Rotating Crystal Method

Monochromatic x-rays are used to gather information when using the rotating crystal technique. In order to still satisfy Bragg's law, the used crystal has to be rotated. Apart from this fact, this method is identical to the Laue method.

Debye-Scherrer Method

The Debye-Scherrer method and modern variations of it allow the investigation of polycrystalline, powdered samples, which are much more common and easier to obtain than single crystals. Inside a polycrystalline sample, the micro- or nanocrystallites are randomly arranged, therefore all different orientations are present. Here, family of planes exist, always satisfying Bragg's law by diffracting x-rays and generate circles on the detector plate. In modern diffractometers a Geiger counter *e.g.* acts as detector and scans 2θ values usually ranging from 10-80°2θ around the sample. A diffraction pattern, see figure 2.2 (b), depicting the intensity of beams against the scanned °2θ, is readily created by the software, making a fast analysis of the investigated sample possible.

2.6 Data Evaluation

The position, intensity and shape of the reflexes in the recorded diffraction pattern give valuable information about the investigated sample. With the aid of the peak position, for example, the interplanar spacing d_{hkl} can be calculated by using Bragg's equation. Much more instructive, if materials with known crystal structure are investigated, is the comparison of the obtained pattern with pattern in databases, *e.g.* the Inorganic Crystal Structure Database, short ICSD [9]. A tentative statement about phase purity can be made by this comparison and whether impurity phases are present.

Rietveld Refinement

If, however, crystals with unknown structure are examined and the exact position of all atoms inside the crystal have to be determined, a single crystal analysis is necessary [8]. If additionally atoms with a low atomic number are present inside the crystal, like Li, also neutron diffraction experiments are a useful tool to determine the position of these. The situation gets much more convenient if a model of the investigated crystal exists, like mentioned above. In such cases the obtained diffraction pattern is compared to a model or calculated pattern by Rietveld refinement. Parameters like lattice constants, position and occupancy by atoms can be refined until a satisfactory accordance between measured and calculated profile is achieved. [4]
The three main pattern components, namely peak position, intensity and shape, are influenced by various parameters. A short overview about the most important ones is given in table 2.3.

Table 2.3: Overview parameters influencing the peak position, intensity and shape [7]

	Crystal structure	**Specimen properties**	**Instrumental parameters**
Peak position	Unit cell parameters (a, b, c, α, β, γ)	Absorption of the sample	Radiation, instrument/sample alignment
Peak intensity	Atomic parameters (x, y, z)	Preferred orientation of the crystallites	Radiation
Peak shape	Crystallinity	Grain size, stress and strain in the crystal	Beam conditioning

Here, the line broadening provides a useful tool to calculate the crystallite size, if the crystallites are small enough (<1 μm).

Line Broadening due to Small Crystallites and Microstress

The reason for the line broadening, lies in the missing destructive interference; Constructive interference of x-rays occurs when the additional distance beam 1 in figure 2.3 has to travel, is a multiple of the wavelength λ, as stated earlier. During the measurement, θ is continuously increased and at a certain point the additional distance is slightly higher with 1.001λ. At this point destructive interference occurs in microcrystalline samples. This is the case, as the beam getting diffracted in the top plane where 1.001λ is valid, is exactely out of phase ($\delta = 0.5\ \lambda$) with the diffracted beam from the 500^{th} plane. In nanocrystalline samples there might be the case that no 500^{th} plane is present and no destructive interference occurs if λ deviates. Hence, the reflex will not occur at an exact θ value, but a little earlier and later, leading to line broadening. [5]

Here, the Scherrer expression (2.3) [10, 11] is used with Γ denoting the full width at half maximum of the reflex, λ the wavelength in Å and τ the according grainsize in Å. κ denotes the numerical shape factor with values between 0.89 and 1 [7].

$$\tau = \frac{\kappa \cdot \lambda}{\Gamma \cdot cos\theta} \tag{2.3}$$

Besides line broadening due to a small crystallite size, it is also observed when microstress is acting inside the crystallites, leading to compressive and tensile forces. This forces lead to smaller or higher d-values, again causing line broadening. It is possible to calculate the line broadening β_ϵ caused by microstress ϵ via [5]:

$$\beta_\epsilon = 4 \cdot \epsilon \cdot tan\theta \tag{2.4}$$

Line broadening, however, occurs also due to instrumental limitations from the diffractometer itself. This additional broadening has to be determined with standards and taken into account for the calculation of the broadening due to small crystallites and microstress [5].

Final Remarks

To sum up, not only provides X-ray diffraction a facile method to determine the crystal structure and phase purity, but it also yields information about material properties like the grain size. One has to keep in mind, however, that only information about the bulk is obtained. As soon as details about a non-uniform distribution of atoms inside a material or the surfcae is of interest, other techniques like TEM are needed. Additionally, trace amounts and amorphous fractions remain undetected in XRD experiments.

3 Ion Dynamics in Crystalline Solids

Outline

A central element of this thesis is the investigation of ion dynamics in (nano)crystalline materials. Therefore this chapter aims at giving an overview about all relevant topics, starting with general aspects of diffusion in solids in section 3.1, including defects and the diffusion in (nano)crystalline materials. Section 3.2 covers theoretical and practical aspects of mechanochemical syntheses to obtain nanocrystalline, metastable materials. As all synthesised materials were characterised by Nuclear Magnetic Resonance (NMR) and impedance spectroscopy, these measurement principles as well as the evaluation and interpretation of the obtained data will be discussed in detail in sections 3.3 and 3.4. Experimental details regarding both techniques and the syntheses can be found in the appendix in chapter A.

3.1 Diffusion in Solids

If a concentration gradient in a liquid or gas, or more generally speaking, in an isotropic medium exists, the particles will move until the gradient is balanced out. This net movement of atoms, ions or other particles, is called diffusion and occurs by a random motion, called Brownian motion.

In an one dimensional isotropic media, the diffusion of particles can be described with Fick's first law [12]:

$$J_x = -D\frac{\partial C}{\partial x} \tag{3.1}$$

It describes the relationship between the particle flux J_x (*e.g.* [J] = mol m^{-2} s^{-1}) crossing a unit area in the direction x, to the particle concentration C (*e.g.* $[\partial C/\partial x]$ = mol m^{-4}). In this equation, D (*e.g.* [D] = m^2 s^{-1}) denotes the diffusion coefficient or diffusivity. [12]

By combining Fick's first law with the continuity equation[1] and by using the vector notation, Fick's second law can be derived, valid for three dimensional cases as present in

[1] $\frac{\partial c}{\partial t} + \nabla j_p = 0$

real solids. It can be further simplified if the diffusivity is independent of concentration to

$$\frac{\partial C}{\partial t} = D \triangle C \tag{3.2}$$

with $\triangle$ denoting the Laplace operator. [12] Here, the diffusion coefficient D is an important parameter to compare the diffusivity in different materials. Diffusion in solid materials occurs at a much slower rate than in isotropic media, as a result of the fact that atoms in solids have restricted paths to move. In solids the self-diffusion, the movement of atoms through matter without an external driving force, is of special interest and depends on several factors. The crystal structure, size of the diffusing atom and the presence of defects may influence the speed of atomic movement drastically. [12, 13] As various diffusion mechanisms exist, with the majority involving defects, defects will be discussed in advance.

3.1.1 Defects in Solids

Defects in ionic solids can be distinguished by their dimensionality. Zero dimensional defects, like vacancies or interstitials only exist around one single lattice point and are therefore also called point defects. These defects are depicted in figure 3.1 (a), where the regular crystal arrangement is broken up by unoccupied lattice points, called vacancies, or atoms sitting on irregular lattice sites, called interstitial atoms [13]. Cation vacancies posses a negative charge and for the sake of charge neutrality of a crystal, they appear together with an anion vacancy, being positively charged. Such a vacancy pair is called a Schottky defect and represents an intrinsic defect. Another defect belonging to this class, is called Frenkel defect, where an atom leaves its original position to occupy a normally empty crystal site. The vacancy in combination with the interstitial atom form together the Frenkel defect.

The reason why intrinsic defects are present in every crystal (above 0 K) lies in the fact that a certain amount of defects minimize the Gibb's free energy G of the crystal, hence making the crystal more stable. The energy is defined by

$$\Delta G = \Delta H - T\Delta S \tag{3.3}$$

with S denoting the entropy and H the enthalpy of the crystal.

If the defect concentration inside the crystal is low, the creation of a defect leads to a rise in entropy S. On the one hand, due to the large number of sites a defect can occupy in the lattice and on the other hand, the crystal neighbourhood of the defect is affected by the disorder.

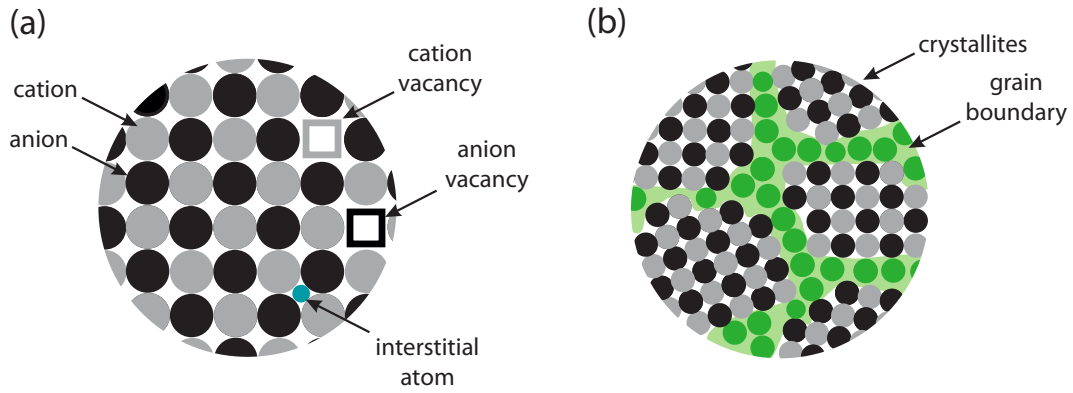

Fig. 3.1: **(a)** Two-dimensional schematic representation of a crystal lattice, composed of cations (grey dots) and anions (black dots). One dimensional defects like a cation (grey square) and anion vacancy (black square), as well as an interstitial atom (blue dot) are illustrated. **(b)** Depicted is an arrangement of two-dimensional (nano-)crystallites (black and grey dots) with an periodic array of atoms, separated by grain boundaries, representing a two dimensional defect. Grain-boundaries are characterised by a reduced atomic density with different spacing between the atoms (green dots). Adapted from reference [12].

This gain in entropy, needed to create a defect, offsets the enthalpy required, thus lowering the Gibb's free energy. A further increase of the defect concentration does not lead in the same extent to a gain in entropy, as there are less and less sites a vacancy can occupy. At a certain defect concentration the gain in entropy is not sufficient anymore to balance out the needed enthalpy. This point marks the minimum of Gibbs free energy with an equilibrium concentration of defects at the given conditions. As apparent from equation (3.3) also a higher temperature influences the Gibbs's free energy and leads to an increase of defects and therefore, to enhanced diffusivity. [4, 14]

Vacancies are also introduced by impurities or doping with aliovalent ions. If, *e.g.* a Sm^{3+} ions occupies a Ba^{2+} site in BaF_2, an additional negatively charged cation vacancy is needed to obtain the charge neutrality of the crystal. Such extrinsic defects are a powerful tool to alter and study the diffusion dynamics in crystals. [12]

Apart from point defects, linear, one dimensional defects can be present inside crystals. These are called dislocations and come along with a change of the arrangements of atoms. [14]

Grain boundaries represent two dimensional defects, which occur between two neighbouring grains, as schematically drawn in figure 3.1 (b). Regions of reduced atomic density characterise these defects. The smaller the grains are, the higher is the volume fraction of atoms located in grain boundaries. Defect rich materials can feature distinct properties than their larger analogous, as defects play a major role in diffusion mechanisms, as explained in the following. [14]

3.1.2 Diffusion Mechanisms

Contrary to diffusion by Brownian motion in liquids and gases, the movement of particles inside a crystal is restricted. Diffusion occurs *e.g.* along dislocations, between crystallites in grain boundaries, both mediated by defects, or by volume diffusion through the crystal. Here, diffusion mechanisms [12, 13] shed light on how atoms move through the crystal.

The **direct interstitial mechanism** describes the movement of an atom residing on an interstitial position to another by passing the bottleneck set up by two atoms on usual crystal sites. That mechanism describes a concerted move of atoms, as atoms have to move aside, while the usually small, diffusing atom passes by. Another diffusion mechanism without the involvement of defects, is the **collective mechanism**. Either there is a direct exchange of atoms side-by-side or a collective motion of three or more atoms, moving in a ring (therefore also called ring mechanism). A rather high activation energy characterises these mechanisms. Far more often the diffusion is mediated by defects. The most prominent representative here is the **vacancy mechanism**, where an atom jumps into a neighbouring vacancy. If aggregates of vacancies are involved, a **divacancy mechanism** takes place. An atom on a regular site can also be kicked out from an atom diffusing from an interstitial site, featuring the **interstitialcy mechanism**.

Irrespective of the mechanism, the diffusion is affected by several parameters, as the activation energy of jumps between lattice sites, temperature and correlation effects.

Atoms residing at their stable lattice sites, representing energy minima, vibrating the whole time with a frequency of approximately 10^{13} s^{-1}. Usually the energy E_A (*e.g.* [E_A] = eV) required for a successful jump from one lattice site to another is high, compared to the thermal energy k_BT, with k_B denoting the Boltzmann constant. From time to time, however, successful jumps are performed, due to a large atomic displacement. The probability p of a jump to occur is given by the Maxwell-Boltzman statistic [13, 14]:

$$p = \mathrm{e}^{\frac{-E_A}{k_B T}} \tag{3.4}$$

Another diffusion influencing factor is the temperature T, as obvious from equation (3.4), as an increase in temperature leads to an increased jump probability. The temperature dependence of the diffusion coefficient D^T is described by an Arrhenius-type equation [13]:

$$D^T = D_0^T \cdot \mathrm{e}^{\frac{-E_A}{RT}} \tag{3.5}$$

In this equation, D_0^T denotes the so called pre-exponential or frequency factor and R the gas constant.

In various cases, atoms perform jumps, which are independent of the previous jump. These jumps are described by the random walk theory. In some cases, however, correlated diffusion occurs. This is due to the fact that if an atom jumps from a stable site into a neighbouring vacancy, the vacancy stays close to the atom for some time. This proximity increases the probability of a back jump, marking correlated motion. A correlation factor f can be defined, as the ratio of the diffusion coefficient D^T of a certain atom to the coefficient D_{random} of a hypothetically, uncorrelated moving atom: [12, 13]

$$f \equiv \frac{D^T}{D_{\text{random}}} \tag{3.6}$$

A correlation factor of 1 describes uncorrelated, random walk of atoms through the crystal, a value of <1 correlated diffusion [14]. Correlation effects can be uncovered by NMR measurements and will be discussed later.

3.1.3 Direct and Indirect Methods to Determine the Diffusion Coefficient

A special case of diffusion is the one of charged particles through a crystal influenced by an applied electrical field. The potential landscape ions are facing is changed in a way that the potential barriers an ion has to overcome are reduced in one direction, while being raised in the opposite. The relative number of jumps an ion will make with and against the field, is expressed by the ionic conductivity σ (*e.g.* S cm^{-1}) and can be measured via impedance spectroscopy, which will be discussed in detail in section 3.3. The conductivity σ is again described by an Arrhenius-type equation [13]:

$$\sigma = \frac{\sigma_0}{T} \cdot \exp(\frac{-E_A}{k_B T}) \tag{3.7}$$

with σ_0, the pre-exponential factor, defined by:

$$\sigma_0 = \frac{n\nu a^2 e^2}{k_B} \tag{3.8}$$

In this equation n represents the number of mobile species, ν the vibration frequency, a the separation length between two stable lattice points and e the charge of the particle. A diffusion coefficient D^σ based on conductivity measurements can be calculated with [12, 15]:

$$D^\sigma = \frac{\sigma_{DC} k_B T}{N q^2} \tag{3.9}$$

σ_{DC} denotes the DC conductivity (for details see section 3.3), N the particle density of the charge carriers and q the charge of them.

Again a statement about correlated diffusion can be made with the Haven ration H_R, bringing into relation the tracer diffusion coefficient D^T and the one deduced from the conductivity D^σ [14]:

$$D^T = H_R \cdot D^\sigma \tag{3.10}$$

If the Haven ratio is 1, the particles move uncorrelated with random jumps. A value of $H_R < 1$ represents correlated motion, a value of $H_R > 1$ motion, where diffusion occurs via defects, which are invisible for impedance spectroscopy, conductivity measurements, respectively.

The determination of the diffusion coefficient by impedance spectroscopy represents a direct method to determine the diffusion coefficient, as the movement of ions is tracked directly. To those methods, also the well known radio tracer method in combination with depth profiling belongs. Such direct methods are sensitive to long range self-diffusion [12, 13].

Contrary to that indirect methods do not track the diffusing atoms, but sense phenomena influenced by diffusion, like relaxation rates, which can be measured by static NMR measurements. Those rates allow to calculate the mean residence time τ of atoms on a lattice site. τ is considerably longer than the jump time between the lattice sites. Hence, the mean square displacement $<r^2(t)>$ of the particles at time t in equation (3.11), can be simplified to d, the length of the atom jumps. [14]

$$D^T = \lim_{t\to\infty} \frac{< r^2(t) >}{2Dt} \tag{3.11}$$

The dimensionality D usually adopts a value of 3 in samples with 3D ion motion. In layered structures D becomes 2, in tunnel like structures 1.

Knowing the mean residence time τ and the average length of a jump d, the diffusion coefficient for uncorrelated 3D motion can be calculated from diffusion-induced NMR relaxation data using the Einstein-Smoluchowski relation [14]:

$$D^T = \frac{d^2}{6\tau} \tag{3.12}$$

3.2 Nanocrystalline Solids and Mechanochemistry

A material is called nanocrystalline if it is made out of structures with length scales being shorter than 100 nm. Also structures, where only one dimension is below 100 nm, like rods or layers, are considered nanocrystalline. As mentioned before, these materials can offer completely different characteristics than their bulky analogous, as they posses a high fraction of atoms inside grain-boundaries and close to defects. If the crystallites are just a few nanometers large, up to 50% of the atoms can be found in grain-boundaries, which are due to the high defect concentration, paths of fast diffusion. This is why especially diffusion parameters differ so strongly in micro- and nanocrystalline materials [14].

Nanostructured solids can be created by two approaches: By the so-called bottom up approach, where the synthesis starts with single atoms builing up nanostructures as in inert-gas condensation, or by a top down approach, where existing larger structures are fractured *e.g.* in ball mills. Ball milling allows the execution of mechanochemical syntheses, which, depending on the material, result in fully amorphous, nanocrystalline or metastable structures, as explained in-depth in the following.

Heat, a different electrochemical potential or radicals, but also the direct absorption of mechanical energy, as in mechanochemistry, can initiate a chemical reaction [16]. Providing the needed energy for the initiation of a reaction by the input of mechanical energy, offers in these cases several advantages. For example no solvents are needed, being accompanied by the avoidance of solubility problems, solvent complexation and energy consumtion [17]. Various fields already rely on mechanochemistry; The synthesis of pigments [18], macromolecules [19], pharmaceutical ingredients [20] or metal-organic fameworks (liquid assisted) [21] represent reports on successful mechanochemical reactions.

The far largest field of application for mechanochemical syntheses are those, involving only solids. Well established fields include the mechanical alloying in metallurgy [20] and the synthesis of ceramics and solid (energy) materials. Fluorides [22–26], lithium compounds [27], ferrites [28] and sulfides [29] are examples of compounds accessible via mechanochemistry. Here, it is possible to synthesise metastable and nanocrystalline forms [22–29] which are impossible to obtain via classical routes, as these use high temperatures which would lead to more stable analogues and crystallite growth.

A straightforward way to conduct a mechanochemical synthesis are mills, for example vibration, pin, rolling or planetary high-energy mills [30]. Here, planetary mills provide the highest energy input possible.

Figure 3.2 (a) shows a schematic drawing of a planetary mill, where two milling beakers are fixed on a larger supporting disc. In operation, the disk turns in one direction, while both beakers move in the opposite direction. This movement in opposite directions allows a unique motion of the balls placed inside the beakers; the balls, made of the same material as the beakers, grind along the beaker walls, while being accelerated until they finally

take off and hit the wall at the other side. In Figure 3.2 (b) a beaker, including balls and sample particles is depicted [22]. Both movements, the grinding along the walls as well as the impact on the wall, induce mechanical energy, responsible for the initiation of the reactions. The thereby occurring processes, involving particles and milling balls, include impact, shear and compression [31], are displayed in figure 3.2 (c). Also the collision of two particles and the impact of particles on the walls without the interaction of balls might play a role, however, less energy is introduced.

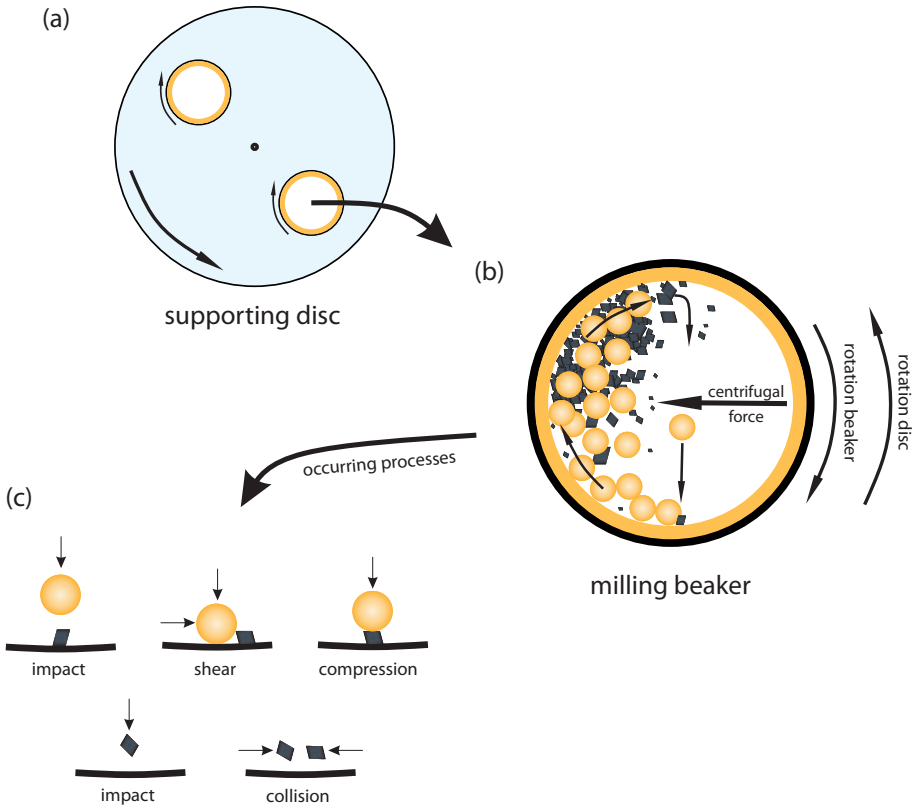

Fig. 3.2: **(a)** A schematic drawing of a high-energy planetary mill, consisting of a supporting disc and two milling beakers moving in opposite directions. **(b)** Detailed illustration of a milling beaker as seen from above. The movement of the milling balls is indicated by arrwos. **(c)** Processes occuring during milling are depicted. Adapted from reference [22, 30].

What happens at the moment of high energy input on an atomistic level is still not resolved completely. Known is that various different processes on an atomistic level play a significant role. As the particles get crushed to smaller fragments, the surface compared to the bulk increases. This change is accompanied by an increase of activity, due to the fact that upon mechanical deformation defects in the crystal structure are introduced. Simulation showed that an intense dislocation activity leads to a mixing of atoms in this region and chemical reactions, respectively [30]. Apart from the contribution of defects

to the reaction, heat is a major player too. A model from Bowden, Tabor and Yoffe proposed approximately 1000 K / μm^2 upon the impact of milling balls on the beaker wall and the sample powder [32–34]. Up to 10.000 K upon collision are proposed by the magma plasma and the spherical model by Thiessen *et al.* [35]. They stated that the impact stress creates "triboplasma", a state existing only at a very limited space and time, in which processes like fracture, dislocation motion and emission of electrons take place. Especially latter is supposed to be decisive for the initiation of chemical reactions. The dislocation motion inside the crystal is thought to be crucial too, as proposed by Gutman [30] in his dislocation model, as they move to the surface and generate areas with high dislocation density and hence activity.

The extremely high temperatures proposed only exist at the moment of impact for an estimated time of 10^{-4} to 10^{-3} s [32–34]. The heat emerging from impact as well as shear result in a temperature of approximately 200 to 250°C inside the beakers of planetary mills [30,36]. Compared to classical solid state reactions where much higher temperatures are needed, syntheses of metastable and nanocrystalline materials are possible in planetary mills. The temperature is, however, sufficient to enable crystallite growth to a certain extent. This process is accompanied by agglomeration, meaning that particles start to stick together. Also the fact that defects and dislocations become unstable and heal out, if the crystallites are too small, hinder further size reduction [12]. The crystal growth and agglomeration stands facing the continuous size reduction, reaching a equilibrium state of milling at a certain point [30]. The obtained mean grain size is most often determined by X-ray Powder Diffraction, the grain size distribution by Transmission Electron Microscopy (TEM) and other techniques [12].

Materials used as milling media have to be resistant to abrasion and high temperatures. Most commonly stainless steel, ZrO_2, WC, SiO_2 or Al_2O_3 are used [37]. If hard samples are milled, caution has to be taken to the contamination of the sample by the milling material, which can occur in minor quantity.

To sum up, mechanochemical reactions are composed of multiple steps, involving atomistic processes like defect formation and propagation, amorphization and chemical reactions. The local character of mechanically induced reactions make in-detail investigations challenging and keep unequivocal models in the dark.

3.3 Impedance Spectroscopy - Revealing Ion Dynamics on the Macroscopic Length Scale

Outline

Impedance spectroscopy represents an indirect method to determine the diffusion coefficient D^{σ} of a material, see subsection 3.1.3, but more commonly, it is used to determine *e.g.* the impedance Z and the conductivity σ of energy materials, as it was done during this thesis.

In this section the measurement principles [38,39] will be explained, followed by further insights in data representation of important variables.

3.3.1 Principles and Device Set-up

In order to conduct an impedance measurement, in the simplest case a cylindrical sample, equipped with two ion blocking electrodes, is exposed to an electric stimulus (most commonly an AC voltage) and the resulting electric response (the AC current) is recorded. Here, a wide range of frequencies ν is usually scanned, with values as low as 10^{-2} up to 10^{7} Hz or even 10^{9} Hz with special cells. The electric response, also a function of the applied frequency, is influenced by microscopic processes of a sample, like motion of ions via defects or the transfer of electrons [38, 39].

The flow of charged particles depends on the ohmic resistance inside the material. One way to define the ohmic resistance is via Ohm's law:

$$R = \frac{I}{U} \tag{3.13}$$

Ohm's law, however, is only valid for an ideal resistor, which is characterised by the fact that the applied AC voltage and the resulting AC current are in phase. This goes hand in hand with an independence on the applied AC frequency. In ionic conductors the situation is far more complex, as the occurring processes are not described by an ideal resistor, but by more complex circuit elements. This entails the fact that Ohm's law cannot be used in such systems. Therefore another form of the resistance, called impedance, has to be introduced [38, 39].

The applied AC voltage *U(t)* in impedance spectroscopy is represented by equation (3.14) with U_0 the amplitude of the voltage signal, ω the frequency (ω=$\nu 2\pi$) and t the time.

$$U(t) = U_0 \sin(\omega t) \tag{3.14}$$

Equation (3.15) expresses the current response *I(t)* of the system and is, apart from the resulting phase shift ϕ, equal to equation (3.14).

$$I(t) = I_0 \sin(\omega t + \phi) \tag{3.15}$$

The sinusoidal signals as well as the phase shift are schematically depicted in figure 3.3.

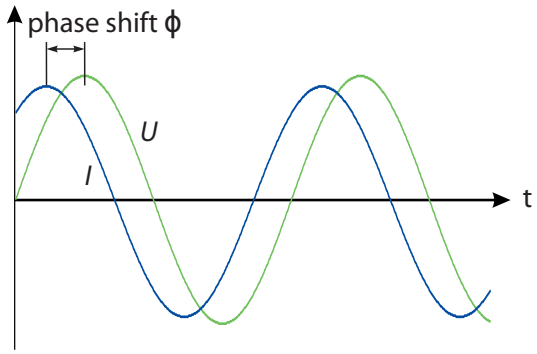

Fig. 3.3: Schematic drawing of the sinusoidal voltage U (in green) and current signal I (in blue) with a certain phase shift ϕ over time t. Adapted from reference [38].

As mentioned, ideal resistors result in a phase shift $\phi = 0$. In contrast to that an electric response completely out of phase, is described by an ideal capacitor. This circuit element is composed of two electrodes, separated by a dielectric medium with the thickness d, which stores electrical energy, when a voltage is applied. The capacitance (in Farad) of a medium is defined by:

$$C = \frac{\epsilon_0 \epsilon A}{d} \tag{3.16}$$

A represents the area of the electrode surface, ϵ_0 stands for the dielectric constant in vacuum, while ϵ is the relative permittivity. Latter defines the ability of a system to store electrical energy and will be of importance, when discussing the data interpretation [38, 39].

Equation (3.14) and (3.15) can be finally combined to define the complex impedance Z:

$$Z(\omega, t) = \frac{U(t)}{I(t)} = \frac{U_0 \sin(\omega t)}{I_0 \sin(\omega t + \phi)} = \mid Z \mid \frac{\sin(\omega t)}{\sin(\omega t + \phi)} \tag{3.17}$$

Euler relationship $e^{i\phi} = \cos(\phi) + i\sin(\phi)$, makes it possible to redefine equation (3.14) and (3.15). In the redefined equation (3.18) of $\bar{U}(t)$ and (3.19) of $\bar{I}(t)$, i stands for the imaginary number:

$$\bar{U}(t) = U_0 e^{i\omega t} \tag{3.18}$$

$$\bar{I}(t) = I_0 e^{i\omega t - i\omega} \tag{3.19}$$

The complex impedance $\bar{Z}$ can be rewritten too:

$$\bar{Z} = \frac{\bar{U}(t)}{\bar{I}(t)} =\mid \bar{Z} \mid (\cos\phi + i\sin\phi) = Z' + iZ'' \tag{3.20}$$

It is composed of the real (Z') and the imaginary part (Z'') of the impedance representing in the first case the resistivity of the sample, in the latter case the ability to store electrical energy, hence, the capacitive part of the sample [38, 39].

3.3.2 Important Variables and Interpretation of the Results

Impedance spectroscopy makes it possible to interpret the obtained data in various ways. The data is represented by several variables, which are interchangeable, giving insights into processes occurring inside the material. Upon these variables, the impedance Z, the conductivity σ, the permittivity ϵ and the electric modulus M will be discussed more in detail [38, 39].

Impedance

The obtained real and imaginary values of the impedance, $Z\,'$ and $Z\,''$, as defined by equation (3.20), can be plotted in a complex impedance or Nyquist plot, see figure 3.4 (a). Each point on the semi circle represents a certain impedance value at the applied frequency. As marked in the figure, infinite high frequencies are present at the origin of the x-axis. Also the impedance can be given by a vector with the length $/Z/$ and the phase angle ϕ, the angle between this vector and $Z\,'$, can be calculated via [38, 39]:

$$\tan\phi = \frac{Z''}{Z'} \tag{3.21}$$

The Nyquist plot, combining capacitative and resistive components, is of special importance and widely used, as already the shape of the emerging arc, gives information about certain sample characteristics. A perfect semi circle, as shown in figure 3.4 (a), is the result of single activation-energy-controlled or charge-transfer processes. In contrast to that more than one semi circle indicates that multiple processes occur, as it is generally the case in polycrystalline materials. An according example is shown in figure 3.4 (b). The blue dots represent measured values at a defined temperature. Such depressed semi circles can be the result of contributions from the sample bulk and the grain boundaries (g.b.) and a more detailed model is required to interpret the data compared to a perfect semi circle. Here, an electric circuit with two RC elements, consisting of a resistor R and a capacitor C in parallel, and one resistor R were used to fit the experimental data [38, 39].

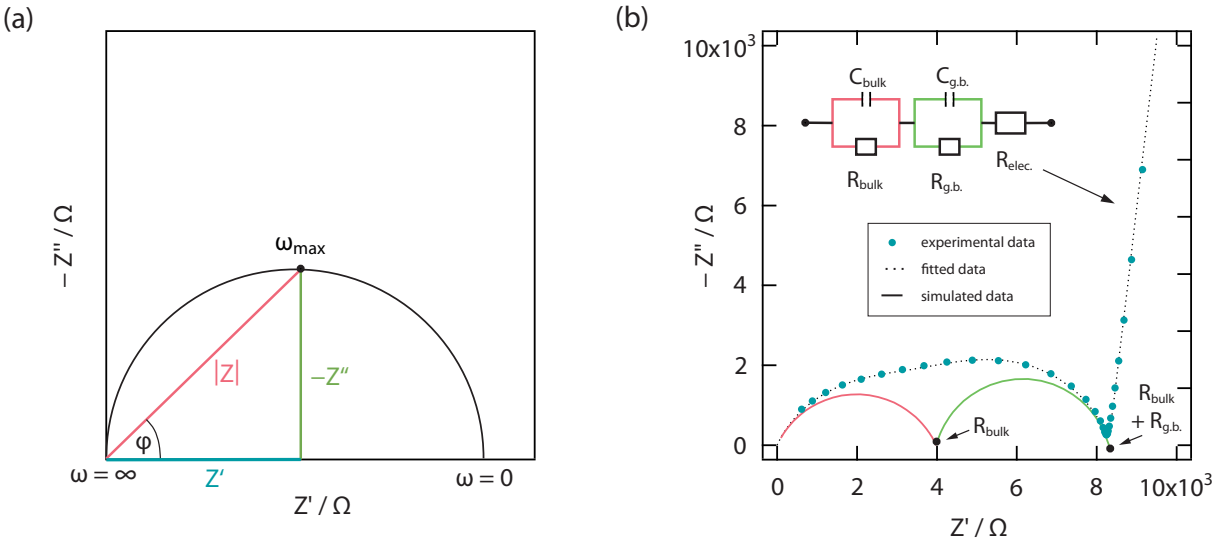

Fig. 3.4: **(a)** Nyquist plot of a process characterised by one time constant. The phase angle ϕ, the impedance as a vector with the length $/Z/$ (in red), as well as the applied frequency $\omega = 2\pi\nu$ is indicated. Adapted from reference [38]. **(b)** Nyquist plot of a polycrystalline sample with contributions of the bulk and grain boundaries (g.b.). The experimental (blue dots), the fitted (dotted line), as well as the simulated data (solid line) are shown. The electric circuit, taken for fitting and simulation of the experimental data, is schematically depicted in the upper part of the plot. See text for further explanation. Inspired by reference [38].

The according circuit diagram is shown in the upper part of figure 3.4 (b). Bulk processes govern the first RC element, the latter one to processes inside the grain boundaries. The resistor $R_{elec.}$ represents the blocking electrode, which give rise to a tail like signal at lower frequencies. With the aid of the supplied data, semi circles representing bulk as well as g.b. can be simulated with the software ZView [40] *e.g.*, see red as well as green semi circle in the lower part of figure 3.4 (b). The intercept of the first semi circle, which occurs at higher frequencies ω and at smaller values of Z', with the x-axis, represents the resistance R of the according element.

Each semi circle and RC element, respectively, is characterised by a certain relaxation time τ:

$$\tau = RC \tag{3.22}$$

To calculate τ the capacitance C is needed, which can be derived from equation (3.23). This equation holds at the frequency of maximum loss $\omega_{\max}$.

$$\omega_{\max} RC = 1 \tag{3.23}$$

The magnitude of the capacitance allows the assignment of the semicircles to certain properties of the sample, as already mentioned, to bulk, g.b. or others, due to different value ranges. A capacitance in the range of C = 10 pF indicates that bulk processes govern this semicircle, higher values of C = 100-100.000 pF point towards grain boundaries [41].

Conductivity

The analysis of conductivity data [38, 39] constitutes an important tool to get further insight into dynamic processes occurring in the sample. To obtain σ', the specific complex impedance has to be calculated beforehand with equation (3.24). The size of the applied blocking electrodes A and their distance to each other d has to be taken into account.

$$\bar{Z}_s = \bar{Z} \cdot \frac{A}{d} \tag{3.24}$$

The complex conductivity $\bar{\sigma}$ is defined via equation (3.25) as the inverse of the specific complex impedance $\bar{Z}_s$ and can be, once again, split up in its real and imaginary part.

$$\bar{\sigma} = \frac{1}{\bar{Z}_s} = \sigma' + i\sigma'' \tag{3.25}$$

The standard data presentation is a double logarithmic plot of the real part of the conductivity σ' in the unit [S cm^{-1}] *e.g.*, against the applied frequency ν, as shown in figure 3.5.

By looking at the depicted isotherm it becomes evident that it can be divided in three regions, as marked. When going from lower frequencies up to 10^2 Hz, the conductivity continuously rises due to the decreasing accumulation of charged ions in front of the ion blocking electrodes marking the electrode polarisation (region 1). The accumulation leads to the formation of space-charge layers, being characterised by a voltage drop and hence the electric field inside the bulk is nearly absent at these frequencies [42].

With increasing frequency, the ions are able to perform successful jumps over long distances. This movement is characteristic for region 2, the frequency-independent σ_{DC} plateau, identifying the DC conductivity of the sample. [42, 43] With increasing temperature, the plateaus usually move to higher σ_{DC} values as well as to a higher frequency range, being Arrhenius activated, see also subsection 3.1.3.

Hence, their σ_{DC} values can be plotted in an Arrhenius type diagram ($\log(\sigma_{DC} \cdot T)$ vs. 1000/T). From a line fit, the activation energy E_A of the occurring long-range motion can be extracted in the according temperature range.

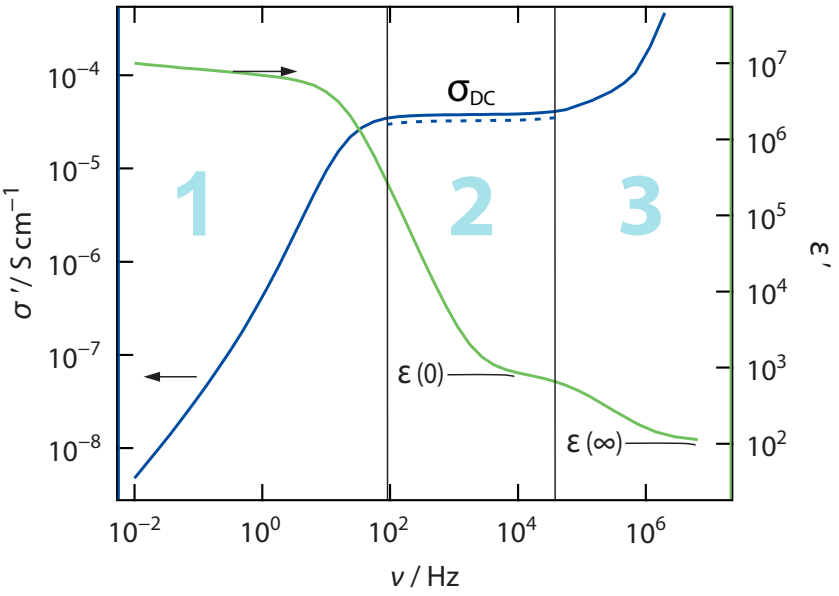

Fig. 3.5: Frequency dependence of the real part of the conductivity σ' and the permittivity ϵ'. Three distinct regions of the conductivity can be distinguished; Region 1 marks the electrode polarisation, region 2 the σ_{DC} plateau and region 3 the dispersive region. Two characteristic values of the permittivity; $\epsilon(0)$ and $\epsilon(\infty)$ can be read off. See text for further explanation.

When appliying higher frequencies, the alternating electric field switches too fast, not allowing long-range motion of the ions anylonger. In this region 3, also called the dispersive region, every ion hop, so to say localized ion motion, contributes to the conductivity, which rises now as a function of the frequency [42].

Jonscher's power law is commonly used to approximate $\sigma'(\omega)$ in this region [44]:

$$\sigma'(\omega) \propto \omega^n \qquad \text{with} \qquad n \geq 1 \tag{3.26}$$

D. L. Sidebottom [45] found that the exponent n depends on the dimensionality the ions sense inside the material. Values of n higher than approximately 0.55 indicate 3D motion, a value between 0.5 and 0.6 points towards 2D pathways, while even lower values of 0.22 - 0.4 were found to characterise 1D structures. A value of $n = 1$ is typical for the nearly constant loss (NCL) [46].

The frequency dependence of the conductivity gives also information about the hopping rates according to D. P. Almond *et al.* [43]. The conductivity is approximated with equation (3.27), being only valid at frequencies at which electrode polarisation effects do not affect σ'.

$$\sigma(\omega) = \sigma(0) + A\omega^n \tag{3.27}$$

$\sigma(0)$ corresponds to the frequency independent conductivity value σ_{DC}, while $\sigma(\omega)$ to the frequency dependent value. For values $\sigma(\omega) = 2\sigma(0)$, the applied angular frequency ω equals the ion hopping rate ω_p.

Both, the assessment of the frequency dependent conductivity region with respect to the present dimensionality and the hopping rate provide important information about the long-range ion transport. Those values can be compared with the ones extracted from NMR data, as discussed later in section 3.4.

Permittivity

Additionally, information about the dipolar relaxation inside the material can be obtained via permittivity data.

The Debye equation (3.28) establishes a connection between the polarisation, in form of the material polarisation P, the applied electric field V, the permittivity in vacuum ϵ_0 and the permittivity ϵ [47].

$$P = (\epsilon - 1)\epsilon_0 V \tag{3.28}$$

The polarisation is strongly dependent not only on the material, but most pronounced on the frequency of the field V. At low frequencies, in the Hz to kHz range, ionic polarisation occurs with a displacement of the ions against each other. Orientational or dipolar polarisation characterises frequencies in the kHz to MHz range. Approximately in the GHz to THz frequency domain, polarisation occurs, due to electrons in the atom cloud experiencing a translational displacement or in other words, the electrons are displaced with respect to the nuclei [39, 44].

Also the permittivity $\bar{\epsilon}$ can be expressed as a complex quantity and, hence, can be split up into a real and imaginary part according to [38]:

$$\bar{\epsilon} = \epsilon' - i\epsilon'' \tag{3.29}$$

The real part, also called the dielectric constant, and the imaginary part or loss factor, are calculated according to equation (3.30), with C denoting the capacity and R the resistance.

$$\epsilon' = \frac{Cd}{\epsilon_0 A} \qquad \text{and} \qquad \epsilon'' = \frac{d}{RA\omega\epsilon_0} \tag{3.30}$$

On the right axis of the diagram in figure 3.5 the real part of the permittivity is plotted. Here, two characteristic values can be extracted; $\epsilon'(0)$ and $\epsilon'(\infty)$. The former correlates with the alignment of the present dipoles, which create polarization, along the direction of the applied electric field. The latter, the high-frequency dielectric constant, marks the limiting permittivity, occurring at high frequencies, as described above as a result from

the displacement of the electrons. This value is therefore not directly traceable back to the hopping motion of ions [39, 48, 49].

Electric Modulus

Another way to represent the acquired data is to plot the real or imaginary part of the complex electric modulus $\bar{M}$ against the frequency ν:

$$\bar{M} = \frac{1}{\bar{\epsilon}} = i\omega\epsilon_0\bar{Z} = M' + iM'' \tag{3.31}$$

The plot of M'' as a function of ν makes it possible to extract ν_{max} of the occurring peaks, characterising electric relaxation phenomena [50]. By plotting ν_{max} in an Arrhenius type diagram, the activation energy can be discerned, being comparable to the value from conductivity [43].

3.4 Solid State Nuclear Magnetic Resonance - Revealing Ion Dynamics on the Microscopic Length Scale

Outline

The structural elucidation of molecules is the principal application of Nuclear Magnetic Resonance (NMR) Spectroscopy. A more or less secondary application represents the investigation of ion dynamics in solid materials, as it was employed in this thesis.

Therefore the following section gives an overview about the physical basics of NMR, measurement principles as pulse sequences, the determination of relaxation times, as well as the structural characterisation of solids via Magic Angle Spinning NMR (MAS NMR) and the device set-up. It is important keep in mind that only one isotope is observable per measurement; hard- as well as software have to be adjusted accordingly. During this thesis, often more than one isotope was investigated within a certain material, also with several different NMR techniques. Not only experimental details, but also a detailed explanation of evaluation strategies are covered within the publications, which can be found right after this chapter.

For physical details covered in-depth and further aspects regarding relaxation time measurements, the reader is referred to references [51–56], which build also the basis of the following section.

3.4.1 Physical Background

One of the intrinsic properties an atomic nucleus posses, is the spin. The spin, which can be envisioned as a rotating object, in turn is defined by an angular momentum $\boldsymbol{I}$, which nearly every nuclei possesses. $\boldsymbol{I}$ is, proven by quantum mechanical calculations, quantized and a vector quantity (written in bold) [51, 56]:

$$\boldsymbol{I} = \sqrt{l(l+1)}\hbar \tag{3.32}$$

l, the spin quantum number, can adopt values of *l = 0, 1/2, 1, 3/2,..* up to *6*. $\boldsymbol{I}$ is proportional to the magnetic moment μ:

$$\boldsymbol{\mu} = \gamma \boldsymbol{I} \tag{3.33}$$

Here, it becomes obvious that nuclei with *l = 0* do neither have an angular momentum, nor a magnetic moment, making them insensitive to magnetic fields and hence, unusable in NMR experiments. In the upper equation, γ denotes the gyromagnetic constant, which differs for every isotope. γ is one parameter, which defines the detection sensitivity of a

nuclei in NMR spectroscopy and is therefore of special importance. Enlisted in table 3.1 are the widely used nuclei within this thesis and the according γ, which is for the most nuclei positive, but exceptions as ^{29}Si exist ($\gamma = -5.319 \cdot 10^7$ rad s^{-1} T^{-1}) [51, 56, 57].

Table 3.1: The in this thesis investigated nuclei [57].

Isotope	**Spin**	**Natural abundance**	**NMR frequency at 11.7 T**	γ **[10^7 rad s^{-1} T^{-1}]**
^{1}H	1/2	99.98 %	500.00 MHz	26.752
^{19}F	1/2	100 %	470.39 MHz	25.162
^{7}Li	3/2	92.58 %	194.32 MHz	10.398
^{6}Li	1	7.42 %	73.58 MHz	3.937

In materials without permanent magnetic moments and in the absence of an external influence, an isotropic distribution of μ inside the sample is present. The situation at hand changes if the nuclei is brought into an external magnetic field $\boldsymbol{B}_0$. Influenced by this outer field, the angular momentum reorients in a way, that $\boldsymbol{I}_z$, its component in z-direction, which is by convention in the direction of the outer field, is defined by:

$$\boldsymbol{I_z} = m\hbar \tag{3.34}$$

The magnetic quantum number m can adopt values of $m = l, l\text{-}1, \ldots -l$, leading to two possible values of $\boldsymbol{I}_z$ for nuclei with $l = 1/2$, see also figure 3.6 (a).

The magnetic moments in the mentioned case of a nuclei with $l = 1/2$, react to the outer field by not aligning exactly, but moving around it on the surface of a cone, with a defined angle between the field $\boldsymbol{B}_0$ and the magnetic moment μ - see figure 3.6 (b) for a schematic drawing. This movement, called precession, of the spins occurs with a defined frequency ω_0, the Lamor frequency, which is proportional to the applied field $\boldsymbol{B}_0$:

$$\omega_0 = -\gamma \cdot \boldsymbol{B_0} \tag{3.35}$$

In table 3.1 examples of the Lamor frequency of selected nuclei can be found. It is noteworthy that particularly low frequencies might impose technical difficulties, as the standard NMR equipment is designed for measuring moderate to high Lamor frequencies. Especially the coil is an integral part of the experiment, which needs to be adjusted to the Lamor frequency [53].

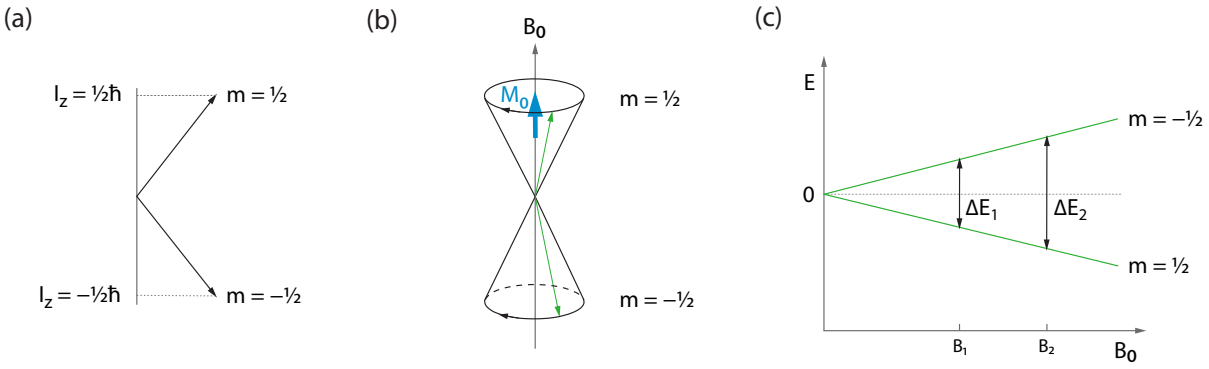

Fig. 3.6: **(a)** Quantization of the spin angular momentum I_z for a nuclei with $l = 1/2$ with a magnetic quantum number $m = \pm\frac{1}{2}$. **(b)** The precession of the magnetic moment of the spins around the external field $\boldsymbol{B}_0$, the z-axis, respectively, is indicated and hence, the net magnetization $\boldsymbol{M}_0$ is aligned with the z-axis too. The precession occurs clockwise, as it is the case for nuclei possessing a gyromagnetic ratio $\gamma > 0$. **(c)** The splitting of the energy levels E, also called Zeeman splitting (for a nuclei with $l = 1/2$), is shown for two different external magnetic field $\mathbf{B}_1$ and $\mathbf{B}_2$ ($\mathbf{B}_2 > \mathbf{B}_1$). Adapted from reference [51].

Even though the magnetic moments precess around the z-axis, the net magnetization points towards it, as indicated. The net magnetization itself is a sum of all z-components of the magnetic moments present [51, 56]:

$$\boldsymbol{M} = \sum\nolimits_i \boldsymbol{\mu_i} \tag{3.36}$$

By introducing the sample into a magnetic field, also the energy of the whole system changes. The energy of a magnetic dipole E_{mag} in an external field $\boldsymbol{B}_0$ is defined by [51,56]:

$$E_{\mathrm{mag}} = -\boldsymbol{\mu_z} \cdot \boldsymbol{B_0} \tag{3.37}$$

As evident from this equation and figure 3.6 (b), energy and field are proportional to each other. The energy is minimized if the spins align with the external field, whereby it takes some time after bringing the system into an external field until induced magnetic moments μ_{ind} build up.

The graph in figure 3.6 (c) additionally shows that not only *(2l+1)* possibilities of the angular moment orientation exists, but also two different energy states. This splitting of the energy levels is called Zeeman splitting and represents the heart piece of NMR spectroscopy, as transitions between those levels are induced and measured. The splitting of the energy levels increases with increasing field.

The energy difference of two neighbouring niveaus spins can occupy, is defined by the equation (3.38), with $\hbar$ denoting Planck's constant divided by 2π [51, 56] :

$$\Delta E = \gamma \hbar \boldsymbol{B_0} \tag{3.38}$$

Information about the occupation at thermal equilibrium is given by the Boltzmann statistics, again for a nuclei with $l = 1/2$:

$$\frac{N_\beta}{N_\alpha} = e^{\frac{-\Delta E}{k_B T}} \approx 1 - \frac{\Delta E}{k_B T} = 1 - \frac{\gamma \hbar \boldsymbol{B_0}}{k_B T} \tag{3.39}$$

Compared to the thermal energy, the difference of the energy levels ΔE is rather small, leading to nearly equally occupied energy levels $N_{\alpha,\beta}$ - the difference is in the range of parts per million (ppm). The higher occupation of the level of lower energy N_α, representing magnetic moments aligned to the outer field, is also the reason why the net magnetization $\boldsymbol{M}$ is aligned with the outer field $\mathbf{B}_0$ [51, 56].

Roughly speaking, NMR spectroscopy represents the measurement of the occupation of energy levels by spins. This is done by irradiating the sample with radio frequency pulses (r.f. pulses). To be able to induce a change of occupation, the energy of the r.f. pulse must exactly match the energy difference of the levels, see equation (3.40). The difference is proportional to the frequency of the r.f. pulse ν_1, which has in turn to match the Lamor frequency of the investigated nuclei [51, 56].

$$\Delta E = h\nu_1 \tag{3.40}$$

The transition of lower to higher energy levels, hence absorption of energy, is more probable. This absorption represents the measured signal, being proportional to the difference in occupation and being also proportional to the concentration of spins inside the sample. If energy absorption and emission occurs equally often, no signal is detectable, leading to a state called saturation. [51, 56]

The so far illustrated example, a nuclei with spin 1/2, represents a rather simple case with only two possible energy states. The situation becomes more complex for nuclei with $l \geqslant 1$. More than two energy levels are present, whereby quantum mechanics dictate that only transitions where the quantum number m changes by 1: $\Delta m = \pm 1$ are possible. [51, 56]

3.4.2 Measurement Principles

The most basic NMR experiment, usually called *onepulse*, consists of three pulse program parts, as can be seen in figure 3.7.

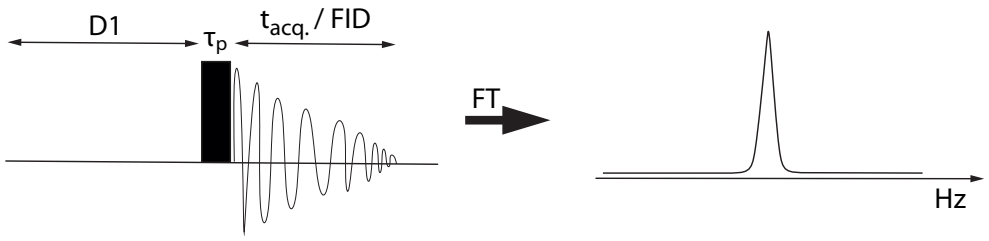

Fig. 3.7: Schematic representation of a onepulse experiment, consisting of a relaxation delay time D1, a r.f. pulse τ_P and the following acquisition time $t_{acq.}$. Fourier transform of the obtained free induction decay (FID) leads to the spectrum seen on the right. Inspired by reference [54].

First, the system is allowed to come to thermal equilibrium during the relaxation delay, denoted as D1. This time is strongly dependent on the investigated material and varies usually from seconds to minutes. The following r.f. pulse τ_p, only lasting for a few μs, originating from the r.f. coil placed usually in the x-axis, deflects the net magnetization away from the z-axis into the x,y-plane. Here, another important parameter is the impulse angle θ, defined by:

$$\theta = \gamma \boldsymbol{B_1} \tau_P \tag{3.41}$$

Practically, the impulse angle within a certain system can be altered by changing the pulse length τ_P.

By applying a r.f. pulse not only the net magnetization is affected, but also the spin occupation of the Zeeman niveaus. A 90° pulse, deflecting the magnetization into the x,y-plane, leads to a equal spin distribution. In contrast to that a 180° pulse, deflects the magnetisation into $-z$-direction and inverts the occupation. [51]

After the r.f. pulse, the x-component of the magnetisation excites a signal in the detector coil, called the free induction decay (FID). The FID is recorded during the acquisition time $t_{acq.}$. Due to the weak signal and hence, a insufficient signal-to-noise ratio, the experiment is conducted several times, making an averaging of the obtained FID possible. [54]

3.4.3 Relaxation

The pulse sequence needed for relaxation measurements differs from the one needed in onepulse experiments. At first 90° pulses destroy the equilibrium magnetisation in z-

direction, before a evolution period τ is taken. Thereafter a 90° pulse is applied to detect the magnetisation in the z-axis as a function of time. The following FID is detected and the amplitudes of the FIDs, after variable τ are analysed, leading finally to the spin-lattice or longitudinal relaxation time T_1. [53, 58, 59] For an outline of the pulse sequence, see figure 3.8.

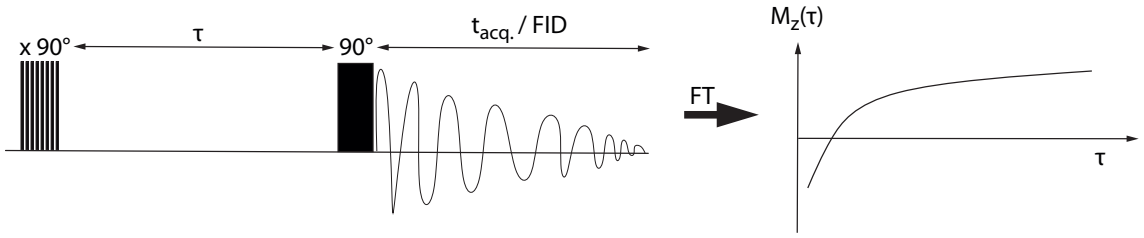

Fig. 3.8: Pulse sequence of an experiment to determine T_1, compromising of a 180° pulse, followed by an evolution time τ, a 90° pulse and the acquisition of the FID, which leads finally to an exponential magnetisation curve. The obtained curve is fitted with a stretched exponential fit to extract T_1. Adapted from reference [55].

The relaxation time T_1 denotes the time, the system needs for returning to thermal equilibrium after the irradiation of the sample with a r.f. pulse. Within this time, $\boldsymbol{M}_z$ becomes $\boldsymbol{M}_0$ again, as described. Furthermore, the spins transfer energy, received during the r.f. pulse, back to the lattice. This relaxation behaviour was analysed mathematically by F. Bloch [60], who described the relaxation in the rotating coordinate system with equation (3.42).

$$\frac{d\boldsymbol{M_z}}{dt} = -\frac{\boldsymbol{M_z} - \boldsymbol{M_0}}{T_1} \tag{3.42}$$

The equation can be altered, if the conditions in the original state $\boldsymbol{M}_t(0) = \boldsymbol{M}_0$ *and* $\boldsymbol{M}_z(0)$ are included [53]:

$$\boldsymbol{M_z} = \boldsymbol{M_0}[1 - e^{\frac{-t}{T_1}}] \tag{3.43}$$

The exponential reversion of the system to the original state is described by this equation. Several time dependent effects influence the relaxation behaviour; Dipole-dipole interactions or quadrupolar electric fields represent the most important ones [53, 55]. These magnetic fluctuations inside the sample, also induced by the diffusion of ions, are dependent on temperature. Therefore the measurement of T_1 is performed as a function of temperature to obtain information about the diffusion behaviour in wide temperature ranges.

The so far mentioned measurements of the spin-lattice relaxation time T_1 allows the

observation of dynamic processes on a short time scale. The relaxation time $T_{1\rho}$, however, reflects processes on a much longer time scale. Values obtained by $T_{1\rho}$ measurements are therefore comparable to those, deduced from impedance spectroscopy, as both sense long range ion dynamics. The pulse sequence of a $T_{1\rho}$ experiments is compromised of a 90° pulse followed by the application of a locking field for a certain time t_{lock}, holding the magnetization in the transversal plane. This locking field operates not in the MHz range as characteristic for T_1 measurements, but at much lower frequencies in the kHz range. After switching off the locking field, the relaxation behaviour is probed by recording a FID [55, 58, 61–63].

Bloembergen, Purcell and Pound were pioneers on this field and introduced the nowadays widely used BPP-Model [64] to analyse relaxation times. The basis of the model builds 3-dimensional (3D) as well as uncorrelated movement of the ions through the (crystalline) sample. The according correlation function *G(t)*, containing temporal information about atomic diffusion processes, is defined via equation (3.44) and again points out an exponential decay [14, 55].

$$G(t) = G(0)e^{-\frac{|t|}{\tau_c}} \tag{3.44}$$

τ_c denotes the motional correlation time of an ion on a crystal site.

As seen in figure 3.9, T_1 measurements carried out over a wide temperature range, give rise to a curve or to be more specific, a diffusion induced rate peak. The spectral density function *J(ω)*, see equation (3.45), is used to fit this rate peak.

$$J(\omega) = G(0)\frac{2\tau_c}{1 + (\omega\tau_c)^2} \tag{3.45}$$

Equation3.45 can also be rewritten:

$$J(\omega) \propto \frac{\tau_c}{(1 + (2\omega\tau_c)^\beta)} \propto T_1^{-1} \tag{3.46}$$

The variable β will be discussed in detail in subsection 3.4.4.

If the ion hopping inside a crystal is not isotropic, occurring in a 3D fashion, respectively, the spectral density function can be adapted. According to Richards P. M. [65], his semi-empirical model, leading to equation (3.47), can be used to fit the diffusion induced NMR rate peak of crystals in which 2D motion occurs.

$$J(\omega) \propto \tau_c ln(1 + \frac{1}{(2\omega\tau_c)^\beta)} \tag{3.47}$$

3.4.4 Interpretation of the Results

The standard presentation of relaxation measurements is an Arrhenius-type logarithmic plot of the inverse times T_1^{-1} or $T_{1\rho}^{-1}$ against $1000/T$. The position of the rate peak in that Arrhenius-type diagram depends not only on the value of T_1^{-1} or $T_{1\rho}^{-1}$ and the temperature, but also on the Lamor frequency and the applied magnetic field. For a visualisation, see figure 3.9.

At low temperatures where the equation $\omega_L \tau_c \gg 1$ is valid, the relaxation rate $1/T_1^{-1}$ increases with increasing temperature until it reaches a maximum. At this maximum the relation $\omega_L \tau_c \approx 1$ holds, as the relaxation rate reaches values in the order of the according Lamor frequency. At higher temperatures where $\omega_L \tau_c \ll 1$ holds, the rates decrease again. As at the maximum of the diffusion induced rate peak the correlation time τ_c is proportional to the inverse Lamor frequency, it can be calculated easily for this temperature. As discussed previously, the correlation time τ_c is needed for the calculation of the diffusion coefficient. The temperature dependent correlation time τ_c follows Arrhenius behaviour and can be described by equation (3.48), with τ_{c0} denoting the pre-factor, E_A the activation energy and k_B the Boltzmann's constant [55].

$$\tau_c = \tau_{c0} \cdot e^{\frac{E_A}{k_B T}} \tag{3.48}$$

Basically all statements made so far, are also valid for relaxation rates $T_{1\rho}^{-1}$ obtained by spin-locking experiments with the difference, that at the maximum of the diffusion induced rate peak, the relation $\omega_1 \tau_c \approx 0.5$ holds, with ω_1 denoting the frequency of the locking field.

It shall be noted that for a given material more than one diffusion induced rate peak can be obtained by T_1 and $T_{1\rho}$ measurements. This is the case, when two different processes govern the diffusion, with correlation times being sufficiently variant to be separated.

Not only the maximum gives valuable information about ongoing diffusion processes, but also the shape of the whole peak. A symmetric diffusion induced rate peak is obtained for diffusion processes, obeying the BPP behaviour, hence uncorrelated, 3D motion of ions through the material. Therefore, the activation energy E_A (see again equation (3.48)) deduced from the slope of the rate peak, equals for the high and low temperature flank. This symmetry leads to a value of $\beta = 2$ in equation (3.46). An asymmetric peak, characterised by $1 < \beta \leq 2$, can have its origin in different circumstances. Disordered materials show a flatter slope at lower temperatures, whereas materials in which restricted 2D motion occurs, at higher temperatures. Also correlated motion leads to asymmetric rate peaks.

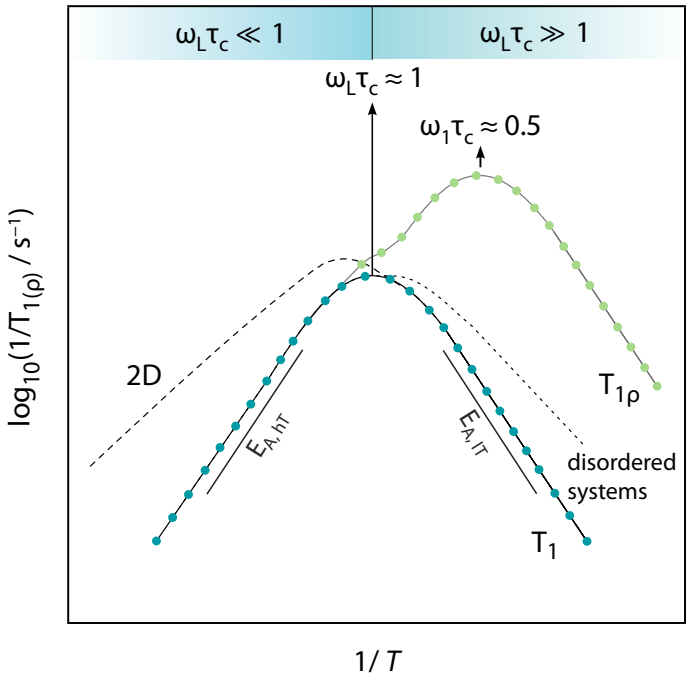

Fig. 3.9: Arrhenius-type representation of relaxation rates $T_{1(\rho)}^{-1}$ showing characteristic diffusion induced rate peaks. At the maximum of these peaks $\omega_L\tau_c \approx 1$ and $\omega_1\tau_c \approx 0.5$ holds for T_1^{-1} (blue dots) and $T_{1\rho}^{-1}$ (green dots), respectively. Spin-locking measurements are characterised by much smaller frequencies ($\omega_1 \ll \omega_L$) compared to the Lamor frequency, leading to maxima at much smaller temperatures, enabling the characterisation of processes occurring at longer time scales. As these processes are usually Arrhenius activated, an activation energy E_A can be deduced from the slope of each rate peak. The whole shape can give further important information about diffusion processes, see text for further explanation. Inspired by reference [55].

The same conclusions can be drawn from $T_{1\rho}^{-1}$ rate peaks, with the maxima being shifted towards lower temperature, due to the smaller frequency of the applied field $\boldsymbol{B}_1$. This enables the detection of slower diffusion processes, which are comparable to the one detained from impedance spectroscopy. It should be noted that the activation energy obtained by NMR can be lower compared to values from impedance spectroscopy due to the fact that not all jumps needed for long-range diffusion are seen in NMR measurements and vice versa.

3.4.5 Magic Angle Spinning NMR

By conducting onepulse experiments in the static set-up, spectra at a certain temperature can be obtained. These spectra are usually composed of broad lines due to anisotropic line broadening, hence not providing structural information, but further insights into the ion dynamics can be retrieved. Spectra recorded in dynamic MAS NMR experiments,

however, can give information about the local structure in crystals.

The anisotropic line broadening originates from nuclear spin interactions as dipole-dipole coupling or quadrupolar coupling in the case of $I > 1/2$ nuclei. Additionally all nuclear spin interactions are dependent on the orientation of the crystallites. While the orientation dependence is averaged in liquid systems by fast molecular movement, it is not in solid systems. Obtaining structural information from solids by NMR is therefore not straightforward [52].

In order to minimize the orientational dependence, the sample is stuffed into a small rotor and spinned at high frequencies, usually around 30 kHz, but up to 111 kHz are possible with high-end probe heads [68]. Thereby the rotor adopts an angle of 54.74° with respect to the outer magnetic field $\boldsymbol{B}_0$. The name of the measurement technique Magic Angle Spinning NMR is derived from this "magic" angle. The reason why exactly 54.74° are needed lies in quantum mechanics and can be found elsewhere [52].

Depending on the investigated nuclei, the anisotropy can not be eradicated completely in each case; Spinning sidebands *e.g.* are commonly found in MAS spectra. They can be, however, identified easily as a strong dependence on the rotation frequency exists [52].

3.4.6 Device Set-up

As discussed, the magnetic moment μ of each individual spin is rather small, with their distribution being nearly isotropic. The detection of such small signals is technically a huge challenge, making complex measuring equipment and a magnet, operating at high field strengths, necessary.

Superconducting, magnetic coils, usually made of Nb or Sn, are immersed into liquid Helium (^{4}He) at a temperature of 4.2 K. To ensure the preservation of such low temperatures, the $\mathrm{He_{liquid}}$ reservoir is surrounded on the one hand by insulation layers and vacuum chambers and on the other hand by another reservoir filled with liquid nitrogen (77 K), see figure 3.10 [56].

As long as the magnet is continuously held at sufficiently low temperatures, it provides a stable, strong magnet field (*e.g.* 23.5 T [69]) without external power sources. The only action needed is the charging with current when setting up the magnet for the first time.

As indicated in figure 3.10 in the middle of the magnet, a bore allows the insertion of different probe heads. They represent the most versatile, yet complex part of a NMR set-up, as, simply by exchanging the head, different experiments are possible, *e.g.* liquid or solid state NMR, temperature variable measurements or Magic Angle Spinning NMR. The probe head does not only position the sample, usually fire-sealed in a glass ampoule, inside the homogeneous part of the magnetic field, it also hosts the needed electronic circuits for conducting experiments. These circuits consist of an high number of different

components, like the transmitter, producing r.f. signals, and the receiver, as the name suggests, receiving the signal and transforming it into a digital one. [56]

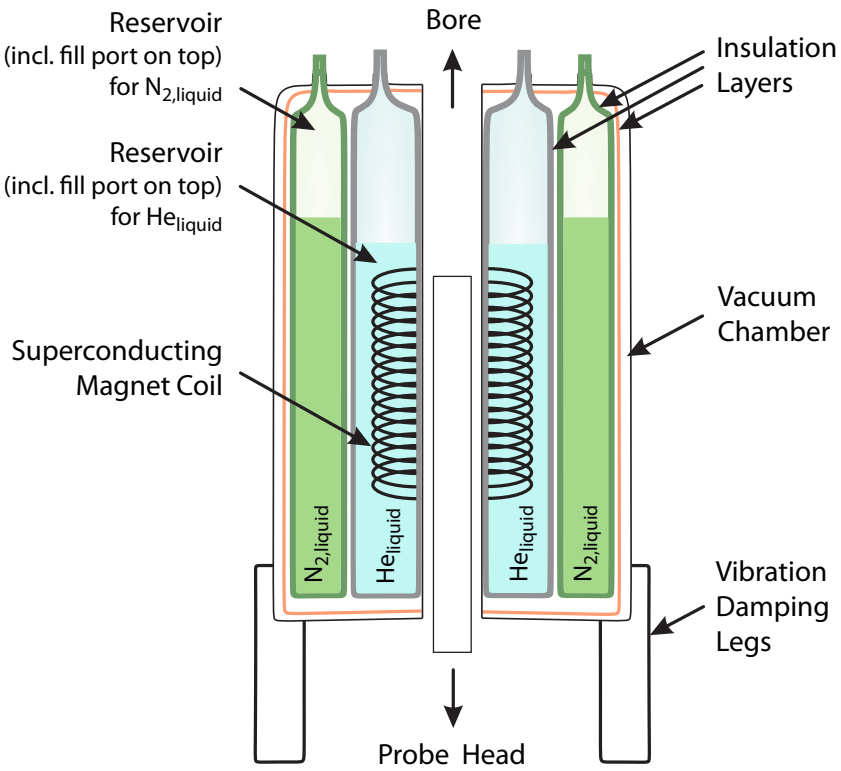

Fig. 3.10: Schematic drawing of a NMR magnet with superconducting coils, being cooled by liquid He. The insulation of the liquid He is realised by another layer of liquid N_2, insulation layers and vacuum chambers. Inspired by reference [70].

Publications in Peer Reviewed Journals and Unpublished Manuscripts

The experimental findings of this thesis are presented in the form of publications in peer reviewed journals and additionally, so far unpublished material in the form of manuscripts and manuscript drafts. During the thesis three material classes, namely Lithium, Fluorine and Silver ion conductors were examined. Hereinafter the results are enlisted, grouped in the stated material classes. Subsequently the publications and manuscripts can be found.

Lithium Ion Conductors

- **Paper 1**: Fast Li ion dynamics in the Mechanosynthesized Nanostructured Form of the Solid Electrolyte Li_3YBr_6
- **Paper 2**: Lithium-Ion Transport in Nanocrystalline Spinel-type $Li[In_xLi_y]Br_4$ as Seen by Conductivity Spectroscopy and NMR
- **Manuscript Draft 1**: Enhanced Ion Dynamics by Interface Engineering in the Dispersed Ionic Conductor LiF:TiO_2
- **Manuscript 1**: Degradation of Single-Crystalline $Li_{6.4}La_3ZrTaO_{12}$ in Humidity: A Nuclear Magnetic Resonance and Neutron Diffraction Study

Fluorine Ion Conductors

- **Paper 3**: Spatial confinement - Rapid 2D F^- diffusion in micro- and nanocrystalline $RbSn_2F_5$

Silver Ion Conductors

- **Manuscript Draft 2**: Temperature stability of the metastable, superionic Ag^+ conductor α^*-Ag_3SI

Preface

Fast Li Ion Dynamics in the Mechanosynthesized Nanostructured form of the Solid Electrolyte Li_3YBr_6

In a constant strive for finding new electrolytes for all-solid-state batteries, Li_3YBr_6 was found to be a promising candidate due its high conductivity at room temperature [1]. We investigated the material with respect to various different features, like structure, phase transitions and macroscopic as well as microscopic dynamics. A major focus was set on structural and dynamic differences between nano- and microcrystalline, which is annealed, Li_3YBr_6. The latter one was subjected to DSC measurements, uncovering a phase transition at $-8°$ approximately, accompanied by a conductivity increase, revealed by impedance spectroscopy. Temperature variable neutron diffraction experiments, performed by Schlem *et. al.* [2], revealed the reason for enhanced dynamics; at 300 K Li resides on the $4g$, $4h$ and $8j$ positions, while at 250 K $8j$ remains unoccupied.

Even though the nanocrystalline Li_3YBr_6 undergoes almost no clearly visible phase transition in the examined temperature range, the conductivity at 20°C remains comparable to that of microcrystalline Li_3YBr_6 (0.44 mS cm^{-1} for nano- vs. 1.52 mS cm^{-1} for microcrystalline Li_3YBr_6). The microscopic dynamics, as probed by static NMR measurements, showed similar results for both materials, while dynamic MAS NMR pointed towards enhanced structural disorder in nanocrystalline Li_3YBr_6.

Concerning sustainability, it was shown that the milling time can drastically be shortened down from 50 h [1] to 1 h, obtaining nanocrystalline Li_3YBr_6, too. The nanocrystalline samples, however, come along with the drawback of high electronic conductivity, making a short annealing step obviously indispensable.

Author Contributions: MG carried out the synthesis of the materials, evaluation as well as the interpretation of the data and wrote the publication. HMRW supervised all steps and helped writing the manuscript.

P1

Fast Li Ion Dynamics in the Mechanosynthesized Nanostructured Form of the Solid Electrolyte Li_3YBr_6

M. Gombotz *and H. Martin R. Wilkening*

ACS Sustainable Chemistry & Engineering, 2021, 9, 2, 743-755
(DOI: 10.1021/acssuschemeng.0c06694)

ACS Sustainable Chemistry & Engineering

pubs.acs.org/journal/ascecg

Research Article

Fast Li Ion Dynamics in the Mechanosynthesized Nanostructured Form of the Solid Electrolyte Li_3YBr_6

Maria Gombotz and H. Martin R. Wilkening*

Cite This: *ACS Sustainable Chem. Eng.* 2021, 9, 743–755

Read Online

ACCESS | Metrics & More | Article Recommendations | Supporting Information

ABSTRACT: The Y-halides Li_3YBr_6 and Li_3YCl_6 have recently gained considerable attention as they might be used as ceramic electrolytes in all-solid-state batteries. Such materials need to show sufficiently high ionic conductivities at room temperature. A thorough investigation of the relationship between ion dynamics and morphology, defect structure, and size effects is, however, indispensable if we want to understand the driving forces behind Li ion hopping processes in these ternary compounds. Li_3YBr_6 can be prepared by conventional solid-state synthesis routes. Nanostructured Li_3YBr_6 is, on the other hand, directly available by mechanosynthesis under ambient conditions. The present study is aimed at shedding light on the question of whether (metastable) mechanosynthesized Li_3YBr_6 might serve as a sustainable alternative to annealed Li_3YBr_6. For this purpose, we studied the impact of structural disorder on ionic transport by combining mechanosynthesis with soft-annealing steps to prepare Li_3YBr_6 in two different morphologies. While structural details were revealed by X-ray powder diffraction and by high-resolution ^{6}Li and ^{79}Br magic angle spinning nuclear magnetic resonance (NMR) spectroscopy, broadband impedance measurements in conjunction with time-domain ^{7}Li NMR relaxation measurements helped us to characterize Li^+ dynamics over a wide temperature range. Interestingly, for Li_3YBr_6, annealed at 823 K, we observed a discontinuity in conductivity at temperatures slightly below 273 K, which is almost missing for nano-Li_3YBr_6. This feature is, however, prominently seen in NMR spectroscopy for both samples and is attributed to a change of the Li sublattice in Li_3YBr_6 Although a bit lower in ionic conductivity, the nonannealed samples, even if obtained after a short milling period of only 1 h, shows encouraging dynamic parameters (0.44 mS cm^{-1}, E_a = 0.34 eV) that are comparable to those of the sample annealed at high temperatures (1.52 mS cm^{-1}, E_a = 0.28 eV). ^{7}Li nuclear magnetic relaxation, being solely sensitive to Li^+ hopping processes on shorter length scales, revealed highly comparable Li^+ self-diffusion coefficients on the order of 10^{-12} m^2 s^{-1}, which we extracted directly from purely diffusion-controlled ^{7}Li NMR rate peaks. Spin-lock ^{7}Li NMR reveals a change from uncorrelated to correlated dynamics at temperatures as low as 220 K.

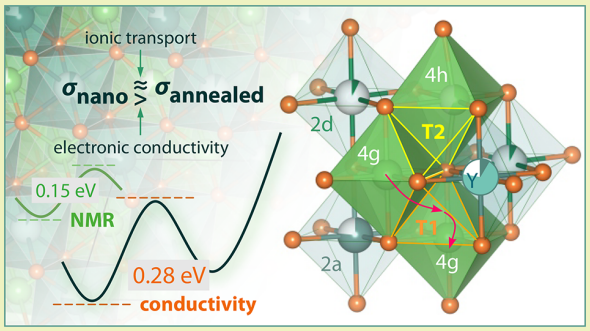

KEYWORDS: *mechanosynthesis, halides, conductivity, NMR, ionic transport, electrolytes*

INTRODUCTION

In the quest of finding new solid electrolytes for all-solid-state batteries, scientists reach out for materials, which could overcome current limitations in ionic conductivity, electrochemical stability, and, thus, compatibility issues with Li metal anodes. Already established classes of materials encompass oxide garnets,[1,2] argyrodite-type thiophosphates,[3,4] and LISICON-type phosphates[5−7] as well as lithium hydrides.[8−10] Still, electrochemical stability issues and obstructive mechanical properties uphold the feverish search for more suitable materials. Furthermore, next-generation electrolytes are to be produced by taking advantage of energy-saving methods.

The characterization and investigation of lithium halides had already been started in the 1980s and 1990s.[11−15] They have, however, gained importance lately as several reports on compounds of the type Li_3MX_6 (Li_3InCl_6,[16,17] Li_3LaI_6,[18] Li_3ErI_6,[19] $Li_3Er(Y)Cl_6$[20]) demonstrated high Li^+ conductivities of up to approximately 2 mS cm^{-1} at ambient temperature. In particular, Li_3YCl_6 and Li_3YBr_6 are considered as promising solid electrolytes with superior properties. Asano et al.[21] reported on (crystalline and partly disordered) Li_3YBr_6 (LYB) as being an auspicious candidate to serve as a solid electrolyte; the two forms are characterized by high chemical stability in inert as well as oxygen atmospheres in a temperature range of up to 623 K. Drawbacks might emerge from a relatively high electronic conductivity of 1×10^{-9} S cm^{-1} [21] and the fact that the electrochemical stability window is limited to 3.15 V.[21,22]

Received: September 11, 2020
Revised: November 18, 2020
Published: December 11, 2020

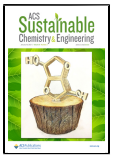

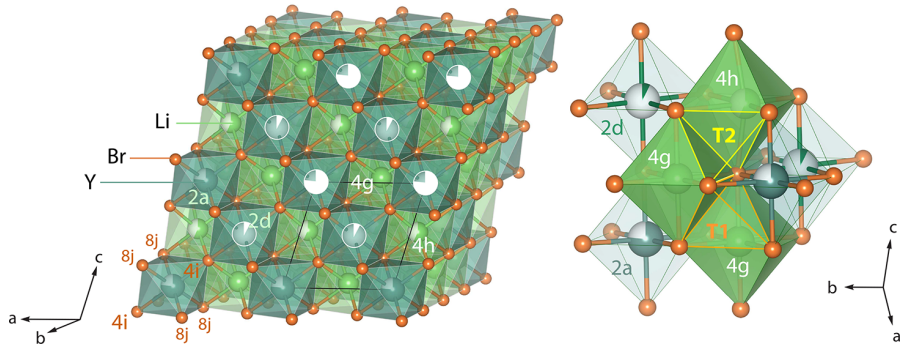

Figure 1. Crystal structure of Li_3YBr_6 (space group $C2/m$) according to the suggestion of Asano et al.[21] that is based on X-ray data. The Li positions refer, thus, to tentative assignments. Nevertheless, the structure provides, from a didactic point of view, first insights into local migration pathways in LYB. The fcc structure and the arrangement of the $LiBr_6$ octahedra allow for an octahedral−tetrahedral−octahedral jump process. Depending on the defect situation and the exact Li (and Y) distribution, Li^+ 4g−4g jumps might have a different activation energy than the 4g−4h jump processes. Exemplarily, tetrahedral voids connecting the Li octahedra are shown. Also (correlated, localized), forward and backward jumps are expected to influence the overall ionic transport. Recently, Zeier and co-workers investigated mechanosynthesized Li_3YBr_6 by neutron diffraction, see Figure 2.[23] Next to differences in Y^{3+} and Li^+ distribution over the available sites, they observed the important occupation of the tetrahedral voids connecting the partially filled 4g sites, as illustrated below.

This value would allow only a limited number of cathode materials to be used in conjunction with LYB. The suitability of annealed, that is, well crystalline, Li_3YBr_6 to act as a powerful solid electrolyte is, however, further underpinned by its high room-temperature conductivity of 1.7 mS cm^{-1}.[21]

An even higher conductivity of 2.2 mS cm^{-1} was predicted from *ab inito* molecular dynamics (AIMD) calculations by Wang et al.[22] These calculations alongside with Rietveld refinement[21] draw a picture of the structure of LYB. Relying on earlier studies, LYB crystallizes with monoclinic structure (space group $C2/m$) with the Li^+ and Y^{3+} ions residing in octahedral sites with one-third of these sites being left vacant. Overall, the structure can be described by a cubic close-packed-like anion arrangement (distorted rock-salt structure), see Figure 1. Quite recently, neutron diffraction has been carried out to refine the structure further.[23] Li^+-ion conduction is expected to occur in all three dimensions. The Li^+ ions jump from one octahedral site to another by passing the tetrahedral sites; two of them are exemplarily marked in Figure 1 as T1 and T2. This situation resembles that in Li_xTiS_2 studied earlier by our group.[24] According to the model by Asano et al., see Figure 1, T1 connects two 4g positions while T2 denotes the void between a 4g site and a partly occupied 4h position. If the octahedral Y-site adjacent to T1 or T2 is occupied by Y^{3+}, the pathway might be influenced due to repulsive interactions. This hypothesis was again supported by AIMD calculations performed by Wang et al.[22]

Quite recently, Zeier and co-workers used variable-temperature neutron diffraction to study the crystal structure of mechanosynthesized Li_3YBr_6 with $C2/m$ symmetry.[23] The exact Li and Y distributions over the available sites seem to depend on the exact synthesis and annealing conditions. As an example, in Figure 2, the structures at 250 K and at 300 K are shown. In contrast to the model by Asano et al., position 2d remains empty in this model; both sites 4g and 4h are partially occupied by Li^+ with Y^{3+} also occupying the 4h position located between the Y-rich sheets. Again tetrahedral voids connect the Li sites (4h and 4g), see Figure 2a. Importantly, at temperatures higher than 250 K, the Li ions continuously occupy the tetrahedral voids (8j), thus introducing a short $Li(4g)_{octa}$−$Li(8j)_{tetra}$ distance of 2.2 Å that is subjected to

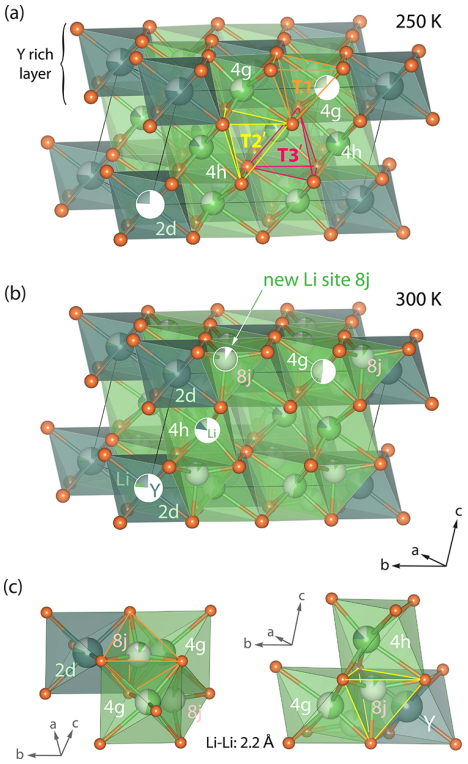

Figure 2. Crystal structure of Li_3YBr_6 (space group $C2/m$) as obtained from neutron diffraction carried out by Schlem et al.[23] (a) At 250 K, the Li ions occupy the sites 4g (73%) and 4h (77%). The 2d remains empty, and Y is distributed over the sites 2a (76%) and 4h (12%). (b) At 300 K, the cation sublattices change with the Li ions starting to occupy the interstitial 8j sites connecting the sites 4g and 4h by face sharing, see c. The occupation of 8j leads to distances of $Li(4g,4h)_{octa}$−$Li(8j)_{tetra}$ of approximately 2.2 Å. Note that 8j shares a common face with the 2d site, which is mainly occupied by Y. Up to 20% of these Y sites remain empty.

repulsive interactions (Figure 2 b). The Li(4g)−Li(4g) distance (3.58 Å) is comparable to the Li(4h)−Li(4g) distance (3.61 Å). The sites Li(4h) in the Y rich layer are, however,

https://dx.doi.org/10.1021/acssuschemeng.0c06694
ACS Sustainable Chem. Eng. 2021, 9, 743−755

separated by 4.62 Å. Although we expect that Li^+ will not occupy the sites 4g and 8j simultaneously, we strongly assume that this structural motif, which is similar to the *frustrated* $8a_{tetra}-16c_{octa}$ situation in spinel-type $Li_{4+x}Ti_5O_{12}$ ($x = 0.3$), is an important structural feature to explain ionic transport in LYB at elevated temperatures. The site 8j connects two 4g sites and the sites 4h and 4g by sharing a common face with the site 2d, which is by 75% occupied by Y. The tetrahedral void called T3′ in Figure 2a, which connects the two 4g sites in the Y poor layer, has no Y cation in its direct vicinity; it is connected to the 2d sites by corner sharing only.

We expect that both the cation disorder, characterized by the partially filled sublattices, and the polyhedra distortions seen in Figure 2c are beneficial for Li^+ transport in the ternary bromide. Taken together, these structural details and the so far conducted calculations on ionic transport make the ternary bromide a highly interesting model substance to precisely study its macroscopic ion transport and microscopic Li^+ hopping processes as a function of temperature.

Here, we used a mechanochemical approach to directly prepare nanocrystalline, structurally disordered Li_3YBr_6 under ambient conditions. In general, mechanosynthesis allows for the synthesis of nonequilibrium compounds. Localized heat and pressure spots ensure preparation conditions that lead to metastable products which are otherwise only accessible at extreme temperature or pressure conditions. Nonequilibrium compounds prepared by high-energy ball milling under dry conditions may show unusual cation (Li^+, Y^{3+}) distributions, as also found for $Li_3Er(Y)Cl_6$,[20] a huge amount of structurally disordered interfacial regions, local distortions, and defect structures that finally determine the overall properties of these types of compounds. Annealing the as-prepared sample yielded highly crystalline LYB that shows macroscopic dynamic properties being similar to those reported earlier.[21] The present study is aimed at shedding light on the question of whether (metastable) mechanosynthesized Li_3YBr_6, prepared using an energy-saving route, might serve as a sustainable alternative to the heat-treated form of Li_3YBr_6. Here, we show that reducing the milling time from 50 h (Asano et al.[21]) to 1 h practically results in the same product with almost the same conduction properties.

Independent of this intention, for both materials, that is, the as-prepared nanostructured form and the microcrystalline sample, a thorough investigation of ion dynamics by means of broadband impedance spectroscopy[25] and time-domain ^7Li nuclear magnetic resonance (NMR) spin−lattice relaxation measurements[26] is still missing. To characterize long-range and local structures, we characterized the samples by X-ray powder diffraction and performed ^6Li and ^{79}Br magic angle spinning (MAS) NMR to reveal local magnetic properties to which the nuclei are subjected. In particular, in both samples, Li^+ ion transport turned out to be fairly fast. Considering microcrystalline LYB, our conductivity and NMR data point to a distinct increase in Li^+ ion dynamics at approximately $T = 263$ K. While this change in ionic conductivity is barely seen for nanocrystalline LYB, ^7Li NMR spin−lattice relaxation was highly useful to visualize the change in ion dynamics that clearly affects Li^+ hopping on a shorter, that is, angstrom length scale. From purely diffusion-induced ^7Li NMR rate peaks, we were able to directly deduce the Li^+ diffusion coefficient of both nano- and microcrystalline LYB. It turned out that the diffusion coefficient D_{Li} of mechanosynthesized, nanostructured LYB, which we prepared under ambient conditions in a high-energy ball mill, is highly comparable to that of the annealed sample. Hence, mechanosynthesized LYB, obtained after a milling time of only 1 h, serves as a promising alternative to microcrystalline LYB. Moreover, we show that the annealing steps to prepare coarse-grained LYB are not needed to achieve high ionic conductivities. However, annealing seems to control electronic conductivity, hence a suitable compromise with regard to thermal treatment has to be found.

EXPERIMENTAL SECTION

Mechanosynthesis of Li_3YBr_6. Synthesis of nanocrystalline LYB was carried out following two different routes, but each time by mixing stoichiometric amounts of LiBr (99.99%, Sigma-Aldrich) and YBr_3 (99.99%, Alfa Aesar), which were dried in a vacuum for 12 h at 60 °C prior to any further handling. The mixture (total of 3 g) was treated in a Fritsch Pulverisette 7 Premium line planetary mill under an Ar atmosphere. We used airtight ZrO_2 beakers (45 mL) equipped with 180 balls (5 mm in diameter) made of the same material. The milling time, according to the procedure described by Asano et al.,[21] was set to 50 h divided into milling periods of 15 min (at 500 rpm). Between each milling period, a break of 15 min was taken to allow the beakers to cool down. Usually, after 15 min of milling, the overall temperature inside the vials does not exceed 333 K. This sample is called nano-50, and if not stated otherwise the nanocrystalline sample refers to this sample. For comparison, and to drastically reduce the milling time, another sample was prepared as follows. The educts (total of 1 g) were mechanically treated by using only 100 milling balls for a time period of only 1 h in total (again 15 min of milling followed by 15 min break). In the following, this sample is called nano-1.

After the synthesis of nanocrystalline Li_3YBr_6, milled for 50 h, a part of the sample powder was pressed into pellets with a diameter of 5 mm and fire-sealed in quartz ampules. The samples were then heated at a rate of 3 K min^{-1} up to 823 K to obtain an annealed, well-crystalline sample. The annealing time was varied from 2 to 6 h and then to 24 h. Due to the high moisture sensitivity of the educts as well as the products, all steps, including filling and emptying of the airtight vials, were strictly carried out inside an argon-filled glovebox (O_2, H_2O < 0.5 ppm) to avoid any contamination with water vapor or oxygen.

X-ray Powder Diffraction and DSC Measurements. The X-ray powder diffraction (XRPD) patterns were collected from LYB directly after milling, as well as after annealing for different times. The diffractograms were recorded at ambient pressure, room temperature, and with an airtight sample holder, in which the sample was covered with Kapton foil. To record the diffractograms, a Bruker D8 Advance diffractometer with Bragg−Brentano geometry and Cu Kα radiation (1.5406 Å) was used. Patterns were recorded from 10 to 100° 2θ with a step size of 0.02° 2θ with a measuring time of 1 s for each step. To determine the nature of the phase transition seen in impedance spectroscopy, differential scanning calorimetry (DSC) was performed with a PerkinElmer DSC 8500 calorimeter. The temperature program with a cooling and heating rate of 5 K min^{-1} was −60 °C up to 80 °C (5 min hold) followed by a cooling period down to −60 °C.

Conductivity Measurements and DC Polarization. The overall conductivity was determined by alternating current impedance spectroscopy. For this purpose, approximately 60 mg of the powder sample was pressed into cylindrical pellets with a final diameter of 5 mm. We applied uniaxial pressure by using a hand press (approximately 0.5 tons). Ion blocking electrodes (Pt) with a thickness of 100 nm were applied via sputtering using a Leica sputter device (EM SCD050). The final pellet sandwiches between Pt electrodes were then placed in a home-built airtight sample holder which was placed in an active BDS 1200 cell (Novocontrol) connected to a broadband impedance spectrometer (Novocontrol, Concept 80). To control the temperature, which was varied between 173 and 453 K, a QUATRO cryosystem was employed. This system is

https://dx.doi.org/10.1021/acssuschemeng.0c06694
ACS Sustainable Chem. Eng. 2021, 9, 743−755

able to control the temperature accurately by a heated gas flow generated by freshly evaporated and dry N_2 gas. The gas flow continuously flushes the sample chamber and ensures a constant temperature inside. The frequency range covered was 10^{-2} to 10^7 Hz. Data analysis was carried out with IGOR Pro software (Wavemetrics).

Direct current (DC) polarization measurements were carried out to determine the electronic conductivity. The corresponding powders were pressed into cylindrical pellets with a diameter of 5 mm by applying uniaxial pressure of approximately 0.5 tons using a hand press. The final thickness of the pellets was measured with a vernier caliper and turned out to be 1.27 mm for nanocrystalline Li_3YBr_6 and 0.72 mm for the microcrystalline sample. Ion blocking electrodes of Pt (50 nm) were applied by using a Leica sputter device, see above. The samples were mounted in Swagelok-type cells and placed into a climate chamber with a temperature of 20 °C. The cells were connected to a Parstat MC potentiostat (Princeton Applied Research) in combination with a low-current option. Measurements were recorded at a constant voltage of 100 mV.

High-Resolution ^{6}Li and ^{79}Br MAS NMR. ^{6}Li and ^{79}Br MAS NMR spectroscopy were performed on a Bruker Avance III 500 spectrometer connected to an Ultrashield 500 MHz widebore magnet with a nominal field of 11.74 T. This magnetic field results in resonance frequencies of 73.6 MHz for ^{6}Li and 125.3 MHz for ^{79}Br, respectively. The sample powders of LYB obtained either directly after milling or after the annealing step at 823 K (2 h) were stuffed into two 2.5 mm rotors made of ZrO_2 each. A suitable Bruker MAS probe was used to acquire the corresponding free induction decays within a single-pulse experiment. For this purpose, the sample was spun at 25 kHz with a target gas flow of 400 L h^{-1}. For the variable-temperature ^{6}Li MAS NMR measurements, the temperature of the bearing gas was varied from 253 to 303 K.

Static, Time-Domain ^{7}Li NMR Measurements. For the determination of the ^{7}Li NMR spin−lattice relaxation rates $1/T_1$ and $1/T_{1\rho}$, the powder samples (nanocrystalline LYB and annealed LYB (2 h, 823 K)) were fire-sealed in glass cylinders with a length of approximately 3 cm and a diameter of 4 mm. ^{7}Li NMR rates were measured with an Avance III 300 NMR spectrometer connected to an ultrashielded 300 MHz magnet (7.04 T, Bruker). This magnetic field corresponds to a ^{7}Li Larmor frequency of 116.6 MHz. For the variable-temperature measurements from 173 to 473 K, a ceramic probe head, designed to withstand temperatures as high as 573 K, was used. The laboratory-frame NMR spin−lattice relaxation rates $1/T_1$ were recorded with the saturation recovery pulse sequence, using $\pi/2$ pulse lengths varying from 2.42 to 2.54 μs for the as-prepared LYB and from 2.65 to 2.86 μs for the annealed sample. The transients $M_z(t_d)$ were evaluated with stretched exponentials $M_z(t_d) \propto 1 - \exp(-(t/T_1)^{\gamma})$ with $0 < \gamma \leq 1$. Additionally, spin-lock rates $1/T_{1\rho}$ were recorded in the same temperature window. The pulse sequence used was introduced by Slichter and Ailion.[27−29] In this experiment, the locking frequency $\omega_1/2\pi$ was set to $\omega_1/2\pi \approx 20$ kHz. Again, stretched exponentials $M_\rho(t_{lock}) \propto \exp(-(t_{lock}/T_{1\rho})^{\gamma_\rho})$ with $0 < \gamma_\rho \leq 1$ were used to analyze the transients and to finally determine $1/T_{1\rho}$.

RESULTS AND DISCUSSION

XRPD to Characterize the Long-Range Structure. To characterize long-range order of the samples prepared, we recorded XRPD patterns immediately after the milling step. The corresponding pattern of mechanosynthesized, i.e., nanocrystalline, Li_3YBr_6 (nano-50) is shown in Figure 3; it coincides with that of nano-1. Abrasion of ZrO_2 seems to be negligible. Broad reflections reveal a nanostructured sample[30] whose mean crystallite size can be estimated with the equation introduced by Scherrer.[31,32] In general, broadening of the reflections is caused by two phenomena: (i) nanometer-sized crystallites and (ii) strain. Ignoring the influence of the latter, the Scherrer equation yields an average crystallite size $\langle d \rangle$ of 6 to 10 nm for the as-milled sample. We used the reflections (002), (131), and (33−1) to estimate $\langle d \rangle$. Although the broad

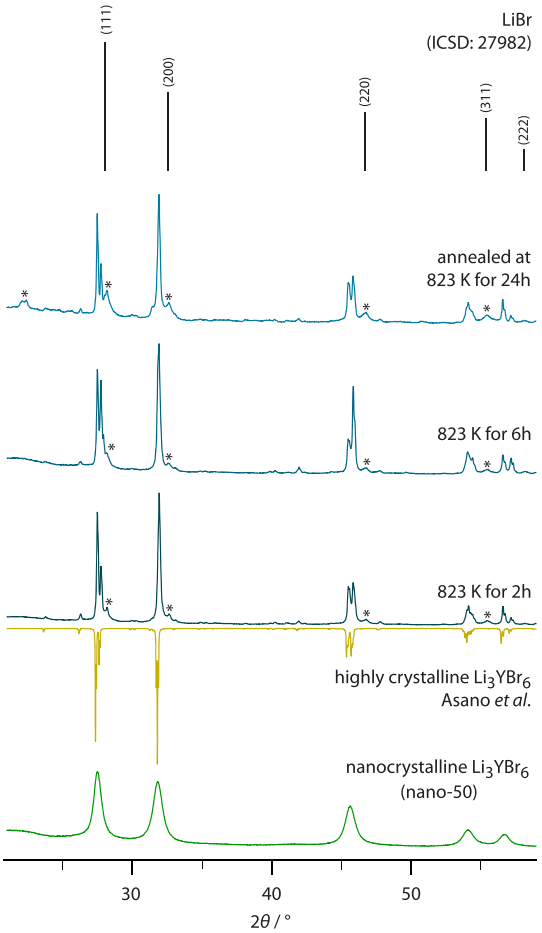

Figure 3. X-ray powder diffractograms of mechanosynthesized (nano-50) and annealed Li_3YBr_6 crystallizing with the monoclinic space group $C2/m$. The sample nano-1 shows the same pattern (not displayed) as nano-50. The annealed samples were heat-treated at 823 K for the durations indicated (2, 6, and 24 h). During the XRPD measurements, the samples were covered by Kapton foil to prevent any reaction with humid air. For comparison, the XRPD pattern of crystalline LYB presented by Asano et al.[21] is also shown. Compared to this pattern, the diffractograms of the annealed samples reveal reflections of low intensity pointing to a very small amount of impurity phases. The sample annealed for 2 h was chosen for further analysis by impedance spectroscopy and NMR measurements.

reflections hinder a detailed structural analysis, we can safely conclude that the educts were successfully converted to LYB as the reflections of nano-Li_3YBr_6 do clearly resemble those of coarse-grained Li_3YBr_6 (see also Figure 3) in both intensity and position on the °2θ scale. Asano et al.[21] suggested that, according to the intensity ratio of the reflections, crystalline LYB is best described with a distorted Y^{3+} distribution. The importance of cation distribution has also been emphasized by Zeier and co-workers, who studied geometry−conductivity relationships for Li_3ErCl_6 and Li_3YCl_6.[20] As mentioned above, a recent neutron diffraction study[23] showed the importance of the sample history on cation distributions in LYB.

Annealing the nanocrystalline sample for 2 h at 823 K causes the reflections to narrow as the crystallite sizes increase to $\langle d \rangle$ > 90 nm. Again, this value has roughly been estimated with the Scherrer equation by evaluating the reflections $(13\bar{1})$, (131), and $(26\bar{2})$. We notice that, upon annealing, new reflections

https://dx.doi.org/10.1021/acssuschemeng.0c06694
ACS Sustainable Chem. Eng. 2021, 9, 743−755

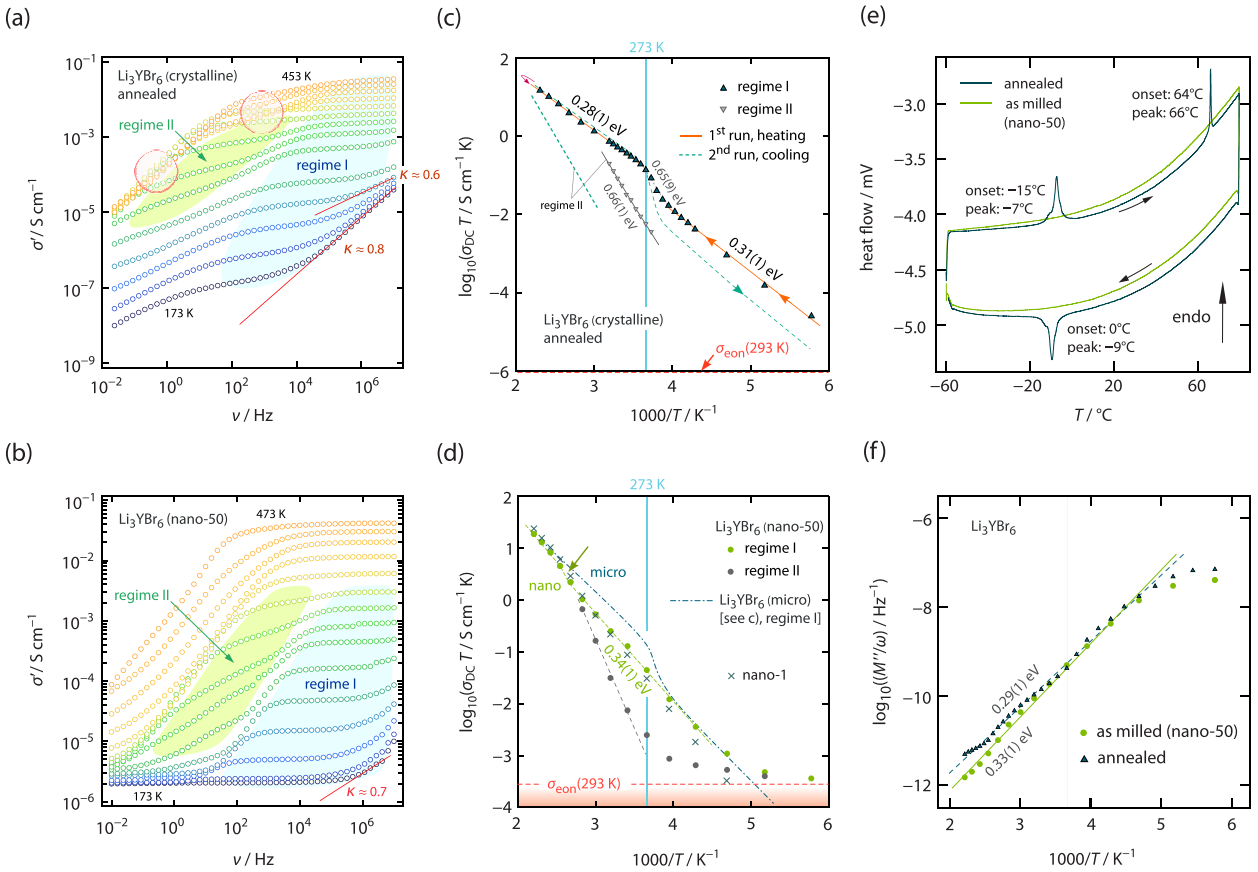

Figure 4. (a) Conductivity isotherms of annealed Li_3YBr_6 (heating run) recorded at temperatures ranging from 173 to 453 K in steps of 20 K. At low temperatures and high frequencies, the isotherms can be approximated with Jonscher's power law ($\sigma' \propto \nu^{\kappa}$) resulting in $0.6 < \kappa < 0.8$ (see solid lines). At temperatures below 333 K, the "direct current" (DC) plateaus split up into two frequency independent regions, which we attribute to the electrical responses in the bulk regions (regime I, associated capacities C lie in the pF range) and in regions affected by grain boundaries (regime II, capacities in the nF range). At lower frequencies, polarization effects appear that result in a strong drop in conductivity. (b) Conductivity isotherms of mechanosynthesized Li_3YBr_6 (heating run), measured under the same conditions as in part a but up to 473 K. Below 373 K, two DC plateaus are visible; regime I again points to bulk properties. (c and d) Arrhenius plots of the DC conductivities read off from the distinct plateaus (I and II) in parts a and b; data for the nano-1 LYB sample (regime 1) are included as well. In c, the change in conductivity of regimes I and II during heating and cooling is illustrated (arrows show the direction of measurements); in d, the Arrhenius line belonging to annealed LYB is also included (see dashed-dotted line). (e) Results from DSC measurements of the two samples. (f) Real part of the complex resistivity ρ', expressed as M''/ω of nanocrystalline and annealed Li_3YBr_6 vs $1000/T$; ρ' was measured at a fixed frequency of 100 Hz.

with rather low intensity appear, which are marked by asterisks in Figure 3. Most likely, they indicate the presence of residual (or reformed) LiBr. Since LiBr is a very poor ionic conductor, we suppose that its contribution to (bulk) ion dynamics and Li^+ diffusivity probed by NMR is negligible. It might increase the grain boundary resistance of the impedance pellets, see below. As the amount of these side phases increases with annealing time, we suppose that they not only were hidden in the pattern of nano-Li_3YBr_6 but reveal decomposition products forming upon heat treatment. The amount of these side phases increases from 10% (2 h) to 20% (24 h); their occurrence identifies LYB as a heat-sensitive compound. Decomposition is not only indicated by the appearance of additional reflections but also by a change in intensities of some of them, see, e.g., the signals at 28° 2θ. As the sample annealed for only 2 h is characterized by a very low amount of impurities, it was selected for further investigations by NMR and impedance spectroscopy.

Conductivity Measurements. Macroscopic transport of Li ions in nanocrystalline and annealed LYB was investigated via broadband impedance spectroscopy. The corresponding isotherms, that is, the real part σ' of the complex conductivity plotted versus frequency ν, are depicted in Figure 4a and b. Coming from high temperatures, the isotherms exhibit distinct frequency independent plateau regions which refer to the so-called direct current (DC) region. With decreasing temperature, the DC plateau characterizing electrical bulk properties (regime I) is only seen at high frequencies. At lower frequencies, grain boundaries and polarization effects increasingly govern $\sigma'(\nu)$ (see regime II). At high temperatures, see the isotherm recorded at 453 K of annealed Li_3YBr_6, strong electrode polarization dominates the shape of $\sigma'(\nu)$; as an example, from $\nu = 10^2$ Hz to $\nu = 10^{-2}$ Hz, the conductivity σ' decreases by 3 orders of magnitude. This strong drop in σ' reveals that Li^+ ions are the main charge carriers in LYB in this temperature range. The same is true for nanocrystalline LYB (nano-50), although the drop in conductivity in the polarization regime turned out to be somewhat less pronounced. In the high-frequency range of regime I, dispersive behavior of $\sigma'(\nu)$ is seen which can be approximated with Jonscher's

https://dx.doi.org/10.1021/acssuschemeng.0c06694
ACS Sustainable Chem. Eng. 2021, 9, 743−755

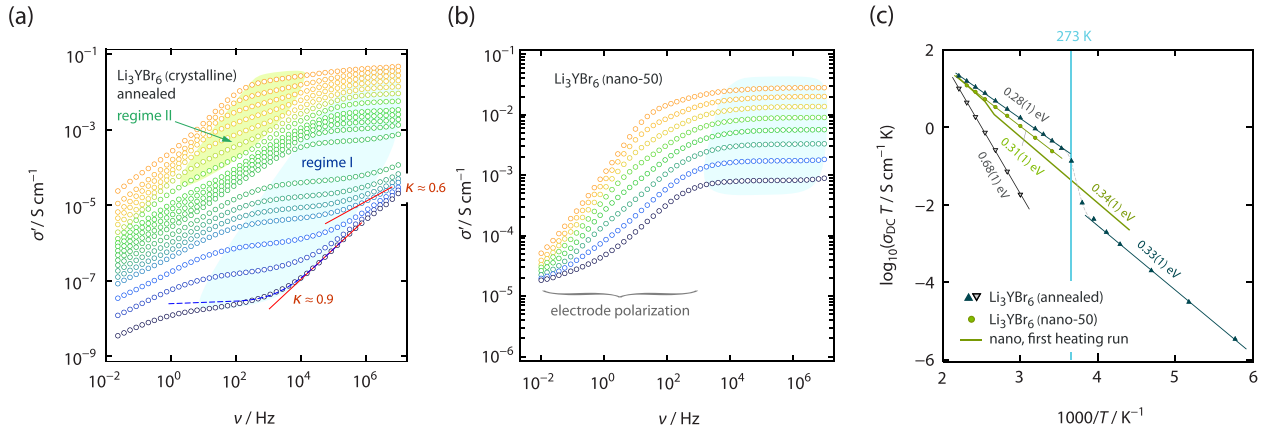

Figure 5. (a) Conductivity isotherms of annealed Li_3YBr_6 (cooling run, 453 to 173 K). (b) Isotherms of the nanostructured, as-milled sample (nano-50) recorded during the cooling run, that is, at temperatures ranging from 453 to 293 K. Above 333 K, the two DC contributions seen in a can be separated from each other, which yield the conductivities shown in the Arrhenius plot, see c. (c) The conductivity regimes follow quite different Arrhenius lines with activation energies of 0.28(1) eV and 0.68(1) eV; while the first is, again, ascribed to bulk ion dynamics, the latter is assumed to characterize ionic transport involving grain boundary regions. For comparison, the conductivity values of the nano-50 sample are shown too.

power law:[33] $\sigma' \propto \nu^{\kappa}$. Solid lines in Figure 4 visualize the power-law dependence; κ values of approximately 0.7 clearly point to 3D Li^+ pathways in LYB.[34] The dispersive regime has frequently been interpreted as a fingerprint of forward and backward jumps of the ions that proceed on a short length scale.[35−37] κ values close to 1 indicate the well-known nearly constant loss behavior in conductivity spectroscopy.[38−41]

Interestingly, the isotherms of nano-LYB (nano-50, see Figure 4b) become almost temperature independent below 193 K and indicate that other charge carriers than Li^+ take part in overall electrical conduction. In this temperature regime, electrode polarization is almost absent; thus, we anticipate that electrons, being able to enter the Pt electrodes, may dominate σ'. For the almost frequency independent isotherms recorded at the lowest temperatures, see Figure 4b, the original DC plateaus cannot be distinguished any longer. At the lowest temperature measured, the final (total) conductivity $\sigma_{DC,total}$ of nano-LYB turned out to be on the order of 2×10^{-6} S cm^{-1}. An independent polarization measurement with a constant voltage amplitude of 0.1 V yielded 0.88×10^{-6} S cm^{-1} at room temperature (see Figure S2). This value solely reflects the electronic conductivity, σ_{eon}. Assuming that σ_{eon} does depend only weakly on temperature, one might assume that the final conductivity measured at 173 K is almost fully determined by σ_{eon}. At ambient temperature, the ratio $\sigma_{eon}/\sigma_{total} = 2 \times 10^{-3}$, showing that, under ambient conditions, 0.2% of the total conductivity is governed by electronic conduction. For annealed LYB, the situation is different: the polarization measurement at 293 K yielded $\sigma_{eon} = 3.0 \times 10^{-9}$ S cm^{-1} (see Figure S2). At this temperature, the total conductivity is 1.25 mS cm^{-1}, resulting in a ratio $\sigma_{eon}/\sigma_{total}$ of 2.4×10^{-6}, which corresponds to a transference number close to 1 for Li^+ ions. Values of σ_{eon} for the two samples are each indicated in Figure 4c and Figure 4d. They clearly reveal that nano-LYB suffers from a relatively high electronic conductivity, which is unwanted for solid electrolytes that shall act as electronic insulators.

In Figure 4c and d, we plotted the DC conductivities as $\sigma_{DC}T$ vs $1000/T$ to find out whether they follow (linear) Arrhenius behavior. Above 273 K, the conductivities of both samples, annealed LYB and nano-LYB (nano-50 and nano-1), follow Arrhenius behavior with comparable activation energies, viz., 0.28(1) eV and 0.34(1) eV. These values are lower than those reported earlier.[21] A value of 0.28(1) eV is, however, in excellent agreement with the value predicted by AIMD simulations performed by Mo and co-workers (0.28(2) eV).[22] The agreement supports the idea of 3D connected octahedral−tetrahedral−octahedral (O−T−O) pathways in LYB, see above.[22] Obviously, Li^+ ions jump between their regularly occupied Li sites via the empty or only partially occupied tetrahedral sites, as indicated in Figure 2. We attribute the kink in $\sigma_{DC}T$ seen for annealed LYB to changes in cation distributions as revealed by neutron diffraction.[23] Above 300 K, the 8j sites are increasingly occupied by Li^+ ions facilitating long-range ionic transport (Figure 2). As mentioned above, the total conductivity σ_{DC} reaches a value of 1.52 mS cm^{-1} at 293 K; this value is comparable to that reported earlier by Asano et al. (1.70 mS cm^{-1}).[21]

Considering the whole temperature range covered in Figure 4c, it becomes obvious that, when coming from low temperatures, the annealed sample undergoes a jump in bulk conductivity at approximately 260 K. This jump is also seen in DSC measurements (see Figure 4e). The transition regime (253 to 278 K) connects two conductivity Arrhenius lines with the activation energies E_a indicated in Figure 4c. Since the activation energies of the two regimes, the poorly conducting LYB (0.31 eV) and the highly conducting LYB (0.28 eV), are very similar, the increase in σ_{DC} is predominantly given by an increase of the pre-exponential factor σ_0 included in the underlying Arrhenius relation $\sigma_{DC}T = \sigma_0 \exp(-E_a/(k_BT))$. For the samples annealed for longer periods (6 and 24 h), the change in overall (ionic) conductivity is very similar (see Figure S1). We did not observe a strong change in conductivity as a function of annealing duration. A second run, that is, the cooling run, see dashed lines in Figure 4c, has only little effect on the conductivity of annealed LYB (2, 6, 24 h) above ambient temperature, it mainly changes ionic transport below 263 K and significantly affects the ionic conductivity in regime II. The corresponding isotherms are shown in Figure 5a.

https://dx.doi.org/10.1021/acssuschemeng.0c06694
ACS Sustainable Chem. Eng. 2021, 9, 743−755

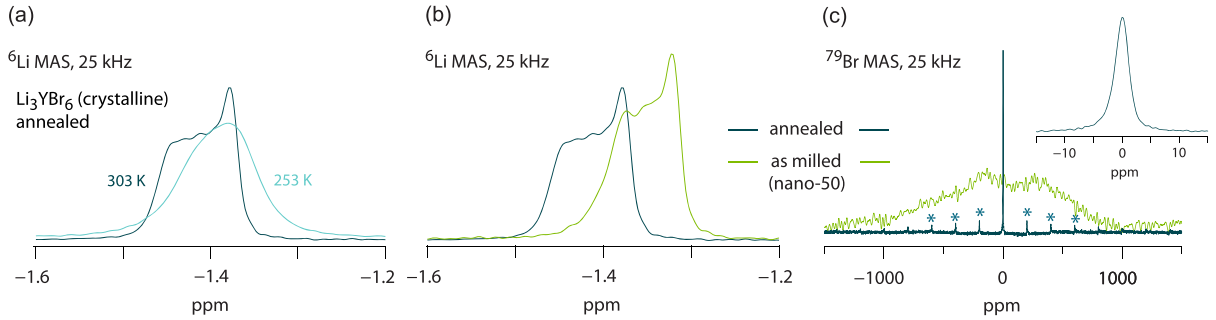

Figure 6. (a) ^{6}Li MAS NMR spectra of annealed Li_3YBr_6 recorded at a spinning speed of ν_{rot} = 25 kHz and at temperatures of 303 and 253 K. (b) ^{6}Li MAS NMR spectra of nanocrystalline (as milled) and annealed (microcrystalline) Li_3YBr_6 (25 kHz, 303 K). The spectra were referenced to the chemical shift of solid $LiCH_3COO$ (0 ppm). (c) ^{79}Br MAS NMR spectra of the two Li_3YBr_6 samples (25 kHz at 303 K). Compared to the annealed sample, the signal of nanocrystalline LYB is characterized by an extremely broad line; spinning sidebands are marked by asterisks. The main signal of annealed LYB was arbitrarily set to 0 ppm. The inset shows that a single (isotropic) line is seen for this sample in agreement with the crystal structure.

In the case of nonannealed nano-LYB (nano-50 and nano-1) the step in σ_{DC} (first heating run) turned out to be almost invisible, see Figure 4 d). Importantly, in terms of conductivity values σ_{DC}, there is no difference between the nano-50 and the nano-1 sample. Obviously, ionic transport in the low-T modification of nano-LYB is enhanced but does not exceed that of the annealed sample. Most likely, structural disorder and Li^+ dynamics in the interfacial regions are responsible for this behavior, see below. Around 260 K, the $\sigma_{DC}T$ of nano-LYB (nano-50) follows Arrhenius behavior, resulting in an activation energy of 0.34(1) eV during the heating run and 0.31(1) eV during the subsequent cooling run (see Figure 5b for the isotherms and Figure 5c for the corresponding Arrhenius lines of the two runs). The total (bulk) conductivity rises from 0.44 mS cm^{-1} (first heating run) to 0.81 mS cm^{-1} (cooling run) and is, therefore, comparable with values for less crystalline LYB presented in the literature earlier (0.72 mS cm^{-1}).[21] This increase in conductivity after the heating run can be attributed to soft annealing effects and *in situ* healing of (point) defects during the conductivity measurements, see also the small kink in the Arrhenius line that the arrow in Figure 4d is pointing at. The different measurement runs reveal the heat-sensitivity of LYB in terms of its transport properties. Presumably, ionic conductivity is tightly connected to cation distributions and defect structures in LYB, which may sensitively depend on synthesis conditions.[20]

Interestingly, ionic transport in nanocrystalline LYB does not exceed that of its crystalline counterpart. Many other examples have been presented in the literature showing that poor (oxide, fluoride, and even sulfide) conductors can be converted into materials with enhanced ionic conductivity.[42−47] These enhancements were usually attributed to defects introduced during ball milling; furthermore, ion transport in nanocrystalline materials may benefit from interfacial ion dynamics[48] and space charge regions[49,50] providing sources for facile ion transport. Here, the crystalline structure of LYB is slightly superior to the nanocrystalline form revealing that the above-mentioned O−T−O migration pathway governs bulk ion transport rather than interfacial effects.

Finally, we used electric resistivity measurements to directly compare the transport behavior of the two model compounds. When plotting ρ', expressed as M''/ω and measured at a fixed frequency of ν_ω = 100 Hz,[3,51] against the inverse temperature, only a single (bulk) electrical relaxation process becomes evident for each sample, see Figure 4f. Usually $\rho'(1/T)$ passes through a rate peak, which is symmetric in shape for uncorrelated 3D ionic motion. The maximum of the peak appears at T_{max} for which the electrical relaxation rate is in the order of ν_ω. Here, the maximum becomes apparent at 173 K. The high-temperature flanks of the two peaks shown in Figure 4f are governed by activation energies (0.29(1) eV and 0.33(1) eV) which agree very well with those deduced from σ_{DC}. This similarity supports our finding that both forms of LYB are to be characterized by very similar dynamic processes.

By comparing the regions of the isotherms that refer to g.b. responses and interfacial effects, we see that annealing does influence not only bulk regions but also these electrical regimes. This feature is highlighted in Figure 4a by circles; the data points reveal that interfacial and g.b. effects irreversibly change with temperature for the annealed sample. For instance, some isotherms measured at high temperatures point to a lower conductivity than found at lower T. This discontinuity might also reflect stability issues of the LYB electrolyte against the Pt electrode. Similar effects have been observed for fluorine-containing solid electrolytes in combination with different electrode materials.[52]

Characterization by NMR. *Local Structures As Seen by ^{6}Li and ^{79}Br MAS NMR.* Additionally to X-ray powder diffraction, ^{6}Li and ^{79}Br magic angle spinning NMR, see Figure 6, was performed to elucidate not only the local structure in the two forms of LYB, but also to get further insight into ion dynamics. Here, we also made use of temperature variable measurements, which we especially used to investigate any structural changes associated with the increase in conductivity at approximately 260 K.

Above the transition temperature, that is, at 303 K, a complex ^{6}Li (spin quantum number I = 1) NMR line is observed, which is most likely composed of at least three contributions including motionally coalesced lines. Indeed, the crystal structure of LYB points to three magnetically distinct Li sites, see above. The fact that the signal on the left (located near −1.38 ppm) is narrower (full width at half height (Δ_{fwhh}) = 0.6 ppm) than that shifted toward more negative parts per million values indicates that some of the Li ions have access to faster exchange processes than others. The narrow signal might reflect Li ions on the partially filled positions such as 4g and 8j, see above. As mentioned above, we assume that these ions, in

https://dx.doi.org/10.1021/acssuschemeng.0c06694
ACS Sustainable Chem. Eng. 2021, 9, 743−755

conjunction with the Y^{3+} site disorder, play a decisive role in explaining the jump in ionic conductivity in annealed LYB. The involvement of 4h sites would result in 3D ionic transport. NMR intensity in between the outer signals is interpreted as a coalesced NMR line because of exchange between the dynamically distinct spin reservoirs. The nonuniform MAS line suggests a distribution of diffusion pathways. At lower temperatures, we recognize that the decrease in Li diffusivity leads to a dipolarly broadened NMR line even under the MAS conditions applied, which already eliminate the main part of the first-order (dipolar) Li−Li interactions. The change in ^{6}Li MAS NMR line shape above and below the transition temperature directly reflects the change of the Li sublattice in LYB as proposed by neutron diffraction.[23] The shape of the NMR line indicates the presence of at least two magnetically distinct Li spins.

The same features are seen for the nonannealed, nanocrystalline sample, see Figure 6b. The shape of the corresponding ^{6}Li NMR line of nano-LYB almost coincides with that of the annealed sample. The overall line of nano-LYB is shifted by 0.06 ppm toward more positive parts per million values, indicating only slight (local) magnetic changes for the ^{6}Li nuclei.

In contrast, the ^{79}Br probe (I = 3/2) clearly reveals that nano-LYB is greatly determined by structural disorder, including point defects and polyhedra distortions, see Figure 6c. While the ^{79}Br MAS NMR spectrum of annealed LYB is composed of a single sharp resonance with a fwhh of only 2.77 ppm (see also the corresponding inset), MAS NMR of nano-LYB yields an extremely broad resonance characterized by Δ_{fwhh} = 1000 ppm. Local point disorder and distortions, sensitively sensed by the ^{79}Br nucleus with its strong quadrupole moment, are responsible for a wide distribution of dipolar magnetic (and electric quadrupolar interactions). Such a distribution of NMR intensities was also observed for various fluorides[25,53] and oxides.[42,54,55] These interactions are much smaller for the ^{6}Li nucleaus which is, in contrast to the anions, subjected to motion-induced averaging phenomena.

^{7}Li NMR Relaxation Rates. To describe Li^+ ion dynamics on the angstrom length scale, we recorded diffusion-induced ^{7}Li NMR spin−lattice relaxation rates in both the laboratory frame of reference ($1/T_1$) and in the rotating-frame of reference ($1/T_{1\rho}$). The rates describe the recovery of longitudinal and (spin-lock) transversal magnetization that is induced by magnetic and electric spin fluctuations controlled by diffusive motions of the ^{7}Li nuclei. The spin fluctuations are generally described by the correlation function $G(t')$; its Fourier transform yields the spectral density function $J(\omega)$. The rate $1/T_1$ is directly proportional to $J(\omega = \omega_0)$, where ω_0 denotes the angular Larmor frequency that is defined by the external magnetic field B_0 and the magnetogyric ratio γ_μ of the ^{7}Li spin: $|\gamma_\mu B_0| = |\omega_0|$. The temperature dependent rates $1/T_{1(\rho)}$ were directly extracted from magnetization transients $M_{1(\rho)}(t_{(lock)})$ recorded at fixed Larmor frequency; M usually follows a stretched exponential behavior.[56,57] If purely induced by diffusion processes, the rate $1/T_1(1/T)$ when plotted as $\log(1/T_1)$ vs the inverse temperature $1/T$ passes through a peak whose position on the reciprocal temperature scale is located at T_{max}. At T_{max}, the condition $\tau\omega_0 \approx 1$ holds;[24,26,58] τ is the mean Li^+ residence time. It is within a factor of 2 identical with the correlation time τ_c governing $G(t')$. The jump rate τ^{-1} usually follows Arrhenius behavior according to $\tau^{-1} = \tau_0^{-1} \exp(-E_{a,NMR}/(k_B T))$; τ_0^{-1} is the Arrhenius prefactor containing the attempt frequency, $E_{a,NMR}$ is the NMR activation energy, and k_B denotes Boltzmann's constant.

The change of $1/T_1$ with temperature (173 to 473 K, heating run only) of both nano-LYB and its annealed counterpart is shown in Figure 7a. When coming from low

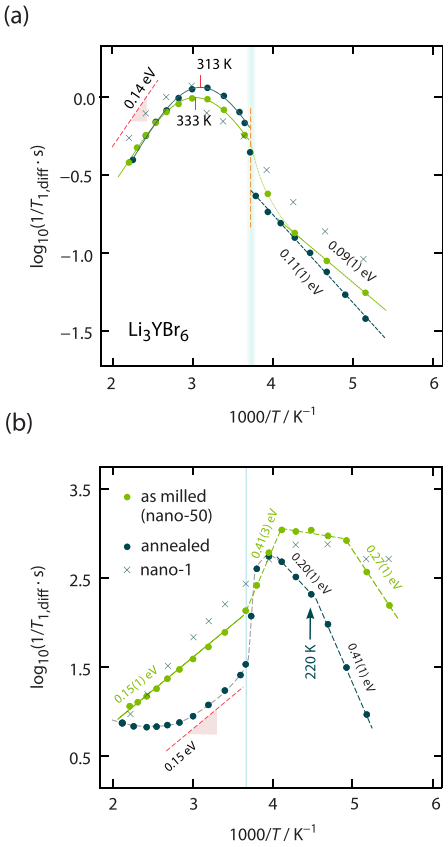

Figure 7. (a) Diffusion-induced ^{7}Li NMR relaxation rates $1/T_1(1/T)$ (116 MHz) of nanocrystalline (as milled, nano-50) and annealed Li_3YBr_6. The dashed lines represent fits according to the Arrhenius law. Solid lines show BPP fits used to extract activation energies $E_{a,NMR}$ in the high-T form of LYB. (b) Temperature dependence of the ^{7}Li NMR spin-lock rates $1/T_{1\rho}(1/T)$ recorded at $\omega_1/2\pi$ = 20 kHz. Values shown refer to activation energies in the respective temperature ranges. See the text for further explanation. The sharp kinks seen for the annealed sample are less pronounced for the nano-1 sample, which reveals smooth transitions.

temperatures, the rates of the two samples behave almost identically. This observation is in agreement with the conductivity data shown in Figure 4d. We see that the elementary hopping processes captured by ^{7}Li NMR spin−lattice relaxation measurements are to be characterized by activation energies of approximately 0.1 eV. At approximately 273 K, an abrupt change in $1/T_1(1/T)$ is detected, which is in agreement with the change in total electrical conductivity for annealed LYB and the structural changes seen by neutron diffraction,[23] as discussed above. Despite the fact that for nano-LYB a more gradual change shows up, ^{7}Li NMR spin−lattice relaxation tells us that microscopic ion dynamics is rather similar for the two classes of samples, that is, nano-50 and the annealed sample.

Above 273 K, the diffusion-induced rates pass through characteristic rate peaks, expected for solid electrolytes with

https://dx.doi.org/10.1021/acssuschemeng.0c06694
ACS Sustainable Chem. Eng. 2021, 9, 743−755

DC ionic conductivities in the order of 1 mS cm^{-1} at room temperature. The shape of the two (symmetric) peaks turned out to be very similar and can be approximated with a Lorentzian-type spectral density function, as introduced by Bloembergen and co-workers.[59]

$$J(\omega_0) \propto \frac{\tau_c}{1 + (\omega_0\tau_c)^\beta} \quad (1)$$

Symmetric rate peaks are produced for $\beta = 2$ and indicate uncorrelated 3D motion. The BBP fit yields an activation energy of 0.14 eV for both samples. Again, as T_1 is sensitive to short-range Li^+ motions, this value characterizes the elementary hopping barriers between adjacent Li positions in LYB. The prefactor τ_0 turned out to be on the order of 10^{-12} s (see Table 1); its inverse value is at the lower limit of typical frequencies for phonons.

Table 1. Overview of the Results Deduced from the Evaluation of the Two $1/T_1$ Rate Peaks Measured at 116 MHz[a]

	T_{max}/K	τ_0/s	D_{NMR}/m^2 s^{-1}	D_σ/m^2 s^{-1}
nano-LYB	333 K	$1.9(5) \times 10^{-12}$	5.9×10^{-12}	2.5×10^{-12}
annealed LYB	313 K	$1.2(5) \times 10^{-12}$	5.9×10^{-12}	3.9×10^{-12}

[a]For comparison, D_σ was calculated from conductivity spectroscopy data.

Importantly, the position of the $1/T_1(1/T)$ peak of nano-LYB is marginally shifted toward higher temperatures indicating almost the same Li diffusivity also in the nanostructured sample. At T_{max} = 313 K (annealed LYB) and at T_{max} = 333 K (nano-LYB), the jump rate τ^{-1} turned out to be 7.3×10^8 s^{-1} if we used $\omega_0/2\pi$ = 116 MHz to calculate τ^{-1} via $\tau\omega_0 = 1$. The Li^+ jump rate can be converted into a self-diffusion coefficient with the aid of the Einstein–Smoluchowski equation, eq 2.[60,61]

$$D_{NMR} = \frac{a^2}{2d\tau} \quad (2)$$

In this equation, a represents the mean Li^+ jump distance, which is approximately 2.2 Å according to the T–O–T distances in LYB. As the Li^+ ion transport was determined via bond-valence energy landscape analysis[21] and AIMD[22] calculations to occur in all three dimensions, d = 3. The corresponding values are listed in Table 1.

For comparison with the results from conductivity spectroscopy, we converted σ_{DC}, measured at 313 and 333 K, respectively, into solid-state diffusion coefficients D_σ with the help of the Nernst–Einstein eq 3.

$$D_\sigma = \frac{\sigma_{DC} k_B T}{N q^2} \quad (3)$$

Here, q denotes the charge of the Li ions and N represents the charge carrier density, which was estimated using structural data to be on the order of 1.12×10^{28} m^{-3} for nano-LYB and 9.9×10^{27} m^{-3} for the annealed sample. As can be seen in Table 1, the diffusion coefficients derived from NMR exceed the ones estimated from conductivity spectroscopy by approximately a factor of 2. This difference, as D_{NMR} is connected to D_σ via $D_{NMR} = (H_r/f)D_\sigma$, can be explained by a Haven ratio H_r or a correlation factor f deviating from 1. We have to keep in mind that not all of the fast exchange processes detected by NMR, especially if restricted to local areas, necessarily contribute to long-range ion transport. In summary, the difference in diffusion-induced $1/T_1(1/T)$ for the LYB nano-50 sample and the annealed one turned out to be marginal, revealing that the elementary steps of ion jump processes, that is, local jumps, are very similar for the two materials. This observation is in contrast to σ_{DC} measurements being sensitive to macroscopic, that is, through-going, ion transport. However, the similarity of the NMR responses agrees very well with results from our M''/ω analysis, which also do not show strong deviations (Figure 4f). The latter solely reflects bulk ion transport, while σ_{DC} might still be influenced by macroscopic properties of the pressed pellets.

For the sake of completeness, we also recorded diffusion-induced ^{7}Li NMR $1/T_{1\rho}$ rates at a locking frequency of 20 kHz. Formally, in spin-lock NMR, the Larmor frequency with values in the MHz range is replaced by an angular locking frequency (ω_1) in the kHz range. Hence, $1/T_{1\rho}$ NMR is sensitive to much slower Li spin fluctuations. Consequently, according to $\tau\omega_1 \approx 0.5$, any rate peaks $1/T_{1\rho}$ are expected to show up at much lower temperatures. The temperature behavior of $1/T_{1\rho}$ is shown in Figure 7b. Above 273 K, we clearly see an abrupt change in $1/T_{1\rho}(1/T)$. This change is in agreement with results from T_1 NMR and conductivity spectroscopy as it represents cation redistributions and structural changes as discussed above. Activation energies of 0.15 eV perfectly agree with those extracted from laboratory-frame $1/T_1(1/T)$ NMR. Thus, local jump processes as seen by laboratory-frame $1/T_1$ do also affect the spin-lock rates. The fact that the flank of annealed LYB lies below that of nano-LYB tells us that larger (dipolar) coupling constants govern $1/T_{1\rho}$.

The same situation is met for the low-T form of LYB. Below 273 K we notice a rather complex temperature behavior. It is important to note that we started at low temperatures to record the rates; hence, they are not influenced by any temperature effects. Although we cannot assign the different flanks seen, whose activation energies range from 0.2 to 0.41 eV, to specific dynamic features, the data indicate that in the low-T form of nano-LYB (nano-50 and nano-1), Li^+ diffusivity is clearly enhanced as compared to that in the annealed sample. The relaxation processes sensed by spin-lock NMR seem to be, however, not relevant for long-range ionic transport as the σ_{DC} of the two forms do not differ much below 273 K, at least during the first heating run, see Figure 4d.

The relatively high activation energy of 0.41 eV for the annealed sample even exceeds that measured by conductivity spectroscopy (0.31 eV). If we indeed assume a more ordered Li^+ sublattice at temperatures well below 250 K, the idea of correlated ion motions could be used to explain this feature. The kink seen at 220 K (Figure 7b) might be related to a transition from correlated to uncorrelated motion experienced by the Li^+ ions. This transition is characterized by a reduction of the activation energy from 0.41 to 0.20 eV. For nano-LYB (nano-50), it is shifted toward lower temperatures. Obviously, σ_{DC} is only able to probe an average activation energy of these dynamic processes.

Finally, we took a look at ^{7}Li NMR spectra (Figure 8) recorded under static, that is, nonrotating, conditions (193 to 473 K), to compare dynamic properties of the two samples prepared. In general, at low temperatures, that is, the so-called rigid lattice regime, the NMR line width is mainly determined by homonuclear ^{7}Li–^{7}Li dipolar interactions. Thermally controlled Li^+ hopping causes these interactions to average.

https://dx.doi.org/10.1021/acssuschemeng.0c06694
ACS Sustainable Chem. Eng. 2021, 9, 743–755

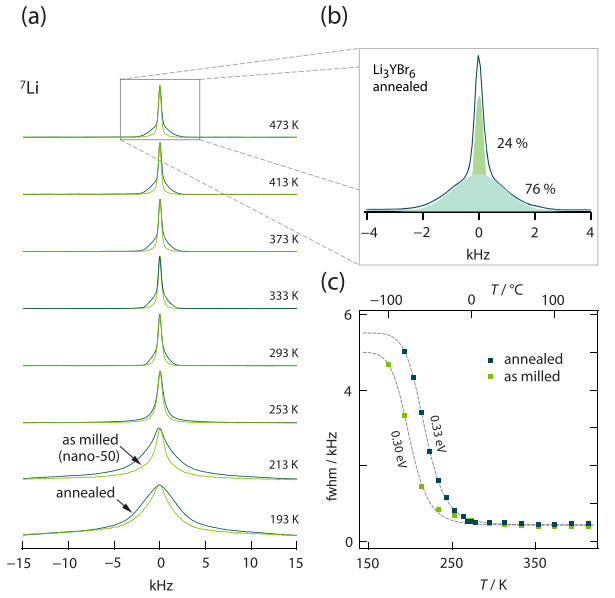

Figure 8. (a) Variable-temperature ^{7}Li NMR spectra of nanocrystalline (as milled, nano-50) and annealed Li_3YBr_6 recorded at the temperatures indicated. While the lines belonging to nano-LYB reveal homogeneous motional narrowing, those of the annealed sample are composed of a broad Gaussian and a narrowed Lorentzian, see b. The sample nano-1 shows the same lines as nano-50. (b) Deconvolution of the ^{7}Li NMR resonance (473 K) of annealed LYB. (c) Motional narrowing curves of nano-LYB (nano-50) and the annealed sample.

The final line width obtained in the regime of extreme narrowing is only governed by inhomogeneities of the external magnetic field B_0. Here, the lines of nano-LYB reveal a homogeneous narrowing, while those of annealed Li_3YBr_6 undergo a heterogeneous process resulting in a two-component line shape, see Figure 8a and b. Two scenarios can explain this striking difference. A two-component line shape would point to two spin reservoirs, a fast and a slow subensemble of Li ions. At first glance, this interpretation for annealed Li_3YBr_6 would be in agreement with the result from ^{6}Li MAS NMR. However, the shape of the ^{6}Li MAS NMR spectra is identical for both annealed LYB and nano-LYB, for which a two-component line shape in static NMR is absent. Therefore, we propose that the two components for structurally ordered, annealed LYB refer to the central line (narrow line) and electric quadrupole intensities (broad line). The latter arise from the interaction of the ^{7}Li quadrupole moment with a nonvanishing electric field gradient (EFG) at the nuclear site. In general, an intensity ratio of 4:6 (dipolar/quadrupolar) is expected for the spin-3/2 nucleus ^{7}Li; this ratio is in fair agreement with that obtained after deconvoluting the ^{7}Li NMR line (473 K) of annealed LYB, see Figure 8b. At the lowest temperatures, both spin transitions govern the overall ^{7}Li NMR line of annealed LYB.

We assume that these NMR intensities are invisible for the nanocrystalline sample if the spectrum is recorded with a single $\pi/2$ excitation pulse. Structural disorder produces a wide distribution of EFGs. As a result, the corresponding quadrupole powder pattern is rather broad and, thus, invisible in the experiments carried out here. The fact that ^{6}Li MAS NMR points to Li ions slightly differing in diffusivity is not in contradiction with this view. The narrow line seen in static NMR comprises the signals resolved by ^{6}Li MAS NMR. As a last remark, the diffusion pathways in annealed LYB do not cause a complete averaging of electric quadrupole interactions. This finding has already been observed also for other Li-containing construers and belongs to the universal features in NMR spectroscopy. It has been explained by anisotropic diffusion pathways to which the Li ions have access.[62]

For both samples, motional line narrowing itself is completed at 273 K. Thus, dynamic information is restricted to the low-T form of LYB. In agreement with $1/T_1$ NMR (and with spin-lock NMR), Li^+ ion exchange processes turn out to be somewhat faster in the nanocrystalline sample than those in the annealed one. As compared to annealed LYB, the corresponding narrowing curve of nano-LYB is shifted toward lower T, see Figure 8c. However, care has to be taken as the line widths belonging to the annealed sample are additionally affected by electric quadrupolar intensities, see above. A possibility to roughly estimate an activation energy from motional narrowing curves is given by the model introduced by Hendrickson and Bray, as discussed by Wilkening et al.[63] (see dashed lines). Values on the order of 0.3 eV agree with those seen by conductivity and resistivity spectroscopy, see above. Presumably, they reflect the average of the activation energies seen in $1/T_\rho$ NMR. The slightly narrower NMR lines seen for nano-LYB support the behavior of $1/T_1$ (and $1/T_{1\rho}$) NMR below 273 K. We have to keep in mind that, to a certain degree, also localized Li^+ hopping processes contribute to dipole−dipole averaging. Such processes would not lead to a net charge transport which is probed by DC conductivity measurements.

SUMMARY AND CONCLUSIONS

Ternary Li-bearing halides with close-packed structures such as Li_3YBr_3 are considered to act as solid electrolytes in modern energy storage systems. Here, we prepared Li_3YBr_3 via a one-pot mechanochemical approach. Importantly, ionic conductivity of the as-milled nanocrystalline powder, even if obtained after a milling time of only 1 h, turned out to be high, almost reaching the 1 mS cm^{-1} limit. Such a value is necessary for applications that operate around ambient temperature. The annealed sample (2 h at 873 K) is characterized by a 3 times higher conductivity σ_{DC} reaching 1.52 mS cm^{-1}. Increased annealing times do not lead to any further significant enhancement of σ_{DC}. The similarity in ionic transport of nanocrystalline and annealed LYB is also seen from an atomic-scale point of view; ^{7}Li ($1/T_1$) NMR relaxometry revealed almost the same diffusion-controlled rate peaks that point to encouraging Li^+ self-diffusion coefficients on the order of 3×10^{-12} m^2 s^{-1}. We found that rapid localized ion jump processes additionally affect the NMR responses; these fast processes may themselves trigger long-range ion transport. In particular, spin-lock ^{7}Li NMR and variable-temperature line shape measurements reveal that such processes are faster in the as-milled, that is, the nanocrystalline, material. The latter experiments also suggest a transition from uncorrelated to correlated motions at approximately 220 K. For structurally disordered nano-LYB, this transition is shifted toward even lower temperatures.

The low activation energy of E_a = 0.28 eV as extracted from conductivity measurements perfectly agrees with that predicted by AIMD simulations (0.28(2) eV) carried out by Mo and co-workers. This agreement confirms the theoretically proposed 3D network of Li^+ long-range ionic conduction including hopping processes between the octahedrally coordinated Li

https://dx.doi.org/10.1021/acssuschemeng.0c06694
ACS Sustainable Chem. Eng. 2021, 9, 743−755

sites through the involvement of unoccupied or partially occupied, face-sharing tetrahedral sites.

Furthermore, ^{7}Li NMR helped us to show that, even without energy-intensive annealing steps or long milling times, the preparation of Li_3YBr_6 with high Li^+ self-diffusivity is possible. Nonetheless, structurally ordered LYB turned out to be slightly superior in terms of ionic conductivity, which is in striking contrast to many oxides studied in their ordered and disordered forms. Most importantly, for nano-LYB, we observed an enhanced contribution of electronic conductivity to the total conductivity. We attribute this finding to the disordered interfacial regions that might provide areas where charge carriers other than Li^+ might contribute to overall electrical conductivity. For instance, space charge zones, defects, and surface effects can serve as explanations for high electronic conductivities. Hence, a short annealing step of 2 h is important in (i) achieving a high ionic conductivity and (ii) lowering the electronic conductivity, being detrimental for, e.g., any battery applications.

■ ASSOCIATED CONTENT

Supporting Information

The Supporting Information is available free of charge at https://pubs.acs.org/doi/10.1021/acssuschemeng.0c06694.

Temperature dependence of ionic conductivity of samples that were annealed for 6 and 24 h, respectively; DC polarization curves to estimate electronic conductivities (PDF)

■ AUTHOR INFORMATION

Corresponding Author

H. Martin R. Wilkening − *Graz University of Technology, Institute of Chemistry and Technology of Materials (NAWI Graz), 8010 Graz, Austria;* orcid.org/0000-0001-9706-4892; Email: wilkening@tugraz.at

Author

Maria Gombotz − *Graz University of Technology, Institute of Chemistry and Technology of Materials (NAWI Graz), 8010 Graz, Austria*

Complete contact information is available at: https://pubs.acs.org/10.1021/acssuschemeng.0c06694

Author Contributions

The manuscript was written through contributions of all authors. All authors have given approval to the final version of the manuscript.

Notes

The authors declare no competing financial interest.

■ ACKNOWLEDGMENTS

We thank J. Hobisch for the DSC measurements and B. Gadermaier for valuable discussions on correlated ion dynamics. Moreover, we thank W. Zeier for providing us the cif files to draw the crystal structures shown in Figure 2. We gratefully acknowledge financial support by the Deutsche Forschungsgemeinschaft (DFG) in the frame of the research unit 1277 (molife, WI3600/2-1 and WI3600/4-1). In addition, the study received considerable funding from the European Union's Horizon 2020 research and innovation program under the grant agreement no. 769929. Furthermore, we thank the unknown reviewers for their valuable comments, which encouraged us to study a sample milled for only 1 h.

■ REFERENCES

(1) Li, Y.; Han, J.-T.; Wang, C.-A.; Xie, H.; Goodenough, J. B. Optimizing Li^+ Conductivity in a Garnet Framework. *J. Mater. Chem.* **2012**, *22*, 15357−15361.

(2) Murugan, R.; Thangadurai, V.; Weppner, W. Fast Lithium Ion Conduction in Garnet-Type $Li_7La_3Zr_2O_{12}$. *Angew. Chem., Int. Ed.* **2007**, *46*, 7778−7781.

(3) Hanghofer, I.; Brinek, M.; Eisbacher, S. L.; Bitschnau, B.; Volck, M.; Hennige, V.; Hanzu, I.; Rettenwander, D.; Wilkening, H. M. R. Substitutional Disorder: Structure and Ion dynamics of the Argyrodites Li_6PS_5Cl, Li_6PS_5Br and Li_6PS_5I. *Phys. Chem. Chem. Phys.* **2019**, *21*, 8489−8507.

(4) Rao, R.; Adams, S. Studies of Lithium Argyrodite Solid Electrolytes for All-Solid-State Batteries. *Phys. Status Solidi A* **2011**, *208*, 1804−1807.

(5) Kamaya, N.; Homma, K.; Yamakawa, Y.; Hirayama, M.; Kanno, R.; Yonemura, M.; Kamiyama, T.; Kato, Y.; Hama, S.; Kawamoto, K.; Mitsui, A. A Lithium Superionic Conductor. *Nat. Mater.* **2011**, *10*, 682−686.

(6) Kanno, R.; Murayama, M. Lithium Ionic Conductor Thio-LISICON: The Li_2S-GeS_2-P_2S_5 System. *J. Electrochem. Soc.* **2001**, *148*, A742.

(7) Tachez, M.; Malugani, J.-P.; Mercier, R.; Robert, G. Ionic Conductivity of and Phase Transition in Lithium Thiophosphate Li_3PS_4. *Solid State Ionics* **1984**, *14*, 181−185.

(8) Matsuo, M.; Nakamori, Y.; Orimo, S.-i.; Maekawa, H.; Takamura, H. Lithium Superionic Conduction in Lithium Borohydride Accompanied by Structural Transition. *Appl. Phys. Lett.* **2007**, *91*, 224103.

(9) Oguchi, H.; Matsuo, M.; Sato, T.; Takamura, H.; Maekawa, H.; Kuwano, H.; Orimo, S. Lithium-Ion Conduction in Complex Hydrides $LiAlH_4$ and Li_3AlH_6. *J. Appl. Phys.* **2010**, *107*, 096104.

(10) Matsuo, M.; Sato, T.; Miura, Y.; Oguchi, H.; Zhou, Y.; Maekawa, H.; Takamura, H.; Orimo, S.-i. Synthesis and Lithium Fast-Ion Conductivity of a New Complex Hydride $Li_3(NH_2)_2I$ with Double-Layered Structure. *Chem. Mater.* **2010**, *22*, 2702−2704.

(11) Lutz, H.; Zhang, Z.; Pfitzner, A. Fast Ionic Conductivity of Ternary Iodides in the Systems LiI-$M^{II}I_2$ (M^{II} = Mn, Cd, Pb). *Solid State Ionics* **1993**, *62*, 1−3.

(12) Pfitzner, A.; Crockcroft, J. K.; Solinas, I.; Lutz, H. D. Neue Halogenozinkate(II) $MZnX_4$ (MI = Li, Na; X = Cl, Br) mit Olivinstruktur. *Z. Anorg. Allg. Chem.* **1993**, *619*, 993−998.

(13) Steiner, H.; Lutz, H. Structural Phase Transitions of Fast Lithium Ion Conductors $Li_2M^{II}Cl_4$ (M^{II} = Mg, Mn, Cd). *J. Solid State Chem.* **1992**, *99*, 1−11.

(14) Lutz, H.; Schmidt, W.; Haeuseler, H. Chloride Spinels: A New Group of Solid Lithium Electrolytes. *J. Phys. Chem. Solids* **1981**, *42*, 287−289.

(15) Maekawa, H.; Iwatani, T.; Shen, H.; Yamamura, T.; Kawamura, J. Enhanced Lithium Ion Conduction and the Size Effect on Interfacial Phase in Li_2ZnI_4−Mesoporous Alumina Composite Electrolyte. *Solid State Ionics* **2008**, *178*, 1637−1641.

(16) Li, X.; Liang, J.; Chen, N.; Luo, J.; Adair, K. R.; Wang, C.; Banis, M. N.; Sham, T.-K.; Zhang, L.; Zhao, S.; Lu, S.; Huang, H.; Li, R.; Sun, X. Water-Mediated Synthesis of a Superionic Halide Solid Electrolyte. *Angew. Chem., Int. Ed.* **2019**, *58*, 16427−16432.

(17) Li, X.; et al. Air-Stable Li_3InCl_6 Electrolyte with High Voltage Compatibility for All-Solid-State Batteries. *Energy Environ. Sci.* **2019**, *12*, 2665−2671.

(18) Xu, Z.; Chen, X.; Liu, K.; Chen, R.; Zeng, X.; Zhu, H. Influence of Anion Charge on Li Ion Diffusion in a New Solid-State Electrolyte, Li_3LaI_6. *Chem. Mater.* **2019**, *31*, 7425−7433.

(19) Schlem, R.; Bernges, T.; Li, C.; Kraft, M. A.; Minafra, N.; Zeier, W. G. Lattice Dynamical Approach for Finding the Lithium Superionic Conductor Li_3ErI_6. *ACS Appl. Energy Mater.* **2020**, *3*, 3684−3691.

(20) Schlem, R.; Muy, S.; Prinz, N.; Banik, A.; Shao-Horn, Y.; Zobel, M.; Zeier, W. G. Mechanochemical Synthesis: A Tool to Tune Cation Site Disorder and Ionic Transport Properties of Li_3MCl_6 (M = Y, Er) Superionic Conductors. *Adv. Energy Mater.* **2020**, *10*, 1903719.
(21) Asano, T.; Sakai, A.; Ouchi, S.; Sakaida, M.; Miyazaki, A.; Hasegawa, S. Solid Halide Electrolytes with High Lithium-Ion Conductivity for Application in 4 V Class Bulk-Type All-Solid-State Batteries. *Adv. Mater.* **2018**, *30*, 1803075.
(22) Wang, S.; Bai, Q.; Nolan, A. M.; Liu, Y.; Gong, S.; Sun, Q.; Mo, Y. Lithium Chlorides and Bromides as Promising Solid-State Chemistries for Fast Ion Conductors with Good Electrochemical Stability. *Angew. Chem., Int. Ed.* **2019**, *58*, 8039−8043.
(23) Schlem, R.; Banik, A.; Ohni, S.; Suard, E.; Zeier, W. Insights into the Lithium Substructure of the Superionic Conductors Li_3YCl_6 and Li_3YBr_6. *chemrxiv* **2020**, DOI: 10.26434/chemrxiv.13224296.v1.
(24) Wilkening, M.; Heitjans, P. Li Jump Process in *h*-$Li_{0.7}TiS_2$ Studied by two-Time ^{7}Li Spin-Alignment Echo NMR and Comparison With Results on Two-Dimensional Diffusion From Nuclear Magnetic Relaxation. *Phys. Rev. B: Condens. Matter Mater. Phys.* **2008**, *77*, 024311.
(25) Preishuber-Pfluegl, F.; Wilkening, M. Mechanochemically Synthesized Fluorides: Local Structures and Ion Transport. *Dalton Trans.* **2016**, *45*, 8675−8687.
(26) Kuhn, A.; Narayanan, S.; Spencer, L.; Goward, G.; Thangadurai, V.; Wilkening, M. Li Self-Diffusion in Garnet-Type $Li_7La_3Zr_2O_{12}$ as Probed Directly by Diffusion-Induced ^{7}Li Spin-Lattice Relaxation NMR Spectroscopy. *Phys. Rev. B: Condens. Matter Mater. Phys.* **2011**, *83*, 094302.
(27) Ailion, D.; Slichter, C. P. Study of Ultraslow Atomic Motions by Magnetic Resonance. *Phys. Rev. Lett.* **1964**, *12*, 168−171.
(28) Slichter, C. P.; Ailion, D. Low-Field Relaxation and the Study of Ultraslow Atomic Motions by Magnetic Resonance. *Phys. Rev.* **1964**, *135*, A1099−A1110.
(29) Ailion, D. C.; Slichter, C. P. Observation of Ultra-Slow Translational Diffusion in Metallic Lithium by Magnetic Resonance. *Phys. Rev.* **1965**, *137*, A235−A245.
(30) Indris, S.; Bork, D.; Heitjans, P. Nanocrystalline Oxide Ceramics Prepared by High-Energy Ball Milling. *J. Mater. Synth. Process.* **2000**, *8*, 245−250.
(31) Patterson, A. L. The Scherrer Formula for X-Ray Particle Size Determination. *Phys. Rev.* **1939**, *56*, 978−982.
(32) Scherrer, P. Bestimmung der Groeße und der inneren Struktur von Kolloidteilchen mittels Roentgenstrahlen. *Göttinger Nachrichten* **1918**, *2*, 98−100.
(33) Jonscher, A. The 'Universal' Dielectric Response. *Nature* **1977**, *267*, 673−679.
(34) Sidebottom, D. L. Dimensionality Dependence of the Conductivity Dispersion in Ionic Materials. *Phys. Rev. Lett.* **1999**, *83*, 983−986.
(35) Preishuber-Pfluegl, F.; Bottke, P.; Pregartner, V.; Bitschnau, B.; Wilkening, M. Correlated Fluorine Diffusion and Ionic Conduction in the Nanocrystalline F^- Solid Electrolyte $Ba_{0.6}La_{0.4}F_{2.4}$ − ^{19}F $T_{1(\rho)}$ NMR relaxation vs. conductivity measurements. *Phys. Chem. Chem. Phys.* **2014**, *16*, 9580−9590.
(36) Breuer, S.; Wilkening, M. Mismatch in Cation Size Causes Rapid Anion Dynamics in Solid Electrolytes: The Role of the Arrhenius Pre-Factor. *Dalton Trans.* **2018**, *47*, 4105−4117.
(37) Funke, K. Jump Relaxation in Solid Electrolytes. *Prog. Solid State Chem.* **1993**, *22*, 111−195.
(38) Banhatti, R.; Laughman, D.; Badr, L.; Funke, K. Nearly Constant Loss Effect in Sodium Borate and Silver Meta-Phosphate Glasses: New Insights. *Solid State Ionics* **2011**, *192*, 70−75.
(39) Laughman, D.; Banhatti, R.; Funke, K. New Nearly Constant Loss Feature Detected in Glass at Low Temperatures. *Phys. Chem. Chem. Phys.* **2010**, *12*, 14102−14108.
(40) Laughman, D. M.; Banhatti, R. D.; Funke, K. Nearly Constant Loss Effects in Borate Glasses. *Phys. Chem. Chem. Phys.* **2009**, *11*, 3158−3167.
(41) Macdonald, J. Nearly Constant Loss or Constant Loss in Ionically Conducting Glasses: A Physically Realizable Approach. *J. Chem. Phys.* **2001**, *115*, 6192−6199.
(42) Wohlmuth, D.; Epp, V.; Bottke, P.; Hanzu, I.; Bitschnau, B.; Letofsky-Papst, I.; Kriechbaum, M.; Amenitsch, H.; Hofer, F.; Wilkening, M. Order vs. Disorder − A Huge Increase In ionic Conductivity of Nanocrystalline $LiAlO_2$ Embedded in an Amorphous-Like Matrix of Lithium Aluminate. *J. Mater. Chem. A* **2014**, *2*, 20295−20306.
(43) Heitjans, P.; Masoud, M.; Feldhoff, A.; Wilkening, M. NMR and Impedance Studies of Nanocrystalline and Amorphous Ion Conductors: Lithium Niobate as a Model System. *Faraday Discuss.* **2007**, *134*, 67−82.
(44) Wilkening, M.; Epp, V.; Feldhoff, A.; Heitjans, P. Tuning the Li Diffusivity of Poor Ionic Conductors by Mechanical Treatment: High Li Conductivity of Strongly Defective $LiTaO_3$ Nanoparticles. *J. Phys. Chem. C* **2008**, *112*, 9291−9300.
(45) Gadermaier, B.; Stanje, B.; Wilkening, A.; Hanzu, I.; Heitjans, P.; Wilkening, H. M. R. Glass in Two Forms: Heterogeneous Electrical Relaxation in Nanoglassy Petalite. *J. Phys. Chem. C* **2019**, *123*, 10153−10162.
(46) Gadermaier, B.; Resch, L.; Pickup, D.; Hanghofer, I.; Hanzu, I.; Heitjans, P.; Sprengel, W.; Würschum, R.; Chadwick, A.; Wilkening, H. Influence of Defects on Ionic Transport in $LiTaO_3$ — A Study using EXAFS and Positron Annihilation Lifetime Spectroscopy. *Solid State Ionics* **2020**, *352*, 115355.
(47) Brinek, M.; Hiebl, C.; Wilkening, H. M. R. Understanding the Origin of Enhanced Li-Ion Transport in Nanocrystalline Argyrodite-Type Li_6PS_5I. *Chem. Mater.* **2020**, *32*, 4754−4766.
(48) Breuer, S.; Pregartner, V.; Lunghammer, S.; Wilkening, H. M. R. Dispersed Solid Conductors: Fast Interfacial Li-Ion Dynamics in Nanostructured LiF and LiF:γ-Al_2O_3 Composites. *J. Phys. Chem. C* **2019**, *123*, 5222−5230.
(49) Maier, J. Nanoionics: Ionic Charge Carriers in Small Systems. *Phys. Chem. Chem. Phys.* **2009**, *11*, 3011−3022.
(50) Maier, J. Nanoionics: Ion transport and Electrochemical Storage in Confined systems. *Nat. Mater.* **2005**, *4*, 805−815.
(51) Gombotz, M.; Lunghammer, S.; Breuer, S.; Hanzu, I.; Preishuber-Pfluegl, F.; Wilkening, H. M. R. Spatial Confinement − Rapid 2D F^- Diffusion in Micro- and Nanocrystalline $RbSn_2F_5$. *Phys. Chem. Chem. Phys.* **2019**, *21*, 1872−1883.
(52) Gombotz, M.; Pregartner, V.; Hanzu, I.; Wilkening, H. Fluoride-Ion Batteries: On the Electrochemical Stability of Nanocrystalline $La_{0.9}Ba_{0.1}F_{2.9}$ against Metal Electrodes. *Nanomaterials* **2019**, *9*, 1517.
(53) Wilkening, M.; Duevel, A.; Preishuber-Pfluegl, F.; da Silva, K.; Breuer, S.; Šepelák, V.; Heitjans, P. Structure and Ion Dynamics of Mechanosynthesized Oxides and Fluorides. *Z. Kristallogr. - Cryst. Mater.* **2017**, *232*, 107−127.
(54) Wohlmuth, D.; Epp, V.; Stanje, B.; Welsch, A.-M.; Behrens, H.; Wilkening, M. High-Energy Mechanical Treatment Boosts Ion Transport in Nanocrystalline $Li_2B_4O_7$. *J. Am. Ceram. Soc.* **2016**, *99*, 1687−1693.
(55) Šepelák, V.; Düvel, A.; Wilkening, M.; Becker, K.-D.; Heitjans, P. Mechanochemical Reactions and Syntheses of Oxides. *Chem. Soc. Rev.* **2013**, *42*, 7507−7520.
(56) Stanje, B.; Rettenwander, D.; Breuer, S.; Uitz, M.; Berendts, S.; Lerch, M.; Uecker, R.; Redhammer, G.; Hanzu, I.; Wilkening, M. Solid Electrolytes: Extremely Fast Charge Carriers in Garnet-Type $Li_6La_3ZrTaO_{12}$ Single Crystals. *Ann. Phys. (Berlin, Ger.)* **2017**, *529*, 1700140.
(57) Epp, V.; Guen, O.; Deiseroth, H.-J.; Wilkening, M. Long-range Li^+ Dynamics in the Lithium Argyrodite Li_7PSe_6 as Probed by Rotating-Frame Spin-Lattice Relaxation NMR. *Phys. Chem. Chem. Phys.* **2013**, *15*, 7123−7132.
(58) Wilkening, M.; Heitjans, P. From Micro to Macro: Access to Long-Range Li^+ Diffusion Parameters in Solids via Microscopic ^{6,7}Li Spin-Alignment Echo NMR Spectroscopy. *ChemPhysChem* **2012**, *13*, 53−65.

(59) Bloembergen, N.; Purcell, E. M.; Pound, R. V. Relaxation Effects in Nuclear Magnetic Resonance Absorption. *Phys. Rev.* **1948**, *73*, 679−712.
(60) Einstein, A. Über die von der molekularkinetischen Theorie der Wärme geforderte Bewegung von in ruhenden Flüssigkeiten suspendierten Teilchen. *Ann. Phys. (Berlin, Ger.)* **2005**, *14*, 182−193.
(61) von Smoluchowski, M. Zur kinetischen Theorie der Brownschen Molekularbewegung und der Suspensionen. *Ann. Phys. (Berlin, Ger.)* **1906**, *326*, 756−780.
(62) Bertermann, R.; Mueller-Warmuth, W.; Jansen, C.; Hiltmann, F.; Krebs, B. NMR Studies of the Lithium Dynamics in Two Thioborate Superionic Conductors: $Li_9B_{19}S_{33}$ and $Li_{4-2x}Sr_{2+x}B_{10}S_{19}$ ($x \approx 0.27$). *Solid State Ionics* **1999**, *117*, 245−255.
(63) Wilkening, M.; Bork, D.; Indris, S.; Heitjans, P. Diffusion in Amorphous $LiNbO_3$ Studied by ^7Li NMR − Comparison With the Nano- and Microcrystalline Material. *Phys. Chem. Chem. Phys.* **2002**, *4*, 3246−3251.

https://dx.doi.org/10.1021/acssuschemeng.0c06694
ACS Sustainable Chem. Eng. 2021, 9, 743−755

Supporting Information

Fast Li ion dynamics in the mechanosynthesized nanostructured form of the solid electrolyte Li_3YBr_6

Maria Gombotz[‡] and H. Martin. R. Wilkening[‡*]

[‡] Institute for Chemistry and Technology of Materials, and Christian Doppler Laboratory for Lithium Batteries, Graz University of Technology, Stremayrgasse 9, 8010 Graz, Austria

*E-mail: wilkening@tugraz.at

Number of pages: 1

Number of Figures: 2 (S1 and S2)

Arrhenius behaviour of ionic conductivities. Figure S1 shows the temperature dependence of the total conductivity of Li_3YBr_6 annealed for different durations at 823 K. We do not see strong changes in conductivity as a function of annealing time.

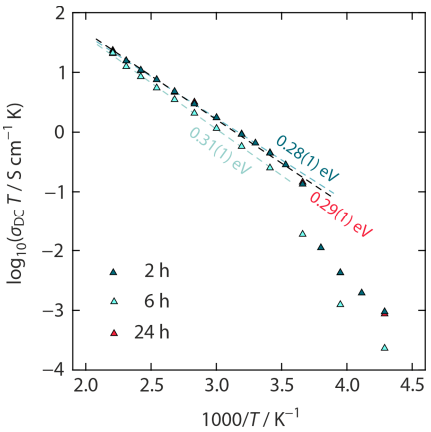

Figure S1. Arrhenius plot of the total conductivities (regime I) of Li_3YBr_6 annealed for 2 h, 6 h, and 24 h. Data obtained after 2 h and 24 h of annealing do almost coincide.

DC polarization measurements. Figure S2 shows the current decay I as a function of time. The final current I_{final} is solely given by electronic conduction. With the help of Ohm's law the (specific) electronic conductivity σ_{eon} can be calculated.

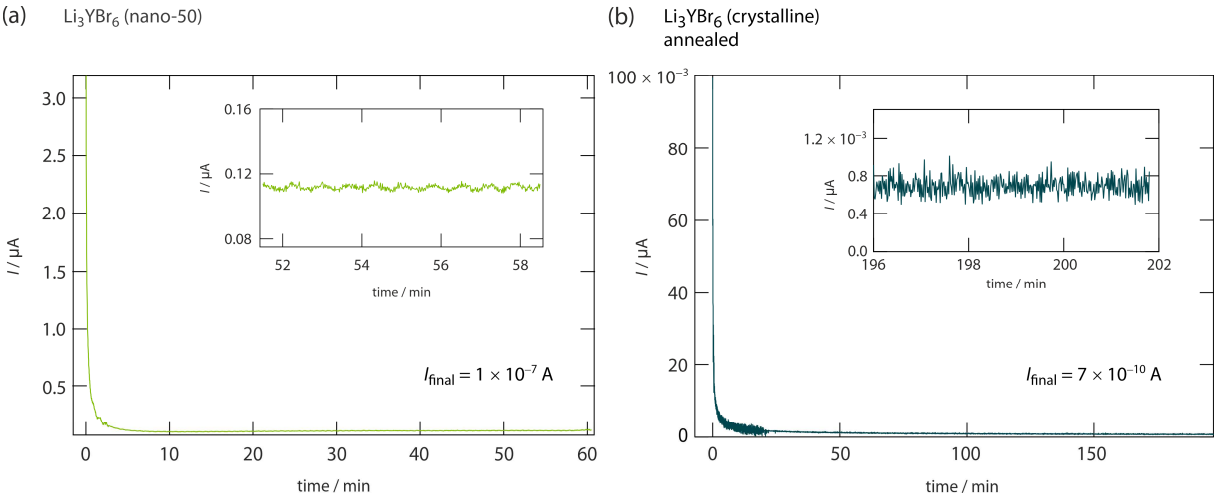

Figure S2. Polarization curves of nano-LYB (nano-50) and annealed LYB, the insets show magnifications of the current response from which I_{final} was deduced.

Preface

Lithium-Ion Transport in Nanocrystalline Spinel-type $Li[In_xLi_y]Br_4$ as Seen by Conductivity Spectroscopy and NMR

The initial aim of this project was the synthesis of Li_3InBr_6 via a facile, mechanochemical route. It became apparent very early that the envisaged stoichiometry could not be obtained, as at first glance, Li_2InBr_4 was the only possible product. This would point towards a "deficiency" of LiBr. Also, the use of LiBr in an over-stochiometric ratio did not lead to success.

Though, the synthesised compound enclosed as a new Li-ion conductor with the formula $Li[In_xLi_y]Br_4$ and was examined closely thereafter. The low-crystallinity of the obtained sample and the necessity of using a Kapton foil for XRPD, due to the hygroscopic character of the material, made it so far close to impossible to obtain detailed results for the structure from Rietveld Refinement. Nevertheless, information about the space group as well as atomic positions could be gathered. Further structural characterization was carried out by ^{6}Li and ^{79}Br MAS NMR. Due to its moderate conductivity of $5.3{\cdot}10^{-6}$ S/cm at 293 K, this material might be only suitable as solid electrolyte in cells operating at higher temperatures. Therefore, the thermal stability of conductivity over time and during temperature cycling, between 273 and 333 K, was examined over a period of 48 h. As the electronic conductivity is of special importance in solid electrolytes, a polarisation measurement was performed, pointing towards a slightly too high electronic conductivity to employ $Li[In_xLi_y]Br_4$ directly as electrolyte without the usage of any protecting layers. Finally, static ^{7}Li NMR measurements were carried out to further elucidate the microscopic dynamics of Li in this so far unknown material.

Author Contributions: MG carried out the synthesis of the material, the characterisation, evaluation and interpretation of the data and wrote the publication. DR carried out the Rietveld refinement, Li pathway calculations and contributed to the data interpretation. HMRW supervised all steps and helped finalizing the manuscript.

P2

Lithium-Ion Transport in Nanocrystalline Spinel-type $Li[In_xLi_y]Br_4$ as Seen by Conductivity Spectroscopy and NMR

***M. Gombotz**, D. Rettenwander and H. Martin R. Wilkening*

Frontiers in Chemistry, 2020, 8, 100, 1-10 (DOI: 10.3389/fchem.2020.00100)

frontiers in Chemistry

ORIGINAL RESEARCH
published: 25 February 2020
doi: 10.3389/fchem.2020.00100

Lithium-Ion Transport in Nanocrystalline Spinel-Type $Li[In_xLi_y]Br_4$ as Seen by Conductivity Spectroscopy and NMR

Maria Gombotz[1]*, *Daniel Rettenwander*[1] and *H. Martin R. Wilkening*[1,2]*

[1] Institute for Chemistry and Technology of Materials, Technical University of Graz, Graz, Austria, [2] ALISTORE-European Research Institute, CNRS FR3104, Hub de l'Energie, Amiens, France

Currently, a variety of solid Li^+ conductors are being discussed that could potentially serve as electrolytes in all-solid-state Li-ion batteries and batteries using metallic Li as the anode. Besides oxides, sulfides and thioposphates, and also halogenides, such as Li_3YBr_6, belong to the group of such promising materials. Here, we report on the mechanosynthesis of ternary, nanocrystalline (defect-rich) $Li[In_xLi_y]Br_4$, which crystallizes with a spinel structure. We took advantage of a soft mechanochemical synthesis route that overcomes the limitations of classical solid-state routes, which usually require high temperatures to prepare the product. X-ray powder diffraction, combined with Rietveld analysis, was used to collect initial information about the crystal structure; it turned out that the lithium indium bromide prepared adopts cubic symmetry ($Fd\bar{3}m$). The overall and electronic conductivity were examined via broadband conductivity spectroscopy and electrical polarization measurements. While electric modulus spectroscopy yielded information on long-range ion transport, ^7Li nuclear magnetic resonance (NMR) spin-lattice relaxation measurements revealed rapid, localized ionic hopping processes in the ternary bromide. Finally, we studied the influence of thermal treatment on overall conductivity, as the indium bromide might find applications in cells that are operated at high temperatures (330 K and above).

Keywords: lithium halogenides, all-solid-state batteries, ceramic electrolytes, diffusion, ionic conductivity, impedance spectroscopy, solid-state NMR

OPEN ACCESS

Edited by:
Neeraj Sharma,
University of New South Wales, Australia

Reviewed by:
Luke O'Dell,
Deakin University, Australia
Xifei Li,
Xi'an University of Technology, China

***Correspondence:**
Maria Gombotz
gombotz@tugraz.at
H. Martin R. Wilkening
wilkening@tugraz.at

Specialty section:
This article was submitted to Electrochemistry, a section of the journal Frontiers in Chemistry

Received: *20 November 2019*
Accepted: *03 February 2020*
Published: *25 February 2020*

Citation:
Gombotz M, Rettenwander D and Wilkening HMR (2020) Lithium-Ion Transport in Nanocrystalline Spinel-Type $Li[In_xLi_y]Br_4$ as Seen by Conductivity Spectroscopy and NMR. Front. Chem. 8:100. doi: 10.3389/fchem.2020.00100

1. INTRODUCTION

Next-generation energy storage systems, which rely on lithium-based batteries, need to be improved in terms of energy density and safety. One possibility for developing powerful batteries is to replace the flammable F-containing liquid electrolytes usually used by ceramic electrolytes (Goodenough, 2013; Bachman et al., 2016; Janek and Zeier, 2016; Zhang et al., 2018). The thermal runaway of such batteries is expected to shift significantly toward higher temperatures.

Suitable ceramics need to show very high ionic conductivities and a sufficiently high electrochemical stability. To achieve high energy densities, the use of Li metal as anode material is necessary. Li metal has already been used as anode material (Wenzel et al., 2016) in the early stages of Li-battery research. However, stability issues, the lack of suitable (liquid) electrolytes (Bruce et al., 2008), and the formation of dendrites (Porz et al., 2017) prevented the commercialization of

such systems. The discovery of highly conducting ceramics has changed this path of development. Of course, many studies have revealed that the Li|electrolyte interface suffers from contact issues (Cheng et al., 2014; Yu et al., 2017; Zhang et al., 2017). These interface issues are closely related to the formation of resistive interfacial phases (Richards et al., 2016). Controlling or preventing their formation is still a problem that needs to be overcome for the majority of ceramics currently discussed as solid electrolytes.

Presently, a range of Li-bearing oxides (Murugan et al., 2007; Buschmann et al., 2011; Thangadurai et al., 2014; Stanje et al., 2017; Uitz et al., 2017), sulfides (Kamaya et al., 2011; Wang et al., 2015; Dietrich et al., 2017), hydrides (Maekawa et al., 2009; Matsuo and Orimo, 2011; Kim et al., 2019), and thiophosphates (Deiseroth et al., 2008; Hanghofer et al., 2019) are being investigated with respect to ionic conductivity, stability and interfacial properties. Besides these classes of materials, halides (Lutz et al., 1990; Marx and Mayer, 1996; Gupta et al., 1997) are also regarded as up-and-coming materials to be employed as solid electrolytes. For instance, mixtures of Li^+ ion conductors with lithium salts, e.g., Li_2S mixed with LiBr, as well as compounds like $LiI_{1-x}Br_x$, which were already being studied in the 80s (Mercier et al., 1985; Schoch et al., 1986), show increased ionic conductivity as compared to the binary halides. The latter, particularly if we consider LiI and LiF, represent extremely poor ionic conductors. Regarding ternary Li-bearing halides with Y or In, compounds like Li_3YBr_6 or Li_3YCl_6 have entered the spotlight of research (Asano et al., 2018). Recently, the performance of a 3.5 V cell with either Li_3YBr_6 or Li_3YCl_6 as electrolyte has been investigated. First-principle analysis confirmed such compounds to have high ionic conductivity as well as relatively broad electrochemical stability. For example, a stability window of 0.59–3.15 V has been reported for Li_3YBr_6 (Wang et al., 2019). Because of this encouraging result, it is worth looking at this interesting class of materials and studying related compounds.

Here, we synthesized a cubic form of defect-rich $Li[In_xLi_y]Br_4$ in a nanocrystalline form. $LiInBr_4$ has been mentioned in the literature in a study carried out by Yamada et al. (2006). The authors speculated whether $LiInBr_4$ should be described by $(Li)_{8b}[In\square]_{16d}Br_4$ or by $(\square)_{8b}[InLi]_{16d}Br_4$, where 8*b* and 16*d* represent the tetrahedral and octahedral voids formed by the Br anion lattice. Preliminary studies also reported on coarse-grained Li_3InX_6 (X = Cl, Br) (Tomita et al., 2008, 2014; Li et al., 2019). In the present case, classical solid-state synthesis routes resulted in samples with a large amount of side phases, so we decided to take advantage of a mechanochemical synthesis approach to prepare $Li[In_xLi_y]Br_4$, which we characterized, apart from X-ray diffraction, also by high-resolution ^{6}Li and ^{79}Br magic angle spinning (MAS) nuclear magnetic resonance (NMR). Preliminary Rietveld analysis of the corresponding X-ray powder pattern revealed that nano-$Li[In_xLi_y]Br_4$ most likely crystallizes with cubic symmetry; roughly speaking the stoichiometry of the sample is best described by $Li[In_{0.62}Li_{1.38}]Br_{3.92}$. We used variable-temperature broadband conductivity and electrical modulus spectroscopy to measure its ionic transport properties. To understand the results from conductivity spectroscopy, we estimated site energies and diffusive barriers with the help of the bond valence energy landscape (BVEL) methodology developed by Chen et al. (2019). Here, at 293 K, the so-called direct current (dc) total ionic conductivity, σ_{dc}, is given by 4.9×10^{-6} S cm^{-1}. Of course, as a higher conductivity is needed for cells operated at room temperature, the ternary bromide might be a suitable electrolyte for cells that are cycled at $T > 330$ K. Furthermore, we characterized our sample in terms of temperature stability, electronic conductivity, and Li self-diffusion. The latter was investigated by means of ^{7}Li NMR line shape and spin-lattice relaxation measurements (Kuhn et al., 2011; Wilkening and Heitjans, 2012; Pecher et al., 2017; Stanje et al., 2017; Uitz et al., 2017; Dawson et al., 2018; Martin et al., 2019). Interestingly, ^{7}Li NMR points to rapid localized ion-hopping processes in the nanocrystalline form of the ternary indium bromide.

2. MATERIALS AND METHODS

2.1. Mechanochemical Synthesis of Nanocrystalline $Li[In_xLi_y]Br_4$

Mechanochemical synthesis was carried out in ZrO_2 beakers with a volume of 45 ml and using milling balls made of the same material with a diameter of 5 mm. The beakers were loaded with LiBr (99.999%, Sigma Aldrich) and $InBr_3$ (99.99%, Alfa Aesar) at a ratio of 3:1. Synthesis was carried out using a high-energy planetary mill Fritsch Pulverisette 7 premium line at a milling speed of 600 rpm. The total milling time was 10 h, whereas after each milling duration of 15 min, the beakers were allowed to cool down and to rest for 15 min. Loading as well as emptying of the beakers was strictly carried out in an argon-filled glovebox (H_2O, $O_2 < 0.5$ ppm), as both the starting materials and the product are highly hygroscopic.

2.2. X-Ray Powder Diffraction

X-ray powder diffraction (XRPD) was carried out on a Bruker D8 Advance diffractometer [Bragg Brentano geometry, CuKα radiation (1.5406 Å)]. Between 10 and 100° 2θ data points were collected for 1 s and with a stepsize of 0.02° 2θ. The measurements, at ambient temperature, had to be performed with a sample holder designed for air-sensitive materials; here, the samples were protected from any moisture by a Kapton® foil. For reasonable background correction, we performed a reference measurement, that is, a blank run using the empty sample holder and the Kapton® foil only. X-PertHighScorePlus software (PANalytical) was used to analyze the pattern according to the method introduced by Rietveld.

2.3. Conductivity and Electric Modulus Spectroscopy

The overall conductivity of site-disordered $Li[In_xLi_y]Br_4$ was investigated by broadband conductivity spectroscopy. Small amounts of the powdered sample were pressed into cylindrical pellets (5 mm in diameter) by applying a uniaxial pressure of 0.8 GPa. The pellets were equipped with ion-blocking electrodes (Pt, 100 nm in thickness) by sputtering (Leica, EM SCD050). Finally, the pellets were put in an air-tight sample holder. All preparation steps were carried out inside an Ar-filled glovebox (H_2O, $O_2 < 0.1$ ppm). Alternating current (ac) impedance data

were recorded with a Novocontrol Concept 80 spectrometer in combination with an active BDS 1200 cell and a ZGS interface (Novocontrol). A QUATRO cryosystem was employed to precisely control and monitor the temperature via Pt100 thermocouples. Here, we varied the temperature T from −40 to 100 °C. The frequency range covered for each isothermal measurement was 10^{-2}–10^{7} Hz.

2.4. Polarization Measurements to Estimate the Electronic Conductivity

The as-prepared nanocrystalline $Li[In_xLi_y]Br_4$ was pressed into a cylindrical pellet (d = 8 mm, h = 1.51 mm) under uniaxial pressure (0.3 GPa). Pt electrodes were applied on both sides via sputtering. Due to its hygroscopic character, the pellet with this electrode sandwich configuration was mounted in an air-tight Swagelok-type cell. We prepared the pellet and the cell in a glovebox (O_2, H_2O < 0.1 ppm) and subsequently placed the cell in a drying oven at 60°C. The cell was then connected to a Parstat MC potentiostat (Princeton Applied Research), which is equipped with a low-current option. We applied a constant voltage U of 300 mV and measured the change of current $I(t)$ over time.

2.5. ^{6}Li and ^{79}Br MAS NMR

High-resolution ^{6}Li and ^{79}Br magic angle spinning (MAS) NMR spectra were acquired with a 500 MHz Bruker Avance III spectrometer connected to a 11.7 T cryomagnet (Bruker Biospin, Ultrashield 500 WB plus). This magnetic field corresponds to resonance frequencies of 73.58 MHz for ^{6}Li and 125.27 MHz for ^{79}Br, respectively. The powder sample was stuffed into 2.5 mm ZrO_2 rotors designed for the MAS probehead used (Bruker). The spinning speed was set to 25 kHz; spectra were recorded at a bearing gas temperature of 303 K (frame cooling: 35% target gas flow, target gas flow: 400 L h^{-1}). ^{6}Li MAS NMR spectra were recorded at selected temperatures viz. at 253, 273, and 303 K. We used single-pulse excitation and converted the free induction decays (FIDs) into spectra by Fourier transformation. LiBr served as reference material (0 ppm) to determine chemical shifts δ_{iso}.

2.6. Static ^{7}Li NMR Spectroscopy

^{7}Li NMR longitudinal spin-lattice relaxation (SLR) rates ($1/T_1$) were recorded on a Bruker Avance III spectrometer with a nominal magnetic field of 7.05 T. This field corresponds to a ^{7}Li Larmor frequency of 116.59 MHz. A home-built NMR probe was used to record the static NMR signal in a temperature range from −40 to 100°C. Diffusion-induced SLR rates in the laboratory frame of reference were recorded by using a saturation recovery pulse, which includes a set of ten 90° pulses, destroying longitudinal magnetization M_z, and delay times t_d, after which the magnetization was detected with a single 90° pulse. The resulting transients $M_z(t_d)$ were analyzed with stretched exponentials to determine $1/T_1$. The spin-lock NMR technique was used to acquire SLR_ϱ rates in the so-called rotating frame of reference. We used a spin-locking frequency to record ^{7}Li NMR diffusion-induced rates $1/T_{1\varrho}$ at a locking field that corresponds to $\omega_1/2\pi$ = 20 kHz. For the static ^{7}Li NMR experiments, the sample was fire-sealed under vacuum in a glass (Duran®) ampoule with a diameter of 5 mm and a length of ∼3 cm.

3. RESULTS AND DISCUSSION

3.1. X-Ray Diffraction and Diffusion Pathways

The crystal structure of nanocrystalline $Li[In_xLi_y]Br_4$ was first characterized using XRPD. We used an airtight sample holder to record the diffraction pattern at ambient temperature; the pattern is shown in **Figure 1**. It perfectly agrees with that presented by Yamada et al. (2006). Our pattern reveals relatively broad reflections, which points to a sample with either low crystallinity or very small crystallites. According to the Scherrer equation (Scherrer, 1918; Heitjans et al., 2007), the mean crystallite size $\langle d \rangle$ is in the order of 17(5) nm if we use the reflections (448), (226), and (004) to estimate $\langle d \rangle$. These reflections correspond to the structure model estimated via Rietveld analysis with information derived from the bond valence energy landscape (BVEL) methodology developed by Chen et al. (2019). For our BVEL estimation, we used the structure model of Li_2MnBr_4. Despite the low crystallinity and the Kapton tape used to avoid degradation of the sample in air, we were able to propose a structure model (see **Table 1**), which summarizes the results from Rietveld refinement.

Indexing of all Bragg peaks is possible with the space group $Fd\bar{3}m$ (no. 227). Only a small amount of an unidentified extra phase is present. In addition, we cannot exclude that small amounts of amorphous LiBr or $InBr_3$, being invisible for X-ray diffraction, are present. Because of the low scattering factor of Li, its exact assignment to crystallographic positions is difficult if not impossible for powder samples. In order to obtain an initial guess for the refinement, we calculated site energies and diffusive barriers based on the BVEL methodology (see above) (Chen et al., 2019). Although the values calculated have unclear physical meaning, they can be used to estimate cation pathways and site preferences. It turned out that the Li ions prefer to occupy the sites 16*d* (octahedral site) and 8*b* (tetrahedral site). By using this information from BVEL calculations, we were able to estimate the Li site occupancies at the Wyckoff positions 16*d* (Li2) and 8*b* (Li1) via Rietveld refinement. The site occupancies are best described by 1.38(11) per formula unit (pfu) and 1.00(32) pfu, respectively. For In, placed at 16*d*, thus sharing the same site with Li2, and Br (32*e*), we obtained 0.62(11) pfu and 3.92(9) pfu, respectively. Finally, this yields the composition $Li_{8b}[In_{0.62}Li_{1.38}]_{16d}Br_{3.92}$, with Li-In positional disorder on 16*d*. Indium is in the oxidation state +3.

This inverse spinel-type structure displays a 3D framework consisting of edge-sharing $InBr_6$ octahedra (see inset in **Figure 1A**). Each 16*d* site shares faces with two tetrahedral 6*b* sites, whereby each 8*b* site shares common faces with four 16*d* sites. This polyhedra connection forms a 3D diffusion pathway, as described by the calculated isosurface of the Li BVEL map (see **Figure 1B**). The corresponding activation energy of this pathway turned out to be ∼0.5 eV. This value is in good

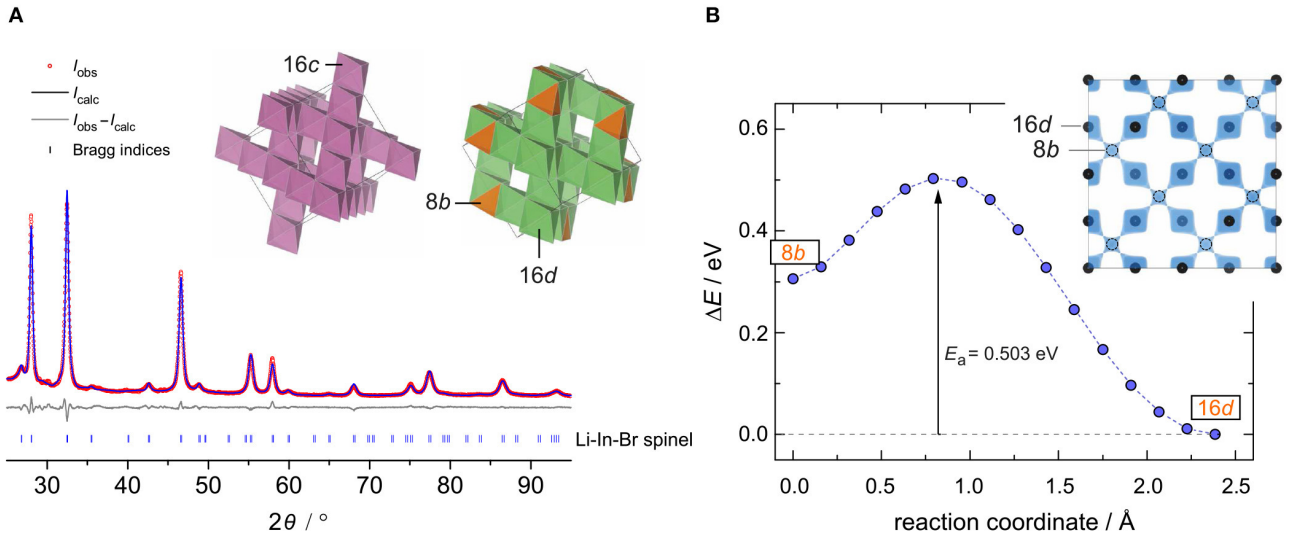

FIGURE 1 | (A) The observed (obs) XRPD pattern as well as the calculated and difference patterns (obs-calc) of the Rietveld refinement for the intended compound $Li[In_xLi_y]Br_4$. Vertical lines below the profile mark the positions of the possible Bragg reflections of spinel-type $Li[In_xLi_y]Br_4$ with its site disorder. Inset: framework formed by $InBr_6$ octahedra, and the Li-ion sublattice composed of tetrahedral and octahedral sites. **(B)** An energetically favored Li^+ diffusion pathway as estimated via the BVEL method; this pathway directly links the two crystallographically positions 16*d* and 8*b*. The corresponding iso-surface is shown in the inset.

TABLE 1 | X-ray diffraction data of $Li[In_xLi_y]Br_4$ with positional disorder on the 16*d* site as determined through Rietveld refinement; space group: $Fd\bar{3}m$ (no. 227); $Z = 8$; lattice parameters: $a = b = c = 11.026141(86)$ Å; *R* factors: $R_{exp} = 1.78$, $R_{wp} = 4.54$, $R_p = 3.53$; goodness of fit (GoF) = 2.56.

	Site	*x/a*	*y/b*	*z/c*	U_{iso}[a]	Occ.[b]
Li1	8*b*	1/8	5/8	1/8	4.60(31)	1.00(32)
Li2	16*d*	1/2	1/2	1/2	1.51(13)	0.69(11)
In	16*d*	1/2	1/2	1/2	1.51(13)	0.310(11)
Br	32*e*	0.25328(10)	0.25328(10)	0.25328(10)	1.316(51)	0.98(9)

[a] × 100 [Å^2], [b] occupation factor; 1.0 denotes full occupation of the site.
U_{iso} and Occ. were at first refined iteratively and finally simultaneously, leading to no change.
The occupation number of Li1 was set to 1, leading to an improved refinement. As Li2 and In share the 16d position, the occupation number of both together was constrained to 1.

agreement with that extracted from conductivity spectroscopy (vide infra).

3.2. Conductivity Measurements and Electrical Modulus

To characterize long-range ionic transport in $Li[In_xLi_y]Br_4$, we measured conductivity isotherms over a relatively broad frequency range (10^{-2}–10^7 Hz). **Figure 2A** shows the isotherms, that is, the real part, σ' of the complex conductivity $\hat{\sigma}$ plotted as a function of frequency ν. The isotherms reveal three characteristic regions that are universally found (Funke et al., 2005; Dunst et al., 2014). At high temperatures and low ν, the ions pile up at the ion-blocking electrode. This charge accumulation causes the effect of electrode polarization, which is not seen at low temperatures, as ionic conductivity sharply decreases with decreasing temperature. At sufficiently high frequencies, electrode polarization passes into the so-called direct current conductivity plateau, which is characterized by σ_{dc}, which we identify as the conductivity value that characterizes long-range ion transport. The same value could be extracted from complex plane representations of the impedance $\hat{Z}$; σ_{dc} refers to the intercept of the location curve with the abscissa of the corresponding Nyquist plot.

With decreasing temperature, we recognize that the dc-plateau of the isotherms shifts toward lower frequencies; simultaneously, at higher frequencies, it passes into a frequency-dependent dispersive regime. At the very low temperatures, the dispersive parts reveal a negligible temperature dependence, which indicates the beginning of the so-called nearly constant loss (NCL) regime (Dyre et al., 2009; Dunst et al., 2016). The latter is often ascribed to caged-like jump processes. While successful ion displacements govern the dc regime, the non-NCL disperse part is sensitive to unsuccessful jumps, including localized motions but also forward-backward jumps. In many cases, $\sigma'(\nu)$ in the dispersive regime can be approximated with Jonscher's power law $\sigma' \propto \nu^{\kappa}$. κ usually takes values ranging from 0.6 to 0.9 if ionic transport occurs in three dimensions. 1D and 2D ionic transport might result in lower values (Sidebottom, 2009). Here, we found $\kappa \approx 0.6$ (253 K), pointing to 3D ionic transport (see **Figure 2A**), as expected from the BVEL estimation (*vide supra*).

σ_{dc} values were directly read off from the distinct dc-plateaus of **Figure 2A**. $\sigma_{dc}T$, plotted vs. $1000/T$, is shown in **Figure 2B**. The linear behavior seen for the 1. run, which corresponds to the heating run, points to Arrhenius behavior according to $\sigma_{dc}T = \sigma_0 \exp(E_a/(k_B T))$. Here, k_B denotes Boltzmann's constant and σ_0 represents the Arrhenius pre-factor. The activation energy E_a turned out to be 0.58(2) eV. Above 313 K, a kink is seen and, at higher T than 313 K, the activation energy reduces to 0.42(3) eV.

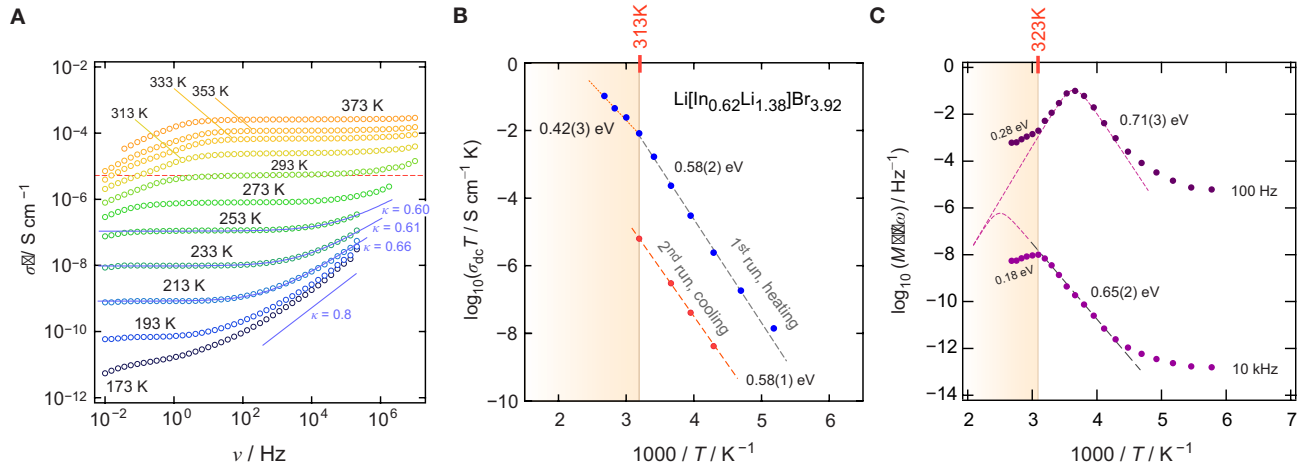

FIGURE 2 | (A) Conductivity isotherms $\sigma'(\nu)$ of $Li[In_xLi_y]Br_4$; isotherms were recorded at temperatures ranging from 173 to 373 K in steps of 20 K (1. run, heating). **(B)** Arrhenius plot to illustrate the temperature dependence of $\sigma_{dc}T$ for both the 1. run (heating) and the 2. run (cooling). **(C)** Real part of the complex resistivity ρ' expressed as M''/ν as a function of the inverse temperature $1/T$ and recorded for a fixed frequency of either $\nu = 10$ *kHz* or $\nu = 100$ Hz.

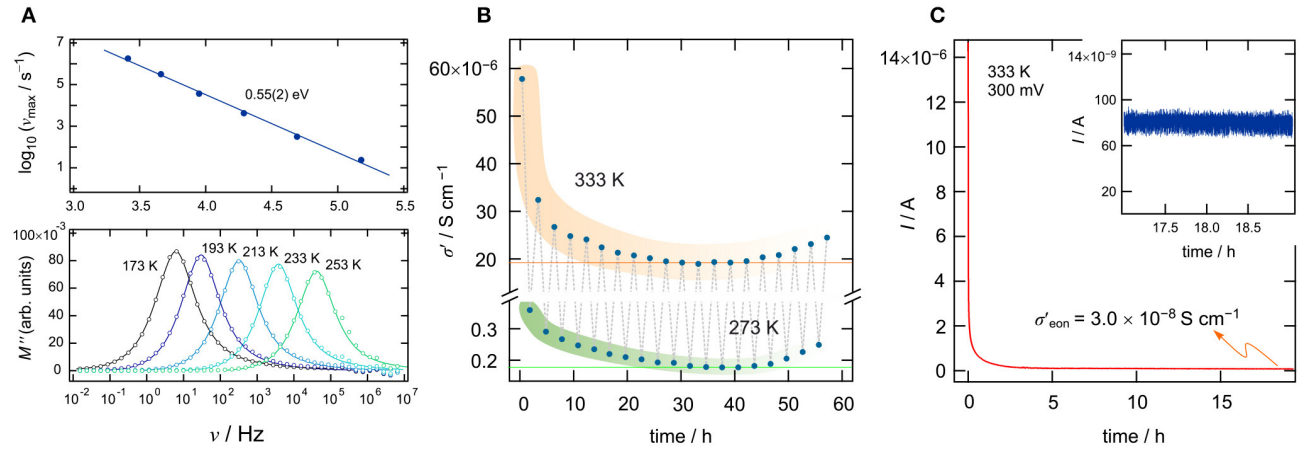

FIGURE 3 | (A) The upper graph shows the Arrhenius behavior of the characteristic frequencies ν_{max} at which the M'' peaks appear. Frequency dependence of the imaginary part of the complex part of the modulus as a function of frequency (ν). **(B)** Longtime measurement of σ_{dc} of $Li[In_xLi_y]Br_4$ over a time period of 58 h; we cycled the temperature in the sample chamber between 273 and 333 K. **(C)** Potentiostatic polarization curve ($U = 300$ *mV*) of $Li[In_xLi_y]Br_4$ sandwiched between two Pt electrodes. The $I(t)$ curve was recorded at $T = 333$ K. After $t = 18$ h, a final current of $I_{final} = 8 \times 10^{-8}$ A has been reached (see also inset), which leads to an electrical conductivity of $\sigma_{eon} = 3 \times 10^{-8}$ S cm^{-1}.

$E_a \approx 0.58$ eV (193–313 K) agrees nicely with the value estimated from BVEL (0.5 eV, see above).

The origin of the change of E_a at 313 K remains so far unknown; it was also observed by Yamada et al. (2006). If no phase transition takes place in $Li[In_xLi_y]Br_4$, one might assume that an order-disorder transition could cause this kink in the Arrhenius line. Such a transition has also been observed for Li_2MnBr_4 and Li_2MgBr_4 but at higher temperatures (Schmidt and Lutz, 1984). In addition, above 313 K, grain growth may already start, which is accompanied by the healing of, for example, point defects. It is well-known than the ionic self-diffusivity in poorly conducting materials can be drastically increased by the introduction of defects, either through mechanical treatment or through radiation (Stathopoulos and Pells, 1983; Ishimaru et al., 2003). Hence, at temperatures above 313 K, the material continuously changes and transforms into a more ordered structure. As expected, the conductivity values recorded during the 2. run, that is, the cooling run (313 K → 233 K), turn out to be lower by ∼3 orders of magnitude as compared to that governing the 1. run.

To investigate ionic transport further by means of electric modulus formalism (Hanghofer et al., 2019), we recorded the quantity M''/ν (see also **Figure 2C**) as a function of temperature and for constant frequency ($\nu = 100$ Hz and $\nu = 10$ kHz, 173 K $\leq T \leq$ 373 K). It turned out that, beginning from very low T, the quantity M''/ν obeys a weaker-than-activated temperature

behavior, in agreement with NCL-type electrical relaxation processes. Above 250 K, we recognize a strong increase with the inverse temperature. From the linear behavior observed, we extracted activation energies of 0.65(2) eV (10 kHz) and 0.71(3) eV (100 Hz). The increase seen if we compare these values to that found by σ_{dc} [0.58(2) eV] indicates that the number of charge carries seems to depend on temperature. Again, above 313 K, and independent of frequency ν, we observe a drastic change in $M''/\nu(1/T)$. The corresponding apparent activation energy of ∼0.18 eV (and 0.28 eV, see **Figure 2**) is much smaller than that seen in conductivity spectroscopy. We attribute this kink and the associated decrease in E_a to changes in morphology and the defect chemistry of the bromide. Finally, we looked directly at the temperature dependence of the electric modulus $M''(\nu)$; the corresponding modulus peaks are shown in the lower part of **Figure 3A**. The Arrhenius behavior of the characteristic frequencies ν_{max} at which the M'' peaks appear is displayed in **Figure 3A**. The linear fit points to an activation energy of 0.55 eV, which is smaller than that seen by σ_{dc}. The lower activation energy again points to a T-dependent charge carrier concentration N^{-1} that increases with temperature. As σ_{dc} is directly proportional to the charge carrier mobility mu_q, the charge of the moving species q and N^{-1}, ν_{max}, being a characteristic electrical relaxation frequency, increases slightly less with T than σ_{dc}.

At 293 K, we obtain an ionic conductivity of $\sigma_{dc} = 4.9 \times 10^{-6}$ S cm^{-1}; this value is far below values needed for ceramic electrolytes in all-solid-state batteries. Thus, the current material is expected to be used in systems operated at higher T. For this reason, we studied the temperature stability of the ionic conductivity of the defect spinel over a time period of 58 h between 273 and 333 K. Moreover, as a sharp decrease in ionic conductivity was observed during the cooling run, we were interested in finding out which final conductivity value will be reached after annealing the sample for many hours at 333 K, which is just slightly above the kink seen in **Figure 2**. Hence, we kept the sample at 333 K for 1 h and then measured $\sigma'(\nu)$. The time needed to record the isotherm was 23 min. After that, we decreased the temperature in the sample chamber to 273 K, waited 1 h, and measured another isotherm $\sigma'(\nu)$; this cycle was repeated several times (see **Figure 3B**). For both the measurements at 333 K and at 273 K, we see the same trend. The conductivity decreases and reaches an almost constant value of $\sigma_{dc} = 2 \times 10^{-5}$ S cm^{-1} at 333 K. The corresponding conductivity at 273 K is two orders of magnitude lower as compared to that measured at 333 K. The reason for the slight increase in conductivity with increasing cycle number is still unknown.

Apart from overall conductivity and thermal stability, the ability of a material to conduct electrons is of significant importance when it comes to its application (Han et al., 2019). Ideally, the electronic conductivity should be orders of magnitude lower than the ionic contribution to the overall conductivity. Only electronically insulting ceramics will prevent soft shorts or the formation of detrimental Li dendrites. Here, we used a symmetric Pt | Li[In$_x$Li$_y$]Br$_4$ | Pt cell to monitor the evolution of current $I(t)$ at a constant voltage $U = 300$ mV. The final current of such a polarization measurement (Breuer et al., 2018a; Gombotz et al., 2019) will give the upper limit of the electronic conductivity σ_{eon}. The curve shown in **Figure 3C** refers to 333 K and reaches a steady state of I after 18 h. The final current ($I_{final} = I(18\,h)$) can be used to estimate σ_{eon} according to $\sigma_{eon} = I_{final}/U \cdot d/(r^2\pi)$, d denotes the thickness of the pellet and r refers to its diameter. For σ_{eon} we obtain $\sigma_{eon} = 3 \times 10^{-8}$ S cm^{-1} at 333 K, which is a factor of 10^3 smaller than the overall conductivity at this temperature ($\sigma_{dc} \approx 6 \times 10^{-5}$ S cm^{-1}). For battery applications, even smaller values for σ_{eon} would be desirable ($\sigma_{dc}/\sigma_{eon} > 10^6$) and, thus, great care has to be taken when In-containing ceramics play a role as solid electrolytes. As an example, for oxide electrolytes, values of σ_{eon} in the order of 10^{-8} S cm^{-1} have been reported to trigger Li dendrite formation in all-solid-state batteries (Han et al., 2019). Li dendrites constitute a major safety problem, as they initiate short circuits and, thus, thermal runaways.

3.3. ^{7}Li NMR Spin-Lattice Relaxation and Line Shapes

To study solely ion dynamics in Li[In$_x$Li$_y$]Br$_4$, we took advantage of ^{7}Li NMR SLR measurements. In general, NMR spectroscopy is a contactless method and does not require any post-preparation steps, such as the application of conducting electrodes. As it is mainly sensitive to bulk ion dynamics, any interfering effects of ion-blocking grain-boundary regions are absent. Of course, the latter holds only for single crystals or polycrystalline materials with crystallites that show diameters in the μm range. For nanocrystalline samples, the ions residing in the large volume fraction of interfacial regions can be, simultaneously with those in the bulk regions, visualized by NMR (Wilkening et al., 2003; Breuer et al., 2018b). Here, we recorded diffusion-induced ^{7}Li SLR rates, in both the laboratory and rotating frame of reference, as a function of the inverse temperature (233–393 K) (Heitjans et al., 2005). The magnetization transients were analyzed in terms of stretched exponential functions (Stanje et al., 2017). The stretching exponents $\gamma_{1(\varrho)}$ are given in the upper graph of **Figure 4A**; the corresponding rates are shown in the Arrhenius diagram below.

Interestingly, the SLR NMR rates $1/T_1$ of nano-Li[In$_x$Li$_y$]Br$_4$ reveal only a slight dependence on reciprocal temperature. We recognize shallow maxima at ca. 333 K and ca. 260 K. Usually, if purely induced by diffusion, the rate $1/T_1(1/T)$ passes through a rate peak whose flanks contain the activation energy. For 3D uncorrelated motion, a symmetric peak is expected (Bloembergen et al., 1948); correlated motion, which originates from structural disorder and/or Coulomb interactions, often produces an asymmetric peak with a lower slope in the limit $\omega_0\tau \gg 1$, that is, on the low-T side of the peak. The same asymmetry is obtained for ionic diffusion in an irregularly shaped potential landscape, with short-range motions being different from long-range ionic transport. In the limit $\omega_0\tau \gg 1$, the flank contains a mean activation energy that characterizes short-range diffusion, i.e., localized site-to-site hopping processes. In the limit $\omega_0\tau \ll 1$, that is, the high-T side of the peak, the slope of the flank contains an average activation energy that might be identified with that sensed by σ_{dc}. Here, the shallow peaks

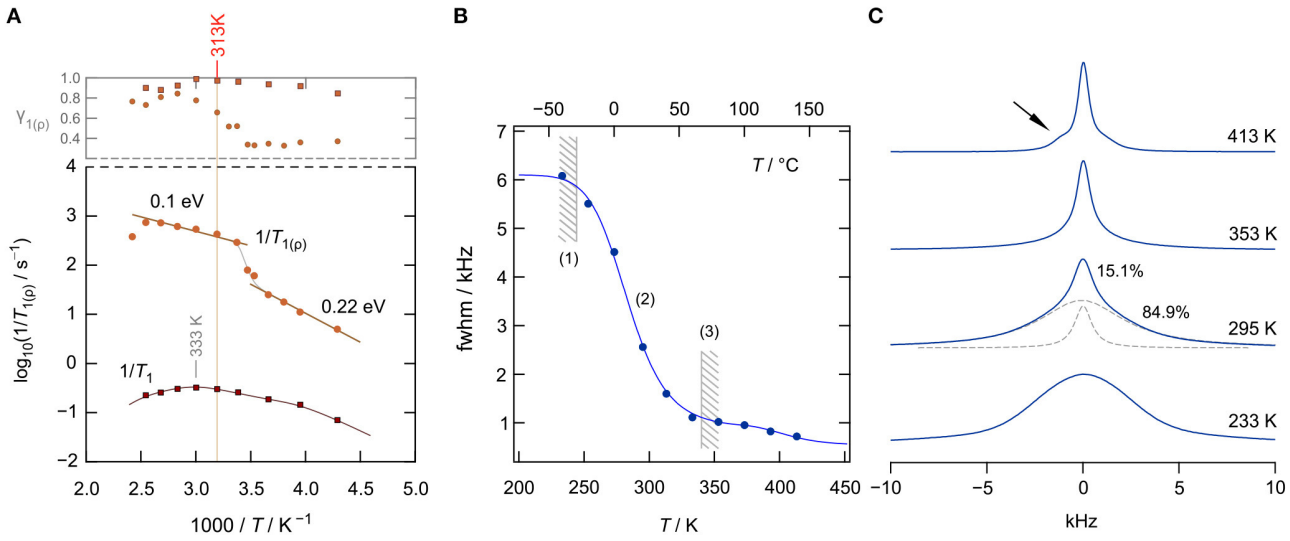

FIGURE 4 | (A) ^{7}Li NMR spin lattice relaxation (SLR) rates $1/T_{1(\varrho)}$ (116.59 MHz) of nanocrystalline, cubic-Li[In_xLi_y]Br_4 as a function of inverse temperature measured (233–393 K). The upper graph shows the $\gamma_{1(\varrho)}$ values used to approximate the magnetization transients. **(B)** ^{7}Li NMR line width (fwhm = full width at half maximum, total fwhm from net spectrum) as a function of temperature; regime (1) denotes the rigid lattice, (2) refers to the motional narrowing regime, and (3) represents the regime of extreme narrowing. The solid line (up to 353 K) represents a fit according to the model Abragam, yielding an activation energy of ~0.25 eV. **(C)** Change of the shape of the ^{7}Li NMR spectra with temperature (233, 295, 353, and 413 K). The spectrum at 295 K has been deconvoluted with a sum of a Gaussian and a Lorentzian function (see dashed lines). Motional narrowing is almost completed at $T = 353$ K.

are characterized by very small values of $E_a \approx 0.1$ eV. Thus, they seem to sample localized ionic motions, which could also originate from Li spins in the interfacial regions (Wilkening et al., 2003; Breuer et al., 2018b) of nanocrystalline Li[In_xLi_y]Br_4. Note that at above 313 K, the Arrhenius line of $\sigma_{dc}T$ reveals a kink. Thus, care has to be taken if we want to interpret the rates $1/T_1$ recorded at $T > 313$ K; they might be affected by irreversible change in the nanostructured sample, which produces only an apparent rate peak.

To study ^{7}Li NMR SLR behavior at temperatures well below 313 K, we recorded spin-lock NMR rates $1/T_\varrho$ in the rotating frame of reference. These rates sense, *per se*, slower ion dynamics as, formally, the Larmor frequency in the MHz range is replaced by a value in the kHz range. Here, we used a locking B_1 field that corresponds to a spin-lock frequency of 20 kHz. The rates obtained are also included in **Figure 4A**. At low T, they follow an activation energy of 0.22 eV, which we attribute to the elementary hopping barrier in site-disordered Li[In_xLi_y]Br_4, also including jump processes in the interfacial regions of the sample. If considering the crystal structure of spinel-type Li[In_xLi_y]Br_4, $1/T_\varrho$ seems to sense (local) hopping between the sites 16*d* and 8*b*. At higher temperatures, the rate shows a sharp increase, passing into a region that is activated with an activation energy of only 0.1 eV. Again, irreversible changes in the heat-sensitive sample seem to be responsible for the anomalous behavior appearing at elevated T.

Alternatively, Li ion dynamics in the ternary indium bromide were studied by recording ^{7}Li NMR spectra; selected spectra are displayed in **Figure 4C**). At low T, that is, the so-called rigid-lattice regime, Li^+ motions are too slow to effectively average dipole-dipole interactions. Thus, the line can be well-described with a broad Gaussian. With increasing T, we clearly see the onset of motional line narrowing. This narrowing process proceeds in a heterogeneous way, i.e., a narrow line appears on top of the broad one. At $T = 295$ K, the area under the narrow line amounts to about 15%, showing that only a fraction of the available Li spins participate in rapid ion exchange. As for other nanocrystalline ceramics, one might attribute this fraction to those spins residing in the structurally disordered interfacial regions (Wilkening et al., 2003; Breuer et al., 2018b) of nanocrystalline Li[In_xLi_y]Br_4. At elevated T, the whole line is affected by motional narrowing. The regime of extreme narrowing is reached at 350 K.

At even higher temperatures, intensities next to the central line appear (see arrow in **Figure 4C**), which we attribute to quadrupole satellites. Likely, grain growth and healing of defects ensure the formation of an ordered phase. In nanocrystalline or amorphous ceramics, satellite intensities are usually smeared out and only appear as a broad foot. Distinct singularities, referring to spin-transitions between the Zeeman levels characterized by $m_I = \pm 1/2$ and $m = \pm 3/2$, are seen in samples with a high degree of crystallinity. Here, σ_{dc} of the annealed sample is, however, much lower than σ_{dc} of the as-prepared, mechanosynthesized sample (see **Figure 2B**). The full narrowing curve of the ^{7}Li NMR central transition is shown in **Figure 4B**. The solid line shows a fit with the model introduced by Abragam (1961) to parameterize the curve; the activation energy turned out to be 0.25 eV, in agreement with the value seen by spin-lock NMR. Details on analyzing NMR line widths with the Abragam formula are given elsewhere (Wilkening et al., 2002). Interestingly, at higher T, a second step in the motional

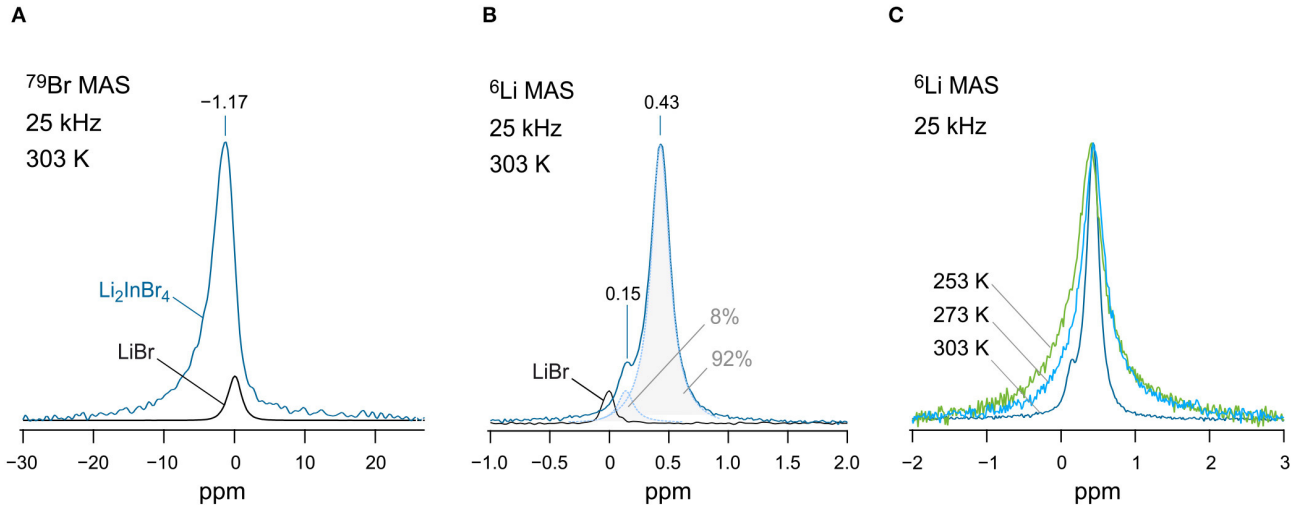

FIGURE 5 | (A) ^{79}Br MAS NMR spectra (125.27 MHz) of nano-Li[In$_x$Li$_y$]Br$_4$ and pure LiBr for comparison. Spectra were recorded at 303 K. LiBr served as a primary reference for both the ^{79}Br MAS NMR and ^{6}Li MAS NMR spectra, see **(B)**. **(B)** ^{6}Li MAS NMR spectra (73.58 MHz) of the nanocrystalline sample; the signal of pure LiBr is shown for comparison. The overall signal of Li[In$_x$Li$_y$]Br$_4$ is composed of two lines appearing at 0.43 and 0.15 ppm. The total NMR signal was deconvoluted with the help of two Lorentzian functions to estimate the area under the signal with low intensity (8%). **(C)** Variable-temperature ^{6}Li MAS NMR spectra (73.58 MHz) recorded at 253, 273, and 303 K. Dipolar interactions cause line broadening at low temperatures.

narrowing curve is seen, which is in line with the deviations seen by σ_{dc} measurements and by the analysis of M''/ν data (see above).

Finally, we checked whether it is possible to distinguish any magnetically inequivalent Li sites by ^{6}Li high-resolution (MAS) NMR. For this purpose, we recorded variable-temperature ^{6}Li NMR spectra (**Figures 5B,C**). Note that the quadrupole moment of the ^{6}Li nucleus is a factor of 50 smaller than that of the ^{7}Li one. Thus, any interfering second-order quadrupole interactions, which are not averaged under ordinary MAS conditions, are almost eliminated, leading to a higher resolution of ^{6}Li NMR spectra. At 253 and 273 K, we detected only a single ^{6}Li line at $\delta_{iso} = 0.43$ ppm. We used LiBr (0 ppm) as a primary reference of the spectra. At 303 K, however, increasing dipole-dipole averaging originating from motional narrowing, which adds up to the elimination of dipolar broadening by MAS, reveals a second line at $\delta_{iso} = 0.15$ ppm. At first glance, we would simply assign this additional line to LiBr. The area under the line with low intensity amounts to ∼8% if we convolute the total signal with a sum of two Lorentzian functions. Interestingly, the line at 0.15 ppm does not match the isotropic shift of LiBr exactly. Furthermore, ^{79}Br MAS NMR gives no strong evidence for LiBr being indeed detectable by NMR (see **Figure 5A**). The signal with low intensity might be attributed to the unidentified phase seen in XRD. Possibly, the presence of In-doped LiBr could serve as an explanation of the signal.

4. CONCLUSION

We successfully synthesized nanocrystalline Li[In$_x$Li$_y$]Br$_4$ directly via a one-pot mechanochemical route. The nanostructured sample was characterized by X-ray powder diffraction and ^{6}Li, ^{79}Br MAS NMR. Li[In$_x$Li$_y$]Br$_4$ needs to be described by a spinel structure with positional disorder on the 16*d* site. Via the bond valence energy landscape methodology, we estimated site energies and a hopping barrier between the Li sites 16*d* and 8*b*. Broadband conductivity helped us to measure long-range ion transport that is characterized by an activation energy of 0.61 eV. Electric modulus data pointed to barriers as high as 0.71 eV if analyzed at 100 Hz. Most likely because of the non-stoichiometry of the sample, a relatively high electronic conductivity in the order of 10^{-8} S cm^{-1} has been found, which is a factor of 10^3 lower than the room-temperature ionic conductivity. Local barriers were probed by diffusion-induced ^{7}Li NMR SLR measurements. In particular, spin-lock NMR yielded an activation energy of 0.22 eV, which either characterizes local (forward-backward) Li jumps between 16*d* and 8*b* or motional events of the Li ions in the interfacial regions. As σ_{dc} is rather low at room temperature, Li[In$_x$Li$_y$]Br$_4$ seems to be a candidate for high-temperature battery cells.

DATA AVAILABILITY STATEMENT

The raw data supporting the conclusions of this article will be made available by the authors, without undue reservation, to any qualified researcher.

AUTHOR CONTRIBUTIONS

MG: synthesis of the material via the mechanochemical synthesis route, characterization, evaluation and interpretation of the data, and writing. DR: rietveld refinement, Li pathway calculations, and data interpretation. HW: supervision, conceptualization,

data interpretation, and writing. All authors contributed to the manuscript revision, read, and approved the submitted version.

FUNDING

This work was supported by TU Graz Open Access Publishing Fund.

ACKNOWLEDGMENTS

We thank Prof. Günther J. Redhammer (Salzburg) for helpful discussion regarding the interpretation and analysis of our preliminary XRPD data. We thank our colleagues at the ICTM (TU Graz) for fruitful discussions.

REFERENCES

Abragam, A. (1961). *The Principles of Nuclear Magnetism*. Oxford: Clarendon.

Asano, T., Sakai, A., Ouchi, S., Sakaida, M., Miyazaki, A., and Hasegawa, S. (2018). Solid halide electrolytes with high lithium-ion conductivity for application in 4 V class bulk-type all-solid-state batteries. *Adv. Mater.* 30:1803075. doi: 10.1002/adma.201803075

Bachman, J. C., Muy, S., Grimaud, A., Chang, H.-H., Pour, N., Lux, S. F., et al. (2016). Inorganic solid-state electrolytes for lithium batteries: mechanisms and properties governing ion conduction. *Chem. Rev.* 116, 140–162. doi: 10.1021/acs.chemrev.5b00563

Bloembergen, N., Purcell, E. M., and Pound, R. V. (1948). Relaxation effects in nuclear magnetic resonance absorption. *Phys. Rev.* 73, 679–712.

Breuer, S., Gombotz, M., Pregartner, V., Hanzu, I., and Wilkening, M. (2018a). Heterogeneous f anion transport, local dynamics and electrochemical stability of nanocrystalline $La_{1-x}Ba_xF_{3-x}$. *Energy Storage Mater.* 16, 481–491. doi: 10.1016/j.ensm.2018.10.010

Breuer, S., Uitz, M., and Wilkening, H. M. R. (2018b). Rapid Li ion dynamics in the interfacial regions of nanocrystalline solids. *J. Phys. Chem. Lett.* 9, 2093–2097. doi: 10.1021/acs.jpclett.8b00418

Bruce, P. G., Scrosati, B., and Tarascon, J.-M. (2008). Nanomaterials for rechargeable lithium batteries. *Angew. Chem. Int. Ed.* 47, 2930–2946. doi: 10.1002/anie.200702505

Buschmann, H., Döelle, J., Berendts, S., Kuhn, A., Bottke, P., Wilkening, M., et al. (2011). Structure and dynamics of the fast lithium ion conductor $Li_7La_3Zr_2O_{12}$. *Phys. Chem. Chem. Phys.* 13, 19378–19392. doi: 10.1039/c1cp22108f

Chen, H., Wong, L. L., and Adams, S. (2019). *SoftBV*—a software tool for screening the materials genome of inorganic fast ion conductors. *Acta Cryst. B* 75, 18–33. doi: 10.1107/S2052520618015718

Cheng, L., Crumlin, E. J., Chen, W., Qiao, R., Hou, H., Franz Lux, S., et al. (2014). The origin of high electrolyte–electrode interfacial resistances in lithium cells containing garnet type solid electrolytes. *Phys. Chem. Chem. Phys.* 16, 18294–18300. doi: 10.1039/c4cp02921f

Dawson, J. A., Attari, T. S., Chen, H., Emge, S. P., Johnston, K. E., and Islam, M. S. (2018). Elucidating lithium-ion and proton dynamics in anti-perovskite solid electrolytes. *Energy Environ. Sci.* 11, 2993–3002. doi: 10.1039/C8EE00779A

Deiseroth, H.-J., Kong, S.-T., Eckert, H., Vannahme, J., Reiner, C., Zaiss, T., et al. (2008). Li_6PS_5X: a class of crystalline li-rich solids with an unusually high Li^+ mobility. *Angew. Chem. Int. Ed.* 47, 755–758. doi: 10.1002/anie.200703900

Dietrich, C., Weber, D. A., Sedlmaier, S. J., Indris, S., Culver, S. P., Walter, D., et al. (2017). Lithium ion conductivity in Li_2S-P_2S_5 glasses—building units and local structure evolution during the crystallization of superionic conductors Li_3PS_4, $Li_7P_3S_{11}$ and $Li_4P_2S_7$. *J. Mater. Chem. A* 5, 18111–18119. doi: 10.1039/C7TA06067J

Dunst, A., Epp, V., Hanzu, I., Freunberger, S. A., and Wilkening, M. (2014). Short-range Li diffusion vs. long-range ionic conduction in nanocrystalline lithium peroxide Li_2O_2—the discharge product in lithium-air batteries. *Energy Environ. Sci.* 7, 2739–2752. doi: 10.1039/C4EE00496E

Dunst, A., Sternad, M., and Wilkening, M. (2016). Overall conductivity and NCl-type relaxation behavior in nanocrystalline sodium peroxide Na_2O_2—consequences for Na-oxygen batteries. *Mater. Sci. Eng. B* 211, 85–93. doi: 10.1016/j.mseb.2016.06.002

Dyre, J. C., Maass, P., Roling, B., and Sidebottom, D. L. (2009). Fundamental questions relating to ion conduction in disordered solids. *Rep. Prog. Phys.* 72:046501. doi: 10.1088/0034-4885/72/4/046501

Funke, K., Cramer, C., and Wilmer, D. (2005). "Concept of mismatch and relaxation for self-diffusion and conduction in ionic materials with disordered structures," in *Diffusion in Condensed Matter-Methods, Materials, Models, 2nd Edn*, eds P. Heitjans and J. Kärger (Berlin: Springer), 857–893.

Gombotz, M., Lunghammer, S., Breuer, S., Hanzu, I., Preishuber-Pflügl, F., and Wilkening, H. M. R. (2019). Spatial confinement–rapid 2D F^- diffusion in micro- and nanocrystalline $RbSn_2F_5$. *Phys. Chem. Chem. Phys.* 21:1872. doi: 10.1039/C8CP07206J

Goodenough, J. B. (2013). Evolution of strategies for modern rechargeable batteries. *Acc. Chem. Res.* 46, 1053–1061. doi: 10.1021/ar2002705

Gupta, H. C., Zwinscher, J., and Lutz, H. D. (1997). Lattice dynamical calculations of deficient NaCl superstructure-type Li_2CoCl_4 and Li_2MnBr_4. *J.Phys. Chem. Solids* 58, 173–175. doi: 10.1016/S0022-3697(96)00082-0

Han, F., Westover, A., Yue, J., Fan, X., Wang, F., Chi, M., et al. (2019). High electronic conductivity as the origin of lithium dendrite formation within solid electrolytes. *Nat. Energy* 4, 187–196. doi: 10.1038/s41560-018-0312-z

Hanghofer, I., Brinek, M., Eisbacher, S. L., Bitschnau, B., Volck, M., Hennige, V., et al. (2019). Substitutional disorder: structure and ion dynamics of the argyrodites Li_6PS_5Cl, Li_6PS_5Br and Li_6PS_5I. *Phys. Chem. Chem. Phys.* 21, 8489–8507. doi: 10.1039/c9cp00664h

Heitjans, P., Masoud, M., Feldhoff, A., and Wilkening, M. (2007). NMR and impedance studies of nanocrystalline and amorphous ion conductors: lithium niobate as a model system. *Faraday Discuss.* 134, 67–82. doi: 10.1039/b602887j

Heitjans, P., Schirmer, A., and Indris, S. (2005). *Diffusion in Condensed Matter—Methods, Materials, Models. 2nd Edn.* Chapter 9. Berlin: Springer, 369–415.

Ishimaru, M., Bae, I.-T., and Hirotsu, Y. (2003). Electron-beam-induced amorphization in SiC. *Phys. Rev. B* 68:144102. doi: 10.1103/PhysRevB.68.144102

Janek, J., and Zeier, W. G. (2016). A solid future for battery development. *Nat. Energy* 1:16141. doi: 10.1038/nenergy.2016.141

Kamaya, N., Homma, K., Yamakawa, Y., Hirayama, M., Kanno, R., Yonemura, M., et al. (2011). A lithium superionic conductor. *Nat. Mater.* 10, 682–686. doi: 10.1038/nmat3066

Kim, S., Oguchi, H., Toyama, N., Sato, T., Takagi, S., Otomo, T., et al. (2019). A complex hydride lithium superionic conductor for high-energy-density all-solid-state lithium metal batteries. *Nat. Commun.* 10:1081. doi: 10.1038/s41467-019-09061-9

Kuhn, A., Narayanan, S., Spencer, L., Goward, G., Thangadurai, V., and Wilkening, M. (2011). Li self-diffusion in garnet-type $Li_7La_3Zr_2O_{12}$ as probed directly by diffusion-induced ^{7}Li spin-lattice relaxation nmr spectroscopy. *Phys. Rev. B* 83:094302. doi: 10.1103/PhysRevB.83.094302

Li, X., Liang, J., Chen, N., Luo, J., Adair, K. R., Wang, C., et al. (2019). Water-mediated synthesis of a superionic halide solid electrolyte. *Angew. Chem. Int. Ed.* 131, 16579–16584. doi: 10.1002/ange.201909805

Lutz, H., Cockcroft, J., Kuske, P., and Schneider, M. (1990). Polymorphism of the fast ionic conductor Li_2MnBr_4 - neutron diffraction and differential scanning calorimetry. *Mat. Res. Bull.* 25, 451–456.

Maekawa, H., Matsuo, M., Takamura, H., Ando, M., Noda, Y., Karahashi, T., et al. (2009). Halide-stabilized $LiBH_4$, a room-temperature lithium fast-ion conductor. *J. Am. Chem. Soc.* 131, 894–895. doi: 10.1021/ja807392k

Martin, D. Z. C., Haworth, A. R., Schmidt, W. L., Baker, P. J., Boston, R., Johnston, K. E., et al. (2019). Evaluating lithium diffusion mechanisms in the complex spinel $Li_2NiGe_3O_8$. *Phys. Chem. Chem. Phys.* 21, 23111–23118. doi: 10.1039/c9cp02907a

Marx, R., and Mayer, H. M. (1996). Darstellung und lithiumteilstruktur von lithiumnnitridtribromid, Li_6NBr_3 und lithiumnitridtriiodid, Li_6NI_3/preparation and lithium sublattice of lithium nitride

trihalides, Li_6NHal_3 (Hal = Br, I). *Z. Naturforsch.* 51b, 525–530. doi: 10.1515/znb-1996-0415

Matsuo, M., and Orimo, S.-I. (2011). Lithium fast-ionic conduction in complex hydrides: review and prospects. *Adv. Energy Mater.* 1, 161–172. doi: 10.1002/aenm.201000012

Mercier, R., Tachez, M., Malugani, J., and Robert, G. (1985). Effect of homovalent (I^- - Br^-) ion substitution on the ionic conductivity of $LiI_{1-x}Br_x$ systems. *Solid State Ion.* 15, 109–112.

Murugan, R., Thangadurai, V., and Weppner, W. (2007). Fast lithium ion conduction in garnet-type $Li_7La_3Zr_2O_{12}$. *Angew. Chem. Int. Ed.* 46, 7778–7781. doi: 10.1002/anie.200701144

Pecher, O., Carretero-González, J., Griffith, K. J., and Grey, C. P. (2017). Materials' methods: NMR in battery research. *Chem. Mater.* 29, 213–242. doi: 10.1021/acs.chemmater.6b03183

Porz, L., Swamy, T., Sheldon, B. W., Rettenwander, D., Froemling, T., Thaman, H. L., et al. (2017). Mechanism of lithium metal penetration through inorganic solid electrolytes. *Adv. Energy Mater.* 7:1701003. doi: 10.1002/aenm.201701003

Richards, W. D., Miara, L. J., Wang, Y., Kim, J. C., and Ceder, G. (2016). Interface stability in solid-state batteries. *Chem. Mater.* 28, 266–273. doi: 10.1021/acs.chemmater.5b04082

Scherrer, P. (1918). Bestimmung der Größe und der inneren Struktur von Kolloidteilchen mittels Röntgenstrahlen. *Göttin. Nachrich.* 2:98.

Schmidt, W., and Lutz, H. D. (1984). Fast ionic conductivity and dielectric properties of the lithium halide spinels Li_2MnCl_4, Li_2CdCl_4, Li_2MnBr_4 and Li_2CdBr_4. *Ber. Bunsenges. Phys. Chem.* 88, 720–723.

Schoch, B., Hartmann, E., and Weppner, W. (1986). New fast solid lithium ion conductors at low and imtermediate temperatures. *Solid State Ion* 18–19, 529–533.

Sidebottom, D. L. (2009). Understanding ion motion in disordered solids from impedance spectroscopy scaling. *Rev. Mod. Phys.* 81, 999–1014. doi: 10.1103/RevModPhys.81.999

Stanje, B., Rettenwander, D., Breuer, S., Uitz, M., Berendts, S., Lerch, M., et al. (2017). Solid electrolytes: extremely fast charge carriers in garnet-type $Li_6La_3ZrTaO_{12}$ single crystals. *Ann. Phys.* 529:1700140. doi: 10.1002/andp.201700140

Stathopoulos, A. Y., and Pells, G. P. (1983). Damage in the cation sublattice of γ-Al_2O_3 irradiated in an HVEM. *Phil. Mag. A* 47, 381–394.

Thangadurai, V., Narayanan, S., and Pinzaru, D. (2014). Garnet-type solid-state fast Li ion conductors for Li batteries: critical review. *Chem. Soc. Rev.* 43, 4714–4727. doi: 10.1039/c4cs00020j

Tomita, Y., Matsushita, H., Kobayashi, K., Maeda, Y., and Yamada, K. (2008). Substitution effect of ionic conductivity in lithium ion conductor, $Li_3InBr_{6-x}Cl_x$. *Solid State Ion* 179, 867–870. doi: 10.1016/j.ssi.2008.02.012

Tomita, Y., Yamada, K., Ohki, H., and Okuda, T. (2014). Structure and dynamics of Li_3InBr_6 and $NaInBr_4$ by means of nuclear magnetic resonance. *Z. Naturf. A* 53, 466–472. doi: 10.1515/zna-1998-6-730

Uitz, M., Epp, V., Bottke, P., and Wilkening, M. (2017). Ion dynamics in solid electrolytes for lithium batteries. *J. Electroceram.* 38, 142–156. doi: 10.1007/s10832-017-0071-4

Wang, S., Bai, Q., Nolan, A. M., Liu, Y., Gong, S., Sun, Q., et al. (2019). Lithium chlorides and bromides as promising solid-state chemistries for fast ion conductors with good electrochemical stability. *Angew. Chem. Int. Ed.* 131, 8123–8127. doi: 10.1002/ange.201901938

Wang, Y., Richards, W. D., Ong, S. P., Miara, L. J., Kim, J. C., Mo, Y., et al. (2015). Design principles for solid-state lithium superionic conductors. *Nat. Mater.* 14, 1026–1031. doi: 10.1038/nmat4369

Wenzel, S., Randau, S., Leichtweiss, T., Weber, D. A., Sann, J., Zeier, W. G., et al. (2016). Direct observation of the interfacial instability of the fast ionic conductor $Li_{10}GeP_2S_{12}$ at the lithium metal anode. *Chem. Mater.* 28, 2400–2407. doi: 10.1021/acs.chemmater.6b00610

Wilkening, M., Bork, D., Indris, S., and Heitjans, P. (2002). Diffusion in amorphous $LiNbO_3$ studied by ^{7}Li NMR – comparison with the nano- and microcrystalline material. *Phys. Chem. Chem. Phys.* 4, 3246–3251. doi: 10.1039/b201193j

Wilkening, M., and Heitjans, P. (2012). From micro to macro: access to long-range Li^+ diffusion parameters in solids via microscopic ^{6,7}Li spin-alignment echo nmr spectroscopy. *ChemPhysChem* 13, 53–65. doi: 10.1002/cphc.201100580

Wilkening, M., Indris, S., and Heitjans, P. (2003). Heterogeneous lithium diffusion in nanocrystalline Li_2O:Al_2O_3 composites. *Phys. Chem. Chem. Phys.* 5, 2225–2231. doi: 10.1039/B300908D

Yamada, K., Kumano, K., and Okuda, T. (2006). Lithium superionic conductors Li_3InBr_6 and $LiInBr_4$ studied by ^{7}Li and ^{115}In NMR. *Solid State Ion* 177, 1691–1695. doi: 10.1016/j.ssi.2006.06.026

Yu, C., Ganapathy, S., Eck, E. R. H. V., Wang, H., Basak, S., Li, Z., et al. (2017). Accessing the bottleneck in all-solid state batteries, lithium-ion transport over the solid-electrolyte-electrode interface. *Nat. Commun.* 8:1086. doi: 10.1038/s41467-017-01187-y

Zhang, W., Schroeder, D., Arlt, T., Manke, I., Koerver, R., Pinedo, R., et al. (2017). (Electro)chemical expansion during cycling: monitoring the pressure changes in operating solid-state lithium batteries. *J. Mater. Chem. A* 5, 9929–9936. doi: 10.1039/C7TA02730C

Zhang, Z., Shao, Y., Lotsch, B., Hu, Y.-S., Li, H., Janek, J., et al. (2018). New horizons for inorganic solid state ion conductors. *Energy Environ. Sci.* 11, 1945–1976. doi: 10.1039/C8EE01053F

Conflict of Interest: The authors declare that the research was conducted in the absence of any commercial or financial relationships that could be construed as a potential conflict of interest.

D1

Enhanced Ion Dynamics by Interface Engineering in the Dispersed Ionic Conductor LiF:TiO_2

M. Gombotz *and H. Martin R. Wilkening*

Manuscript draft

Enhanced Ion Dynamics by Interface Engineering in the Dispersed Ionic Conductor LiF:TiO_2

Maria Gombotz, Veronika Pregartner and H. Martin R. Wilkening

Institute for Chemistry and Technology of Materials, Graz University of Technology, Austria

1 Introduction

Lithium fluoride, known to be a poor ionic conductor, was chosen as a model substance to investigate the influence of the insulator TiO_2 on ion dynamics in this material. In general, in such two-phase systems percolating pathways at the conductor|insulator interface may lead to enhanced ion dynamics. This effect was already examined *e.g.* in the systems Li_2O:Al_2O_3[1], Li_2O:B_2O_3[2] and LiF:γ-Al_2O_3[3].

Analogously to the latter example, different properties in the composites $(1-x_v)$LiF:$x_v$$TiO_2$ (x_v = 0.1 - 0.5) were examined within this study. Via XRD it was proven that LiF and TiO_2 do not react upon the conducted mechanochemical synthesis. All composites as well as micro- and nanocrystalline LiF, for comparison, were thereafter subjected to temperature variable impedance measurements to study the impact of an increasing amount of insulator within the composites on the conductivity. It was found that a maximum of 40vol% TiO_2 leads to an increase of conductivity, thereafter the value decreases. This highly conducting sample was then examined by static ^{7}Li and ^{19}F NMR experiments. As these measurements allow the observation of Li^+ and F^- dynamics separately, it was possible to show that compared to nanocrystalline LiF[3], both ions are able to move faster when 40vol% of TiO_2 are added, however, with Li^+ being the dominant mobile species in the investigated temperature range.

2 Experimental

$(1-x_v)$LiF:$x_v$$TiO_2$ (x_v = 0.1 - 0.5) composites in the nanocrystalline form were prepared by high-energy ball milling. Therefore overnight in vacuum dried amounts of LiF (Alfa Aesar, 99.98%) and TiO_2 (Sigma Aldrich, Anatase, $\leq$99%) were milled for 15 h in ZrO_2 beakers, loaded with 180 balls 5 mm in diameter, made of the same material. The milling was carried out in a Fritsch 7 premium line high-energy planetary mill at 600 rpm with a milling program, where 15 min of milling are followed by 15 min of a break to allow cooling of the beakers.

After the synthesis the purity of the samples were checked by X-ray Powder Diffraction using a Rigaku Miniflex with CuK_α (λ = 1.5406 Å) radiation. The scanned $^\circ 2\theta$ range covered values between 20 and 60$^\circ 2\theta$. The step size was set to 0.01$^\circ 2\theta$ with a scan speed of 5$^\circ 2\theta$/min.

To reveal the most conductive sample, the conductivity of all composites $(1-x_v)$LiF:$x_v$$TiO_2$ (x_v = 0.1 - 0.5) as well as nano-and microcrystalline LiF were determined by impedance spectroscopy. To do so, the sample powder was pressed to pellets with a diameter of 5 mm (uniaxial pressure of 0.5 t) and on both sides 50 nm ion blocking electrodes made of Gold were sputtered with a Leica EM SCD 050 sputter device. Thereafter the con-

[1] M. Wilkening *et al.*, Phys. Chem. Chem. Phys., 2003, 5, 2225-2231

[2] S. Indris *et al.*, J. Non-Cryst. Solids, 2002, 307-310, 555-561

[3] S. Breuer *et. al.* J. Phys. Chem. C, 2019, **123**, 5222

ductivity was measured with a Novocontrol Concept 80 broadband dielectric spectrometer in combination with a ZGS active sample cell. The measured frequencies covered a range of $3.6{\cdot}10^{-2}$ Hz up to 10^7 Hz, the temperatures a range between 20°C and 200°C. The temperature was regulated by a QUATRO cryosystem, whereby freshly evaporated N_2 flushed the sample cell continuously.

^{7}Li and ^{19}F spectra of 0.6 LiF : 0.4 TiO_2 were recorded under static conditions with a Bruker cryomagnet in combination with a Bruker Avance 300 spectrometer. The nominal magnetic field of 7.4 T of this magnet results in a resonance frequency of 470.59 MHz for ^{19}F and 116.59 MHz for ^{7}Li, respectively. The temperature was varied between −60°C and 240°C.

3 Results and Discussion

As a first step, the phase purity of micro- and nanocrystalline LiF was checked by XRD. The corresponding powder pattern is shown in Figure 1 together with a reference (ICSD: 18012).

A minor impurity at approximately 26°2θ was found in nanocrystalline LiF, which matches indeed TiO_2 in the anatase modification but is much more probably an impurity from the milling beakers. The fwhm of nanocrystalline LiF, milled for 15 h, is higher for the detected reflexes compared to microcrystalline LiF, as expected due to the decreased grain size achieved by milling. By adding the insulator TiO_2 the reflexes get broader, indicating a further reduction. An interesting fact, also seen in the powder pattern is that the used TiO_2 in anatase modification partly transforms to rutile, most likely due to the high energy input during milling. Furthermore it was ensured by XRD that LiF does not undergo a reaction with TiO_2, hence both materials occur separately and percolation pathways are able to form between them.

The conductivity of all samples investigated by XRD was determined by impedance spectroscopy. As an example, the conductivity isotherms of 0.6 LiF : 0.4 TiO_2 are depicted in Figure 2 (a).

The isotherms show three characteristic regions; the electrode polarisation at low frequencies, the frequency independent σ_{DC}-plateau and the dispersive region at higher frequencies. Here, long-range transport of ions is characteristic for the σ_{DC}-plateau, hence this value is read off and can

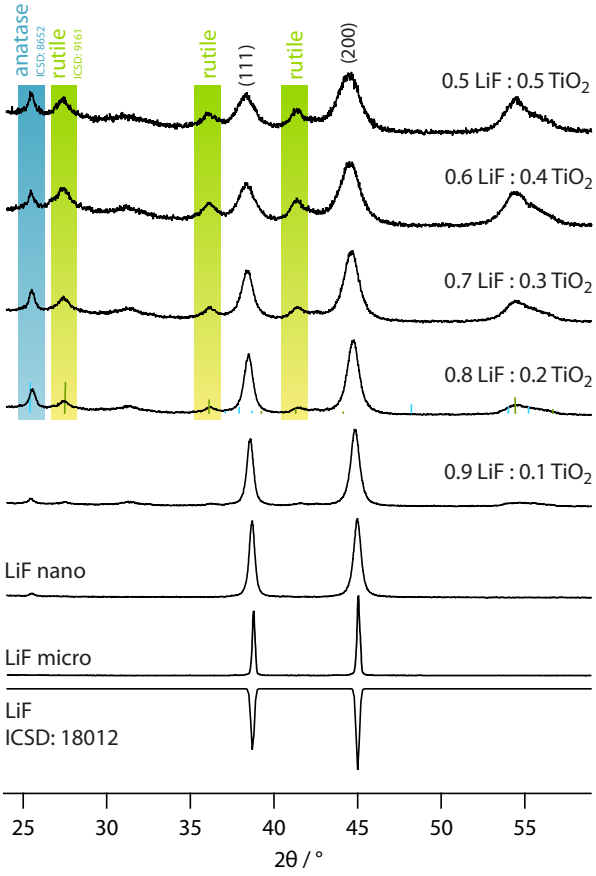

Figure 1: *X-ray powder pattern of micro- and nanocrystalline LiF, as well as a LiF reference (ICSD: 18012) and all $(1-x_v)$LiF:$x_v TiO_2$ (x_v = 0.1 - 0.5) composites. With increasing amount of TiO_2, the fwhm of all reflexes increases, indicating a decreasing crystallite size. Additionally, as marked, the used TiO_2 in anatase modification is partly transformed to rutile during the mechanochemical treatment.*

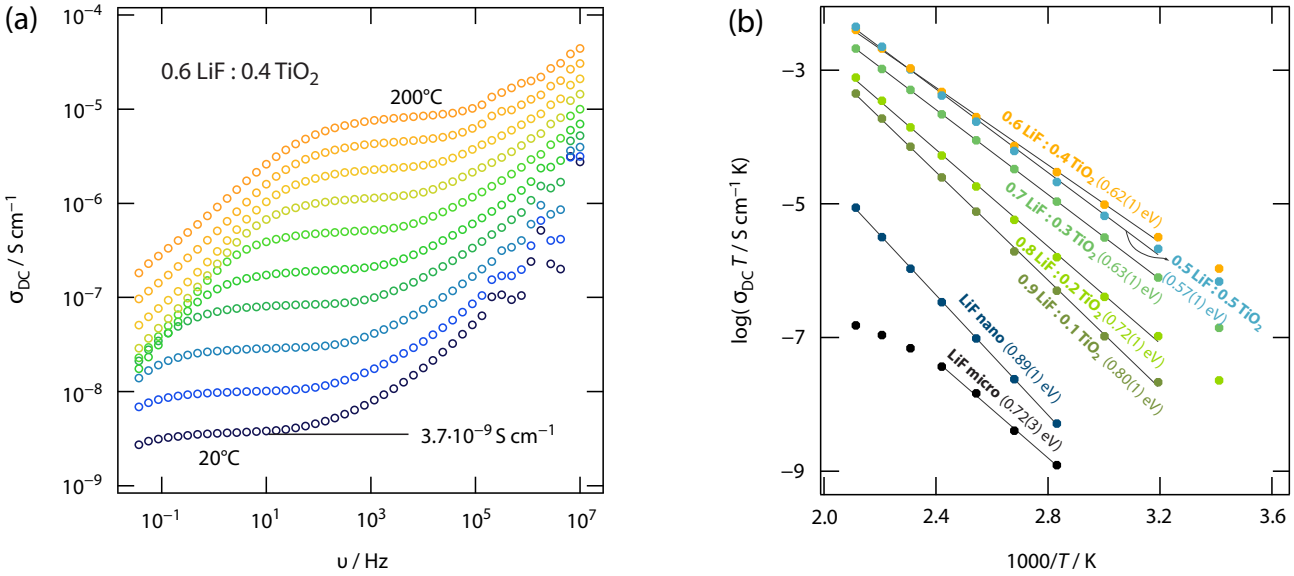

Figure 2: ***(a)*** *Conductivity isotherms of the most conductive composite 0.6 LiF : 0.4 TiO_2 in a temperature range from 20°C up to 200°C, as indicated.* ***(b)*** *Arrhenius plot showing nano- as well as microcrystalline LiF and all $(1-x_v)$LiF:$x_v TiO_2$ (x_v = 0.1 - 0.5) composites. A clear increase in conductivity when going from microcrystalline LiF to 0.6 LiF : 0.4 TiO_2 can be seen. The solid lines represent line fits to extract the activation energy of the samples shown.*

be plotted in an Arrhenius-type diagram, see Figure 2 (b), to extract the activation energy. The lowest conductivity is found for the microcrystalline LiF sample, reaching $1.1 \cdot 10^{-11}$ S cm^{-1} at 100°C. A slight increase is found for the nanocrystalline sample with $6.4 \cdot 10^{-11}$ S cm^{-1}, again at 100°C. Interestingly, the nanocrystalline LiF shows a higher activation energy of 0.89(1) eV compared to 0.72(3) eV for microcrystalline LiF. By adding TiO_2 the conductivity is increased drastically; it reaches the highest values in the sample with 40vol% added TiO_2 (0.6 LiF : 0.4 TiO_2) with $1.9 \cdot 10^{-7}$ S cm^{-1} at 100°C. This constitutes an increase of nearly 4 orders of magnitude compared to microcrystalline LiF. Also the activation energy decreases to 0.62(1) eV. Obviously, the ion movement occurs in a faster manner by adding the insulator, as expected. The formed percolation pathways between LiF and TiO_2 are most efficient when 40vol% TiO_2 are present within the sample, as the addition of more TiO_2 leads then to a decrease in conductivity, as the pathways get interrupted by more, non-conducting TiO_2.

As in LiF both ions, Li^+ and F^- are mobile, NMR experiments can help to reveal the mainly mobile ion. Therefore, ^{7}Li and ^{19}F NMR spectra of 0.6 LiF : 0.4 TiO_2 were recorded under static conditions in a wide temperature range between −60°C and 240°C in 20°C steps. At temperatures below 40°C, *e.g.* at 60°C, see Figure 3 (a), a homogeneous line is seen for ^{7}Li spectra. Starting at 40°C and above up to 240°C, a heterogeneous, motional line narrowing can be tracked. In the middle a sharp spike emerges, which is characteristic for systems, where a fraction of the mobile ions are way more faster than the other. This fraction of fast ions can be estimated by fitting the spectra with two Gaussian or Lorentzian curves, depending on the overall shape. While at 40°C only 0.5% of the Li ions belong to those fast ions, at 240°C already 67.7% do so. ^{7}Li spectra of nanocrystalline LiF[4] show motional narrowing beginning at a temperature of 200°C, compared to 40°C within this composite. This is a clear evidence that Li^+ ion dynamics are enhanced by the addition of TiO_2.

The mobility of F ions in 0.6 LiF : 0.4 TiO_2 result in a quite different form of ^{19}F spectra. At temperatures up to 40°C the spectra is composed of a broad inhomogeneous line. Above 180°C, analogously to the ^{7}Li spectra, inhomogeneous, motional narrowing starts and the two contributions to the line can be fitted with Gaussian or Lorentzian curves. Even at 240°C, only 5% of F^- can be considered as fast ions in 0.6 LiF : 0.4 TiO_2. Contrary to the present spectra, ^{19}F spectra of nanocrystalline LiF[4] do not show motional nar-

[4] S. Breuer *et. al.* J. Phys. Chem. C, 2019, **123**, 5222

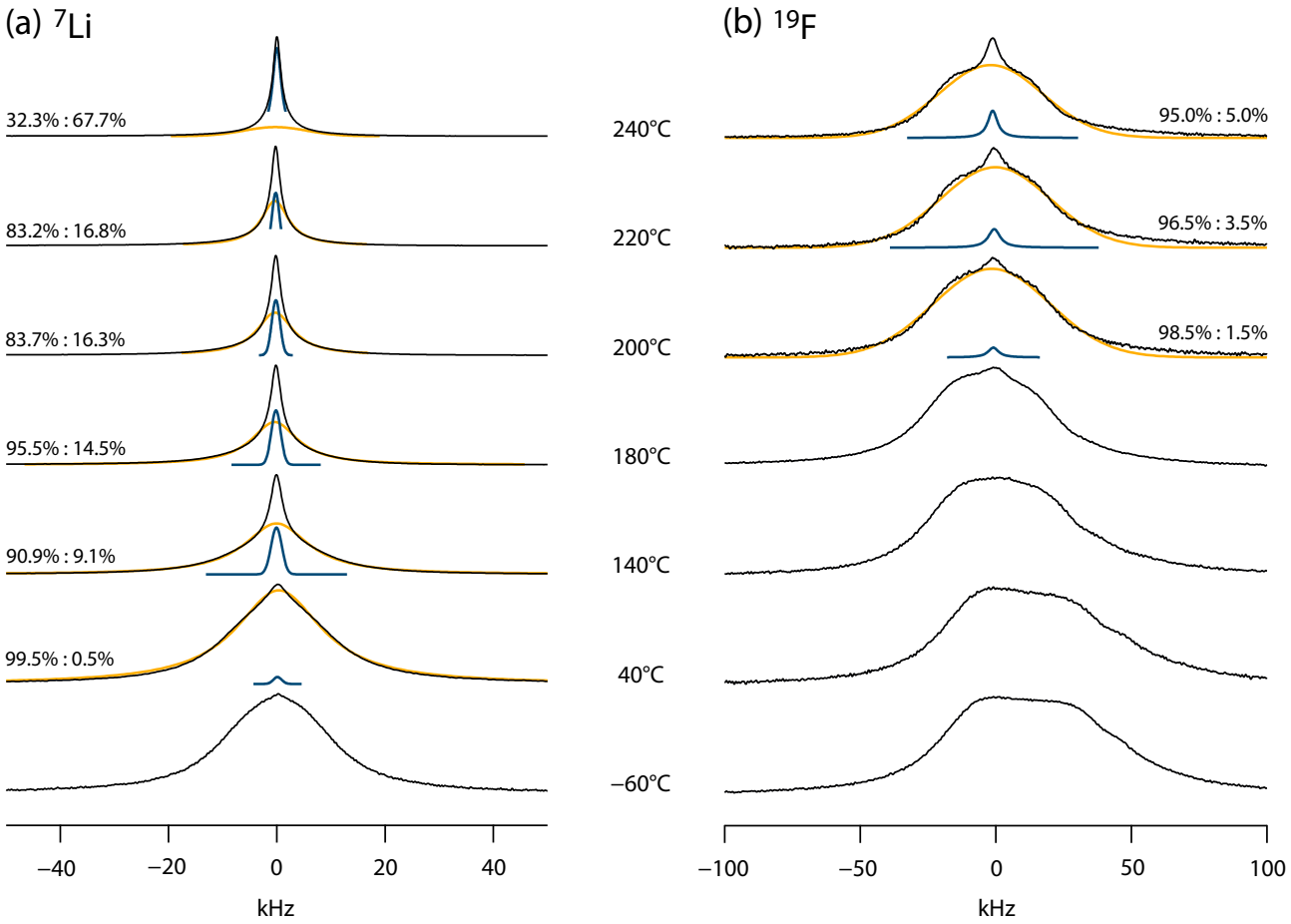

Figure 3: *Temperature variable* ***(a)*** ^{7}*Li NMR and* ***(b)*** ^{19}*F spectra of 0.6 LiF : 0.4* TiO_2 *recorded between* $-60°C$ *and* $240°C$ *in* $20°C$ *steps. Selected spectra were fitted with Gauss and Lorentzian curves to estimate the fraction of fast ions, represented by the sharp part of the spectra, a result of heterogeneous motional narrowing.*

rowing at all. Hence, not only Li^+ dynamics are accelerated, but also F^- dynamics, although to a much smaller extent, as only a small fraction of F^- can be considered fast.

4 Conclusion

Within this study, the influence of the insulator TiO_2 on the conductivity of the poor ionic LiF was examined by investigating the composites $(1-x_v)$LiF:$x_v TiO_2$ (x_v = 0.1 - 0.5). The mechanochemical syntheses of those materials ensured the close contact of LiF and TiO_2 and furthermore, transformed the utilised anatase modification of TiO_2 partly into rutile, as seen in XRD. An addition of 40vol% TiO_2 lead to an increase in conductivity by four orders of magnitude compared to the microcrystalline analogue. This fact clearly shows that the formation of the assumed percolation pathways at the interface between insulator and the ionic conductor, enables high diffusivity along them. This behaviour was also seen in static NMR experiments, where F^- and Li^+ show an earlier onset of motional narrowing as compared to nanocrystalline LiF indicating enhanced ion dynamics for both ions. With a way larger fraction of Li^+ ions being regarded as fast, Li^+ was revealed as the dominant mobile ion.

Preface:

Degradation of Single-Crystalline $Li_{6.4}La_3ZrTaO_{12}$ in Humidity: A Nuclear Magnetic Resonance and Neutron Diffraction Study

The material class of garnets with the general formula $Li_3B_2C_3O_{12}$ [72], is considered one of the most promising candidates for solid electrolytes to be employed in all-solid-state batteries [73, 74]. However, the general sensitivity of garnets towards humid air inhibits their straightforward implementation, as the degradation product, Li_2CO_3, forms highly resistive layers on the surface, increasing the resistance at interfaces between electrolyte and electrode [75, 76]. Another dentrimental factor is the so far unknown behaviour upon Li^+/H^+ exchange during exposure of the garnet to humid air. The garnet structure is reported to change [72] or remain unaffected [77] during H^+ uptake. To establish valid counteractions, allowing the implementation of garnets as solid electrolytes despite the mentioned drawbacks, the on-going degradation mechanisms, and their impact on ion dynamics have to be investigated further.

Possible structural transformations and changes in Li^+ dynamics in the garnet material $Li_{6.4}La_3ZrTaO_{12}$ were the central questions to be answered during this study. A single crystal of the stated material was immersed in different solutions before being characterised in-depth. The investigation of structural changes encompassed of neutron diffraction as well as ^1H and ^6Li MAS NMR measurements, revealing the incorporation of hydrogen in the structure without changing the overall crystal structure. The course of resistance of the different samples was probed via impedance spectroscopy, the changes in dynamic parameters was investigated by means of static ^1H and ^7Li NMR relaxometry. We were able to show that the corresponding Li diffusion coefficient is only slightly slowed down, even if the crystal is stored in water for 31 days. Importantly, H^+ was proven to be mobile inside the crystal, marking the first study tracking this diffusion processes in garnets.

Author Contributions: MG carried out the MAS NMR as well as static NMR measurements, evaluated and interpreted the impedance and NMR data and wrote the publication. CH prepared the samples and carried out the impedance measurements. RU synthesised the samples. MM and GR performed the neutron diffraction measurements, interpreted the data and contributed to the writing of the publication. DR conceptualised the project. HMRW supervised the project.

M1

Degradation of Single-Crystalline $Li_{6.4}La_3ZrTaO_{12}$ in Humidity: A Nuclear Magnetic Resonance and Neutron Diffraction Study

M. Gombotz, *C. Hiebl, R. Uecker, M. Meven, G. Redhammer, D. Rettenwander and H. M. R. Wilkening*

Unpublished manuscript

Journal Name

ARTICLE TYPE

Cite this: DOI: 10.1039/xxxxxxxxxx

Degradation of Single-Crystalline $Li_{6.4}La_3ZrTaO_{12}$ in Humidity: A Nuclear Magnetic Resonance and Neutron Diffraction Study†

Maria Gombotz,*[a] Caroline Hiebl,[a] Reinhard Uecker,[b] Martin Meven,[c] Guenther Redhammer,[d] Daniel Rettenwander,[a] and H. Martin R. Wilkening[a,e]

Received Date
Accepted Date

DOI: 10.1039/xxxxxxxxxx

www.rsc.org/journalname

For the realisation of all-solid-state batteries highly conductive solid electrolytes are needed, ideally with stability against atmosphere. The promising material class of lithium-stuffed garnets exhibits disadvantages, as even traces of oxygen and water in gloveboxes can trigger degradation [S. Uhlenbrock *et al., Solid State Ionics*, 2018, **320**, 259-265]. The response upon degradation and the thereby on-going exchange of Li^+ by H^+ differs substantially for various garnet-materials, which makes the ion-exchange an interesting field of research. In this study, we took $Li_{6.4}La_3ZrTaO_{12}$ single crystals to study the amount of H^+ in the material after immersion in water for 7 and 31 days via Neutron diffraction. After the successful exchange of a maximum of 0.4 pfu was proven, the influence on resistivity via impedance spectroscopy was investigated, giving no clear correlation between resistivity and degree of ion exchange. Furthermore, polycrystalline LLZTO was immersed in water and glacial acetic acid to further shed light on structural details via ^{6}Li and ^{1}H Magic Angle Spinning NMR. ^{7}Li and ^{1}H relaxation rates were determined to investigate the influence of Li^+/H^+ exchange on diffusional parameters in detail, pointing towards rapid motion of H^+ inside the garnet crystal.

1 Introduction

Since the discovery of $Li_7La_3Zr_2O_{12}$-type garnets[1], these types of solid Li-ion electrolytes are considered as one of the most promising candidates for making all-solid-state batteries possible[2]. Recently though, the instability of garnets against H_2O and CO_2, so to say humid air, has gained more attention[3] since the reaction product Li_2CO_3 is the origin of highly resistive interfaces between electrolyte and electrodes[4] and thus, reducing the cell performance. The ongoing reaction[5] in LLZO

$$Li_{56}La_{24}Zr_{16}O_{96}(s) + H_2O(g) \rightleftharpoons Li_{54}La_{24}Zr_{16}O_{96}(s) + 2LiOH(s) \quad (1)$$

and

$$Li_{56}La_{24}Zr_{16}O_{96}(s) + CO_2(g) \rightleftharpoons Li_{54}La_{24}Zr_{16}O_{96}(s) + Li_2CO_3(s) \quad (2)$$

requires Li^+/H^+ exchange inside the crystal. As even garnets stored in Ar-filled gloveboxes show formation of Li_2CO_3[6], this phenomenon got attention, as such a great air sensitivity might hamper the implementation of garnets as solid-state electrolytes. As the Li^+/H^+ exchange is a crucial step, it was thereupon analysed in a great variety of garnet materials like $Li_{7-x}H_xLa_3Sn_2O_{12}$[7,8], Nb-doped $Li_7La_3Zr_2O_{12}$[9–12], Ta-doped $Li_7La_3Zr_2O_{12}$[13], $Li_{6.5}La_3Zr_{1.5}Ta_{0.5}O_{12}$[14], $Li_{6-x}H_xCaLa_2Nb_2O_{12}$[15] or $Li_{7-x}H_xLa_3Zr_2O_{12}$[16]. All studies have one thing in common; garnets with a lithium concentration above the permitted three Li ions per formula unit $Li_3B_2C_3O_{12}$[7] are especially prone to the exchange of Li^+ by H^+ ions. Apart from this common feature, depending on the structure, chemical composition and doping elements, the response from the garnet upon reaction with H^+ was quite different. Tetragonal $Li_{7-x}H_xLa_3Sn_2O_{12}$ changed to cubic structure upon H^+ insertion[7], whereas even the space-group of others like Al-doped LLZO[17], $Li_{7-x}La_3(Zr, Ta)_2O_{12}$[6] or $Li_5La_3Nb_2O_{12}$[12] remained the same.

The amount of thereby exchanged Li^+ strongly depends on the

[a] Graz University of Technology, Institute for Chemistry and Technology of Materials, 8010 Graz, Austria. E-mail: rettenwander@tugraz.at, wilkening@tugraz.at, gombotz@tugraz.at
[b] Leibniz Institute for Crystal Growth (IKZ), 12489 Berlin, Germany.
[c] Institute of Crystallography, RWTH Aachen University, 52056 Aachen and Juelich Centre for Neutron Science (JCNS) at Heinz Maier-Leibnitz Zentrum (MLZ), 85748 Garching, Germany.
[d] Department Chemistry and Physics of Materials, Division Materials Science and Mineralogy, University of Salzburg, 5020 Salzburg, Austria.
[e] ALISTORE - European Research Institute, CNRS FR3104, Hub de l'Energie, Rue Baudelocque, 80039 Amiens, France.

surface exposed to humid air / H_2O, as demonstrated by Yow Z. F. *et al*[13]. They immersed $Li_{6.6}La_3Zr_{1.6}Ta_{0.4}O_{12}$ in water for 7 days, reaching an exchange level of 8.8% after 7 days for a dense pellet, whereas for a powdered sample a value of 54.3% in the same time was hit, highlighting the role of surface exposure.

As the ratio of surface to bulk plays a significant role, we used single crystalline $Li_{6.4}La_3ZrTaO_{12}$ to precisely study the effect of Li^+/H^+ exchange while having a fixed bulk to surface ratio. As a further advantage, the possible contribution of grain boundaries to the kinetics of the ion exchange is eradicated.

Rather harsh conditions, which do not reflect reality, can be used on the one hand to accelerate on-going reactions or, as in this case, to study general reactions. As the major focus lies on the diffusion of H^+ in $Li_{6.4}La_3ZrTaO_{12}$ in this study, the crystals were immersed in distilled H_2O for different periods of time. As X-rays show only a low sensitivity to Lithium, single-crystal Neutron diffraction was performed, allowing precise determination of the sites occupied by Li^+ and H^+. Equally to previous studies[10,14,17], which showed for different garnets that Li^+ gets exchanged exclusively by H^+ on octahedral sites, we were able to show that H^+ occupies the 96*h* position in $Li_{6.4}La_3ZrTaO_{12}$ after immersion in water. The amount of exchanged Li^+ was, as expected from the low ratio of surface to bulk, relatively small with 0.3 pfu after 7 days and 0.4 pfu after 31 days in water. Primarily the small increase in the amount of exchanged Li^+ after 31 days is not taken by surprise, but can be traced to the poor accessibility of Li^+ inside the crystal and the slow diffusion of H^+ through it, as proven by static NMR measurements, see later.

Diffusion is affected in many cases[18] already by doping element concentrations in extremely low amounts, making the immersed crystals an interesting role model for conductivity studies. Up to now, studies showed that there is no straightforward correlation between conductivity and the degree of Li^+/H^+ exchange. Conductivity either stayed unaffected[8,10] or decreased[13,19] upon Li^+/H^+ exchange. Hence, the overall resistance of $Li_{6.4}La_3ZrTaO_{12}$ crystals immersed for the same time span as for scND measurements, was measured via impedance spectroscopy and lead to the controversial result of increasing resistance for the sample immersed for 7 days, while decreasing again for the sample immersed for 31 days.

The final questions which were to be answered were, if H^+ diffuses in the crystal, as indicated by Hiebl *et al.*[17] and to elucidate the mechanism of Li^+/H^+ exchange. The method of choice when it comes to the characterisation of the dynamics of one specific mobile ion in a solid compound is solid state NMR[20]. Here, the relaxation times $T_{1(\rho)}$ were measured as a function of temperature for ^{7}Li and ^{1}H, for two different samples; a finely grinded crystal immersed for 1 h in dest. H_2O or glacial acetic acid. The successful exchange of Li^+ by H^+ by immersion in acids is reported in several studies in literature[11,12,21,22]. It was shown that the amount of exchanged Li^+ in $Li_{5+x}Ba_xLa_{3-x}Nb_2O_{12}$ increases when CH_3COOH is used compared to H_2O, but only for a composition of x = 0. For x = 1, the percentage of Li decreased. It has to be mentioned that, to our knowledge, only this study exists and the amount of exchanged Li^+ was investigated not with an accurate method like ND, but with TG. Therefore we choose this system for further investigations anyway.

In this case it was not possible to use a big single crystal, as ^{6}Li and ^{1}H MAS NMR was performed too, to investigate the structure closer, which makes it inevitable to use powder material. Both techniques could, for the first time, show that compared to the pristine material, significant H^+ mobility is measurable after H^+/Li^+ exchange. This mobility, however, does not fundamentally change the Li^+ mobility.

2 Experimental

2.1 Single Crystal Synthesis

Conventional Czochralski technique was used to grow LLZTO single crystals with the nominal composition $Li_{6.4}La_3ZrTaO_{12}$. Li_2CO_3, La_2O_3, ZrO_2, and Ta_2O_5 served as starting materials and were dried and mixed in the required stoichiometry with a 10% excess of Li_2CO_3. Then they were uniaxial pelletized, isostatically pressed at 2800 kbar and sintered at 1373 K for 16 h in air in capped magnesia crucibles whilst the pellets were covered with LLZTO mother powder to avoid Li-loss during the sintering process. The sintered LLZTO samples were molten by radio frequency induction heating using a 25 kW microwave generator and an iridium seed (pulling rate 1.5 mm h^{-1}, rotation speed 1 rpm) was used for the crystal growth performed under N_2 atmosphere. An active afterheater was applied to adjust the temperature gradient in the set up. Thermal insulation was established by an outer alumina ceramic tube filled with zirconia granules. The final composition $Li_{6.4}La_3ZrTaO_{12}$ was confirmed by inductively coupled plasma optical emission spectroscopy (ICP-OES).

2.2 Single Crystal Neutron Diffraction

Single crystal intensity data sets were collected at the HEiDi diffractometer at 300 K with λ = 0.793 Å (Ge-(420)) monochromator on a 2 x 2 x 1.5 mm block, cut from the original large singe crystal. HEiDi is a four circle single crystal diffractometer with an acentric Eulerian cradle using the high flux of hot neutrons at beam tube SR9A of the FRM II reactor[23]. First, the pristine sample was measured and after data collection, it was emerged in distilled water for 7 days. After this treatment, a new data collection was performed. Finally, the same crystal was put in H_2O dest. once again for additional 24 days and measured a third time (see Table 2 for more details). For the full structure characterization, data acquisition was done up to $\sin\theta/\lambda$=0.808 with about 675 Bragg reflections. Full structure analysis was done using the WinGX package of programs[24] and SHELXL-2014[25] in combination with the FULLPROF - Suite for combined simultaneous refinement of single-crystal X-ray (SCXRD) and single-crystal neutron diffraction (SCND) analysis and bond-valence sum map display. Details on data collection, crystal data and refinements are given in Table 2, fractional atomic coordinates are given in Table 3, the anisotropic atomic displacement parameters can be found in Table 4.

2.3 Impedance Spectroscopy

Impedance spectroscopy was carried out on a pristine LLZTO crystal as well as on crystals, one emerged in H_2O for 7 days and one

for 31 days, respectively. Ion-blocking electrodes, made of Au, were sputtered on both sides of the rod-shaped crystals with a Leica sputter device (EM SCD050). A broadband impedance spectrometer (Novocontrol, Concept 80 - actice BDS 1200 cell, ZGS interface) was used to perform alternating current (AC) impedance measurements at a controlled temperature of 293 K. The temperature was regulated by a QUATRO cryosystem. During the measurement dry, freshly evaporated N_2 flows around the sample. Data evaluation was done with IGOR Pro (Wavemetrics) and ZView (Princeton Applied Research).

2.4 Magic Angle Spinning Nuclear Magnetic Resonance

Single pulse experiments were applied to record ^{6}Li and ^{1}H Magic Angle Spinning (MAS) NMR spectra on a Bruker Avance III 500 spectrometer of grinded LLZTO emerged in H_2O or glacial acetic acid for 1 h each. Resonance frequencies of 500 MHz for ^{1}H and 73.58 MHz for ^{6}Li result from the nominal magnetic field of 11.7 T. We used 2.5 mm rotors made of ZrO_2 and an appropriate Bruker MAS probe head to acquire free induction decays (FIDs). The spinning speed was set to 25 kHz with a target gas flow of 400 L h^{-1} and a frame cooling of 35% of the target gas flow. The bearing gas temperature was set to 303 K, whereas the sample temperature is usually higher due to the friction during rotation.

2.5 Static Solid State Nuclear Magnetic Resonance

^{1}H and ^{7}Li spectra as well as spin-lattice relaxation rates were recorded in the laboratory frame of reference (R_1) and in the rotating frame of reference ($R_{1\rho}$) with a Bruker Avance III 300 NMR spectrometer of LLZTO soaked in H_2O or glacial acetic acid one hour each. The spectrometer operates at a nominal magnetic field of 7.04 T. A commercial ceramic probe head was used to perform temperature variable measurements from 173 K up to 533 K. For measurements in the rotating frame of reference a locking frequency of $\nu_1/2\pi \approx 20$ kHz was applied. The saturation recovery method was used to acquire the rates in the laboratory frame of reference (300 MHz for ^{1}H, 116.59 MHz for ^{7}Li). Before the measurements were carried out, the as prepared H-substituted $Li_{6.4}La_3ZrTaO_{12}$ was fire-sealed in a glass cylinder with a length of approximately 3 cm and a diameter of 4 mm. This was done under vacuum to avoid any contamination.

3 Results & Discussion

3.1 Single Crystal Neutron Diffraction

Analysis of systematic extinctions yield space group $Ia\bar{3}d$ for the pristine as well as both H_2O treated (7 and 31 days) single crystals. It should be highlighted that the high-quality neutron diffraction data on the single crystal allow to refine all the atoms with anisotropic atomic displacement parameters and yield - to our best knowledge - the most precise structural data for Ta-substituted LLZO, especially with respect to Li-sites (see SI, Table 2).

As already outlined in an earlier publication[26], the Zr/Ta ratio of the studied single crystal deviates slightly form a 1:1 stoichiometry. Even if the nuclear bond scattering lengths of Zr and Ta are similar for the neutron case (7.16 and 6.91 fm respectively), the site distribution of the two elements on the octahedrally coordinated 16*a* site in here is very similar to the one found from the single crystal X-ray diffraction experiment, namely ($Zr_{0.90}Ta_{1.10}$), however shows very slow convergence. To have more firm determination, simultaneous refinement of both, 300 K SCND and SCXRD data (with slightly more weights given to the neutron diffraction data), where performed and the very same site occupation distribution was obtained. Both Li sites show distinct amounts of vacancies, with the regular tetrahedral site Li1 at 24*d* being filled by $\sim 2/3$, while the Li2 site in interstitial 96*h* position is filled by $\sim 1/3$. Here the refinements on the SCND data alone yield slightly different occupation numbers with the occupation of 0.676(19) and 0.351(8) as compared to 0.659(19) and 0.341(7) from the simultaneous refinement for the Li1 and Li2 sites respectively. Using the later values and a slight deficit on the La-site, which is also revealed by the simultaneous refinement and which is in line with findings on other LLZO garnet type materials[27,28], a charge balanced formula can be obtained with $Li_{6.07}La_{2.95}Zr_{0.90}Ta_{1.10}O_{12}$; using the SCND data alone, a surplus of positive charges due to a fully occupied La site and the somewhat higher Li-site occupancies is found. Is should be noted here that using the structural model, given in Table 3, no significant and interpretable residual electron densities are observed. It is evident, that Li1 on the regular tetrahedral position shows largest anisotropic displacements of all atoms at 300 K, Li2 shows large anisotropic atomic displacement also, however to a somewhat smaller, but more elongated extent. The elongation runs in the direction of the neighbouring Li1-sites and evidences the Li-diffusion pathways. The data for the H_2O treated samples were first evaluated without any constraints. In here - as it is to be expected - the Zr/Ta ratio was the same within e.s.d. to the one of the pristine material. The site occupation number at the Li1 site is slightly smaller while the one at the Li2 site larger. This was interpreted as a replacement of Li^+ by H^+ (which has a more negative bound scattering length) only at the Li2 site, while the tetrahedral 24*d* position seems to be almost unaffected. For the final refinements thus the site occupation factors for La, Zr/Ta and the amount of vacancies on Li2 sites were fixed to the data obtained for the pristine sample, while the nuclear density at Li1 was allowed to refine freely and the one at the Li2 site then was modelled by a mixed refinement of $Li^+ + H^+$. Also, for the H_2O treated sample, full anisotropic refinement of atomic displacement parameters was possible and a small replacement of Li^+ by H^+ in an amount of 0.30 H atoms per formula unit could be detected after 7 days, which increases slightly to 0.40 H atoms after a total of 31 days of treatment in distilled water. No interpretable residual nuclear density peaks were identified in difference Fourier map inspection. So indeed - even if the amount of Li^+/H^+ replacement is small - there is a detectable replacement, which affects - at least in a first step - selectively the interstitial 96*h* position. This is in line with recent observations[17].

3.2 Impedance Spectroscopy

Impedance spectroscopy of pristine LLZTO as well as H_2O treated samples (7 and 31 days), was performed at 20°C over a large

frequency range (10^{-2} Hz up to 10^{7} Hz). This was done, to investigate the influence of Li^+/H^+ exchange on the resistance. The corresponding Nyquist plots for all samples are depicted in Figure 1.

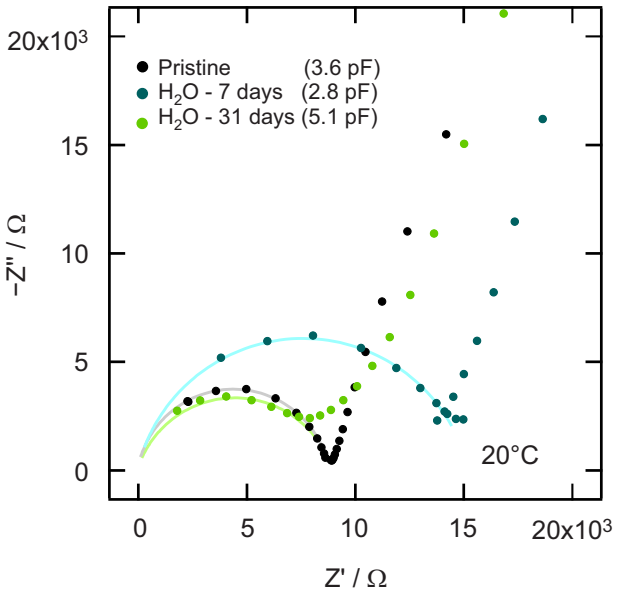

Fig. 1 Nyquist plot of pristine LLZTO and LLZTO immersed in dest. H_2O for 7 and 31 days, respectively. Data points were acquired from 10^{-2} Hz up to 10^{7} Hz. The solid lines represent fits, leading to capacities of 3.6 pF for pristine LLZTO, 2.8 pF after immersion in dest. H_2O for 7 days and 5.1 pF after 31 days.

In the Nyquist plot, the imaginary part of the impedance, −Z" is plotted against the real part of the impedance, Z'. A resistor parallel in combination with a constant phase element, was used to simulate the electric response of all samples. This simulation yields a capacity of 3.6 pF for pristine LLZTO, which is typical for a bulk response, as expected from a single crystal. The simulated value decreases slightly down to 2.8 pF after immersion for 7 days, before increasing again to 5.1 pF after 31 days. As evident, the resistance follows no plausible course in this quite narrow value window. Here, the quality of surface polishing before immersion might play a role too, making it hard to state whether the small variation in resistance is due to different degree of ion exchange or influenced by other circumstances. Temperature variable relaxation measurements via NMR give further information, see below.

3.3 Local structures as seen by ^{6}Li and ^{1}H MAS NMR

The successful exchange of Li^+ inside the crystal, being replaced by H^+ selectively on the 96*h* position, was proven by neutron diffraction. To gather more information about the structural change upon Li^+/H^+ exchange, high-resolution ^{1}H NMR spectra were acquired. To do so, pristine LLZTO crystals were crushed and then immersed in water or glacial acetic acid for 1 h each. Even though this sample had to be treated differently than that for neutron diffraction, it is expected that the response of the sample upon immersion is comparable. This assumption is based on the fact that an increased surface-to-bulk ratio correlates with a faster exchange, as proven by Yow et al.[13]. A shorter immersion time of the crushed crystal was therefore chosen. Furthermore, as reported in literature[11,12,21], the response upon immersion in acids differs from the one in H_2O, depending presumably on the amount of Li in the structure. To give greater clarity on the exchange mechanisms here, spectra as well as relaxation rates were recorded too.

^{1}H NMR test measurements of pristine LLZTO verified that initially no protons were present in the sample. The recorded ^{1}H spectra are shown in Figure 2 a) and, as assumed from neutron diffraction data, reveal one magnetically equivalent site for hydrogen in water treated LLZTO, namely on the 96h position. Depicted in Figure 2 a) too, is the spectrum of LLZTO immersed in glacial acetic acid. The obtained spectrum is defacto identical with the water-treated one, apart from the higher fwhm (1229 Hz compared to 1615 Hz). Spinning side bands show up as well as a line at ≈ −5 ppm, indicating minor impurities.

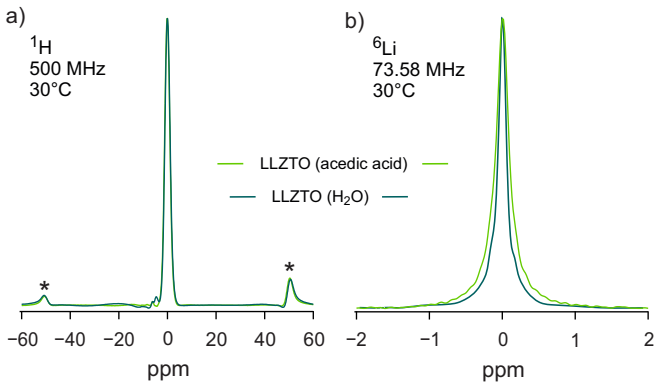

Fig. 2 a) ^{1}H and b) ^{6}Li MAS spectra recorded at a spinning frequency of 25 kHz and a temperature of 303 K for LLZTO immersed in H_2O and glacial acetic acid. At −50 ppm and 50 ppm in the ^{1}H spectrum spinning side bands show up.

MAS NMR does not only give information about structural features, but can also give a first insight into ion dynamics. ^{6}Li spectra of both samples are consisting of one NMR line only. LLZTO offers several different sites for Li. From the fact that only one line is seen, it becomes clear that the diffusion of lithium takes place in such a fast manner that all ions sense the same environment. The full width at half maximum (fwhm) of water treated LLZTO, 10.68 Hz, is significantly lower than the one of acid treated LLZTO, 15.93 Hz. This difference in the fwhm originates from the fact that Li^+ dynamics in acid treated LLZTO are slower, possibly due to the incorporation of a larger amount of H^+.

3.4 ^{7}Li and ^{1}H relaxation rates

A more detailed insight in ion dynamics in water and acid treated LLZTO one can get from spin-lattice relaxation rates. ^{7}Li relaxation rates were acquired in the laboratory and rotating frame of reference. The combination of these two techniques gives in-

formation about the dynamics on a large time scale. The measurement of diffusion-induced T_1 rates in the MHz range, reveals details about localized Li dynamics, whereas information about the long-range transport, can be accessed via the measurement of $T_{1\rho}$ rates, performed in the kHz range.
The inverse $T_{1(\rho)}$ rates $1/T_{1(\rho)} = R_{1(\rho)}$ are plotted as a function of 1000 / T in an Arrhenius type diagram, see Figure 3.

When taking a look at the ^{7}Li R_1 rates of both samples, it becomes evident that they show a similar behaviour in the temperature range recorded, which is not surprising, as the amount of Li^+/H^+ exchange is supposed to be rather low. At temperatures below -40°C the rates barely depend on temperature, marking non-diffusion induced processes. (This processes include coupling of ions to phonons or paramagnetic impurities.) At higher temperatures, localized motion governs the R_1 rates leading to a linear increase of R_1 rates, when being plotted in the Arrhenius type diagram. Here, linear fits of the low-T regime result in an activation energy, calculated with Eq. 3, of 0.22(1) eV for acid treated LLZTO and of 0.20(1) eV for H_2O treated LLZTO.

$$\frac{1}{\tau_c} = \frac{1}{\tau_{c,0}} \cdot e^{-\frac{E_A}{k_B T}} \tag{3}$$

At a temperature of approximately 185°C the diffusion induced rate peak reaches its maximum for both samples. When going to even higher temperatures, one would normally get another linear regime. In this case, however, it was not possible to increase the temperature further and to get as a next step, information about the dynamics dominating in this regime.
By changing from the laboratory to the rotating frame of reference, it is possible to shift the diffusion induced rate peak to lower temperatures, as lower measuring frequencies in the kHz range are used. This was accomplished for these two samples and the results are shown in Figure 3 a), where $R_{1\rho}$ rates are plotted against the inverse temperature. Identical to R_1 rates, below -60°C the rates are governed by non-diffusion induced processes. When increasing the temperature, the rates follow Arrhenius behaviour leading to a higher activation energy of 0.41(1) eV for acid-treated LLZTO than for the water-treated sample (0.30(3) eV). This trend continues at the high temperature flank, were again water-treated LLZTO has a slightly lower E_A=0.34(1) eV than acid treated LLZTO with E_A=0.38(1) eV.
A detailed investigation of this phenomenon is possible by using a modified spectral density function, see Eq. 4, to fit the diffusion-induced rate peak.

$$J(\omega_0) \propto \frac{\tau_c}{1+(\omega\tau_c)^\beta} \tag{4}$$

This modified density function, as introduced by Bloembergen, Pourcell and Pound[30], represents the Fourier transform of the function G(t'), describing the motional correlation function. If this function is single exponential, the value β becomes 2. The BPP-fit of $R_{1\rho}$ for both samples yields a value of $\beta = 2$. In this case the rate peak is symmetric and uncorrelated, 3-dimensional Li^+ motion occurs in this temperature regime. This is somewhat contrary to the different E_A, extracted from linear fits for the two flanks of each sample, indicating an asymmetric peak shape. Here, not enough data points most probably cause inaccurate linear fits leading to deviating values.
BPP fits were carried out for R_1 rates too, leading to slightly lower values of β, namely 1.87 for water treated, 1.74 for acid treated LLZTO, respectively.
Table 1 gives an overview about the different activation energies E_A, calculated using on the one hand linear fits at the low and high temperature flank, respectively, and on the other hand as extracted from BPP fits over the whole temperature range (weaker-than activated background excluded).

One can make use out of the fact that at the peak maximum, the correlation time $1/\tau_c$ is defined via Eq. 5 for R_1 and via Eq. 6 for $R_{1\rho}$.

$$\tau_0\omega_0 \approx 1 \tag{5}$$

$$\tau_1\omega_1 \approx 0.5 \tag{6}$$

With this equations, where $\omega_{0,1}$ denotes the Lamor or locking frequency, it was possible to calculate for each sample two correlation times, which can be found in Table 1. As described in an earlier publication from Stanje *et al.*[26] the ^{7}Li diffusion coefficient can be calculated with the Einstein-Smoluchowski equation 7, where a denotes the distance between two Li sites, here the 24*d* and 96*h* position.

$$D = \frac{a^2}{6\tau} \tag{7}$$

This results in a diffusion coefficient in the order of $D_{R1} \approx 10^{-12}$ m^2 s^{-1} for both samples at 186°C, being comparable with the one for pristine LLZTO (D $\approx 10^{-12}$ m^2 s^{-1} at 130°C). The nearly identical diffusion coefficients reflect only the behaviour at the rate peak. Especially at the high temperature flank obviously different dynamics govern the R_1 rates of pristine LLZTO, as evidenced by the varying slope and the thereby defined E_A, see Figure 4. By this fact it becomes clear that the incorporation of hydrogen influences the local dynamics of ^{7}Li.

The diffusion coefficient deduced from $R_{1\rho}$ is $D \approx 10^{-15}$ m^2 s^{-1}, valid for water-treated LLZTO at 9°C, for acid-treated LLZTO at 26°C and for pristine LLZTO at 15°C, see Figure 4, hence, being comparable for all samples. However, by taking a look at the slopes of the linear fits in the low as well as high temperature flank, it becomes obvious that long range transport, as sensed by spin-lock measurements, is influenced by the Li^+/H^+ exchange too. At low temperatures the activation energy of $R_{1\rho}$ rates of pristine LLZTO is with a value of 0.24(1) eV significantly below the ones of water and acid treated LLZTO. The opposite trend can be observed when looking at the high temperature flank; the long-range ion dynamics in pristine LLZTO in this temperature range occur with an activation energy of 0.42 eV, which is significantly above the ones from water and acid treated LLZTO. Therefore, it can be assumed that below ambient temperatures the long-range dynamics are slowed down by the exchange of Li^+ by H^+. At higher temperatures, however, this dynamic processes seem to be

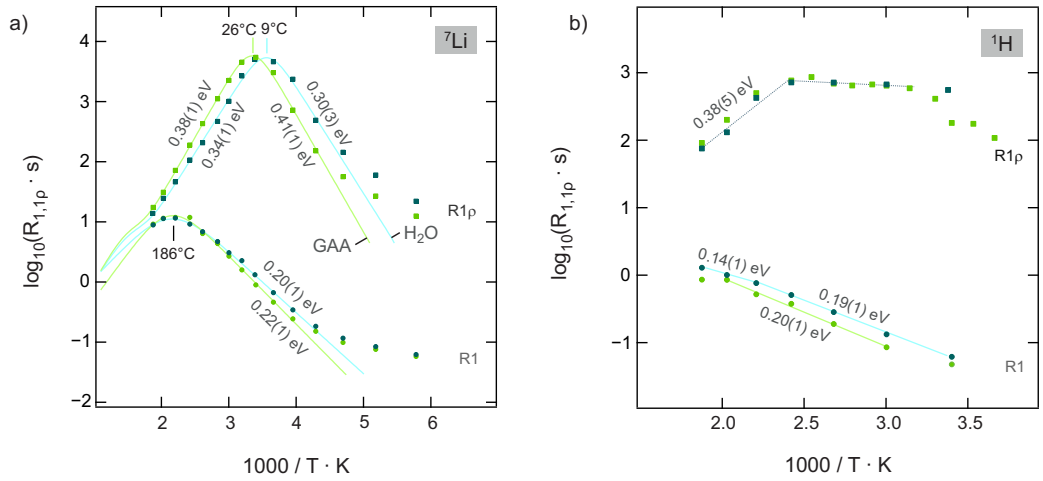

Fig. 3 a) Arrhenius plot presenting ^{7}Li relaxation rates $R_{1(\rho)}$ of LLZTO immersed in dest. H_2O and glacial acetic acid for 1 h, as a function of temperature. The rates were recorded in the laboratory frame (116.6 MHz) and rotating frame (20 kHz) of reference in a temperature range between −100 to 260°C. The solid lines represent BPP fits, see text for further explanation. b) ^{1}H relaxation rates $R_{1(\rho)}$ of LLZTO immersed in dest. H_2O and glacial acetic acid for 1 h were recorded in the laboratory (300 Hz) as well as the rotating (20 kHz) frame of reference as a function of temperature. Measurements were done in a temperature range from 20 to 260°C. The solid lines represent linear fits to calculate the activation energy of ongoing diffusion processes.

Table 1 Characteristic values extracted from R_1 and $R_{1\rho}$.

		water treated LLZTO	glacial acetic acid LLZTO
T_1	low T. flank E_A	0.20(1) eV	0.22(1) eV
	T_{max}	186°C	186°C
	β	1.87	1.74
	BPP fit E_A	0.23(3) eV	0.39(1) eV
	τ_c	$1.37{\cdot}10^{-6}$ s at 186°C	$1.37{\cdot}10^{-6}$ s at 186°C
$T_{1\rho}$	low T. flank E_A	0.30(3) eV	0.41(1) eV
	high T. flank E_A	0.34(1) eV	0.39(1) eV
	T_{max}	9°C	26°C
	β	2	2
	BPP fit E_A	0.35(1) eV	0.30(6) eV
	τ_c	$3.98{\cdot}10^{-6}$ s at 9°C	$3.98{\cdot}10^{-6}$ s at 26°C

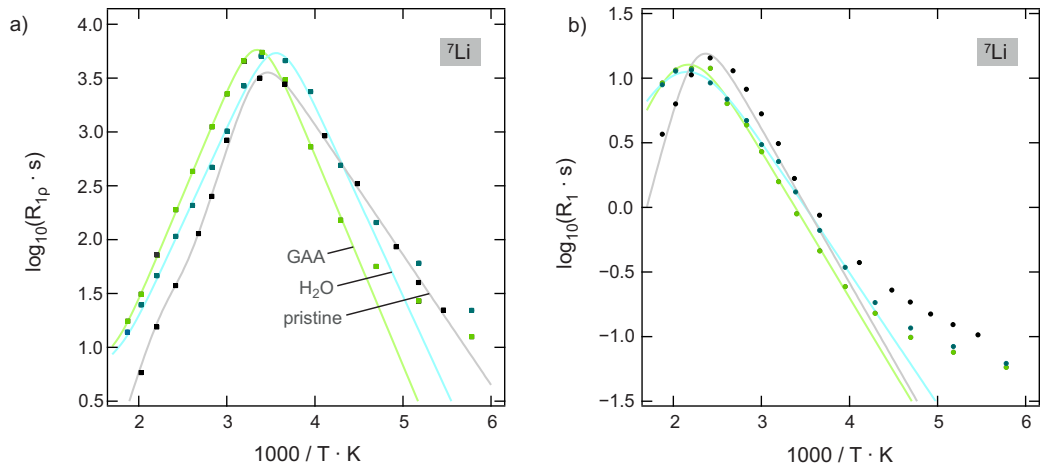

Fig. 4 a) Temperature dependence of the relaxation rates $R_1 = 1/T_1$ recorded in the laboratory frame of reference (300 MHz) of pristine LLZTO from an earlier publication[26], LLZTO immersed in glacial acetic acid and dest. H_2O for 1 h. The temperature range covered −100°C up to 260°C. The data was approximated using BPP fits, represented by solid lines, see text for further explanation. b) Temperature dependence of the relaxation rates $R_{1\rho} = 1/T_{1\rho}$ recorded in the rotating frame of reference (20 kHz) of the same samples in the identical temperature range. Solid lines represent again BPP fits.

accelerated.
These facts also help clarify the slightly deviating resistance values as seen by impedance spectroscopy. Even though the samples were treated differently, we can see here that at room temperature all samples show a comparable behaviour. The deviating resistances might be therefore measuring fluctuations. The resistances at higher temperatures would be interesting.
If we now go back and take a look at Figure 3 b), where ^{1}H relaxation rates $R_{1(\rho)}$ are plotted in an Arrhenius diagram too, we can extract information about the dynamics of hydrogen in LLZTO. Local dynamics are sensed, as said, by measuring relaxation rates R_1 in the laboratory frame of reference. ^{1}H dynamics in both sample are to be characterised by a low activation energies of 0.19(1) eV for acetic and 0.20(1) eV for water treated LLZTO. Respectively a slight difference can be, however, seen in the value of the relaxation rates, which are higher for acid treated LLZTO, pointing towards facilitated dynamics in this material, possibly due to a larger amount of incorporated hydrogen. The relaxation rates $R_{1\rho}$ are depicted in Figure 3 b), pointing towards more complex processes going on. The relaxation rates below 40°C do not follow a linear trend, making the calculation of an activation energy impossible. At elevated temperatures in a range between 70 to 260°C the activation energy increases to a value of 0.38(5) eV, leading to the assumption that here, indeed dynamics on a long-range scale are sensed and the hydrogen ions are able to diffuse from one 96*h* to the next 96*h* site.

3.5 ^{7}Li NMR line shapes

^{7}Li NMR spectra were recorded at temperatures ranging from −100°C up to 260°C. The line widths of these spectra (their full width at half maximum (fwhm)), as shown in Figure 5 a), give an insight into Li^+ ion dynamics in LLZTO immersed in water and acetic acid. Additionally, line widths of pristine LLZTO are plotted from an earlier publication[26] for comparison. A distinct difference between all three samples is only found at temperatures below 20°C. At this temperature, motional narrowing (MN), occurring due to increasing hopping frequency, is completed. The on-set temperature for MN differs - it increases from −80°C for pristine LLZTO up to −60°C for acid treated LLZTO. This indicates a slow-down of Li^+ diffusion with increasing H^+ content. Rigid lattice line widths at temperatures as low as −100°C are similar for acid and water treated LLZTO. As depicted in Figure 5 b), identical to ^{6}Li high-resolution spectra, ^{7}Li spectra show only one line.

To probe ^{1}H ion dynamics identical measurements as for ^{7}Li were done. When looking at the temperature dependent line width, plotted in Figure 5 c), as a function of temperature, significant differences become evident. The ^{1}H line widths of acid treated LLZTO at temperatures below 120°C are clearly higher than the ones of water treated LLZTO. This fact can be interpreted either with an higher degree of Li^+/H^+ exchange and / or with slowed down dynamics in this material. Line shapes, as presented in Figure 5 d), do not give further information about H^+ dynamics as they are similar for all temperatures, due to their nearly identical appearance. The same is valid for ^{1}H high-resolution spectra.

4 Conclusions

In this study we reported on the successful exchange of lithium by hydrogen in single crystals of the lithium rich garnet $Li_{6.4}La_3ZrTaO_{12}$ by immersion in water. Single crystal neutron diffraction leads to the result that Li^+ gets exchanged by H^+ only on the 96*h* position. A maximum amount of 0.4 pfu hydrogen was exchanged after immersion of the crystal for 31 days in water. The main amount of Li^+ was already exchanged by $^+$H after only 7 days, namely 0.3 pfu. Impedance spectroscopy lead to no clear correlation between immersion time and resistance. Therefore, ion dynamics were further investigated by ^{7}Li and ^{1}H static NMR measurements. ^{7}Li NMR relaxations rates recorded in the rotating frame of reference, being *per se* sensitive to long-range dynamics, point towards a slowed down Li^+ diffusion at temperature below 20°C by Li^+/H^+ exchange. Above this temperature, however, the dynamics seem to be accelerated. By measuring ^{1}H relaxation rates we were, for the first time, able to show that hydrogen is mobile itself in LLZTO.

Conflict of interest

There are no conflicts to declare.

References

1 R. Murugan, V. Thangadurai and W. Weppner, *Angewandte Chemie International Edition*, 2007, **46**, 7778–7781.
2 Q. Liu, Z. Geng, C. Han, Y. Fu, S. Li, Y. bing He, F. Kang and B. Li, *Journal of Power Sources*, 2018, **389**, 120 – 134.
3 K. Hofstetter, A. J. Samson, S. Narayanan and V. Thangadurai, *Journal of Power Sources*, 2018, **390**, 297 – 312.
4 L. Cheng, E. J. Crumlin, W. Chen, R. Qiao, H. Hou, S. Franz Lux, V. Zorba, R. Russo, R. Kostecki, Z. Liu, K. Persson, W. Yang, J. Cabana, T. Richardson, G. Chen and M. Doeff, *Phys. Chem. Chem. Phys.*, 2014, **16**, 18294–18300.
5 L. Cheng, C. H. Wu, A. Jarry, W. Chen, Y. Ye, J. Zhu, R. Kostecki, K. Persson, J. Guo, M. Salmeron, G. Chen and M. Doeff, *ACS Applied Materials & Interfaces*, 2015, **7**, 17649–17655.
6 S. Uhlenbruck, C. Dellen, S. M'uller, S. Lobe, C.-L. Tsai, M. Finsterbusch, M. Bram and O. Guillon, *Solid State Ionics*, 2018, **320**, 259 – 265.
7 C. Galven, J. Dittmer, E. Suard, F. Le Berre and M.-P. Crosnier-Lopez, *Chemistry of Materials*, 2012, **24**, 3335–3345.
8 C. Galven, J.-L. Fourquet, M.-P. Crosnier-Lopez and F. Le Berre, *Chemistry of Materials*, 2011, **23**, 1892–1900.
9 C. Liu, K. Rui, C. Shen, M. E. Badding, G. Zhang and Z. Wen, *Journal of Power Sources*, 2015, **282**, 286 – 293.
10 L. Truong, M. Howard, O. Clemens, K. S. Knight, P. R. Slater and V. Thangadurai, *J. Mater. Chem. A*, 2013, **1**, 13469–13475.
11 L. Truong and V. Thangadurai, *Chemistry of Materials*, 2011, **23**, 3970–3977.
12 L. Truong and V. Thangadurai, *Inorganic Chemistry*, 2012, **51**, 1222–1224.

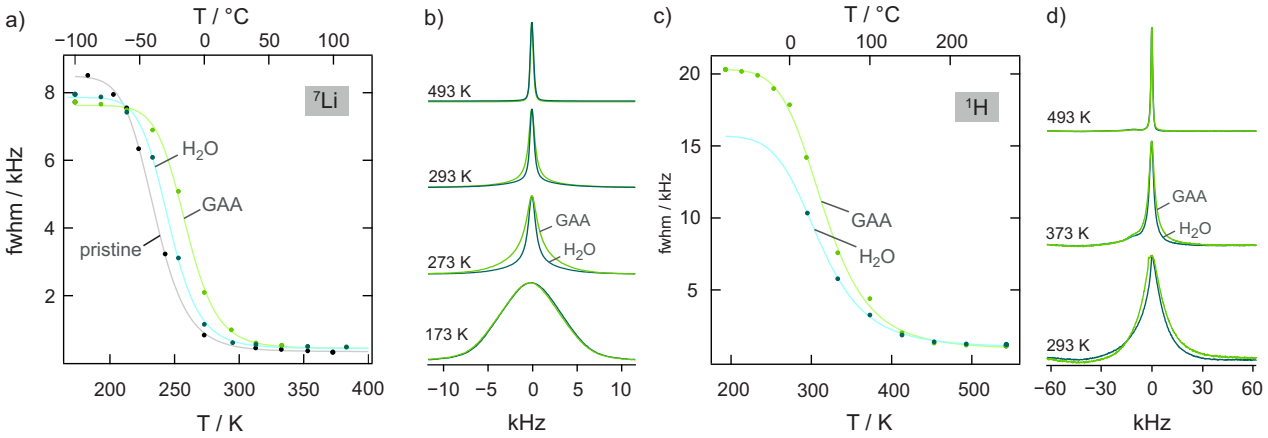

Fig. 5 a) ^{7}Li NMR line widths of previously investigated LLZTO[26] and LLZTO treated with H_2O and glacial acetic acid as a function of temperature. Line widths were recorded in a temperature range from −100°C up to 260°C from static ^{7}Li measurements. As the motional narrowing sets in for all samples latest at 20°C, temperatures higher than 393 K are not depicted. b) Selected ^{7}Li NMR line shapes of LLZTO treated with H_2O and glacial acetic acid at temperatures ranging from −100°C up to 220°C. c) Selected ^{1}H NMR line shapes of H_2O and glacial acetic acid treated LLZTO in a temperature range from 20°C up to 220°C, collected from static ^{1}H NMR measurements. b) ^{1}H NMR line width as a function of temperature. H_2O treated LLZTO was measured in a temperature range between 20°C and 220°C, glacial acidic acid treated LLZTO in a range between −100°C and 260°C.

13 Z. F. Yow, Y. L. Oh, W. Gu, R. P. Rao and S. Adams, *Solid State Ionics*, 2016, **292**, 122 – 129.

14 Y. Li, J.-T. Han, S. C. Vogel and C.-A. Wang, *Solid State Ionics*, 2015, **269**, 57 – 61.

15 C. Galven, E. Suard, D. Mounier, M.-P. Crosnier-Lopez and F. Le Berre, *Journal of Materials Research*, 2013, **28**, 2147–2153.

16 A. Orera, G. Larraz, J. A. Rodrí guez Velamazmazán, J. Campo and M. L. Sanjuán, *Inorganic Chemistry*, 2016, **55**, 1324–1332.

17 C. Hiebl, D. Young, R. Wagner, H. M. R. Wilkening, G. J. Redhammer and D. Rettenwander, *The Journal of Physical Chemistry C*, 2019, **123**, 1094–1098.

18 J. Allen, J. Wolfenstine, E. Rangasamy and J. Sakamoto, *Journal of Power Sources*, 2012, **206**, 315 – 319.

19 R. H. Brugge, A. K. O. Hekselman, A. Cavallaro, F. M. Pesci, R. J. Chater, J. A. Kilner and A. Aguadero, *Chemistry of Materials*, 2018, **30**, 3704–3713.

20 S. Breuer, V. Pregartner, S. Lunghammer and H. M. R. Wilkening, *The Journal of Physical Chemistry C*, 2019, **123**, 5222–5230.

21 Y. Shimonishi, A. Toda, T. Zhang, A. Hirano, N. Imanishi, O. Yamamoto and Y. Takeda, *Solid State Ionics*, 2011, **183**, 48 – 53.

22 F. Gam, C. Galven, A. Bulou, F. Le Berre and M.-P. Crosnier-Lopez, *Inorganic Chemistry*, 2014, **53**, 931–934.

23 M. Meven and A. Sazonov, *Journal of large-scale research facilities*, 2015, **1**,.

24 L. J. Farrugia, *Journal of Applied Crystallography*, 2012, **45**, 849–854.

25 G. M. Sheldrick, *Acta Crystallographica Section C*, 2015, **71**, 3–8.

26 B. Stanje, D. Rettenwander, S. Breuer, M. Uitz, S. Berendts, M. Lerch, R. Uecker, G. Redhammer, I. Hanzu and M. Wilkening, *Annalen der Physik*, 2017, **529**, 1700140.

27 R. Wagner, G. J. Redhammer, D. Rettenwander, G. Tippelt, A. Welzl, S. Taibl, J. Fleig, A. Franz, W. Lottermoser and G. Amthauer, *Chemistry of Materials*, 2016, **28**, 5943–5951.

28 R. Wagner, G. J. Redhammer, D. Rettenwander, A. Senyshyn, W. Schmidt, M. Wilkening and G. Amthauer, *Chemistry of Materials*, 2016, **28**, 1861–1871.

29 M. Nyman, T. M. Alam, S. K. McIntyre, G. C. Bleier and D. Ingersoll, *Chemistry of Materials*, 2010, **22**, 5401–5410.

30 N. Bloembergen, E. M. Purcell and R. V. Pound, *Phys. Rev.*, 1948, **73**, 679–712.

5 Supporting Information

Table 2 Crystal data and structure refinement of pristine and H_2O treated garnet-type of the nominal composition $Li_6La_3ZrTaO_{12}$ as determined from single crystal neutron diffraction measurements; all data according to the cubic space group *Ia*$\bar{3}$*d*, data were collected at 300(2) K with λ = 0.793 Å, Z = 8

	pristine	H_2O treated - 7 days	H_2O treated - 31 days
a / Å	12.8775(2)	12.8829(12)	12.8883(5)
Volume / Å^3	2135.48(10)	2138.2(2)	2140.9(2)
calc. density / Mg m^{-3}	5.803	5.827	5.820
Absorption coefficient / mm^{-1}	0.034	0.034	0.034
F / 000	3215	3232	3232
Crystal size / mm^3	2 x 2 x 1.6	2 x 2 x 1.6	2 x 2 x 1.6
Theta range for data collection	4.325 to 39.899°	4.324 to 39.548°	4.322 to 39.528°
Index ranges h	1 ... 20	0 ... 13	−20 ... 20
k	−14 ... 14	0 ... 10	0 ... 13
l	0 ... 14	−20 ... 20	−20 ... 20
Reflections collected	674	186	1572
R_{int} / %	2.78	3.04	5.40
Data / restraints parameters	401 / 1 / 31	162 / 1 / 31	393 / 1 / 31
Goodness-of-fit on F^2	1.006	1.117	0.966
R indices [I>2σ(I)]	2.58	1.63	1.98
R_1	2.81	3.94	3.28
wR_2			
R indices (all data) R_1	6.42	1.63	3.26
wR_2	3.28	3.94	3.52
Extinction coefficient	0.0076(3)	0.0046(5)	0.0046(4)
Largest diff. peak and hole (e.Å^{-3})	0.383 and −0.490	0.262 and −0.300	0.372 and −0.282

Table 3 Fractional atomic coordinates as obtained from structure refinement of the single crystal studied. U(eq) is defined as one third of the trace of the orthogonalized $U_i j$ tensor, *Occ* is the site occupation number, normalized to 1 for full occupation.
*Value fixed to the one of the pristine sample (combined x-ray and neutron diffraction data refinement).

Position	*x / a*	*y / b*	*z / c*	*Occ**	*U(eq)*
Pristine sample at 300 K					
La 24*d*	0.1250	0	0.25	0.981(4)	0.00795(12)
Zr 16*c*	0	0	0	0.451(3)	0.00529(12)
Ta 16*c*	0	0	0	0.549(3)	0.00529(12)
O1 96*h*	0.10314(4)	0.19792(4)	0.28048(4)	1.00	0.01204(10)
Li1 24*d*	0.375	0	0.25	0.659(19)	0.0390(16)
Li1 96*h*	0.1511(4)	0.1738(4)	0.4372(5)	0.341(7)	0.0231(12)
H_2O treated sample at 300 K / 7 days					
La 24*d*	0.1250	0	0.25	1.004(24)	0.00827(12)
Zr 16*c*	0	0	0	0.451*	0.00540(22)
Ta 16*c*	0	0	0	0.549*	0.00540(22)
O1 96*h*	0.10326(4)	0.19809(4)	0.28038(8)	1.00	0.01209(21)
Li1 24*d*	0.375	0	0.25	0.641(12)	0.0412(18)
Li1 96*h*	0.1505(8)	0.1736(9)	0.4370(9)	0.316(9)	0.027(2)
H2 96*h*	0.1505(8)	0.1736(9)	0.4370(9)	0.025(9)	0.027(2)
H_2O treated sample at 300 K / 31 days					
La 24*d*	0.1250	0	0.25	0.997(10)	0.00824(142)
Zr 16*c*	0	0	0	0.451*	0.00543(11)
Ta 16*c*	0	0	0	0.549*	0.00543(11)
O1 96*h*	0.10311(3)	0.19800(3)	0.28047(3)	1.00	0.01214(10)
Li1 24*d*	0.375	0	0.25	0.603(11)	0.036(2)
Li1 96*h*	0.1503(4)	0.1740(3)	0.4378(4)	0.308(7)	0.0282(10)
H2 96*h*	0.1503(4)	0.1740(3)	0.4378(4)	0.033(7)	0.0282(10)

Table 4 Anisotropic atomic displacement parameters for the LLZTO single crystal studied.

Atom	U_{11}	U_{22}	U_{33}	U_{23}	U_{13}	U_{12}	U(eq)
Pristine sample at 300 K							
La1	0.0104(3)	0.00675(17)	0.00675(17)	0.0018(2)	0	0	0.00795(15)
Zr1	0.00529(12)	0.00529(12)	0.00529(12)	−0.00007(15)	−0.00007(15)	−0.00007(15)	0.00529(12)
Ta1	0.00529(12)	0.00529(12)	0.00529(12)	−0.00007(15)	−0.00007(15)	−0.00007(15)	0.00529(12)
O1	0.00931(18)	0.0132(2)	0.01364(19)	0.00173(15)	0.00074(14)	0.00043(15)	0.01204(12)
Li1	0.0118(19)	0.056(3)	0.053(3)	0	0	0	0.0390(16)
Li1	0.032(3)	0.016(2)	0.021(2)	−0.0051(18)	0.012(12)	−0.011(2)	0.0231(12)
H_2O at 300 K / 7 days							
La1	0.0106(3)	0.0071(3)	0.0071(3)	0.0025(4)	0	0	0.0083(3)
Zr1	0.0054(2)	0.0054(2)	0.0054(2)	−0.0003(3)	−0.0003(3)	−0.0003(3)	0.0054(2)
Ta1	0.0054(2)	0.0054(2)	0.0054(2)	−0.0003(3)	−0.0003(3)	−0.0003(3)	0.0054(2)
O1	0.0088(3)	0.0135(4)	0.0140(4)	0.0015(3)	0.00067(3)	0.0007(3)	0.0121(3)
Li1	0.011(5)	0.057(6)	0.057(6)	0	0	0	0.041(5)
Li1	0.031(5)	0.026(5)	0.025(5)	−0.002(3)	0.008(4)	−0.004(4)	0.027(2)
H2	0.031(5)	0.026(5)	0.025(5)	−0.002(3)	0.008(4)	−0.004(4)	0.027(2)
H_2O at 300 K / 31 days							
La1	0.0106(2)	0.00719(15)	0.00719(15)	0.0225(13)	0	0	0.00834(14)
Zr1	0.00543(11)	0.00543(11)	0.00543(11)	−0.00015(10)	0.00015(10)	0.00015(10)	0.00543(11)
Ta1	0.00543(11)	0.00543(11)	0.00543(11)	−0.00015(10)	0.00015(10)	0.00015(10)	0.00543(11)
O1	0.00959(14)	0.01293(16)	0.01389(15)	0.00151(10)	0.00075(10)	0.00014(10)	0.01214(10)
Li1	0.011(2)	0.049(3)	0.049(3)	0	0	0	0.0363(19)
Li1	0.039(3)	0.0213(17)	0.0243(18)	−0.0055(14)	0.0142(18)	−0.0105(19)	0.0282(11)
H2	0.039(3)	0.0213(17)	0.0243(18)	−0.0055(14)	0.0142(18)	−0.0105(19)	0.0282(11)

Preface:

Spatial confinement - Rapid 2D F^- diffusion in micro- and nanocrystalline $RbSn_2F_5$

As discussed later in detail in Chapter 4, F^--ion conductors are applied as solid electrolytes in first-generation Fluorine-ion Batteries. As in the case of Li^+-ion conductors, there is a constant strive for finding (solid) compounds with higher conductivity, which would make the cell operation at ambient temperatures possible. $RbSn_2F_5$ belongs to these promising materials, possessing a good conductivity of $6.3 \cdot 10^{-5}$ S/cm at 20°C, yet being not stable when used as solid electrolyte, as found in the preceding master thesis.

Within this thesis, this compound was used as a model compound to study its 2-dimensional diffusion properties. The understanding of the differences between ions sensing confined (2D) or unrestricted (3D) space during diffusion is of interest, as commercially used electrode materials (like $LiCoO_2$) posses a layered 2D structure.

This study discusses in detail its structure, evaluated via XRPD and MAS NMR, macroscopic dynamics as analysed by impedance spectroscopy and microscopic dynamics explored via static NMR in the laboratory as well as in the rotating frame of reference. The relaxation data gained from $T_{1\rho}$ measurements was fitted with a spectral density function designed for 2D diffusion. The activation energies characterising these processes, were consistent with the ones extracted from conductivity spectroscopy, proving that 2D transport of F^- ions occurs in $RbSn_2F_5$.

Additionally, the difference in ionic conductivity of nano- and microcrystalline $RbSn_2F_5$ is only minor. This was somewhat surprising as any introduction of defects usually increases the conductivity, at least of moderate ion conductors [78, 79]. Here, however, ion dynamics seem to occur with ease already in microcrystalline $RbSn_2F_5$ due to the structural layers present.

A part of this study was carried out within the scope of the preceding master thesis, whereby the characterisation of microcrystalline $RbSn_2F_5$ and detailed interpretation of the NMR data was conducted during this thesis.

Author Contributions: MG carried out the synthesis (with the aid of FP-P), characterization (with the aid of SB and IH) and analysis of the data (with the aid of HMRW). SL acquired MAS NMR spectra. HMRW supervised all steps and helped with writing the paper.

P3
Spatial confinement - Rapid 2D F^- diffusion in micro- and nanocrystalline $RbSn_2F_5$

***M. Gombotz**, S. Lunghammer, S. Breuer, I. Hanzu, F. Preishuber-Pflügl, and H. Martin R. Wilkening*

Phys. Chem. Chem. Phys., 2019, 21, 1872-1883 (DOI: 10.1039/C8CP07206J)

PCCP

PAPER

View Article Online
View Journal | View Issue

Cite this: *Phys. Chem. Chem. Phys.*, 2019, **21**, 1872

Spatial confinement – rapid 2D F^- diffusion in micro- and nanocrystalline $RbSn_2F_5$†

Maria Gombotz,*[a] Sarah Lunghammer,[a] Stefan Breuer,[a] Ilie Hanzu,[ab] Florian Preishuber-Pflügl‡[a] and H. Martin R. Wilkening*[ab]

Received 22nd November 2018,
Accepted 3rd January 2019

DOI: 10.1039/c8cp07206j

rsc.li/pccp

Diffusion of small ions in materials with confined space for translational dynamics can be quite different to isotropic (3D) diffusion, which is found in the majority of solids. Finding credible indications for 2D diffusion is not as easy as it looks at first glance, especially if only powder samples are available. Here we chose the ternary fluoride $RbSn_2F_5$ as a new model system to seek out low-dimensional anion diffusion in a nanocrystalline material. We prepared $RbSn_2F_5$ *via* mechanochemically-assisted solid state synthesis and used both ac conductivity spectroscopy and spin-lock NMR relaxation measurements to find evidence that the fluorine ions preferably diffuse between the Rb-rich layers. In both cases the diffusion induced spin-lock NMR rates are only consistent with conductivity data if they are analyzed with the semi-empirical spectral density function for 2D jump diffusion as introduced by P. M. Richards [*Solid State Commun.*, 1978, **25**, 1019].

1 Introduction

Solid-state ionic conductors represent an essential component in microelectronics and devices to electrochemically store electricity.[1–4] In the last ten years, quite a number of new compounds with exceptionally fast ion transport have been presented.[5–12] In particular, highly conducting Li-bearing and Na-containing materials were developed to serve as non-flammable electrolytes in ion batteries.[12–15] Also cation-mixed fluorides,[16,17] such as $La_{1-x}Ba_xF_{3-x}$, see ref. 18–21, and $Ba_{1-x}Ca_xF_2$ ($0 < x < 1$), see ref. 22, re-entered the scientific stage as they might be used as solid electrolytes in fluorine-based energy storage systems.[23,24] Such ternary fluorides are anticipated to take a leap forward in batteries with high energy densities.

Besides such application-oriented challenges, fluorine ion conductors offer attractive model systems to study ultra-rapid jump processes[8,25] from a fundamental point of view. To develop new functional materials we need to improve our understanding about the influence of crystal structure and morphology on ion transport. The highly reversible insertion and de-insertion processes in rocking-chair batteries, relying on insertion compounds, take advantage of layered materials that offer fast 2D diffusion pathways. From an atomic scale point of view it is, if only powder samples are available, a challenge to undoubtedly show that 2D diffusion prevails.[26–29] The same troubles hold for 1D diffusion taking place along or inside the channels.[30,31] Intrachannel and intralayer hopping processes may water the reasoning for 1D or 2D diffusion down.

Only few examples have been presented in literature[26,27] for which rapid 2D diffusion of Li, Na or F ions has either unequivocally been shown or at least strongly anticipated. These examples include Na-beta″-alumina,[33–35] cathode materials based on Li_yCoO_2 ($y \leq 1$) and $LiFePO_4$,[36,37] Li containing transition metal sulfides (or selenides), such as Li_xTiS_2 ($0 < x \leq 1$)[38–41] or Li_zNbS_2 ($0 < z \leq 1$),[29] hexagonal $LiBH_4$,[27] polycrystalline $ZrBe_2H_{1.4}$,[26,42] and the ternary fluorides $PbSnF_4$, see ref. 43 and 44, and $BaSnF_4$.[45] In some of these examples only a multi-method approach turned out to be successful to show that low-dimensional diffusion is present. For Li_xMS_2 (M = Ti, Nb) and $ZrBe_2H_{1.4}$ the use of variable-frequency nuclear magnetic resonance (NMR) relaxation measurements turned out to be successful to prove low-dimensional diffusion as the main motional process. For instance, McDowell *et al.*[26] impressively showed *via* variable-frequency ^1H NMR spin–lattice relaxation measurements that the protons in the metal-hydride $ZrBe_2H_{1.4}$ are indeed subjected to 2D diffusion.

For many cathode materials, which are used in insertion batteries,[37,46–48] the NMR technique will, however, be of very limited use as paramagnetic centers cause short relaxation times which drastically narrow the time window needed for dimensionality analyses. In addition, strong spin-electron interactions govern

[a] *Christian Doppler Laboratory for Lithium Batteries, and Institute for Chemistry and Technology of Materials, Graz University of Technology (NAWI Graz), Stremayrgasse 9, 8010 Graz, Austria. E-mail: wilkening@tugraz.at, gombotz@tugraz.at; Fax: +43 316 873 32332; Tel: +43 316 873 32330*
[b] *Alistore-ERI European Research Institute, 33 rue Saint Leu, 80039 Amiens, France*

† Electronic supplementary information (ESI) available: Further NMR spectra and conductivity data. See DOI: 10.1039/c8cp07206j

‡ Present address: Schunk Carbon Technology GmbH, Au 62, 4822 Bad Goisern, Austria.

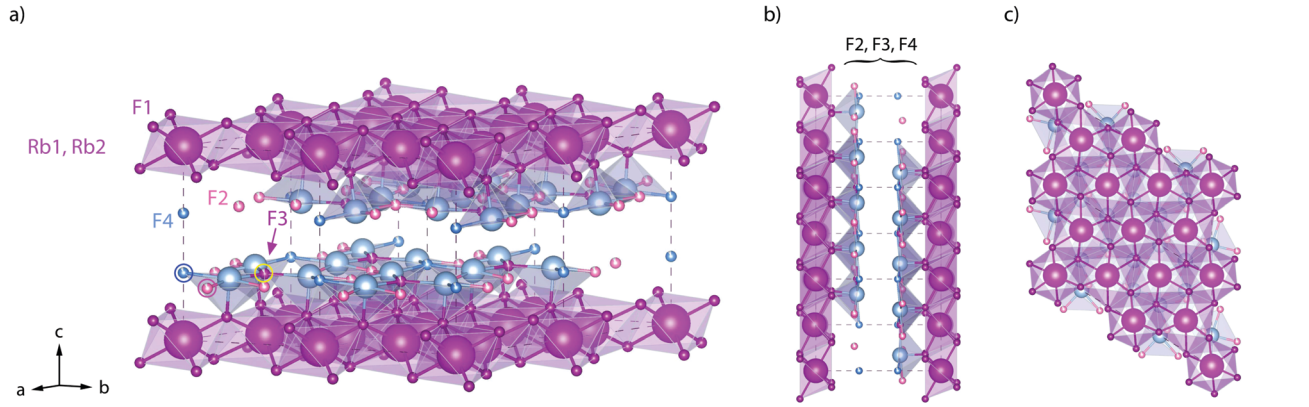

Fig. 1 Crystal structure of $RbSn_2F_5$ below the phase transition at approximately T = 368 K. The illustration shows the arrangement of atoms according to the structure refinement of Yamada *et al.*[32] (space group $P\bar{3}$, no. (147); a = 7.3857(4) Å, c = 10.104(1) Å, Z = 3.) (a) view to illustrate the fluorine ions in the Sn-rich layers. (b) View along the b-axis. (c) View along the b-axis to visualise the hexagonal arrangement of the Rb^+ cations. The F sites between the Rb-rich layers (labelled F2, F3, and F4) are only filled by 90%; F1 sites are fully occupied.

the NMR relaxation rates rather than diffusive motions. Focussing here on rapid anion dynamics, ternary fluorides provide some very encouraging materials useful as model substance to test NMR relaxation models proposed for 2D diffusion.[49–51]

Here, $RbSn_2F_5$ attracted our attention. It belongs to the family of the pseudo-binary system MF-SnF_2 where M is a monovalent cation such as Rb^+, K^+, Na^+ or Cs^+.[52] Within this family $RbSn_2F_5$ offers the highest ion conductivity[53] followed by KSn_2F_5 and $NaSn_2F_5$.[54,55] Up to now it has only been prepared by solid-state reaction[52] or hydrothermal synthesis in aqueous solution as first reported by Donaldson and O'Donoghue in 1964.[56] In 1987 the structure of KSn_2F_5, to which $RbSn_2F_5$ is isomorphous, was resolved as being trigonal, *i.e.*, crystallizing with the space group $P\bar{3}$.[57] Later structure refinement was also carried out by Yamada *et al.*[32] In Fig. 1 the crystal structure of $RbSn_2F_5$ is illustrated, which clearly shows the two-dimensional nature of this compound. In 1991 Hirokawa *et al.*[58] suggested to interpret NMR data by using a 2D spectral density. Later, in 2004, Yamada *et al.*[32] pointed out that also conductivity isotherms are in line with low-dimensional transport. A direct comparison of results from both NMR and conductivity spectroscopy is, however, still missing. While earlier studies focussed on coarse-grained polycrystalline samples with μm-sized crystallites, F self-diffusion in nanocrystalline $RbSn_2F_5$ has not been reported yet. Thus, the present study also aims at discussing possible effects on 2D diffusion in $RbSn_2F_5$ when the mean crystallite size is reduced to *ca.* 20 nm.

For this purpose, that is, to compare F diffusion in microcrystalline $RbSn_2F_5$ with that in the nanocrystalline form, we synthesized the layer-structured fluoride employing a mechanochemically-assisted ceramic route. Using a one pot synthesis, nanocrystalline $RbSn_2F_5$ was directly obtained after high-energy ball milling[59] the binary starting materials RbF and SnF_2. Through soft annealing we converted the as-prepared material into a microcrystalline sample. Spin-lock ^{19}F NMR[60] instead of ordinary spin–lattice relaxation NMR[61] was used to record purely diffusion-controlled relaxation rates. For non-nanocrystalline $RbSn_2F_5$ the NMR rates are consistent with results from conductivity measurements only if we analyse the NMR rate peak with the model of Richards[49,62] introduced for 2D jump diffusion. This result is also consistent with the electrical responses seen by conductivity spectroscopy. These findings, being in close agreement to results from literature,[32] build the basis for the analysis of F anion dynamics in nanocrystalline $RbSn_2F_5$.

2 Experiment

Mechanochemical synthesis[59,63] of nanocrystalline $RbSn_2F_5$ was carried out in ZrO_2 cups (45 ml) loaded with ZrO_2 balls (5 mm diameter) and the corresponding educts. We made use of a high-energy planetary mill (Fritsch Pulverisette 7 premium line) to form the ternary fluoride. To guarantee moisture free reaction conditions the educts (RbF (Sigma Aldrich 99.8%), SnF_2 (Sigma Aldrich 99%)) were dried in vacuum over night. Handling of the milling cups, *i.e.*, filling and emptying of the beakers was carried out in an Ar-filled glovebox (H_2O and O_2 < 0.5 ppm). We milled the starting materials at a rotation speed of 600 rpm for 10 h according to the following procedure: 15 min milling followed by 15 min cooling of the beakers. Subsequently, the powders were annealed at 373, 423 and 473 K for 4 or 8 h in a tube furnace under vacuum or Ar atmosphere. For this annealing step 100 mg of the milled sample was pressed to pellets with a diameter of 5 mm using a hand press and by applying a force of 0.5 tons for 2 minutes. Annealing caused grain growth of the $RbSn_2F_5$ crystallites and densified the powder.

The milled and annealed samples were characterised by X-ray diffraction (XRD) under atmospheric pressure and at room temperature. A Bruker D8 Advance diffractometer with Bragg Brentano geometry and CuKα radiation (1.5406 Å) was used to collect the diffractograms. Data points were recorded from 10 to 100° 2θ with a stepsize of 0.02° 2θ; the measuring time for each step was 1 second. Rietveld Refinement was performed with X-PertHighScorePlus (PANalytical).

Magic angle spinning (MAS) NMR was carried out on a Bruker Avance III 500 spectrometer at a nominal magnetic field

of 11.7 T. This external magnetic field translates in resonance frequencies of 186.40 MHz for ^{119}Sn, 470.30 MHz for ^{19}F and 163.60 MHz for ^{87}Rb. We used a Bruker MAS probe designed for 2.5 mm rotors (ZrO_2) to acquire free induction decays (FIDs) at a spinning speed of 25 kHz (target gas flow: 400 L h^{-1}, frame cooling: 35% of target gas flow). The bearing gas temperature was 293 K.

Spectra were obtained after Fourier transformation of the FIDs and referenced to the isotropic chemical shifts δ_{iso} of LiF ($\delta_{iso}(^{19}F)$ = −204.3 ppm), SnO_2 ($\delta_{iso}(^{119}Sn)$ = −604.3 ppm) and $RbNO_3$ ($\delta_{iso}(^{87}Rb)$ = −30 ppm site 3), respectively. The relaxation rates $1/T_1$ and $1/T_{1\rho}$ were determined with a Bruker Avance III 300 NMR spectrometer at a magnetic field of 7.04 T, *i.e.*, at a ^{19}F NMR resonance frequency of 281.79 MHz. Prior to the relaxation measurements the powder sample was fire-sealed in a glass cylinder with a length of approximately 3 cm and 4 mm in diameter. The rates were recorded with the saturation recovery pulse sequence where at first a train of 10 closely spaced 90° pulses destroys any longitudinal magnetization M_z before its recovery as a function of delay time t_d was then detected with a single 90° pulse. The transients $M_z(t_d)$ were analyzed with stretched exponentials $M_z(t_d) \propto 1 - \exp(-(t/T_{1\rho})^{\gamma})$ with $0 < \gamma \leq 1$. While T_1 NMR is sensitive to fast F anion dynamics, slower motional processes were measured with the spin-lock technique introduced by Slichter and Ailion[64–66] utilizing the pulse sequence $90°(t_{lock})$ − acq.[67–70] The locking frequency ω_1 was set to $\omega_1/2\pi \approx 100$ kHz and the duration of the locking pulse t_{lock} was varied from 100 μs to 10 ms. Note that the recycle delay for the spin-lock experiments was at least $5 \times T_1$ to ensure complete longitudinal relaxation between each scan. Once again, stretched exponentials served to parameterize the spin-lock transients $M_\rho(t_{lock}) \propto \exp(-(t_{lock}/T_{1\rho})^{\gamma_\rho})$ $(0 < \gamma_\rho \leq 1)$ to extract $T_{1\rho}(1/T)$.

To carry out the impedance spectroscopy measurements, approximately 60 mg of the sample powder was pressed to cylindrical pellets with a final diameter of 5 mm, using a hand press. As for the annealing step, we applied a uniaxial pressure of 0.5 *t* for 2 min. Au electrodes, which block ion transport, with a thickness of 100 nm were sputtered onto both sides of the pellets using a Leica sputter device (EM SCD050).

Alternating current (ac) impedance measurement were then performed with a broadband spectrometer (Novocontrol, Concept 80) in combination with an active BDS 1200 cell and a ZGS interface.[71] The temperature was varied from 173 K to 473 K controlled by a QUATRO cryosystem. Our conductivity measurements covered a frequency range from 10^{-2} Hz to 10^7 Hz. All experiments were performed under a constant flow of dry, freshly evaporated N_2 gas. ZView (Princeton Applied Research) and IGOR Pro (Wavemetrics) software were used to analyze the data.

For Hebb–Wagner-type polarisation measurements under N_2 atmosphere we used pellets with 5 mm in diameter and employed a Parstat MC potentiostat (Princeton Applied Research) equipped with a low-current option. All preparation steps, including the metallisation, were carried out in Ar filled gloveboxes with an O_2 and H_2O content of less than 1 ppm.

3 Results and discussion

3.1 X-ray diffraction

The phase purity of mechanosynthesized $RbSn_2F_5$ before and after the annealing steps was studied by XRD, the corresponding diffractograms are shown in Fig. 2. Directly after milling a diffractogram is obtained that is composed of relatively broad reflections due to both small, nm-sized crystallites and lattice strain. It already resembles that of the low-temperature modification of Rb_2SnF_5 showing that the ternary fluoride is directly obtained *via* this one-pot mechanochemical synthesis.

Soft annealing, *i.e.*, holding the sample for 8 h at 473 K under dry, oxygen-free inert gas atmosphere, clearly narrows the reflections because of crystallite growth and/or the release of strain. Lower annealing temperatures also lead to narrow reflections but the narrowing turned out to be less pronounced. Worth noting, if we simply store the ball-milled sample for several month in dry Ar atmosphere, we recognize a significant growth in average grain size. Therefore, crystallization also takes place under ambient conditions. At his temperature the crystallization kinetics are, of course, much slower than at high *T*.

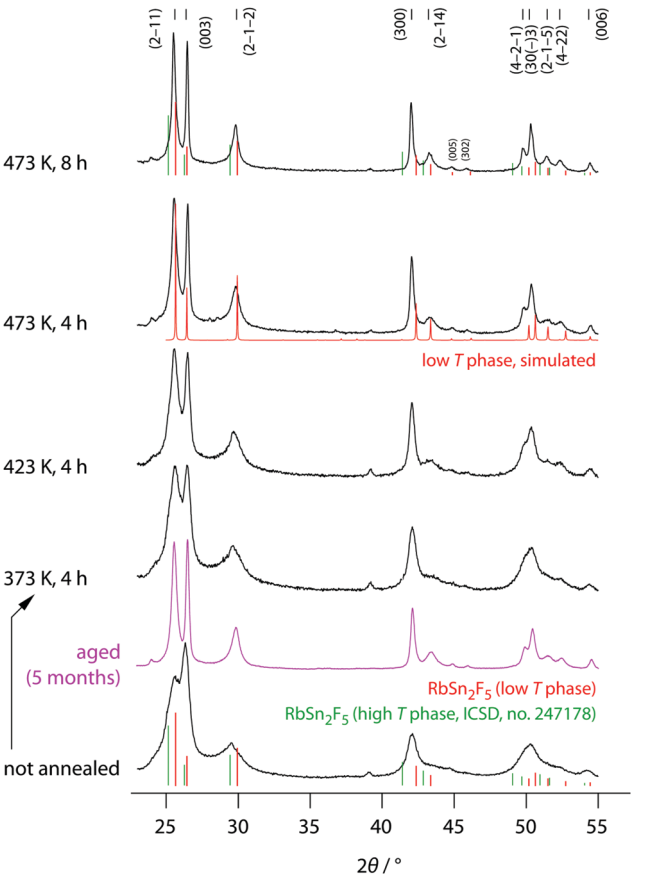

Fig. 2 X-ray diffractograms of all $RbSn_2F_5$ samples prepared. XRD patterns were recorded at room temperature before and after the annealing steps indicated. The vertical bars shows the expected positions of the reflections for the low-*T* and high-*T* modification, respectively. While the reflections for the phase being stable above 368 K were taken from literature (ICSD no. 247178, recorded at 538 K); those for the low-*T* modification were constructed according to the structure model proposed by Yamada *et al.*[32]

Obviously, crystal growth is driven by the high F anion conductivity of the samples. For comparison, at 293 K the ionic conductivity σ_{dc} is 6.24×10^{-5} S cm^{-1}, see below.

The final reflections seen after soft annealing are in agreement with the structure refinement proposed by Yamada *et al.*[32] assuming $P\bar{3}$ symmetry and vacancies on the F1, F2 and F3 positions, see also Fig. 1. In Fig. 2 the positions of the main reflections of both the high-T and low-T phase of $RbSn_2F_5$ are indicated by vertical lines. We also included a simulation of the XRD pattern of the low-T form of $RbSn_2F_5$.

Annealing the samples at temperatures higher than 473 K, *e.g.*, at 568 K for several hours, causes decomposition of the ternary fluoride. Light microscopy revealed small regions that shine metallic. We assume that, due to disproportionation of Sn^{4+}, metallic tin is formed at sufficiently high T; *cf.* also Fig. S1 (see ESI†). Scanning electron microscopy showed a mixture of needle-like crystallites and rectangular tubes with a length of up to 20 μm, see also Fig. S1 (ESI†).

Below 368 K the ternary fluoride crystallizes with $P\bar{3}$ symmetry ($Z = 3$); at higher temperatures $RbSn_2F_5$ reversibly transforms to $P\bar{3}$ with $Z = 1$. The same transition has been reported for K_2SnF_5.[57] Yamada *et al.* investigated this contraction along the *c*-axis. The contraction is accompanied by an expansion along the *ab*-axis.[32] Defect disorder in the vacancy-rich (F1, F2, F3)-sublattices, caused by the phase transition, leads to an easily measurable increase in F anion conductivity. This increase is also seen here; we used broadband conductivity spectroscopy to study electrical responses over a wide range of temperature and a broad frequency region.

3.2 F anion transport in $RbSn_2F_5$

Conductivity isotherms of annealed $RbSn_2F_5$ are shown in Fig. 3a. If we look at data recorded up to 10^7 Hz distinct frequency-independent (direct current, dc) plateaus are visible that merge into dispersive regimes. At first glance, these regimes can be approximated with a Jonscher power law, $\sigma' \propto \nu^{\kappa}$. Here, the exponent turned out to depend only slightly on temperature and amounts to $\kappa \approx 0.6$. While for 3D ionic conductors κ usually shows values ranging from 0.65 to 0.85; 2D ionic transport is assumed to be characterized by exponents of approximately 0.55. As pointed out by Sidebottom,[72] for 1D ion transport even lower values of 0.3 are expected. The latter has recently been found for channel-like ion transport in $BaMgF_4$.[73] Considering κ extracted from the fits shown in Fig. 3, the shape of the dispersive regions provides indications that 2D ion dynamics prevails in $RbSn_2F_5$.

We will see later on that this view is supported by diffusion-induced nuclear spin relaxation. It is also in line with earlier reports on 2D ionic conduction in coarse-grained $RbSn_2F_5$ investigated by both impedance spectroscopy and NMR.[32,58]

A closer look at the data, especially if we include conductivity data recorded up to the GHz range, reveals that the situation is, however, more complex than can be recognized at first glance. At very low temperatures the isotherms, irrespective if we look at those from micro- or nanocrystalline $RbSn_2F_5$ (see Fig. 3a and b) deviate from the $\sigma' \propto \nu^{0.6}$ behaviour. Instead the dispersive regimes merge into a classical nearly constant loss (NCL) regime,[74,75] being characterized by $\kappa \rightarrow 1$. At sufficiently low T it is thus difficult to separate the two contributions from each other. On the other hand, at high temperatures, *i.e.*, before the phase transformation of $RbSn_2F_5$ occurs, we can recognize that σ' passes into a second dc plateau at frequencies above 10^6 Hz, see the arrow in Fig. 3a.

To clarify this feature we extended our measurements to frequencies in the GHz range. Fig. 4 shows the conductivity isotherm recorded at 333 K. It is clearly composed of two dc plateaus, the one occurring at high frequencies definitely belongs to bulk ion dynamics, while the one extending over a large frequency range at lower ν might also be influenced by grain boundary contributions. Importantly, the dispersive regime of the bulk plateau, whose conductivities obey an Arrhenius law with a very similar activation energy as σ_{dc} (see Fig. 3c) (0.52 eV),

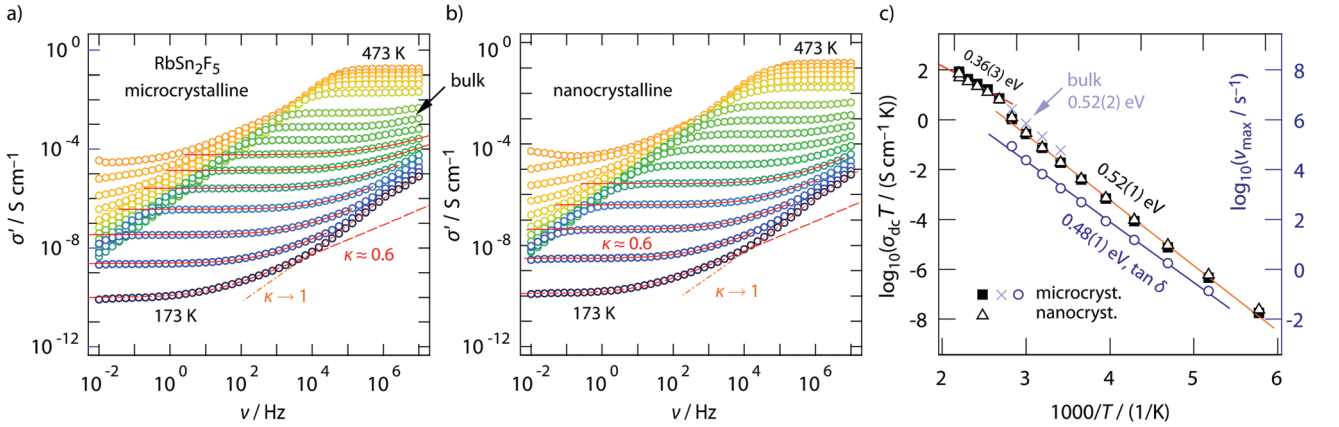

Fig. 3 (a) and (b) Conductivity isotherms of micro- and nanocrystalline $RbSn_2F_5$. Dashed and solid lines show fits with appropriate Jonscher expressions, see text. Spectra were recorded at temperatures ranging from 173 K to 473 K in steps of 20 K. (c) Arrhenius plot illustrating the temperature dependence of the dc conductivity of micro- and nanocrystalline $RbSn_2F_5$. The change in slope at approximately 370 K is assigned to the phase transformation $RbSn_2F_5$ undergoes at this temperature. Below 370 K, ion transport, in both micro- and nanocrystalline $RbSn_2F_5$, is characterised by an activation energy of 0.52 eV. A very similar value is obtained when tan δ peaks are analysed, the corresponding frequencies ν_{max} yield 0.48 eV, see right axis.

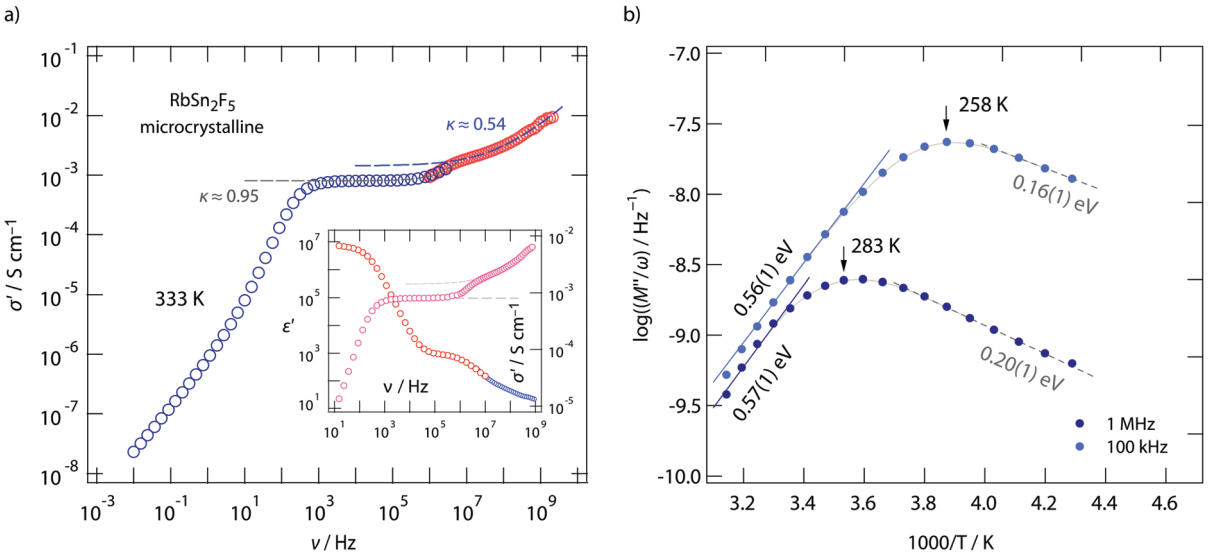

Fig. 4 (a) Broadband conductivity isotherm (333 K) of microcrystalline $RbSn_2F_5$. At low frequencies electrical response is governed by piling up of F anions at the ion-blocking electrodes. This region passes into the first dc plateau whose dispersive region is given by $\sigma' \propto \nu^{0.95}$. Most likely, it is affected by interfacial processes. The second plateau at higher ν represents bulk ion dynamics with $\sigma' \propto \nu^{0.54}$ indicating 2D ionic conduction. The inset shows the corresponding permittivity spectrum. (b) temperature dependence of the electrical resistivity (M''/ω) measured for two frequencies. The asymmetric peaks reveal two activation energies characterising long-range ion transport and short-range dynamics.

is characterised by $\kappa = 0.54$. This value is even closer to what we expect for 2D ionic conduction.[72]

The two contributions to the overall electrical response of σ' can also be distinguished in the Nyquist plots of Fig. 5, where the imaginary part $-Z''$ of the complex impedance $\hat{Z}$ is plotted *versus* its real part Z'. The higher the temperature the better the separation; at low T the two semicircles merge into each other. Together with the NCL-type response, showing up at even lower T, they cannot be separately analyzed at $T \ll 293$ K.

We analyzed the complex impedance data by using suitable equivalent circuits consisting of individual resistances R and constant phase elements (CPEs) representing the responses from bulk, grain-boundaries (g.b.) and electrodes. The complex impedance $\hat{Z}_{CPE}$ of a constant phase element can be simply expressed by

$$\hat{Z}_{CPE} = 1/(Qj\omega)^n \text{ with } j = \sqrt{-1} \quad (1)$$

Q has the numerical value of the admittance at $\omega = 1$ rad s^{-1}. Thus, the capacitance C of the CPE is given by

$$C = R^{(1-n)/n}Q^{1/n} \quad (2)$$

Values for C are included in Fig. 5. $C < 10$ pF clearly points to a bulk response the semicircles at high frequencies describe.

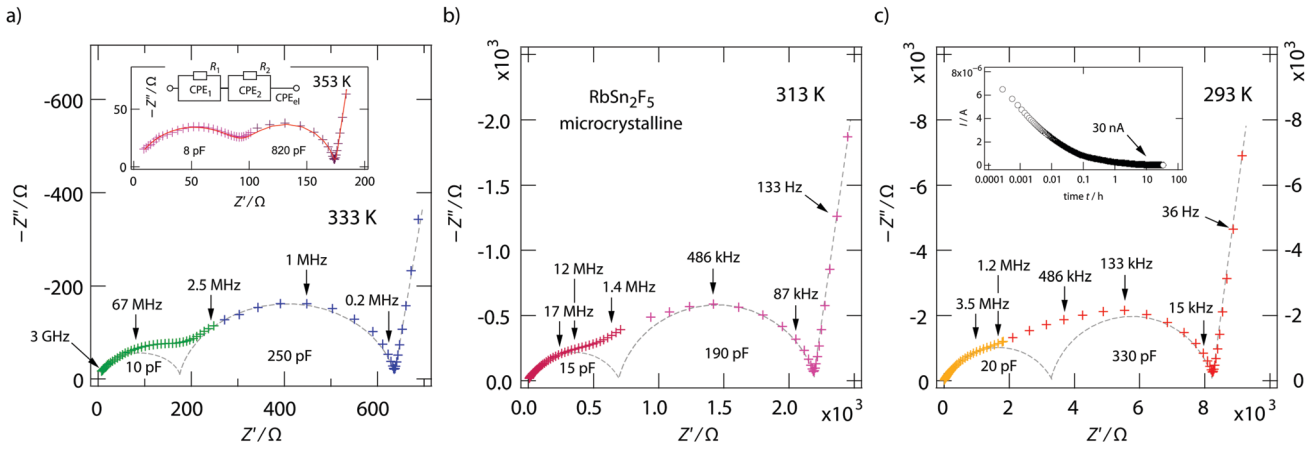

Fig. 5 (a) Nyquist representation of the complex impedance data of microcrystalline $RbSn_2F_5$. The depressed semicircle at high frequencies shows bulk ion dynamics, whereas the electrical response leading to the second one seems to be influenced by interfacial processes. The spike at low ν originates from polarisation effects. Circles indicted by dashed lines show results from analysing the overall response with appropriate electrical equivalent circuits. Here, we used a parallel combination of three (R-CPE) elements. A complete fit is shown as solid line for the curve measured at 353 K. The values in pF show the capacities obtained from the fits. The inset in (c) shows the polarisation curve that has been measured at 393 K.

As an example, the inset of Fig. 5a shows two semicircles with nearly the same R. Whereas the high-frequency arc, being assigned to the bulk process, is characterized by n = 0.74, indicating correlated ionic transport, the g.b. semicircle yields $n = 0.94 \approx 1$, almost behaving like an ideal RC unit. This result is expected for a grain-boundary electrical response. Finally, we used a polarisation measurement[25] to estimate the electronic contribution to the overall conductivity probed by impedance spectroscopy. For this purpose, a pressed $RbSn_2F_5$ pellet outfitted with ion blocking Au electrodes was used. We applied a potential of 0.2 V and followed the current I over time t (see the inset of Fig. 5c). The final current measured at 393 K, *i.e.*, after steady-state conditions had been reached, is in the order of 30 nA and points to an electronic conductivity of 1.46×10^{-7} S cm^{-1}. This value is by several orders of magnitude lower than the total conductivity at 393 K (4.3×10^{-2} S cm^{-1}). Hence, the F^- transference number is close to 1 showing that $RbSn_2F_5$ is a pure ionic conductor.

The two electrical relaxation processes are also seen in permittivity spectra. Whereas isotherms recorded at high T are less suitable to separate them (see the inset of Fig. 4a), at low T the real part, ε', of the complex permittivity $\hat{\varepsilon}$ clearly reveals two contributions, see ESI† (Fig. S2). We attribute these two processes to electrical relaxation in the bulk and caused by g.b. regions. Similar features are also seen for the nanocrystalline sample, for which σ_{dc} almost coincides with that of the annealed sample, see Fig. 3c. In both cases, below 370 K the product $\sigma_{dc}T$ follows an Arrhenius line characterized by 0.52 eV. This activation energy perfectly agrees with that published by Yamada *et al.*[32] and Hirokawa *et al.*,[58] both studies report on an activation energy of 0.54 eV.

Almost the same activation energy is obtained if we analyze tan δ peaks (0.48 eV, see Fig. 3c, right axis) or electric modulus peaks M'' (0.49 eV), not shown here for the sake of brevity. The slight increase from 0.48 eV to 0.52 eV, which is seen when we compare the temperature behaviour of $\sigma_{dc}T$ with that of ν_{max} from tan δ, points to a very slight increase of the charge carrier concentration N with increasing temperature. For comparison, Yamada *et al.* reported that N did not change much with T.[32]

If we look at electrical properties recorded at fixed frequency but variable temperature further information about the energy landscape the F anions sense can be extracted. In Fig. 4b the temperature dependence of the resistivity, expressed as M''/ω, is shown for two frequencies, *viz.* ν = 100 kHz and ν = 1 MHz. Asymmetric relaxation peaks are obtained with the high-T flanks yielding 0.56 eV in very good agreement with $\sigma_{dc}T(1/T)$. Importantly, the low-T flank is characterized by a much smaller value of approximately 0.2 eV. According to Ngai's coupling concept of ionic transport,[75–77] such values can be identified as the activation barriers characterising short-range ion hopping processes. By using ^{19}F spin–lattice relaxation NMR we extracted very similar values, see below. Comparing results from conductivity spectroscopy with those from NMR will help us to describe the shape of the underlying motional correlation function that governs the electrical and nuclear magnetic responses of 2D dynamics in $RbSn_2F_5$.

3.3 Local structures and F anion diffusivity in $RbSn_2F_5$ as seen by NMR

^{19}F NMR provides insights into both local structure and dynamics of solids. In Fig. 6 ^{19}F, ^{119}Sn and ^{87}Rb MAS NMR spectra are shown, which were recorded to characterize the annealed sample. ^{119}Sn MAS NMR, carried out at 25 kHz spinning speed, reveals a single, anisotropically broadened line in agreement with the layered crystal structure. The chemical shift anisotropy turned out to be −1850 ppm. The ^{87}Rb NMR spectrum shows a broad resonance at 695 ppm, when referenced to SnO_2 (0 ppm). At a spinning speed of 25 kHz we were not able to resolve the two Rb positions of $RbSn_2F_5$. Either they show very similar chemical shifts or (local) structural disorder, even for the annealed sample, leads to a wide distribution of magnetic and quadrupolar electric

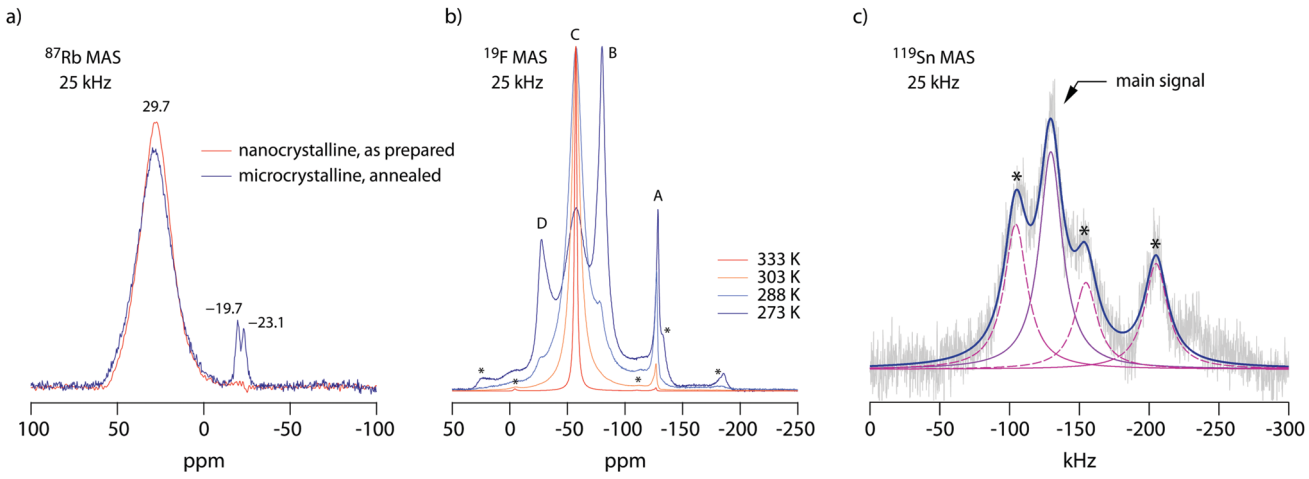

Fig. 6 (a)–(c) ^{119}Sn, ^{87}Rb and ^{19}F MAS NMR spectra of microcrystalline $RbSn_2F_5$, which was obtained by a mechanochemical route with subsequent soft annealing at 473 K. The small intensities at −19 and −23 ppm for ^{87}Rb most likely indicates some very minor decomposition products. For comparison, RbF is expected to show NMR lines at −19.3 ppm when referenced to RbCl (or $RbNO_3$). The line at −23 ppm might be attributed to RbF doped with residual Sn. Asterisks mark spinning sidebands. See text for further explanation.

interactions causing broad resonances. At low temperatures the ^{19}F MAS NMR spectrum reveals several, at least 4, lines with distinct chemical shifts and intensities (labelled A, B, C and D, see Fig. 6b). This result is expected when we remember the various magnetically inequivalent F sites in the structure of $RbSn_2F_5$. With increasing temperature the lines coalesce yielding a single line (see line C) in the center of gravity of the spectrum. This line already shows up at 243 K. Thus, even lower temperatures are needed to completely freeze F anion exchange in $RbSn_2F_5$ illustrating its fast ion dynamics with respect to the NMR time scale.

Variable-temperature ^{19}F NMR spectra recorded under static conditions also reveal this coalescence, see Fig. 7. In the rigid-lattice regime, which is reached at sufficiently low T, we deal with a dipolarly broadened signal composed of several contributions as expected from MAS NMR. With increasing T dipole–dipole interactions are averaged; in the extreme narrowing regime, *i.e.*, above 313 K, a single line governs the spectra, once again showing that nearly all F anions participate in fast self-diffusion processes. Only the very shallow signal at −75 ppm reveals some F anions that do not contribute to the coalesced signal, see the arrow in Fig. 7.

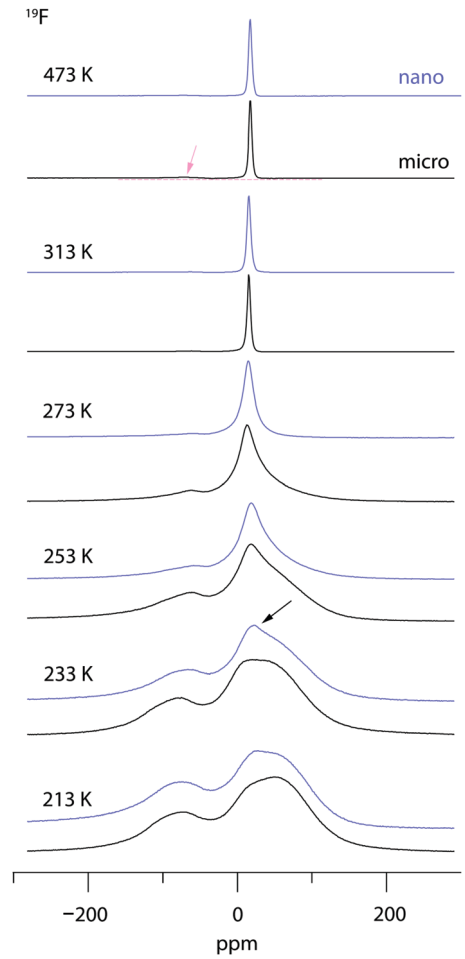

Fig. 7 ^{19}F NMR spectra of microcrystalline and nanocrystalline $RbSn_2F_5$ recorded under static conditions and at the temperatures indicated. At temperatures above 313 K the lines of both samples almost fully coalesce revealing that nearly all F anion sites participate in ionic diffusion. Motional narrowing and coalescence turned out to occur at slightly higher T for the annealed sample with less structural disorder. The arrow points to a narrow tip on top of the dipolarly broad line of as-prepared, nanocrystalline $RbSn_2F_5$; for this sample changes in line shape show up at slightly lower temperature than for the sample annealed at 473 K. This difference is also seen when the spectra recorded at 253 K are compared.

Comparing the spectra for microcrystalline $RbSn_2F_5$ with those of nanocrystalline $RbSn_2F_5$ we see that heterogeneous motional narrowing starts at slighter lower T for the nanocrystalline sample, see Fig. 7. While the ionic conductivity of microcrystalline and nanocrystalline $RbSn_2F_5$ reveals no significant difference, in defect-rich ball-milled $RbSn_2F_5$ (local) structural disorder slightly increases ionic motion – at least on the length scale to which NMR line shapes are sensitive. Obviously, the defect structure of nano-$RbSn_2F_5$ is not of detrimental nature for long-range ion transport. Ions at the grain boundary or interfacial regions might benefit from such disorder, while those having access to long-range 2D pathways along the inner surfaces already participate in fast exchange processes. However, in contrast to other systems the enhancement seen for nanocrystalline $RbSn_2F_5$ turned out to be marginal. For comparison, for poorly conducting oxides with 3D pathways, the introduction of defects usually leads to an enhancement in ion dynamics by several orders of magnitude.[78–80] As an example, this behaviour has also been observed for nanocrystalline $LiNbO_3$ and $LiTaO_3$ prepared by high-energy ball milling.[78,79]

Diffusion-induced ^{19}F NMR spin–lattice relaxation rates $R_{1(\rho)}$ for both annealed and as-prepared $RbSn_2F_5$ are shown in Fig. 8. Whereas spin–lattice relaxation in the laboratory frame (R_1), *i.e.*, being measured at Larmor frequencies in the MHz range, is sensitive to short-range F motions on the angstrom scale, with the rates recorded at locking frequencies in the kHz range ($R_{1\rho}$) we sense long-range ion transport. Below 220 K the rates R_1 are dominated by non-diffusion induced processes. ^{19}F spins couple to phonons or paramagnetic impurities. Above 220 K spin–lattice relaxation gets increasingly controlled by F motional processes. The flanks seen in Fig. 8a result in activation energies of *ca.* 0.25 eV. This value agrees well with those seen on the low-T flank of the M''/ω-curves shown in Fig. 4b. As $RbSn_2F_5$ reversibly transforms into a different crystal structure at 368 K, the R_1 rates show deviations from Arrhenius behaviour at this temperature. Spin–lattice relaxation in nanocrystalline (ball-milled) $RbSn_2F_5$ is faster by approximately 1 order of magnitude if we compare R_1 rates measured at 330 K. Obviously, local F dynamics is somewhat faster in the non-annealed form; this increase in local diffusivity, however, does not affect long-range ion transport in $RbSn_2F_5$ as σ_{dc} is the same for the two samples.

The behaviour of σ_{dc} is also seen in $R_{1\rho}$. Obviously, $R_{1\rho}$ measurements are able to detect the same long-range ion dynamics as is sensed by σ_{dc}. The $R_{1\rho}$ rates of annealed and non-annealed $RbSn_2F_5$ almost coincide and follow the expected behaviour for a diffusion-induced relaxation processes when $R_{1\rho}$ is plotted *vs.* $1/T$. In general, $R_{1\rho}$ (and R_1) will pass through a diffusion-induced rate peak whose maximum shows up when the jump rate τ^{-1} reaches the order of the locking (or Larmor) frequency: $\omega_{1(0)}\tau^{-1}$. While in the limit $\omega_1\tau \gg 1$ the flank of the

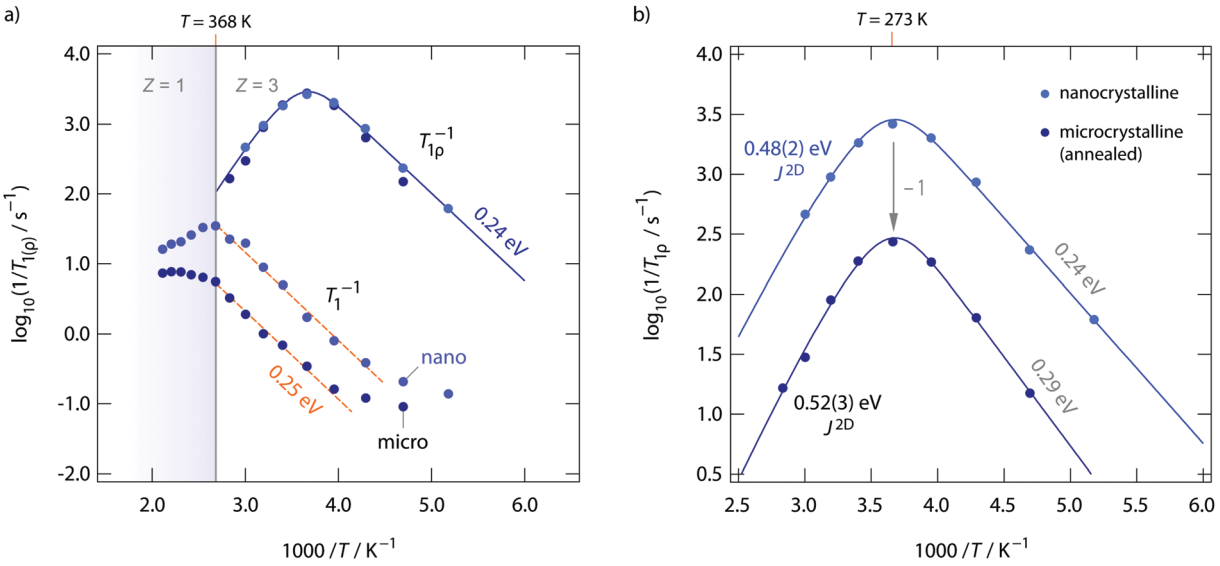

Fig. 8 (a) and (b) Temperature dependence of the ^{19}F NMR spin–lattice relaxation of $RbSn_2F_5$ recorded in both the rotating-frame (100 kHz) and laboratory-frame (281.79 MHz) of reference. The dashed lines in (a) show fits with an Arrhenius law. The solid line through the $R_{1\rho}$ of nano-$RbSn_2F_5$ rates shows a so-called Richards' fit that takes into account 2D diffusion. The fit is shown in a magnified view in (b) together with the one for microcrystalline $RbSn_2F_5$. The latter is, for the sake of clearness, shifted down by a factor of 10 (= 1 on the log scale). Anaylzing the rate peaks $R_{1\rho}(1/T)$ with J^{2D} yields E_a = 0.48 eV and E_a = 0.52 eV, respectively. The latter value is in perfect agreement with that deduced from σ_{dc}.

$R_{1\rho}(1/T)$ peak is influenced by correlation effects and structural disorder, the flank in the regime $\omega_1\tau \ll 1$ should sense dynamic parameters being comparable to long-range ion dynamics. Here, the low-T flanks yield 0.29 eV and 0.24 eV, respectively. Once again, these values agree well with those obtained from R_1 measurements and the analysis of $M''\omega$. The high-T flank, however, results in 0.39 eV for nano-$RbSn_2F_5$ and 0.41 eV for micro-$RbSn_2F_5$. These activation energies are clearly smaller than those seen by σ_{dc}. Obviously, simply analyzing the high-T flanks of the ^{19}F NMR relaxation peaks, which does not take into account any effects from low-dimensional diffusion, yields activation energies being inconsistent with that seen by conductivity spectroscopy. E_a extracted from the slope of high-T flanks is only of use when 3D diffusion processes are to be analyzed.

If we take into account 2D diffusion and use the semi-empirical relaxation model introduced by Richards[49,62] to analyze the $R_{1\rho}(1/T)$ NMR peaks we obtain a different result. The solid lines in Fig. 8a show fits with spectral density functions $J(\omega_1)^{2D} \propto R_{1\rho}$ that include a logarithmic frequency dependence of the $R_{1\rho}$ rates in the limit $\omega_1\tau \ll 1$. This dependence is characteristic for 2D diffusion. $J(\omega_1)^{2D}$, for uncorrelated motion, results in an asymmetric rate peak with the high-T slope being smaller than that in the low-T regime. For correlated motion, instead, the low-T flank is lower than that expected for 3D diffusion. Correlation effects are taken into account by the factor β in the following expression for $J(\omega_1)^{2D}$

$$J(\omega_1)^{2D} \propto \tau_c \ln(1 + 1/(2\omega_1\tau_c)^{\beta}) \propto R_{1\rho} \qquad (3)$$

Here, τ_c denotes the motional correlation time. This spectral density function[40] is based on the BPP-type one, named after Bloembergen, Purcell and Pound,[81] which describes, if β = 2, uncorrelated, isotropic (3D) jump diffusion:

$$J(\omega_1)^{3D} \propto \tau_c/(1 + (2\omega_1\tau_c)^{\beta}) \qquad (4)$$

It is valid for homonuclear ^{19}F–^{19}F spin fluctuations; here we restricted ourselves to a single term for a good approximation of the rates measured. The limiting cases of eqn (3) for the high- and low-T slopes of the corresponding $R_{1\rho}(1/T)$ relaxation peak are the following ones:[82]

$$J(\omega_1)^{2D} \propto \tau_c \ln(1/(2\omega_1\tau_c)), \quad \text{for } \omega_1\tau_c \ll 1 \qquad (5)$$

$$J(\omega_1)^{2D} \propto {\tau_c}^{1-\beta}(2\omega_1)^{-\beta}, \quad \text{for } \omega_1\tau_c \gg 1 \qquad (6)$$

For β = 2, eqn (5) is identical with the result for 3D uncorrelated motion. ${\tau_c}^{-1}$ is expected to be identical with the jump rate τ^{-1} within a factor of 2–3. τ^{-1} is assumed to be thermally activated according to an Arrhenius law:

$$\tau^{-1} = {\tau_0}^{-1} \exp(-E_a/(k_B T)) \qquad (7)$$

k_B is Boltzmann's constant, ${\tau_0}^{-1}$ represents the pre-factor which usually shows values being in agreement with those expected for phonon frequencies.

Using $J(\omega_1)^{2D}$, see eqn (3), to analyse the rate peaks of Fig. 8, yields fits that properly agree with the temperature behaviour of the rates measured, see the solid lines in Fig. 8. The activation energies for micro- and nanocrystalline $RbSn_2F_5$ turn out to be 0.52 eV and 0.48 eV, respectively. Especially the value for micro-$RbSn_2F_5$ perfectly agrees with that from conductivity measurements (0.52 eV). In contrast, eqn (4), *i.e.*, using a 3D diffusion model, yields 0.39 eV (almost the same value is obtained if only the high-T slope is analyzed, as mentioned above). Although the quality of the two types of fits are very similar, only the spectral density of Richards developed for 2D diffusion is in agreement with the expectation that E_a from this model equals that deduced from σ_{dc}.

Here, as mentioned above, we have restricted $J(\omega_1)^{iD}$ (with $i = 2, 3$) to a single term. Including higher-order terms does not change the quality of the fits and has no effect on E_a and τ_0^{-1}. The pre-factors τ_0^{-1} of the fits shown in Fig. 8b are in the order of 2×10^{15} s^{-1}. Such a value is relatively high but in agreement with similar observations for surface diffusion.[83] Obviously, F diffusion along the buried or inner planes[84] of $RbSn_2F_5$ resembles ion dynamics on surfaces.

In both cases, *i.e.*, for nanocrystalline and microcrystalline $RbSn_2F_5$, the correlation factor β turned out to be 1.51 (nano) and 1.57 (micro), respectively. β directly influences the slope on the low-T side, the smaller value of 1.45 leads to a slightly smaller slope for nano-$RbSn_2F_5$ as seen in Fig. 8b. Considering the frequency limits of $J(\omega_1)^{3D}$ ($R_1 \propto \tau_c$ and $R_1 \propto {\tau_c}^{1-\beta}{\omega_0}^{-\beta}$) we see that the activation energies on the low-T and high-T side are connected to each other *via*

$$E_a^{\text{low-}T} = (\beta - 1)E_a^{\text{high-}T} \quad (8)$$

For 2D ionic motion essentially the same equation holds true, we have, however, to replace E_a(high-T) with the activation energy from the fit with $J(\omega_1)^{2D}$.[29] If we simply take the slope of the $R_{1(\rho)}(1/T)$ peak we must consider that E_a^{2D} is related to $E_a^{3D} = E_a$(high-T) *via* $E_a^{3D} = 3/4E_a^{2D}$;[49] with the values obtained here we have 0.39 eV = 3/4 × 0.52 eV. With β = 1.57 the relationship E_a^{2D}(low-T) = $(\beta - 1)E_a^{2D}$ is also fulfilled as we indeed have found 0.29 eV ≈ 0.57 × 0.52 eV. The same also holds for nanocrystalline $RbSn_2F_5$ with $\beta - 1 \approx 0.5$ and E_a^{2D}(low-T) = $1/2E_a^{2D}$.

In summary, while long-range ion transport in microcrystalline $RbSn_2F_5$ is characterized by 0.52 eV, short-range motions, taking into account correlation effects such as strictly confined hopping processes, local disorder and Coulomb interactions are best described by an activation energy of 0.29 eV. For nanocrystalline $RbSn_2F_5$ this value is somewhat reduced to 0.24 eV; this slight change is also reflected in ^{19}F NMR line narrowing, see above. This view on ion transport is also in agreement with the model introduced by Ngai. Independent of any dimensionality effects in Ngai's coupling concept dispersive regions in $\sigma'(\nu)$ would be expected that follow a $\nu^{n=\beta-1}$ behaviour, which is fulfilled in the present case.

To further compare results from NMR with those from conductivity spectroscopy, we can use the rate $R_{1\rho}(1/T)$ peak to estimate a self-diffusion coefficient for F^- hopping in $RbSn_2F_5$. At the peak maximum, which is seen at 273 K, the condition $\omega_1\tau_c \approx 0.5$ is valid; here, we have $1/\tau_c = 2.5 \times 10^6$ s^{-1}. Using the Einstein–Smoluchowski equation[85,86] $D = a^2/(2d\tau)$ with $d = 2$ for 2D diffusion we obtain $D = 2.8 \times 10^{-14}$ m^2 s^{-1} if we insert a mean jump distance of $a \approx 3$ Å. The jump distances of the F anions labelled F2, F3 and F4 (see Fig. 1) range from 2.89 to 2.97 Å. The distance from F1 to F2 is 2.95 Å. For comparison, at 273 K the bulk ionic conductivity is in the order of 1.4×10^{-5} S cm^{-1}. This value translates, according to the Nernst–Einstein equation[87,88] using a charge carrier density of 3×10^{27} m^3, into a solid-state diffusion coefficient D_σ of 6.7×10^{-14} m^2 s^{-1}. Thus, as the two diffusion coefficients only differ by a factor of 2, ^{19}F NMR spin–lattice relaxation, if the maximum of the rate peak is used to estimate D, and conductivity spectroscopy sense the same motional process in layer-structured $RbSn_2F_5$.

Finally, we shall discuss the change in ion dynamics when going from microcrystalline $RbSn_2F_5$ to its structurally disordered, nanocrystalline form. Many studies, dedicated to comparing diffusion properties of nanocrystalline ceramics with those from coarse-grained materials of the same chemical composition, report on huge differences at least if poorly conducting oxides or fluorides are considered, see above.[17,59,78–80] For materials with rapid ion dynamics from the start, the influence of structural disorder or size effects on ion transport is expected to be moderate or marginal if not without any positive effect on ion transport. If we consider layered materials structural disorder might even slow down ionic transport rather than increase it. For nanocrystalline Li_xTiS_2 ($0 < x \leq 1$), crystallizing with a layered structure, Winter and Heitjans did not found any large increase in Li diffusivity when compared to its coarse-grained form.[89,90] Li diffusion in the TiS_2 host is governed by very similar activation energies for the two forms. The incorporation of Rb for Ba in the fast 2D ionic conductor $BaSnF_4$ increases ionic conductivity;[59] most likely aliovalent doping affects, however, the slower interlayer exchange process rather than fast intralayer diffusion.[59,91] For the layer-structured form of $LiBH_4$,[27,92] crystallizing with hexagonal symmetry and showing 2D diffusion, downsizing the mean crystallite diameter through ball-milling has only small effect on Li ion conductivity.[92] On the other hand, the poorly conducting orthorhombic form of $LiBH_4$ with 3D diffusion, clearly benefits from nanostructuring. In such a sample, NMR relaxation measurements clearly revealed a subset of rapidly diffusing Li ions.[93]

Here, the nanocrystalline form of $RbSn_2F_5$ does not reveal strongly enhanced ion dynamics as compared to the annealed material with sharpened X-ray reflections. Conductivity spectroscopy clearly shows that ionic conductivities are the same for the two morphologies. On the contrary, one might even expect a slight decrease if defects disturb the fast 2D diffusion pathways that are already equipped with a large number fraction of vacant F anion sites. While we cannot recognize any strong effect on long-range ion transport from conductivity measurements, ^{19}F NMR line shapes point to slightly faster ion dynamics in the nanocrystalline form as seen by the motionally averaged line emerging at lower temperatures for non-annealed $RbSn_2F_5$. Presumably, disordered grain-boundary structures act as hosts for these mobile ions being able to contribute to dipole–dipole averaging already at slightly lower temperatures. This observation is consistent with enhanced R_1 relaxation rates of nano-$RbSn_2F_5$ if compared to those of microcrystalline $RbSn_2F_5$. Moreover, the corresponding activation energy on the low-T side of the spin-lock NMR peak is reduced from 0.29 eV to 0.24 eV.

Although the effects are small, on the short-range or angstrom length scale we see enhanced dynamics for the as-prepared form. Also magnetic field fluctuations of spatially confined jump processes might contribute to faster relaxation processes communicated to other ^{19}F spins *via* spin-diffusion. At least, the F anions residing near the defect sites do not become trapped.

Such trapping effects could easily explain any decrease in overall ion transport of layer-structured materials.

In other cases, fast localized dynamics are able to trigger through-going macroscopic transport.[25] These dynamic processes might be involved in also causing the huge increase in conductivity seen for the aforementioned nanocrystalline oxides, fluorides and carbonates prepared by milling.[91,94] Prominent examples include, for example, $LiXO_3$ (X = Ta, Nb),[78,79] $LiAlO_2$,[80] BaF_2,[95] CaF_2[17,96,97] and Li_2CO_3,[94] as mentioned above. Here, the subtle changes when going from the micro scale to nm-sized crystallites are, however, hardly comparable with the boosts in 3D ionic conductivity seen for the disordered systems. To sum up, for the fast 2D ionic conductor $RbSn_2F_5$ site disorder is of limited help to further enhance the already rapid long-range ion transport along the internal or buried interfaces.

4 Conclusions and outlook

Layer-structured $RbSn_2F_5$ has been prepared by a one-pot mechanochemical approach in a nanocrystalline form. We softly annealed the as-prepared sample in inert gas atmosphere to obtain microcrystalline $RbSn_2F_5$ with a mean crystallite diameter in the μm range. Annealing temperatures have to be adjusted carefully to avoid decomposition of the product. Also storing the as-prepared nanocrystalline material in Ar atmosphere for several months lead to grain growth as seen by sharp X-ray reflections. Obviously, the crystallization behaviour is triggered by fast F^- diffusion in the ternary fluoride. Indeed, conductivity spectroscopy and ^{19}F NMR relaxation show rapid F ion dynamics.

Careful analysis of both the conductivity isotherms and variable-temperature Nyquist curves, which are composed of bulk and grain boundary regions, revealed indications that F dynamics in $RbSn_2F_5$ is of 2D nature. Importantly, only if analyzed with a spectral density formalism which was developed for 2D diffusion the ^{19}F NMR data are consistent with dynamic parameters from conductivity spectroscopy. NMR relaxation measurements point to highly correlated F^- exchange processes for both the nanocrystalline and microcrystalline form. Local jump processes in micro-$RbSn_2F_5$ are to be characterized by an average activation energy as low as 0.24 eV; an even lower value of only 0.16 eV can be inferred from dielectric spectroscopy. An activation energy of 0.52 eV, on the other hand, determines long-range ion transport.

By comparing our results on microcrystalline and nanocrystalline $RbSn_2F_5$ we see that structural site disorder does not lead to any drastic enhancement of ion dynamics as it has been recognized for other ionic conductors. Obviously, for layer-structured materials, as it is also known for $LiCoO_2$ used as cathodes in lithium-ion batteries, the structurally perfect layers guiding the ions along the internal interfaces. This guidance is crucial to ensure long-range ion transport being fast enough that additional disorder does not lead to any further enhancement. Quite the contrary, one might also expect the opposite behaviour. Against this background, it seems worth considering the effect of dimensionality as a design principle for fast ion conductors.

Conflicts of interest

There are no conflicts to declare.

Acknowledgements

Financial support by the Deutsche Forschungsgemeinschaft (DFG Research Unit 1277, grant no. WI 3600 4-1 5-2, WI3600/2-1(4-1) and WI3600/5-2 (SPP 1415)) as well as by the Austrian Federal Ministry of Science, Research and Economy, and the Austrian National Foundation for Research, Technology and Development (Christian Doppler Laboratory of Lithium Batteries: Ageing Effects, Technology and New Materials) is greatly appreciated.

References

1 P. Knauth, *Solid State Ionics*, 2009, **180**, 911.
2 P. Knauth and H. Tuller, *J. Am. Ceram. Soc.*, 2002, **85**, 1654.
3 K. Funke, *Sci. Technol. Adv. Mater.*, 2013, **14**, 043502.
4 P. Heitjans and S. Indris, *J. Phys.: Condens. Matter*, 2003, **15**, R1257.
5 N. Kamaya, K. Homma, Y. Yamakawa, M. Hirayama, R. Kanno, M. Yonemura, T. Kamiyama, Y. Kato, S. Hama, K. Kawamoto and A. Mitsui, *Nat. Mater.*, 2011, **10**, 682.
6 S. Hori, T. Saito, K. Suzuki, M. Hirayama, A. Mitsui, M. Yonemura, H. Iba and R. Kanno, *Nat. Energy*, 2016, **1**, 16303.
7 R. Murugan, V. Thangadurai and W. Weppner, *Angew. Chem., Int. Ed.*, 2007, **46**, 7778.
8 V. Epp, O. Gün, H.-J. Deiseroth and M. Wilkening, *J. Phys. Chem. Lett.*, 2013, **4**, 2118–2123.
9 A. Hayashi and M. Tatsumisago, *Electron. Mater. Lett.*, 2012, **8**, 199.
10 A. Hayashi, K. Noi, A. Sakuda and M. Tatsumisago, *Nat. Commun.*, 2012, **3**, 856.
11 S. Narayanan, V. Epp, M. Wilkening and V. Thangadurai, *RSC Adv.*, 2012, **2**, 2553.
12 V. Thangadurai, S. Narayanan and D. Pinzaru, *Chem. Soc. Rev.*, 2014, **43**, 4714–4727.
13 J. C. Bachman, S. Muy, A. Grimaud, H.-H. Chang, N. Pour, S. F. Lux, O. Paschos, F. Maglia, S. Lupart, P. Lamp, L. Giordano and Y. Shao-Horn, *Chem. Rev.*, 2016, **116**, 140–162.
14 J. Lau, R. H. DeBlock, D. M. Butts, D. S. Ashby, C. S. Choi and B. S. Dunn, *Adv. Energy Storage Mater.*, 2018, **8**, 1800933.
15 Z. Zhang, Y. Shao, B. Lotsch, Y.-S. Hu, H. Li, J. Janek, L. F. Nazar, C.-W. Nan, J. Maier, M. Armand and L. Chen, *Energy Environ. Sci.*, 2018, **11**, 1945–1976.
16 S. Breuer, S. Lunghammer, A. Kiesl and M. Wilkening, *J. Mater. Sci.*, 2018, **53**, 13669–13681.
17 A. Düvel, B. Ruprecht, P. Heitjans and M. Wilkening, *J. Phys. Chem. C*, 2011, **115**, 23784–23789.
18 C. Rongeat, M. Reddy, R. Witter and M. Fichtner, *J. Phys. Chem. C*, 2013, **117**, 4943–4950.
19 C. Rongeat, M. Anji Reddy, R. Witter and M. Fichtner, *ACS Appl. Mater. Interfaces*, 2014, **6**, 2103–2110.
20 F. Preishuber-Pflügl, P. Bottke, V. Pregartner, B. Bitschnau and M. Wilkening, *Phys. Chem. Chem. Phys.*, 2014, **16**, 9580–9590.

21 S. Breuer, M. Gombotz, V. Pregartner, I. Hanzu and M. Wilkening, *Energy Storage Mater.*, 2019, **16**, 481–490.
22 S. Breuer and M. Wilkening, *Dalton Trans.*, 2018, **47**, 4105–4117.
23 M. Anji Reddy and M. Fichtner, *J. Mater. Chem.*, 2011, **21**, 17059–17062.
24 I. Mohammad, R. Witter, M. Fichtner and M. Anji Reddy, *ACS Appl. Energy Mater.*, 2018, **1**, 4766–4775.
25 S. Lunghammer, D. Prutsch, S. Breuer, D. Rettenwander, I. Hanzu, Q. Ma, F. Tietz and H. Wilkening, *Sci. Rep.*, 2018, **8**, 11970.
26 A. F. McDowell, C. F. Mendelsohn, M. S. Conradi, R. C. Bowman and A. J. Maeland, *Phys. Rev. B: Condens. Matter Mater. Phys.*, 1995, **51**, 6336.
27 V. Epp and M. Wilkening, *Phys. Rev. B: Condens. Matter Mater. Phys.*, 2010, **82**, 020301.
28 V. Epp, S. Nakhal, M. Lerch and M. Wilkening, *J. Phys.: Condens. Matter*, 2013, **25**, 195402.
29 B. Stanje, V. Epp, S. Nakhal, M. Lerch and M. Wilkening, *ACS Appl. Mater. Interfaces*, 2015, **7**, 4089–4099.
30 A. Kuhn, P. Sreeraj, R. Pöttgen, H.-D. Wiemhöfer, M. Wilkening and P. Heitjans, *J. Am. Chem. Soc.*, 2011, **133**, 11018.
31 D. Prutsch, B. Gadermaier, H. Brandstätter, V. Pregartner, B. Stanje, D. Wohlmuth, V. Epp, D. Rettenwander, I. Hanzu and H. M. R. Wilkening, *Chem. Mater.*, 2018, **30**, 7575–7586.
32 K. Yamada, M. M. Ahmad, Y. Ogiso, T. Okuda, J. Chikami, G. Miehe, H. Ehrenberg and H. Fuess, *Eur. Phys. J. B*, 2004, **40**, 167–176.
33 G. C. Farrington and J. L. Briant, *Science*, 1979, **204**, 1371.
34 J. L. Bjorkstam, P. Ferloni and M. Villa, *J. Chem. Phys.*, 1980, **73**, 2932–2936.
35 J. L. Bjorkstam and M. Villa, *J. Phys.*, 1981, **42**, 345–351.
36 J. Li, W. Yao, S. Martin and D. Vaknin, *Solid State Ionics*, 2008, **179**, 2016–2019.
37 B. L. Ellis, K. T. Lee and L. F. Nazar, *Chem. Mater.*, 2010, **22**, 691–714.
38 M. Wilkening, W. Küchler and P. Heitjans, *Phys. Rev. Lett.*, 2006, **97**, 065901.
39 M. Wilkening and P. Heitjans, *Phys. Rev. B: Condens. Matter Mater. Phys.*, 2008, **77**, 024311.
40 W. Küchler, P. Heitjans, A. Payer and R. Schöllhorn, *Solid State Ionics*, 1994, **70/71**, 434.
41 J. R. Dahn, W. R. McKinnon, R. R. Haering, W. J. L. Buyers and B. M. Powell, *Can. J. Phys.*, 1980, **58**, 207–213.
42 F. Kimmerle, G. Majer, U. Kaess, A. J. Maeland, M. S. Conradi and A. F. McDowell, *J. Alloys Compd.*, 1998, **264**, 63–70.
43 E. Murray, D. F. Brougham, J. Stankovic and I. Abrahams, *J. Phys. Chem. C*, 2008, **112**, 5672–5678.
44 M. Castiglione, P. A. Madden, P. Berastegui and S. Hull, *J. Phys.: Condens. Matter*, 2005, **17**, 845.
45 S. Chaudhuri, F. Wang and C. P. Grey, *J. Am. Chem. Soc.*, 2002, **124**, 11746–11757.
46 M. S. Whittingham, *Chem. Rev.*, 2004, **104**, 4271.
47 J. B. Goodenough and Y. Kim, *Chem. Mater.*, 2010, **22**, 587.
48 B. L. Ellis and L. F. Nazar, *Curr. Opin. Solid State Mater. Sci.*, 2012, **16**, 168.
49 P. M. Richards, in *Topics in Current Physics*, ed. M. B. Salamon, Springer, Berlin, 1979, vol. 15.
50 P. Heitjans, A. Schirmer and S. Indris, in *Diffusion in Condensed Matter*, ed. P. Heitjans and J. Kärger, Springer, 2005, ch. 9, p. 367.
51 K. Volgmann, V. Epp, J. Langer, B. Stanje, J. Heine, S. Nakhal, M. Lerch, M. Wilkening and P. Heitjans, *Z. Phys. Chem.*, 2017, **231**, 1215–1241.
52 S. Vilminot, R. Bachmann and H. Schulz, *Solid State Ionics*, 1983, **9-10**, 559–562.
53 M. Ahmad, K. Yamada and T. Okuda, *Solid State Commun.*, 2002, **123**, 185–189.
54 M. M. Ahmad, K. Yamada and T. Okuda, *Phys. B*, 2003, **339**, 94–100.
55 L. N. Patro and K. Hariharan, *Mater. Sci. Eng., B*, 2009, **162**, 173–178.
56 J. D. Donaldson and J. D. O'Donoghue, *J. Chem. Soc.*, 1964, 271–275.
57 J. Battut, J. Dupuis, S. Soudani, W. Granier, S. Vilminot and H. Wahbi, *Solid State Ionics*, 1987, **22**, 247–252.
58 K. Hirokawa, H. Kitahara, Y. Furukawa and D. Nakamura, *Ber. Bunsenges. Phys. Chem.*, 1991, **95**, 651–658.
59 F. Preishuber-Pflügl and M. Wilkening, *Dalton Trans.*, 2016, **45**, 8675–8687.
60 A. Kuhn, S. Narayanan, L. Spencer, G. Goward, V. Thangadurai and M. Wilkening, *Phys. Rev. B: Condens. Matter Mater. Phys.*, 2011, **83**, 094302.
61 R. Bertermann and W. Müller-Warmuth, *Z. Naturforsch., A: Phys. Sci.*, 1998, **53**, 863.
62 P. M. Richards, *Solid State Commun.*, 1978, **25**, 1019.
63 V. Šepelák, A. Düvel, M. Wilkening, K.-D. Becker and P. Heitjans, *Chem. Soc. Rev.*, 2013, **42**, 7507–7520.
64 D. Ailion and C. P. Slichter, *Phys. Rev. Lett.*, 1964, **12**, 168.
65 C. P. Slichter and D. Ailion, *Phys. Rev.*, 1964, **135**, A1099.
66 D. C. Ailion and C. P. Slichter, *Phys. Rev.*, 1965, **137**, A235.
67 D. C. Look and I. J. Lowe, *J. Chem. Phys.*, 1966, **44**, 2995.
68 T. J. Rowland and F. Y. Fradin, *Phys. Rev.*, 1969, **182**, 760.
69 D. Wolf, *Phys. Rev. B: Solid State*, 1974, **10**, 2724.
70 E. Fukushima and S. B. W. Roeder, *ExperimentalPulse NMR: A Nuts and Bolts Approach*, Addison-Wesley Pub. Co., Advanced Book Program, Reading, Mass., 1981.
71 S. Lunghammer, Q. Ma, D. Rettenwander, I. Hanzu, F. Tietz and H. Wilkening, *Chem. Phys. Lett.*, 2018, **701**, 147–150.
72 D. L. Sidebottom, *Rev. Mod. Phys.*, 2009, **81**, 999.
73 F. Preishuber-Pflügl and M. Wilkening, *Dalton Trans.*, 2014, **43**, 9901–9908.
74 K. Funke, C. Cramer and D. Wilmer, in *Diffusion in Condensed Matter - Methods, Materials*, Models, ed. P. Heitjans and J. Kärger, Springer, Berlin, 2nd edn, 2005, ch. 21, pp. 857–893.
75 K. L. Ngai, *Relaxation and Diffusion in Complex Systems*, Springer, New York, 2011.
76 C. Leon, J. Habasaki and K. L. Ngai, *Z. Phys. Chem.*, 2009, **223**, 1311.
77 K. Ngai, *Phys. Rev. B: Condens. Matter Mater. Phys.*, 1993, **48**, 13481.
78 M. Wilkening, V. Epp, A. Feldhoff and P. Heitjans, *J. Phys. Chem. C*, 2008, **112**, 9291.
79 P. Heitjans, M. Masoud, A. Feldhoff and M. Wilkening, *Faraday Discuss.*, 2007, **134**, 67.

80 D. Wohlmuth, V. Epp, P. Bottke, I. Hanzu, B. Bitschnau, I. Letofsky-Papst, M. Kriechbaum, H. Amenitsch, F. Hofer and M. Wilkening, *J. Mater. Chem. A*, 2014, **2**, 20295–20306.
81 N. Bloembergen, E. M. Purcell and R. V. Pound, *Phys. Rev.*, 1948, **73**, 679.
82 M. Uitz, V. Epp, P. Bottke and M. Wilkening, *J. Electroceram.*, 2017, **38**, 142–156.
83 J. Hinterberg, A. Adams, B. Blümich, P. Heitjans, S. Kim, Z. A. Munir and M. Martin, *Phys. Chem. Chem. Phys.*, 2013, **15**, 19825–19830.
84 P. Heitjans and M. Wilkening, *Mater. Res. Bull.*, 2009, **34**, 915.
85 A. Einstein, *Ann. Phys.*, 1905, **14**, 182–193.
86 M. von Smoluchowski, *Ann. Phys.*, 1906, **326**, 756–780.
87 R. McKee, *Solid State Ionics*, 1981, **5**, 133–136.
88 H. Mehrer, *Diffusion in Solids.*, Springer, Berlin, 2006.
89 R. Winter and P. Heitjans, *J. Phys. Chem. B*, 2001, **105**, 6108.
90 R. Winter and P. Heitjans, *J. Non-Cryst. Solids*, 2001, **293**, 19.
91 M. Wilkening, A. Düvel, F. Preishuber-Pflügl, K. Da Silva, S. Breuer, V. Ŝepelák and P. Heitjans, *Z. Kristallogr. – Cryst. Mater.*, 2017, **232**, 107–127.
92 V. Epp and M. Wilkening, *ChemPhysChem*, 2013, **14**, 3706–3713.
93 S. Breuer, M. Uitz and H. M. R. Wilkening, *J. Phys. Chem. Lett.*, 2018, **9**, 2093–2097.
94 D. Prutsch, S. Breuer, M. Uitz, P. Bottke, J. Langer, S. Lunghammer, M. Philipp, P. Posch, V. Pregartner, B. Stanje, A. Dunst, D. Wohlmuth, H. Brandstätter, W. Schmidt, V. Epp, A. Chadwick, I. Hanzu and M. Wilkening, *Z. Phys. Chem.*, 2017, **231**, 1361–1405.
95 B. Ruprecht, M. Wilkening, R. Uecker and P. Heitjans, *Phys. Chem. Chem. Phys.*, 2012, **14**, 11974.
96 W. Puin, S. Rodewald, R. Ramlau, P. Heitjans and J. Maier, *Solid State Ionics*, 2000, **131**, 159–164.
97 W. Puin and P. Heitjans, *Nanostruct. Mater.*, 1995, **6**, 885–888.

Supplementary Information

Spatial confinement — Rapid 2D F^- diffusion in micro- and nanocrystalline $RbSn_2F_5$

Maria Gombotz,*[a] Sarah Lunghammer,[a] Stefan Breuer,[a] Ilie Hanzu,[a,b] Florian Preishuber-Pflügl,[a‡] and H. Martin R. Wilkening*[a,b]

[a] Christian Doppler Laboratory for Lithium Batteries, and Institute for Chemistry and Technology of Materials, Graz University of Technology (NAWI Graz), Stremayrgasse 9, 8010 Graz, Austria. Fax: +43 316 873 32332; Tel: +43 316 873 32330.

E-Mail: wilkening@tugraz.at ; E-mail: gombotz@tugraz.at

[b] Alistore-ERI European Research Institute, 33 rue Saint Leu, 80039 Amiens, France.

‡ Present address: Schunk Carbon Technology GmbH, Au 62, 4822 Bad Goisern, Austria

In Fig. S1 scanning electron microscopy images of $RbSn_2F_5$ are shown which were recorded after different annealing steps of the fluoride in Ar atmosphere. At elevated annealing temperatures we clearly see that the sample decompose. Metallic spots (needles) seen in light microscopy indicate Sn^0. SEM reveals that microcrystalline $RbSn_2F_5$ is composed of small particles and rectangular tubes (or needles). Some of the tubes reach lengths in the order of 20 μm.

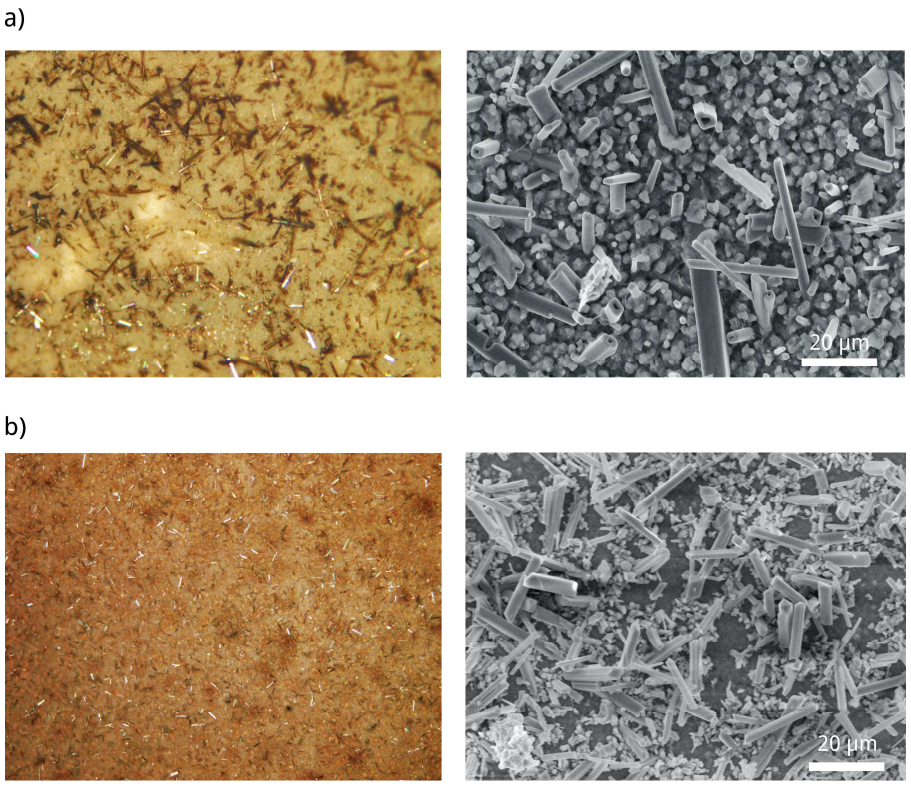

Fig. S1 a) $RbSnF_5$ annealed at 265 °C. left: image obtained via light microscopy (Olympus BX60) under 20 fold magnification; right: SEM picture (VEGA3 TESCAN electron microscope, 20 kV) under 2500 fold magnification. b) $RbSnF_5$ annealed at 225 °C. left: image obtained via light microscopy under 20 fold magnification; right: SEM picture under 2000 fold magnification. Annealing at 200 °C does not reveal any spots of metallic Sn.

In Fig. S2 the electrical permittivity spectra of microcrystalline $RbSn_2F_5$ are shown. They also reveal a two-step behaviour that mirrors electrical responses due to bulk and g.b. regions.

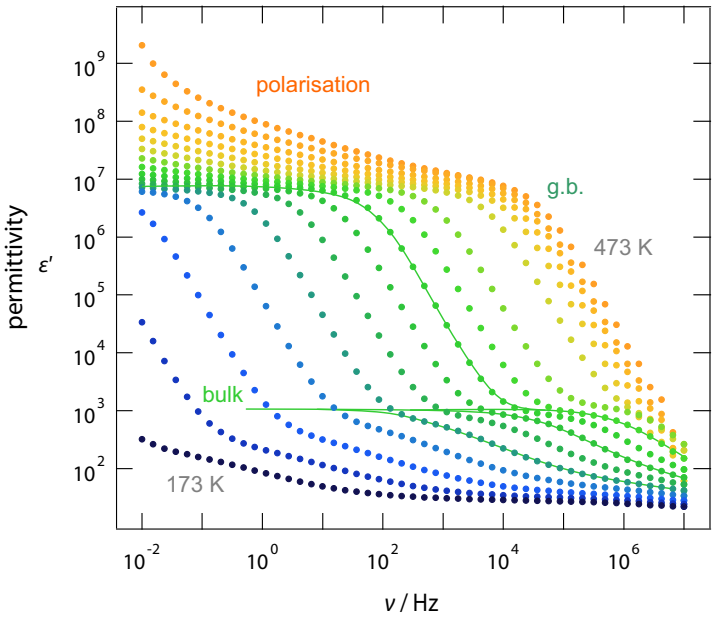

Fig. S2 Permittivity spectra of $RbSn_2F_5$ annealed at 473 K. The solid lines are to guide the eye; they help identify the bulk and g.b. responses (as indicated). Temperatures varied from 173 K to 473 K (in steps of 20 K).

D2

Temperature stability of the metastable, superionic Ag^+ conductor α^*-Ag_3SI

M. Gombotz *and H. Martin R. Wilkening*

Manuscript Draft

Temperature stability of the metastable, superionic Ag^+ conductor α^*-Ag_3SI

Maria Gombotz and H. Martin R. Wilkening

Institute for Chemistry and Technology of Materials, Graz University of Technology, Austria

1 Introduction

Solid ion conductors with negligible electronic conductivity play a capitol role in many field of materials science, particularly in energy science where fast ion conductors are needed to realize all-solid-state lithium and sodium batteries and to develop oxide fuel cells, for example. Silver ion conductors served as both model substances to study the principles governing fast ion transport and functional materials in energy storage devices. Without doubt, the most prominent examples are α-AgI (and its variants), Ag_2X (X = S, Se, Te) and MAg_4I_5 (M = Rb, K, NH_4).

The superionic conductor β-Ag_3SI, crystallizing with 'anti-perovskite' structure, can be prepared in high purity via solid-state reaction. Its successful synthesis was first reported in 1960 by Reuter and Hardel[1]. β-Ag_3SI was obtained by heating a mixture of AgI and Ag_2S above 200°C. Already in this first publication, the authors report on the existence of two different phases of Ag_3SI, namely the β and the α phase; the transition temperature was 235°C. In later studies[2,3], a closer look was taken not only to grasp the crystal structures, but also to investigate the phase transition itself with the help of differential thermal analysis (DTA). DTA showed a high stability of the α phase up to temperatures as high as 550°C.

Ceramic solid-state synthesis is by far the most widely adopted route to prepare phase-pure β-Ag_3SI[4,5]. The crucial part of the synthesis concerns, however, prolonged annealing of the α-Ag_3SI at, *e.g.*, 203 °C[4].

Even though X-ray and neutron diffraction studies on single crystals of Ag_3SI, see, for example, references[6,7] already existed, a detailed investigation of all possible phases Ag_3SI can adopt, was lacking. Therefore, Hull *et. al.*[4] carried out an investigation of γ-, β-, α- and its quenched relative α^*-Ag_3SI via Neutron diffraction experiments. The highly conducting, high-temperature α phase crystallises in the space group $Im\bar{3}m$. In this body-centered cubic crystal, S^{2-} and I^- are distributed randomly over the 2*a* positions marking the absence of long-range anion order. Due to the elevated temperatures in which α-Ag_3SI exists, thermal vibrations lead to a significant anisotropy of Ag^+ residing on 24*h* positions. These crystal sites are trigonal interstices within the anion sublattice. Metastable α^*-Ag_3SI, obtained by quenching α-Ag_3SI, still adopts the space group $Im\bar{3}m$, however, Ag^+ is now found on 24*g*, which is between the octahedral and tetrahedral cavities, and 48*i* sites. Slow cooling of α-Ag_3SI results in β-Ag_3SI crys-

[1] B. Reuter and K. Hardel, Angw. Chem., 1960, 72, 4, 138-139

[2] B. Reuter and K. Hardel, Z. f. anorg. u. allg. Chem., 1965, 340, 168-180

[3] B. Reuter and K. Hardel, Z. f. anorg. u. allg. Chem., 1965, 340, 158-167

[4] S. Hull et al., J. of Phys.: Condens. Mat., 2001, 13, 10, 2295-2316

[5] Hoshino S. et al., J. of the Phys. Soc. of Jap., 1979, 47, 4, 1252-1259

[6] J.-J. Didisheim et al., Solid State Ionics, 1986, 18-19, 1150-1162

[7] E. Perenthaler et al., 1981, 5, 493-496

tallising in a primitive cubic cell in the space group $Pm\bar{3}m$. Long range ordering of I^- and S^{2-}, now residing on 1*b* and 1*a* sites, respectively, occurs. Ag^+ occupies the 12*h* position. The according structure of β- and α^*-Ag_3SI is depicted in figure 1 and 3, clearly showing the more ordered structure of the β-phase. Lowering the temperature below $-117°C$, induces a phase transition to the γ phase, where not only the anion sublattice is ordered with I^- and S^{2-} on 1*a*, but also the cation sublattice becomes ordered with Ag^+ on the 3*b* positions.

The conductivity of β- and γ-Ag_3SI was already examined in literature[8,9,10,11,12], leading to conductivities of approximately 0.06 up to 0.02 S cm^{-1} at room temperature for the β-phase, $7{\cdot}10^{-6}$ up to $1{\cdot}10^{-5}$ S cm^{-1} for the γ-phase at $-120°C$. Hull *et. al.*[11] also examined the conductivity of α^* and α-Ag_3SI, reaching similar values as in this study.

Especially α^*-, but also β-Ag_3SI is reported to suffer from severe instabilities. The first report on β-Ag_3SI[13] already mentioned the decomposition of β-Ag_3SI by simply exposing it to either light or water. A systematic investigation of the stability of α^*, however, is still missing in literature. Therefore this study aims to shed light on the time as well as temperature range, α^* can withstand before transforming into β-Ag_3SI again.

2 Experimental

For the synthesis of β-Ag_3SI, stochiometric amounts of as received AgI and Ag_2S were milled for 4 h in a planetary mill (Fritsch Pulverisette Premium line 7). Therefore the beakers, made of ZrO_2, loaded with 180 balls made of the same material and with a diameter of 5 mm, were rotated at 400 rpm for 15 min. Thereafter a break of 15 min was taken to prevent overheating of the sample, as well as beakers. The powdered black sample was pelletized to cylindrical specimens with a diameter of 5 mm, using a hand press. For this purpose an uniaxial pressure of 0.5 t tons was applied. The pressed pellets were fire-sealed in quartz ampoules for the following temperature treatment; heating to 550°C with 5 K/min - hold for 120 h, slowly cooling to 220°C - hold for 48 h, slowly cooling down to room temperature (natural cooling of the oven).

The obtained β-Ag_3SI specimen were equipped on both sides with 50 nm Pt layers as blocking electrodes. This was done by sputtering with a Leica EM SCD050 sputtering device.

Additionally, X-ray diffraction was performed to ensure the successful synthesis of the meta-stable β-phase. A Bruker D8 Advance diffractometer was used to scan a $°2\theta$ range of 25 to 60° with a stepsize of $0.02°2\theta$, measuring for 1 s each. The diffractometer operates with a Bragg Brentano geometry and Cu is used as target to generate CuKα radiation with a wavelength of 1.5406 Å. To prevent a reaction during the measurement, a holder for air-sensitive samples was used, where the powder is covered with a Capton foil.

To study ion dynamics in all four phases Ag_3SI can adopt, impedance spectroscopy was performed to obtain the conductivity, while heating from $-140°C$ up to 260°C and during the subsequent cooling in the same temperature range. A Novocontrol Concept 80 broadband spectrometer in combination with an active BDS 1200 cell and a ZGS interface (Novocontrol) was used. The measured frequencies covered a range from 10^{-1} up to 10^7 Hz. The temperature was controlled by a QUATRO cryo-system (Novocontrol). All measurements were carried out by flushing the sample chamber with a constant flow of freshly evaporated and dry N_2.

The long-time stability of the conductivity of α^*-Ag_3SI at 30°C and 60°C was tracked for 140 h and 48 h, respectively. Beforehand the sample was heated up to 260°C to convert β- into α-Ag_3SI. Additionally, the sample was cycled again between 0 and 60°C, with intermediate steps at 20°C for a total of 30 h.

For comparison of the conductivity the Ag^+ conductors $RbAg_4I_5$ and KAg_4I_5 were synthesised via a mechanochemical route. For the former one, 3g of educts (RbI and AgI) in stochiometric amounts were milled at 400 rpm for a total of 5 h, with a sequence of 15 min milling, followed by a break of 15 min to allow cooling of the beakers. The

[8] Michihiro Y. et al., Solid State Ionics, 1989, 35, 3, 337-341

[9] S. Hull et al., J. of Phys.: Condens. Mat., 2001, 13, 10, 2295-2316

[10] Kojima A. et al., J. of the Phys. Soc. of Jap., 1979, 47, 4, 1252-1259

[11] S. Hull et al., J. of Phys.: Condens. Mat., 2007, 19, 40, 406214

[12] B. Reuter and K. Hardel, Naturwissenschaften, 1961, 48, 161

[13] B. Reuter and K. Hardel, Angw. Chem., 1960, 72, 4, 138-139

latter one was synthesised by milling 3 g of educts (KI and AgI) in stochiometric amounts with the same milling sequence as described above, but for 10 h at 600 rpm. Both syntheses were carried out in tungsten carbide beaker loaded with 170 balls made of the same material and a diameter of 5 mm. The characterisation of $RbAg_4I_5$ and KAg_4I_5 included XRD as well as impedance spectroscopy, carried out in the same way as for Ag_3SI.

Additionally the electronic conductivity of β- and α^*-Ag_3SI was determined via polarisation experiments. For this purpose, cylindrical pellets with a diameter of 8 mm were pressed with an uniaxial pressure of 0.5 t and again, equipped with 50 nm thick Pt electrodes. A Parstat MC potentiostat (Princeton Applied Research) equipped with a low-current option was used to carry out chronoamperometric measurements at a potential of 100 mV over a time span of 200 min and at room temperature (20°C). α^*-Ag_3SI was heated in advance to 260°C to ensure a complete phase transformation.

Static ^{109}Ag NMR spectra of β-Ag_3SI at 20°C were acquired with a Bruker Avance III spectrometer in combination with a superconducting magnet operating at 7.4 T. The low resonance frequency of only 13.9 MHz at this nominal magnetic field made the application of a special probe head, allowing to insert a large amount of sample, favourable. Therefore the sample was fire-sealed in a glass tube ($\sim$ 20 mm in length, 10 mm in diameter).

3 Results and Discussion

To ensure the successful synthesis of β-Ag_3SI, a XRD pattern was recorded at room temperature, see Figure 1 (a). Apart from a slight shift of all reflexes to lower angles, most likely due to sample preparation, the sample reflexes coincide with the reference. The reflexes at 32 and 37°2θ show a small shoulder, as well as a small reflex at approximately 39°2θ, indicating most likely a small impurity with γ-AgI.

Additionally x-ray pattern of the synthesised Ag^+ conductors $RbAg_4I_5$ and KAg_4I_5 were recorded and are depicted in Figure 1 (b) and (c). Both pattern coincide well with the shown references. At lower angles, until approximately 30°θ a strong underground is visible, because, due to the

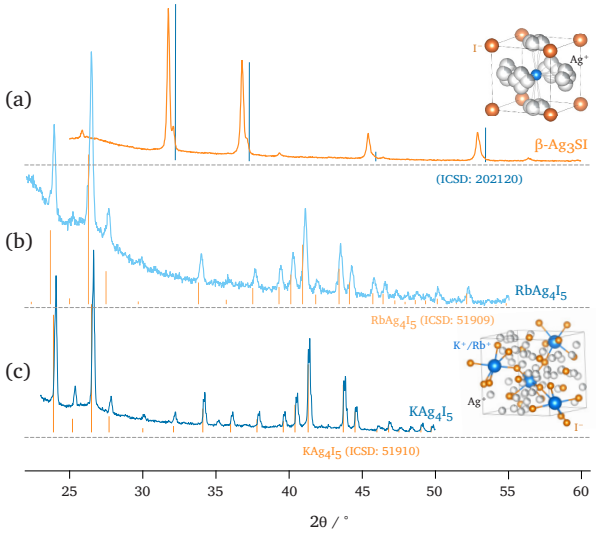

Figure 1: ***(a)*** *XRD pattern of the synthesised β-Ag_3SI with a reference (ICSD: 202120), showing a shift of approximately 0.4°2θ compared to the reference with small, additional reflexes indicating minor γ-AgI impurities. The inset on the right side shows the according crystal structure.* ***(b)*** *Depicted is the pattern of the synthesised Ag^+ conductor $RbAg_4I_5$ with a reference (ICSD: 51909) pointing towards its phase purity.* ***(c)*** *The pattern of isomorph, phase pure compound KAg_4I_5 is depicted alongside with a reference (ICSD: 51910). The crystal structure of $RbAg_4I_5$ as well as KAg_4I_5 is shown as inset on the right side.*

sensitivity towards moisture and air, the measurements had to be performed with special sample holders, protecting the sample with a Kapton foil.

Starting the conductivity measurements, β-Ag_3SI was first cooled down to $-140°C$, below the transition temperature from $\beta \longrightarrow \gamma$ at $-116°C$[14]. The conductivity measurements therefore started at the γ phase and while heating up, immediately the γ to β transition between -120 and $-100°C$ was traceable by an large conductivity increase about two orders of magnitude, see Figure 2 (a).

At these low temperatures, the conductivity isotherms show two characteristic regions, namely the frequency-independent σ_{DC}-plateau at low frequencies, marking the long-range transport of the ions inside the crystal, and the frequency dependent dispersive region. The latter one disappears for temperatures above $-120°C$ due to increasing conductivity. This effect is also accompanied by the emergence of the electrode polarisation at low frequencies. The transition of β- to α-Ag_3SI is seen between 220°C and 260°C. At this temperature a maximal conductivity of 0.8 S cm^{-1} was measured. Upon cooling, see Figure 2 (b), the quenched α^* phase was preserved and no disproportionate decrease of conductivity was found down to $-140°C$. At 20°C we detected for the α^* phase a σ_{DC} conductivity of one order of magnitude higher (0.038 S cm^{-1}) than for the β-phase (0.003 S cm^{-1}) (see green dots in Figure 2 (a) and (b)).

In Figure 2 (c) the according Arrhenius plot can be found. Here, the transition with the accompanying changes in conductivity are clearly visible and indicated by different colors. Mentionable is the bended heating curve for β-Ag_3SI, which was already reported by Kojima *et. al.*[15]. The high-temperature α phase seems to exist down to a temperature of 200°, as the conductivity is dropping thereafter, indicating the transition to the α^* phase. Cooling of this phase is characterised by an activation energy of 0.19(2) eV and is similar to former values of 0.13 eV[15].

As mentioned, the Ag^+ conductors $RbAg_4I_5$ and KAg_4I_5 were successfully synthesised - see inset at the right upper part of Figure 3 for their structure - and their conductivity was measured too. Figure 3 shows the according Arrhenius diagram of both samples in comparison with α^*-Ag_3SI. At temperatures below 25°C, $RbAg_4I_5$ and KAg_4I_5 show superior conductivity. With increasing temperature, however, the conductivity of KAg_4I_5 falls behind the one of α^*-Ag_3SI, while $RbAg_4I_5$ still stays the most conductive phase. As due to their highly hygroscopic character, $RbAg_4I_5$ and KAg_4I_5 had to be protected by a sample holder, not allowing measurements over 180°C, no statement about the conductivities in the stability window of α-Ag_3SI can be made.

To evaluate the thermal stability of α^*-Ag_3SI three different conductivity measurements were carried out. Either by keeping the sample at a constant temperature of 30°C or 60°C, or by cycling the sample between 0 and 60°C. Prior to that the sample was in all cases heated to 260°C to complete the transition of β- to α- and further to its quenched relative α^*-Ag_3SI.

In Figure 5 (a) the conductivity as a function of time, measured at 30°C is depicted. At first, the decrease in conductivity is more pronounced, before it decreases defacto linearly with time from 34 to 15 mS cm^{-1} after 140 h. It is expected that a further decrease, until the conductivity of β-Ag_3SI is reached, would take place with ongoing time. Here, however, the set-up possess limitations, not allowing longer measurements, as the slightly air-sensitive sample starts to degrade. The degradation or oxidation was verified by XRD, see Figure 4 (b), for the according pattern. Unidentified impurity phases emerge, however, the majority of the sample is composed of the β-phase, clearly indicating a transformation of α^*- to β-Ag_3SI.

To check weather the conductivity drops faster at a higher, constant temperature of 60°C, α^*-Ag_3SI was held at this temperature for approximately 48 h. Here, a steeper decrease of conductivity from 74 to 9 mS cm^{-1} after 25 h can be observed, see Figure 5 (b). In contrast to the measurement at 30°C the conductivity remains then constant. The conductivity value of β-Ag_3SI (5 mS cm^{-1}) is almost obtained after 48 h. Hence, a higher temperature indeed speeds up the transformation of α^*-Ag_3SI back to β-Ag_3SI. Again, see Figure 4 (c), the sample does undergo degradation, but β-Ag_3SI seems to be also the predominant phase.

To evaluate the temperature cycling stability of α^*-Ag_3SI, the sample was cycled between 60°C and 0°C, see Figure 5 (c). When comparing this course of conductivity to the one from the mea-

[14] S. Hull et al., J. of Phys.: Condens. Mat., 2007, 19, 40, 406214

[15] A. Kojima, J. of the Phys. Soc. of Jap., 1988, 57, 1, 176-187

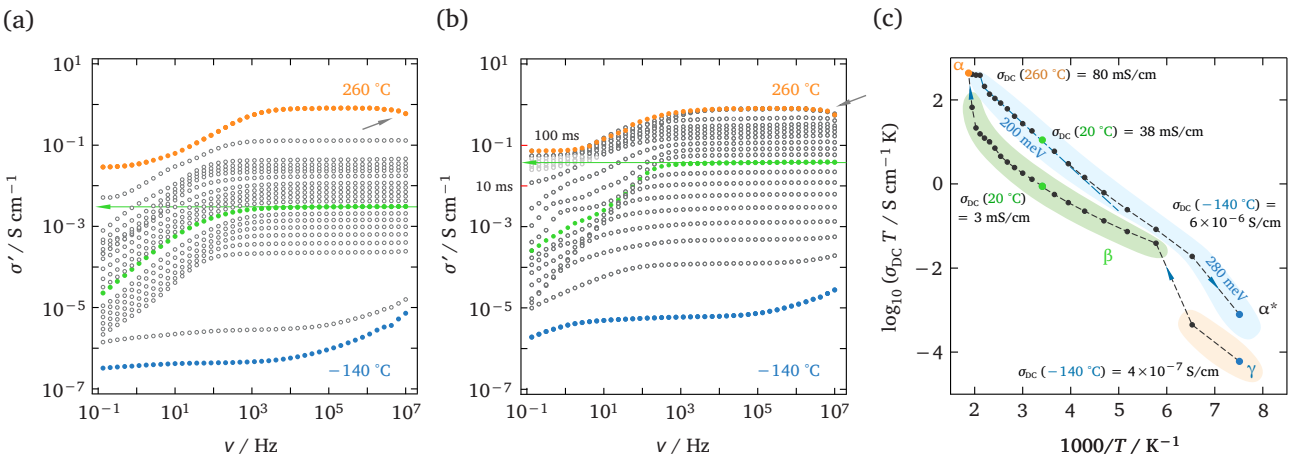

Figure 2: ***(a)*** *Conductivity isotherms recorded in 20°C steps during the heating cycle, showing the phase transition from γ to β and finally to α-Ag_3SI.* ***(b)*** *The isotherms during the subsequent cooling cycle, with α^* being the present phase, are depicted.* ***(c)*** *The Arrhenius-type diagram illustrates the phase transitions in the temperature range between −140°C to 260°C, during heating ($\gamma \longrightarrow \beta \longrightarrow \alpha$) and cooling ($\alpha \longrightarrow \alpha^*$).*

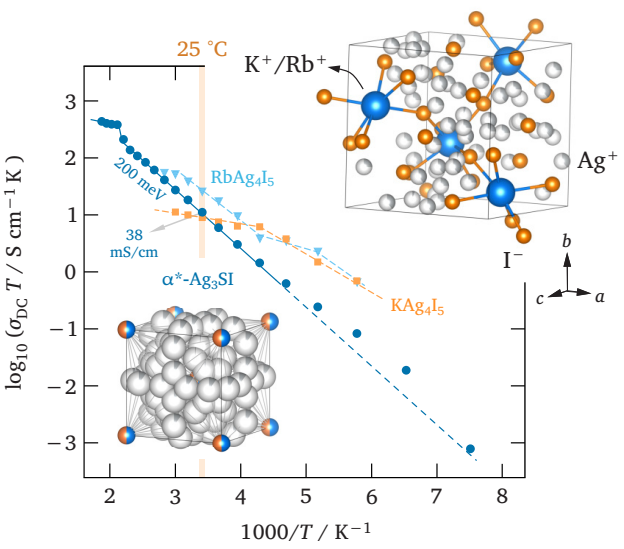

Figure 3: *Arrhenius plot of $RbAg_4I_5$ and KAg_4I_5 in a temperature range between −100°C and 100°C in comparison with $\alpha^{(*)}$-Ag_3SI depicted in a temperature range between −140°C and 260°C.* ***Inset on the right*** *Exemplaric structure of $RbAg_4I_5$ (ICSD reference: 519109) and the isomorphous KAg_4I_5 crystallising in the cubic space group $P4_132$.*

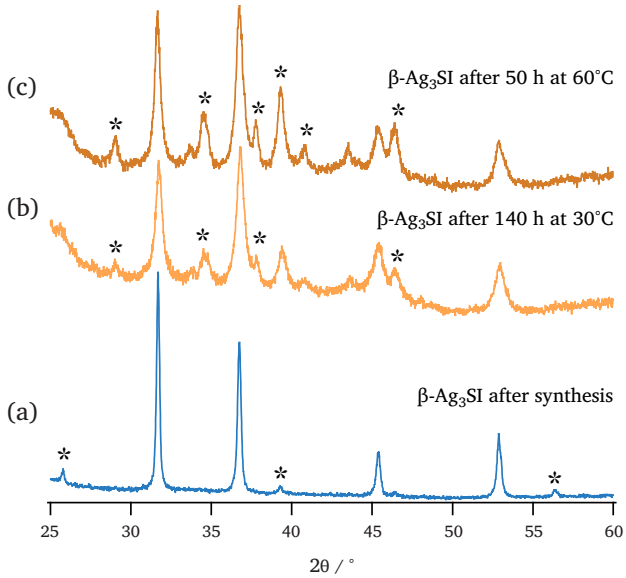

Figure 4: *Powder pattern of* ***(a)*** *β-Ag_3SI after synthesis,* ***(b)*** *β-Ag_3SI after 140 h at 30°C during the impedance measurement and* ***(c)*** *β-Ag_3SI after 50 h at 60°C again during the impedance measurement. Both pattern,* ***(b)*** *and* ***(c)****, exhibit additional impurity reflexes marked with an asterisk.*

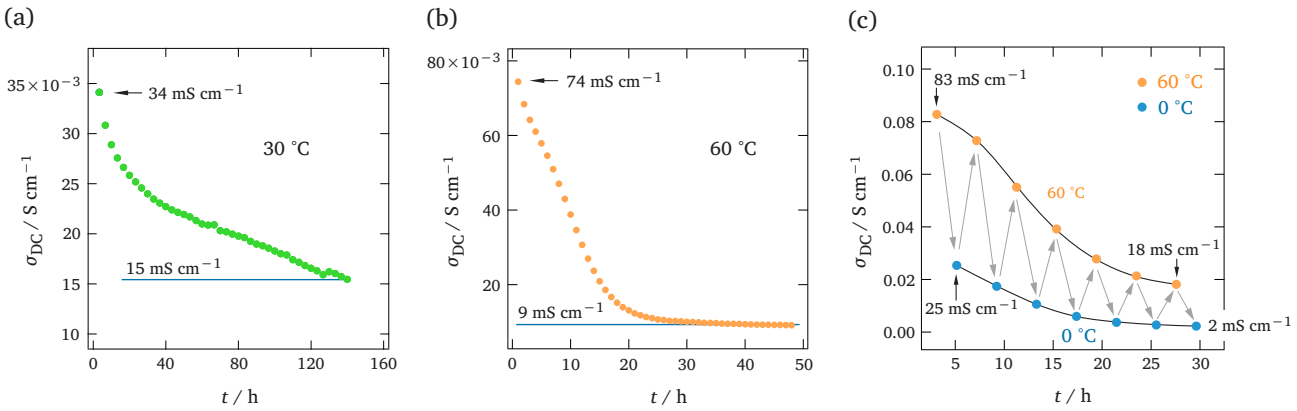

Figure 5: ***(a)*** *Long time measurement of σ_{DC} of α^*-Ag_3SI (heated up to 260°C in advance) at 30°C, showing a decrease from 34 mS cm^{-1} to 15 mS cm^{-1} after 140 h.* ***(b)*** *Long time measurement of σ_{DC} of α^*-Ag_3SI (heated up to 260°C in advance) at 60°C, indicating a fast transformation from β- to α^*-Ag_3SI already after 25 h. A decrease from 74 mS cm^{-1} to 9 mS cm^{-1} is traceable.* ***(c)*** *Long time measurement of the σ_{DC} of α^*-Ag_3SI (heated up to 260°C in advance) between 60°C and 0°C for 30 h, showing again the instability of the α^* phase, transforming back to β-Ag_3SI after approximately 30 h.*

surement at a constant temperature of 60°C, distinct similarities can be seen. In both cases, the conductivity drops from 74 mS cm^{-1} (T = const. = 60°C) and 83 mS cm^{-1} (T = 0 - 60°C), to 10 mS cm^{-1} and 18 mS cm^{-1}, respectively, at a temperature of 60°C. Obviously the reordering of the anion and cation sublattice, from β- to α^*-Ag_3SI is strongly dependent on the temperature and cannot be slowed down by cooling it regularly.

In impedance spectroscopy experiments ionic and electronic conductivity contributes to the final signal. Hence, to separate these contributions further experiments are needed. Therefore polarisation measurements on β- and α^*-Ag_3SI were performed to determine the electronic conductivity at 20°C and a potential of 100 mV. As depicted in Figure 6 and the lower inset, the current in both samples decays rather fast, as expected due to their high overall conductivity of 3.2 mS cm^{-1} for β-Ag_3SI and 33 mS cm^{-1} for α^*-Ag_3SI.

After approximately 200 min a steady-state current is reached within both samples; 8.08·10^{-8} A for the β-, 1.11·10^{-8} A for the α^*-phase, see upper inset in Figure 6. By taking into account the height d=1.07 mm, as well as the sample radius r=4 mm, the applied voltage U and the steady-state current A, the electronic conductivity σ_{DC} can be calculated via the following equation:

$$\sigma_{EL} = \frac{I}{U} \cdot \frac{d}{r^2\pi} \qquad (1)$$

The electronic conductivity for β-Ag_3SI is slightly higher (1.96·10^{-7} S cm^{-1}) than the one of

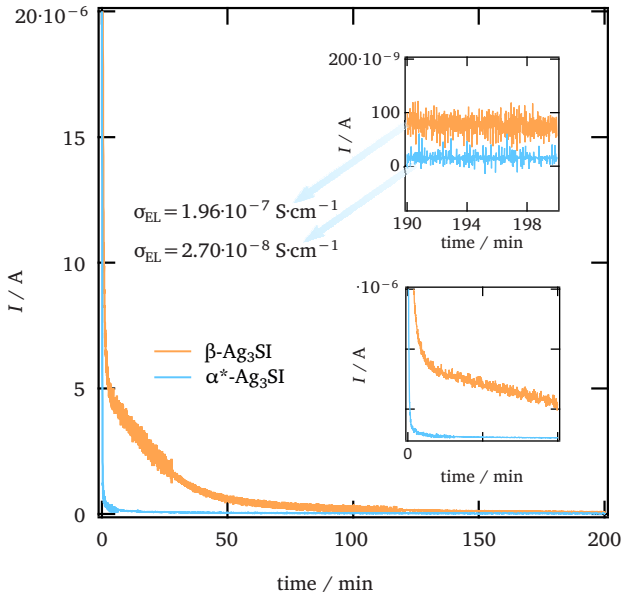

Figure 6: *Chronoamperic measurement at a constant voltage of 100 mV of β- (in orange) and α^*-Ag_3SI (in blue). By taking into account the dimensions of the sample (d=1.07 mm, r=4 mm) and the steady-state current reached after approximately 200 min, the electronic conductivity could be estimated, see text for further explanation.*

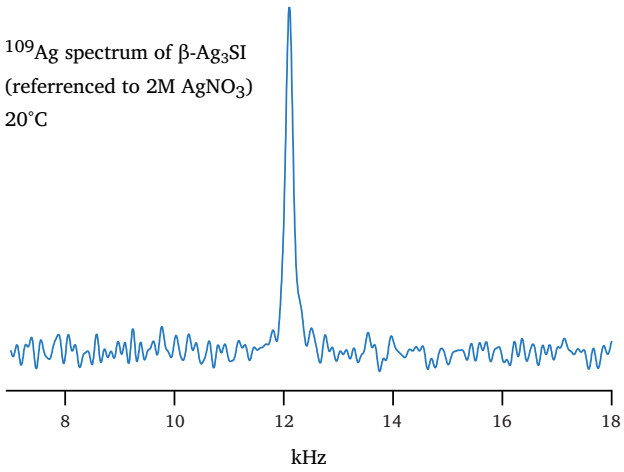

Figure 7: *^{109}Ag NMR spectra of β-Ag_3SI recorded at 20°C. The applied magnetic field of 7.4 T results in a resonance frequency as low as 13.9 MHz. One sharp line is observed, reinforcing the fast ion dynamics seen already at this moderate temperature.*

α^*-Ag_3SI ($2.70 \cdot 10^{-8}$ S cm^{-1}). By comparing the overall conductivity with the calculated electronic conductivity, it can be said that the conduction in both samples is dominated by Ag^+ ion movement.

Local ion dynamics can also be visualised with static NMR measurements. In the case of ^{109}Ag NMR both, the low sensitivity of the nuclei and the low resonance frequency of only 13.9 MHz at 7.4 T, make it hard to record spectra. Here, it was possible to obtain a spectrum at 20°C, see Figure 7.

One sharp resonance line with a fwhm of only ∼100 Hz can be seen, being in line with one magnetic equivalent site of Ag^+ in Ag_3SI. The line appears at 12 kHz (referenced to 2M $AgNO_3$), demonstrating a similar chemical shift as $RbAg_4I_5$ (18 kHz)[16] $RbAg_4I_5$ line at approx. 780 ppm (11.7 T). Such a narrow line clearly demonstrates the fast Ag^+ ion dynamics in β-Ag_3SI.

4 Conclusion

Ag_3SI, particularly the α^* and β phase, were closely examined during this study. The phase pure β-phase was obtained via solid state synthesis and its crystal structure was confirmed via XRD. Impedance spectroscopy was utilized to determine the conductivity in a wide temperature range between −140°C and 260°C. Here, we were able to track the phase transformation from γ- to β- and finally to α-Ag_3SI while heating. During cooling the highly conductive, but metastable α^*-phase was preserved, which transforms back to β-Ag_3SI in the course of time and as a function of temperature. With long-term conductivity measurements at different temperatures, we were able to visualise this transformation, which was found to occur faster at higher temperatures and remains identical, when the sample is cooled intermediately. Polarisation measurements showed low electronic conductivities in β- and α^*-Ag_3SI, making clear that Ag^+ is the dominant mobile species in both materials. The superionic character of β-Ag_3SI, reaching 0.003 S cm^{-1} at room temperature, was further elucidated by recording static ^{109}Ag NMR spectra. One sharp resonance line underlined again the fast ion dynamics also on the microscopic length scale.

[16] Spencer T. L. *et al.*, J. Phys. Chem. C, 2013, 117, 19, 9558-9565

4 Fluorine-ion Batteries

Outline

Fluorine-ion Batteries (FIB) belong to a group of battery systems, which are in their early stages of development, as compared to Li-ion Batteries (LIB). Only tentative screenings of electrode and electrolyte materials are reported. In the course of this doctoral thesis the electrochemical stability of the so far most promising solid electrolyte $La_{0.9}Ba_{0.1}F_{2.9}$ was examined for the first time and published in *Nanomaterials*. In the following an overview about the current state of art, advantages and faced limitations of FIB is given, the corresponding publication in *Nanomaterials* [80] can be found in Section 4.6.

4.1 State of the Art

The growing use of batteries in applications where high energy densities are needed, like in electric or hybrid vehicles, make the further development of LIB and the exploration of new systems indispensable. Here, FIB belong to the promising new systems. The use of multivalent fluorides as electrodes, make it possible that through a conversion reaction more than one F anion is released per metal atom upon discharging, hence, more than one electron is transferred. This results compared to LIB in increased volumetric capacities (>1000 Ah l^{-1}) [81–83]. For the realisation of such systems, electrochemical stable electrolytes with high ionic conductivity are needed.

History

The conduction of F^- through solid matter is already on the mind of researchers since 1893, when Faraday mentioned PbF_2 [84]. 30 years later in 1923 Tubandt C. [85] measured transference numbers in the same compound and already faced side reactions with Ag as anode, highlighting the reactivity of F^- conductors. First galvanic cells were built by Kennedy J. H. *et al.* [86] and Schoonman J. [87] in 1976 by using Pb as anode, a mixture of fluorides as solid electrolyte (PbF_2/CuF_2 or β-PbF_2:AgF/BiO_xF_{3-2x}) and Cu or Bi as cathode. In both cases the cells could be discharged. A subsequent charging was, however, not possible, indicating undesired side-reactions.

Thereafter, in the shade of LIB, galvanic cells relying on Fluorine as charge carrier

remained relatively unobserved (with the exception of one patent [88]), until 2011, when A. Reddy *et al.* [89] picked the topic up again. Here the first rechargeable FIB was reported. Since then, various publications exist, reporting on several issues regarding the development of such cells [83, 90–96].

4.2 Working Principle

As already mentioned, in FIB predominately multivalent fluorides are employed as cathode material. Upon receiving an electron, a F anion is released and migrates through the (solid) electrolyte to the metal anode. Here, a (reversible) reaction occurs between the F anion and the metal to form again a (multivalent) fluoride. Simultaneously an electron is released and hence, supplies electric power when being connected to an external load.

For the discharge of a FIB, the occurring reactions are listed below:

Discharge:

$$\begin{aligned} \text{Cathode: } & x\text{e}^- + \text{M'F}_x \longrightarrow \text{M'} + x\text{F}^- \\ \text{Anode: } & x\text{F}^- + \text{M} \longrightarrow \text{MF}_x + x\text{e}^- \\ \textbf{Total: } & \text{M} + \text{M'F}_x \longrightarrow \text{MF}_x + \text{M'} \end{aligned}$$

A primary cell cannot be further used after discharge, as the reactions occurring are irreversible. As fluorine cells are considered a future alternative to secondary, rechargeable LIB, the reactions have to be reversible, when the cells are charged by applying an electric current.

Apart from some exceptions, the approach to build full cells was always similar. Fully charged cells were assembled by using a metal anode, a solid electrolyte and a cathode, composed of a mixture of active material (a multivalent fluoride), Carbon and the used electrolyte, as schematically drawn in figure 4.1.

This outlines only one possibility to build such cells. Therefore several different approaches to design fully dis/charged or half charged cells, by using mainly solid, but also liquid electrolytes, will be discussed in the following.

4.3 Electrodes used

The research being done on electrode materials for FIB differs in essential features compared to LIB. Only ten years ago in 2011, the first rechargeable FIB was introduced, hence, the development of FIB lies behind the one of LIB. After a pre-selection of electrode materials, *e.g.* regarding reaction potentials, it was more or less a trial and error

study to screen out suitable electrodes.

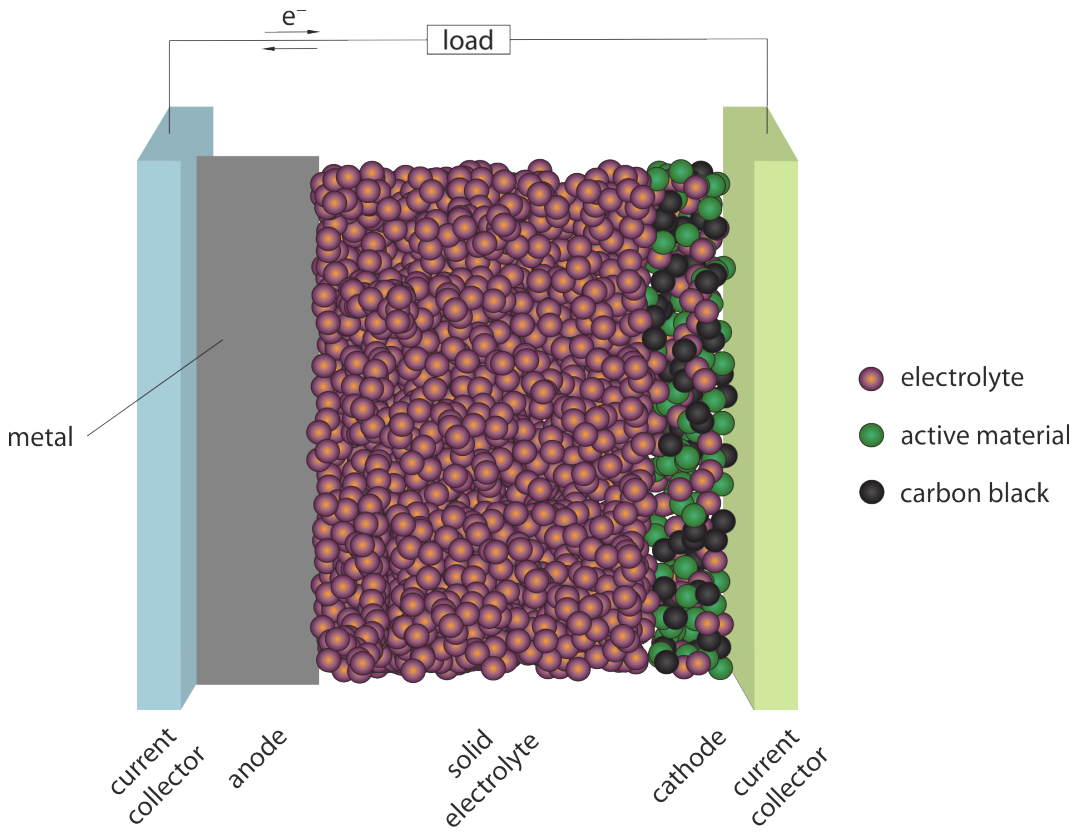

Fig. 4.1: A schematic drawing of a charged Fluorine-ion Battery as build *e.g.* by Reddy A. *et al.* [89] consisting of a metal anode and a composite cathode (active material, electrolyte, carbon black), both connected with current collectors. The fluorine is transported from one electrode to the other through a solid electrolyte.

Anodes

Two promising approaches to design a cycling stable anode material are reported. One approach was, to take a metallic anode, *e.g.* Li [94], La [91], Zn [93] or Ce [89, 92, 93, 97], mostly as a relatively thick layer of up to 120 μm [89]. The main disadvantage of metallic anodes lies in the fact that those materials are prone to surface oxidation even if stored in gloveboxes [90]. Another approach was the blending of the active material - a mixture of a metal (*e.g.* Mg [90, 96] or Pb [95]) and/or the according metal fluoride (*e.g.* MgF_2 or PbF_2) - with Carbon and the electrolyte used. The supposed improvement here is that less or no surface sensitive metals are used as the cell is assembled in a half-charged or discharged state. Furthermore the increased electronic conductivity, due to the use of Carbon, and the increased ionic conductivity, due to the addition of the electrolyte

used, are thought to be beneficial. Recently, SnO_2, Indium Tin Oxide (ITO) and carbon nanotubes were tested as substitute for Carbon, due to enhanced stability, here, achieving the best results with carbon nanotubes [98]. An overview over several different cells is given in Table 4.1. It is essential to draw attention to the operating temperature, which lies, due to the moderate conductivity of the electrolytes used, in the majority of the cases above 150°C.

Cathodes

Similar approaches were taken designing cathode; Either metals like Bi [90,98] or Cu [90] were used, when assembling the cells in the discharged state. In the more frequent case of charged cells, multivalent metal fluorides were employed as cathodes. Various materials including CuF_2 [89, 91], BiF_3 [89, 92, 97], SnF_2 [89] or $KBiF_4$ [89] were tested in a pure form or in combination with the electrolyte used and Carbon, see Table 4.1. To achieve a complete mixing, the materials were milled in planetary mills leading to composite or solid solution cathodes. In the case of BiF_3, solid solution cathodes in combination with $La_{0.9}Ba_{0.1}F_{2.9}$ as electrolyte, achieved higher capacities (190 mAh/g) compared to the composite cathode (126 mAh/g) [89].

Lately, also the intercalation compounds La_2CoO_4 [95] and $La_2NiO_{4.13}$ [99] were reported as cathode materials with high cycling stability. In combination with $La_{0.9}Ba_{0.1}F_{2.9}$ as electrolyte and anodes, composed either of a mixture of Zn, ZnF_2, carbon black and $La_{0.9}Ba_{0.1}F_{2.9}$ or Pb, PbF_2 and carbon black, up to 220 cycles were possible, however, these cells were only charged up to a capacity of 30 mA h g^{-1} to conserve the whole system and operated again at high temperatures (170°C) [95, 99].

4.4 Side Reactions within Solid Systems

Side reactions on the electrode side are common. Rongeat *et al.* [90] observed the formation of $\beta - BiF_{3-2x}O_x$, when BiF_3 was used as cathode, or Cu_2O, in the case of CuF_2. Thieu *et al.* [91] detected metallic Cu from the CuF_2 cathode inside the solid electrolyte $La_{0.9}Ba_{0.1}F_{2.9}$, as well as the formation of LaOF at the La anode. Even more drastic issues were observed, when metals like Al or Ti were used as anode, allowing no discharge at all. In this case passivating oxide layer, present despite careful preparation, were assumed to hinder reactions [83]. A common issue, proposed by several authors [89, 90, 98] is the expansion and contraction of the materials upon cycling, leading to the irreversible loss of contact between electrodes and electrolyte, hence also hindering successful cycling.

4.5 Electrolytes used

4.5.1 Solid Electrolytes

The first rechargeable Fluorine-ion battery [89] relied on the solid electrolyte $La_{0.9}Ba_{0.1}F_{2.9}$. Due to the low conductivity of this material at room temperature, the cell had to be operated at high temperature ($\geq$150 °C). Nevertheless solid electrolytes are preferred anyway, as liquid systems, consisting of various compounds like a conducting salt and solvents, are far more complex.

While cathode as well as anode materials were investigated relatively extensive, the electrolyte of choice remained $La_{0.9}Ba_{0.1}F_{2.9}$ [83, 90–93, 95, 96, 98, 99]. $Ba_{0.7}Sb_{0.3}F_{2.3}$, the only other electrolyte reported (to my knowledge), in combination with Ce as anode turned out to be unstable [93]. Other materials like $La_{0.95}Sr_{0.05}F_{2.95}$ [83], $Ce_{0.97}Sr_{0.03}F_{2.97}$ [83, 100] or $Sm_{0.94}Ca_{0.06}F_{2.94}$ [101] were only theoretically investigated as electrolytes.

Fluorine ion conductors with higher ionic conductivity at room temperature, like $BaSnF_4$, which would make a cell operation at desired low temperatures possible, exist. However, being electrochemically unstable with high potential electrodes, these materials remained neglected until 2018, when Mohammad *et al.* [97, 102] reported on two different strategies, using $BaSnF_4$ as electrolyte. The first strategy is to use Zn and Sn as anode materials, representing low potential materials, hence being compatible with the electrolyte $BaSnF_4$. With Zn as anode 20 cycles with an initial capacity of 56 mA h g^{-1} at room temperature were obtained. As in the long term high potential electrodes have to be employed, Mohammad *et al.* [97] introduced $La_{0.9}Ba_{0.1}F_{2.9}$ as interlayer between $BaSnF_4$ and the Ce anode. This configuration enabled the operation of the cell at room temperature for 5 cycles with a capacity of 2.5 to 7 mA h·g^{-1} (theoretical capacity: 302 mA h·g^{-1}). The experiments showed that the introduction of interlayers at the electrolyte | electrode interface might pave the way for the usage of highly conductive, though less stable electrolytes.

4.5.2 Liquid Electrolytes

Liquid electrolytes posses a striking advantage compared to solid electrolytes; the conductivity is in general much higher, allowing the cell operation at room temperature. Besides a high conductivity, an electrolyte has to be soluble to a significant extent in commonly used solvents, must be stable against decomposition, and passivation of the electrodes should not occur [103]. Compared to Lithium based systems, it is much harder to find such electrolytes for FIB, as Fluorine is extremely reactive and furthermore metal fluorides are hardly soluble in common solvents [81].

Gschwind *et al.* [103] introduced ammonium bifluoride in a methylated polyethylen glycol matrix as electrolyte. It was possible to dissolve the electrolyte in a mixture of

acetonitril and dimethylcarbonate in a concentration of 0.05 M reaching conductivities of ≈3 mS cm^{-1} at room temperature. In combination with a BiF_3 composite cathode, a discharge with a specific capacity of 189 mA h g^{-1} (63% of the theoretical capacity) was possible. The incorporation of the electrolyte in a polymer matrix was again investigated with PEO600000 · NH_4F_2H [104]. All these cells were, however, only dischargeable once. Ethers were also found to be a suitable media to dissolve fluorine electrolytes [81, 104]. Bis(2,2,2 - trifluoroethyl)ether (BTFE) is able to dissolve neopentyl-substituted alkylammonium fluoride salt derivates to a sufficient extent reaching up to 10^{-2} S cm^{-1} at room temperature. Successful operation of the cell was possible for 8 cycles, here, it was stated that this was mainly due to the coating of the CuF_2 cathode particles with a thin layer of $La_{0.9}Ba_{0.1}F_{2.9}$, making it more resistant to the liquid electrolyte [81, 104].

4.6 Conclusion

All reported systems, either relying on solid or liquid electrolyte systems, suffer from several issues so far. The needed high temperature and the fast capacity fade due to irreversible reactions represent major obstructions. Even though the reason for the electrochemical instability was found in some studies, it remained relatively unexplored in others. Detailed reports on the electrochemical stability of the mainly used solid electrolyte $La_{0.9}Ba_{0.1}F_{2.9}$ were missing completely, therefore, it was the point of interest for our studies (see preface and the according publication 4.6).

Table 4.1: Overview of several different FIBs, reported in literature.

Anode	**Cathode**	**Electrolyte**	**Reported Cycles**	**Capacity [mAh g^{-1}]**	**Temperature [°C]**	**Further remarks**
Ce	**composite** CuF_2 + C + $La_{0.9}Ba_{0.1}F_{2.9}$ *30+10+60 wt%*	$La_{0.9}Ba_{0.1}F_{2.9}$	1	322 (61%)	150	discharged with 10 μA g^{-1} 2.6 V initially [89]
Ce	**composite** BiF_3 + C + $La_{0.9}Ba_{0.1}F_{2.9}$ *30+10+60 wt%*	$La_{0.9}Ba_{0.1}F_{2.9}$	1	126 (42%)	150	discharged with 10 μA g^{-1} 2.5 V initially [89]
Ce	**solid solution** BiF_3 + C + $La_{0.9}Ba_{0.1}F_{2.9}$ *30+10+60 wt%*	$La_{0.9}Ba_{0.1}F_{2.9}$	38	190 (63%)	150	discharged with 10 μA g^{-1} capacity down to 50 mAh g^{-1} after 38 cycles 2.15 V initially [89]
Ce	**composite** $KBiF_4$ + C *90+10 wt%*	$La_{0.9}Ba_{0.1}F_{2.9}$	1	177 (77%)	150	discharged with 10 μA g^{-1} 2.4 V initially [89]
Ce	**composite** SnF_2 + C *90+10 wt%*	$La_{0.9}Ba_{0.1}F_{2.9}$	1	183 (54%)	150	discharged with 10 μA g^{-1} 2.0 V initially [89]
Li	**composite** BiF_3 + C + $Ba_{0.6}La_{0.4}F_{2.4}$ *30+10+60wt%*	$Ba_{0.6}La_{0.4}F_{2.4}$	2	120	160	discharged with 4 mA g^{-1} 2.8 V initially [94]
Al, Ti	AlF_3, TiF_4, CoF_3, BiF_3, CuF_2, FeF_3, ZnF_2	Higlyme or tetragylme/NH_4F_2H (not clearly stated)	0	0	RT	no discharge possible [83]
Mn and Mn/C	AlF_3, TiF_4, BiF_3	Higlyme or tetragylme/NH_4F_2H (not clearly stated)	0	20-60	RT	discharged with 10 μA down to 0.1 V [83]

La	**composite** CuF_2 + $La_{0.9}Ba_{0.1}F_{2.9}$ + C *30+60+10 wt%*	$La_{0.9}Ba_{0.1}F_{2.9}$	23	360 (68%) (1st cycle), 40 (23rd cycle)	150	side reactions: diffusion of Cu into the electrolyte, formation of LaOF cycled with ± 4 mA g^{-2} [91]
composite CeF_3 + C *90+10 wt%*	Bi	$La_{0.9}Ba_{0.1}F_{2.9}$	2	1st charging 404 (105%) (4mA/g)	150	charged with 4 mA g^{-1} up to 4 V side reactions ($\beta - BiF_{3-2x}O_x$, BiF_5) [90]
solid solution CaF_2 + LaF_3 + C *54+36+10 wt%*	Bi	$La_{0.9}Ba_{0.1}F_{2.9}$	1	1st charging 406 (105%)	150	charged with 4 mA g^{-1} up to 4 V side reactions ($\beta - BiF_{3-2x}O_x$, BiF_5) drop to 5 mAh g^{-1} for discharge [90]
composite MgF_2 + $La_{0.9}Ba_{0.1}F_{2.9}$ + C *30+60+10 wt%*	Bi	$La_{0.9}Ba_{0.1}F_{2.9}$	only 1 charging	406 (105%)	150	charged with 4 mA g^{-1} up to 3.5 V side reactions assumed [90]
composite Mg + MgF_2 + $La_{0.9}Ba_{0.1}F_{2.9}$ + C *20+20+50+10 wt%*	Bi	$La_{0.9}Ba_{0.1}F_{2.9}$	50	266 (1st charge) (69%)	150	cycling between 1.4 and 3.2 V with ± 4 mA g^{-2} sharp decay of capacity formation of $\beta - BiF_{3-2x}O_x$ [90]
composite Mg + MgF_2 + $La_{0.9}Ba_{0.1}F_{2.9}$ + C *20+20+50+10 wt%*	Cu	$La_{0.9}Ba_{0.1}F_{2.9}$	20	390 (16%)	150	cycling between 1.4 and 3.5 V with ± 4 mA g^{-1} sharp decay of capacity formation of Cu_2O [90]
composite Bi + $La_{0.9}Ba_{0.1}F_{2.9}$ + C *30+60+10 wt%*	**composite** MgF_2 + $La_{0.9}Ba_{0.1}F_{2.9}$ + SnO_2 *30+60+10 wt%*	$La_{0.9}Ba_{0.1}F_{2.9}$ (thin film $\approx 10\mu$m)	30	242 (63%)	160	cycled with 4 mA g^{-2} drop to $\approx$30 mA h g^{-1} after 30 cycles [98]
composite Bi + $La_{0.9}Ba_{0.1}F_{2.9}$ + C *30+60+10 wt%*	**composite** MgF_2 + $La_{0.9}Ba_{0.1}F_{2.9}$ + ITO *30+60+10 wt%*	$La_{0.9}Ba_{0.1}F_{2.9}$ (thin film $\approx 10\mu$m)	30	268 (70%)	160	cycled with 4 mA g^{-2} drop to $\approx$40 mA h g^{-1} after 30 cycles [98]

composite $Bi + La_{0.9}Ba_{0.1}F_{2.9} + C$ *30+60+10 wt%*	**composite** $CaF_2 + La_{0.9}Ba_{0.1}F_{2.9}$ + ITO *30+60+10 wt%*	$La_{0.9}Ba_{0.1}F_{2.9}$ (thin film $\approx 10\mu$m)	30	307 (80%)	160	cycled with 4 mA g^{-2} drop to 49 mA h g^{-1} after 30 cycles [98]
composite $Bi + La_{0.9}Ba_{0.1}F_{2.9} + C$ *30+60+10 wt%*	**composite** $CaF_2 + La_{0.9}Ba_{0.1}F_{2.9}$ + Carbon Nanotubes *30+60+10 wt%*	$La_{0.9}Ba_{0.1}F_{2.9}$ (thin film $\approx 10\mu$m)	30	317 (82%)	160	cycled with 4 mA g^{-2} drop to 67 mA h g^{-1} after 30 cycles [98]
composite Zn + c-$BaSnF_4$ + Carbon Nanotubes *50+40+10 wt%*	**composite** BiF_3 + Carbon Nanotubes + t-$BaSnF_4$ *40+10+50 wt%*	t-$BaSnF_4$	10	213	150	cycled with 40 μA g^{-2} rapid capacity fade [102]
composite Sn + c-$BaSnF_4$ + Carbon Nanotubes *50+40+10 wt%*	**composite** BiF_3 + Carbon Nanotubes + t-$BaSnF_4$ *40+10+50 wt%*	t-$BaSnF_4$	10	281 (93%)	150	cycled with 20 μA g^{-2} decay of capacity down to 138 mA h g^{-1} in cycle 10 [102]
composite Ce + Carbon Nano Tubes *90+10 wt%*	**compsite** $Ba_{0.7}Sb_{0.3}F_{2.3}$ + Carbon Nanotubes *90+10 wt%*	$La_{0.9}Ba_{0.1}F_{2.9}$	5	301 (66%)	150	cycled with 10 μA g^{-2} rapid capacity fade [93]
composite $Ce + La_{0.9}Ba_{0.1}F_{2.9}$ + Carbon Nanotubes *50+40+10 wt%*	**composite** BiF_3 + $BaSnF_4$ + Carbon Nanotubes *40+50+10 wt%*	t-$BaSnF_4$ (+ $La_{0.9}Ba_{0.1}F_{2.9}$ between anode and electrolyte)	5	251 (83%)	150	cycled with 10 μA g^{-2} quick capacity fade down to 119 mA h g^{-1} after 5 cycles [97]
composite $PbF_2 + Pb + C$ *45+45+10 wt%*	**composite** $\underline{La_2CoO_4} + La_{0.9}Ba_{0.1}F_{2.9} + C$ *30+60+10 wt%*	$La_{0.9}Ba_{0.1}F_{2.9}$	50	30 (45%)	170	cell initially charged up to 65 mA h g^{-1} charging with 10 μA g^{-2} discharging with -1 μA g^{-2} slow capacity fade conversion of the intercalation material La_2CoO_4 to $La_2CoO_4F_y$ during charging (expansion in c-axis) [95]

composite Zn + ZnF_2 + C + $La_{0.9}Ba_{0.1}F_{2.9}$ *20+20+10+50 wt%*	**composite** $La_2NiO_{4.13}$ + $La_{0.9}Ba_{0.1}F_{2.9}$ + Carbon Nanotubes *30+60+10 wt%*	$La_{0.9}Ba_{0.1}F_{2.9}$	220	30	170	initial charging with 30 mA h g^{-1} charging with 24 $\mu A\,g^{-2}$ discharging with -5.0 $\mu A\,g^{-2}$ [99]
composite Ce + $La_{0.9}Ba_{0.1}F_{2.9}$ + Carbon Nanotubes *50+40+10 wt%*	**composite** BiF_3 + $BaSnF_4$ + Carbon Nanotubes *40+50+10 wt%*	t-$BaSnF_4$ (+ $La_{0.9}Ba_{0.1}F_{2.9}$ between anode and electrolyte)	5	27	RT	cycled with 10 $\mu A\,g^{-2}$ rapid capacity fade, however, cycling not possible with $BaSnF_4$ or $La_{0.9}Ba_{0.1}F_{2.9}$ alone [97]
composite Sn + c-$BaSnF_4$ + Carbon Nanotubes *50+40+10 wt%*	**composite** BiF_3 + Carbon Nanotubes + t-$BaSnF_4$ *40+10+50 wt%*	t-$BaSnF_4$	10	120 (40%)	RT	cycled with 10 $\mu A\,g^{-2}$ fast decay of capacity [102]
composite Zn + c-$BaSnF_4$ + Carbon Nanotubes *50+40+10 wt%*	**composite** BiF_3 + Carbon Nanotubes + t-$BaSnF_4$ *40+10+50 wt%*	t-$BaSnF_4$	20	56	RT	cycled with 10 $\mu A\,g^{-2}$ capacity stable (activation of Zn particles?) [102]

Preface:

Fluoride-Ion Batteries: On the Electrochemical Stability of Nanocrystalline $La_{0.9}Ba_{0.1}F_{2.9}$ Against Metal Electrodes

In numerous publications mostly during the last years, but also back in the 20^{th} century, galvanic cells with F^- as the active species were reported [83, 90–96, 99]. In a rather short research period, $La_{1-x}Ba_xF_{3-x}$ (x = 0.1) was preferentially chosen as solid state electrolyte in FIB. Contrary to LIB, where the electrochemical stability of a new (solid state) electrolyte is tested basically immediately after synthesis, this aspect was neglected when it comes to $La_{0.9}Ba_{0.1}F_{2.9}$ and solid electrolytes for FIB in general. Mainly the fact that no reference electrode for cyclic voltammetry (CV) is existing, imposes difficulties when interpreting the gained voltammogram.

The idea behind this research topic was to make first steps into testing the electrochemical stability of a solid electrolyte via CV in a two electrode set-up. It was immediately clear that $La_{0.9}Ba_{0.1}F_{2.9}$, the commonly used electrolyte, is the material of interest. Due to previous publications and work with this compound, synthesis as well as basic characterization was easy to obtain. Close attention, however, had to be paid setting up the CV experiments. It was for example necessary to test the influence of different sizes of working electrodes, besides tackling problems like the introduction of parasitic current to the set-up, originating from the oven, to accomplish sufficiently low scan rates.

We demonstrated that in the broad range of tested metal electrodes (Ni, Pt, Au, Ag, Cu), no material was stable in contact with nano-crystalline $La_{0.9}Ba_{0.1}F_{2.9}$. Migration processes, as well as side-reactions at the metal | electrolyte interface were found to pose severe problems in most electrodes, whereby Ni was found to be the most promising candidate, as it might form a stable passivating layer. Overall this manifests the high reactivity of F^- and the need for finding stable diffusion layers to make FIBs a competitive system in the future.

Author Contributions: M.G. and V.P. carried out the synthesis, XRPD and impedance spectroscopy. M.G. and I.H. set up the parameters for CV. M.G. carried out CV, analysed the data and wrote the publication. H.M.R.W. supervised and completed the publication.

For a detailed study of F anion transport in this material, see also:

Heterogeneous F anion transport, local dynamics and electrochemical stability of nanocrystalline $La_{1-x}Ba_xF_{3-x}$
S. Breuer, M. Gombotz, V. Pregartner, I. Hanzu, H. M. R. Wilkening
Energy Storage Materials, Vol. 16, 2018, p. 481-190, DOI: 10.1016/j.ensm.2018.10.010

P4

Fluoride Ion Batteries: On the Electrochemical Stability of Nanocrystalline $La_{0.9}Ba_{0.1}F_{2.9}$ Against Metal Electrodes

M. Gombotz*, V. Pregartner, I. Hanzu and H. M. R. Wilkening*

Nanomaterials, 2019, Vol. 9, 1517 (DOI: 10.3390/nano9111517)

nanomaterials

MDPI

Article

Fluoride-Ion Batteries: On the Electrochemical Stability of Nanocrystalline $La_{0.9}Ba_{0.1}F_{2.9}$ against Metal Electrodes

Maria Gombotz [1,*], Veronika Pregartner [1], Ilie Hanzu [1,2,*] and H. Martin R. Wilkening [1,2]

[1] Institute for Chemistry and Technology of Materials, Technical Universtiy of Graz, Graz 8010, Austria; veronika.pregartner@tugraz.at (V.P.); wilkening@tugraz.at (H.M.R.W.)

[2] ALISTORE—European Research Institute, CNRS FR3104, Hub de l'Energie, Rue Baudelocque, 80039 Amiens, France

* Correspondence: gombotz@tugraz.at (M.G.); hanzu@tugraz.at (I.H.)

Received: 27 September 2019; Accepted: 23 October 2019; Published: 25 October 2019

Abstract: Over the past years, ceramic fluorine ion conductors with high ionic conductivity have stepped into the limelight of materials research, as they may act as solid-state electrolytes in fluorine-ion batteries (FIBs). A factor of utmost importance, which has been left aside so far, is the electrochemical stability of these conductors with respect to both the voltage window and the active materials used. The compatibility with different current collector materials is important as well. In the course of this study, tysonite-type $La_{0.9}Ba_{0.1}F_{2.9}$, which is one of the most important electrolyte in first-generation FIBs, was chosen as model substance to study its electrochemical stability against a series of metal electrodes viz. Pt, Au, Ni, Cu and Ag. To test anodic or cathodic degradation processes we carried out cyclic voltammetry (CV) measurements using a two-electrode set-up. We covered a voltage window ranging from −1 to 4 V, which is typical for FIBs, and investigated the change of the response of the CVs as a function of scan rate (2 mV/s to 0.1 V/s). It turned out that Cu is unstable in combination with $La_{0.9}Ba_{0.1}F_{2.9}$, even before voltage was applied. The cells with Au and Pt electrodes show reactions during the CV scans; in the case of Au the irreversible changes seen in CV are accompanied by a change in color of the electrode as investigated by light microscopy. Ag and Ni electrodes seem to suffer from contact issues which, most likely, also originate from side reactions with the electrode material. The experiments show that the choice of current collectors in future FIBs will become an important topic if we are to develop long-lasting FIBs. Most likely, protecting layers between the composite electrode material and the metal current collector have to be developed to prevent any interdiffusion or electrochemical degradation processes.

Keywords: solid fluoride electrolytes; ceramics; LaF_3; fluorine-ion batteries; metal current collectors; electrochemical stability; cyclic voltammetry

1. Introduction

Lithium-ion batteries are by far the most widely used electrochemical energy storage systems. Since this battery technology starts to suffer from several issues, such as the exploitation of cobalt or nickel mines [1] in geopolitical disputed regions, alternative systems gain more and more importance. One of these alternate post-lithium systems, besides the development of sodium-ion batteries [2], relies on fluorine anions as the electrochemically active species.

The first explicit reference of a highly conducting F-bearing solid-state electrolyte, namely PbF_2, was already in 1834 by Michael Faraday [3,4], who discovered ionic conduction in AgI and PbF_2, see refs. [5,6] for an overview. In 1921, Carl Tubandt measured transference numbers of a series of solid electrolytes including PbF_2 [7]. It then took several decades until 1971 when Baukal [8]

and 1976 when Kennedy et al. [9] and Schoonman [10] constructed the first fluoride thin-film galvanic cells, see also refs. [11,12]. In 2011 Reddy et al. [13] revived the topic with a closer investigation of possible cathode materials [14–16], whereby $La_{0.9}Ba_{0.1}F_{2.9}$, see also ref. [17], was chosen as solid state electrolyte due to its high conductivity of 2.8×10^{-4} S cm^{-1} at 160 °C. Also polymer matrix [18] and liquid electrolytes [19] were investigated. Recently, several studies concerning various anode [20,21] and cathode materials [22] appeared; their suitability and performance have always been investigated in combination with $La_{0.9}Ba_{0.1}F_{2.9}$ as the ceramic electrolyte of choice. To the best of our knowledge, no detailed studies concerning the electrochemical stability of solid-state fluoride electrolytes against metallic current collectors have been reported yet, neither of $La_{0.9}Ba_{0.1}F_{2.9}$ nor of other F^- conductors such as $Ba_{0.7}Sb_{0.3}F_{2.3}$, which is not stable against Ce as anode material [23], $Ce_{1-x}Sr_xF_{3-x}$ ($0 \leq x < 0.15$) [24] or $Sm_{1-x}Ca_xF_{3-x}$ ($0.05 \leq x < 0.15$) [25]. Since a solid-state electrode must also contain a certain amount of (solid) electrolyte, it is important and meaningful to evaluate the stability of the electrolyte with respect to the current collector material.

In the course of this study, the electrochemical stability of nanocrystalline $La_{0.9}Ba_{0.1}F_{2.9}$, synthesized following a mechanochemical route, was examined by cyclic voltammetry (CV). Prior to our stability tests we checked the purity of the tysonite phase via X-ray powder diffraction and carried out electrochemical impedance spectroscopy (EIS) to determine its F ionic conductivity. The crystal structure of $La_{0.9}Ba_{0.1}F_{2.9}$ is illustrated in Figure 1. Here, we investigated the electrochemical stability of $La_{0.9}Ba_{0.1}F_{2.9}$ in combination with various metal electrodes namely Cu, Ag, Au, Pt and Ni, which were applied to the compacted electrolyte pellets by direct current sputtering.

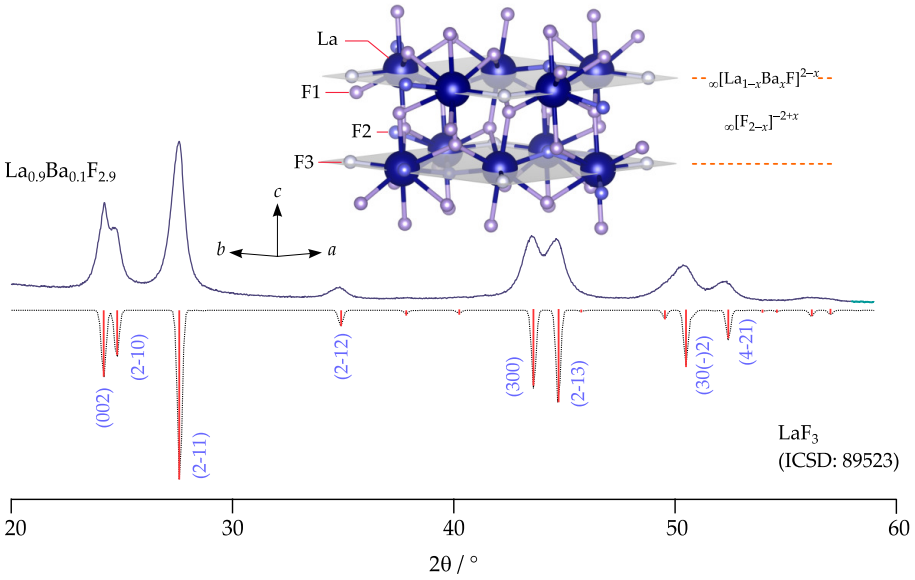

Figure 1. X-ray powder diffractogram of mechanosynthesized, nanocrystalline $La_{0.9}Ba_{0.1}F_{2.9}$; the pattern was recorded at room temperature and ambient atmosphere. It is compared to that of LaF_3, which serves as a reference (ICSD: 89523, $P\bar{3}c1$); LaF_3 crystallizes with the well-known tysonite structure providing three different F sites labeled F1 (12*g*), F2 (4*d*) and F3 (2*a*). Each site is fully occupied by fluorine anions. F1 anions reside in the $_\infty[F_{2-x}]^{-2+x}$ interslabs and are located in distorted La_4 tetrahedra.

Usually, electrochemical stability of electrolytes is tested via CV in a three electrode set-up. As fluorine is not solid at ambient conditions, it cannot easily serve as a reference electrode, which makes the interpretation of the CV results obtained from a two electrode set-up, as applied here, rather difficult [26]. We also varied the size of the working electrode (WE); diameters were varied from 2.5 to 8 mm, to find out whether it has any influence on the results. Our CV measurements cover a voltage window from −1 to 4 V. This voltage window is similar to that used in earlier reports (1 to 3.5 V [13] and 0 to 3.5 V [22]). Compared to a recently published study [27] on $La_{0.9}Ba_{0.1}F_{2.9}$,

where we carried out CV at a rate of 100 mV/S, here we reduced the scan rate to 2 mV/s. Screening of five different metal electrode materials offers a quite diverse picture and highlights the reactivity of fluorine-containing electrolytes, as in none of the electrolyte/electrode configurations a stable electrochemical state could be achieved under the conditions mentioned above.

2. Materials and Methods

2.1. Mechanochemical Synthesis

Nanostructured $La_{0.9}Ba_{0.1}F_{2.9}$ was mechanosynthesized with the help of a high-energy planetary mill (Fritsch Pulverisette 7 Premium line, Fritsch GmbH, Idar-Oberstein, DE). For this purpose, stoichiometric amounts of the educts viz. LaF_3 (99.99%, Alfa Aesar, Kandel, DE) and BaF_2 (99.99%, Sigma Aldrich, Darmstadt, DE) were loaded into a ZrO_2 milling beaker with a volume of 45 mL. We added 180 balls made of the same material; the diameter of each milling ball was 5 mm. The milling procedure was carried out at a rotation speed of 600 rpm; the mixture was milled for 10 h whereby 15 min milling was followed by a break of 15 min to allow cooling of the mixture and the beaker. Loading as well as unloading of the beakers was strictly carried out under inert atmosphere; we used an Ar-filled glovebox (O_2, $H_2O < 0.5$ ppm) to avoid any contamination by water vapor or moisture.

2.2. X-Ray Powder Diffraction

The powdered sample was analyzed by X-ray powder diffraction (XRPD) to ensure that the educts have fully been transformed to $La_{0.9}Ba_{0.1}F_{2.9}$ crystallizing, as LaF_3 does, in the tysonite phase. Diffractogramms were recorded with a Bruker D8 Advance diffractometer operating with Bragg Brentano geometry and CuKα radiation (1.5406 Å). XRPD reflections were recorded over a 2θ range of 10 to 100°2θ (stepsize 0.02°2θ, 1 s measuring time per step). With the aid of the program X-PertHighScorePlus (PANalytical, Malvern, UK) we analyzed the diffractogramms according to the refinement procedure introduced by Rietveld.

2.3. Broadband Impedance Spectroscopy

The ionic conductivity of the as-prepared $La_{0.9}Ba_{0.1}F_{2.9}$ was checked by solid-state impedance spectroscopy. Hence, the powder samples were pressed to cylindrical pellets with a diameter of 5 mm and a thickness of ca. 1 mm; we used a press of P. O. Weber and applied a uniaxial force of 0.5 t. Ion blocking Pt electrodes with a thickness of 100 nm were applied on both sides of the pellet by sputtering (Leica sputter device (EM SCD050, Leica Microsystems, Wetzlar, DE)). Impedance data were recorded with a Novocontrol Concept 80 broadband spectrometer in combination with an active BDS 1200 cell [28] and a ZGS interface (Novocontrol). Impedance data were recorded over a frequency range from 10^{-2} Hz to 10^{7} Hz at temperatures ranging from 20 to 200 °C. A QUATRO cryo-system (Novocontrol, Montabaur, DE) controlled the temperature of all measurements, which were carried out under a constant flow of dry, freshly evaporated N_2 gas.

2.4. Cyclic Voltammetry

For all-solid-state cyclic voltammetry measurements approximately 120 mg of the sample powder were pressed into cylindrical pellets with a diameter of 8 mm. After uni-axial pressing (0.4 t) the thickness of the pellets ranged from 0.9 to 1 mm. As reference and counter electrode (CE) different materials of high purity (Au, Ag, Cu, Pt, Ni) were sputtered on one complete side of the pellets. We studied pellets equipped with sputtered working electrodes (Leica, EM SCD050) of the following diameters *d*: 2.5, 4, 6 and 8 mm. Again, all preparation steps were carried out in a glovebox filled with Ar (H_2O, $O_2 < 0.5$ ppm). The sample chamber of the sputter device was purged with Ar 5.0 for five times before the sputter process was started to avoid any contamination with moisture or O_2. Cyclic voltammetry was performed with a Parstat MC potentiostat (Princeton Applied Research) equipped with a low-current option. We carried out all measurements at a temperature of 200 °C in a cell,

which was continuously purged with N_2. Scanning rates ranged from 0.002 to 0.1 V/s whereby the voltage was varied from −1 V to 4 V. A schematic drawing of the cell set-up is shown in Figure A1.

2.5. Scanning Electron Microscopy

The surface of the pellets (Ag and Au as electrode, working electrode $d = 2.5$ mm) before and after CV were investigated by digital light microscopy (Di-Li Digital-Mikroskop, TCapture) and by scanning electron microscopy (SEM, VEGA3 TESCAN), in both the secondary electron (SE) and backscattered electron (BSE) mode. SEM was combined with energy dispersive X-ray spectroscopy (EDX) to analyze the elemental distribution at the electrode/electrolyte interface. IGOR Pro (Wavemetrics) software was used for data analysis.

3. Results and Discussion

The phase purity of the mechanosynthesized $La_{0.9}Ba_{0.1}F_{2.9}$ sample was verified by XRPD. The diffractogram, which is depicted in Figure 1, is composed of broad reflections due to the small grain size obtained after the milling process. According to Scherrer's equation we estimate that the mean crystallite diameter is in the order of 10 to 20 nm; a similar result has been reported recently for the same material [27]. XRPD reveals that the solid solution crystallizes with the tysonite structure of LaF_3 (ICSD: 89523). Lattice constants, slightly deviating from that of Ba-free LaF_3, point to successful incorporation of the Ba^{2+} ions. Conductivity spectroscopy revealed that, as expected for the electrolyte $La_{0.9}Ba_{0.1}F_{2.9}$, the ionic conductivity at a temperature of 200 °C was $\sigma'(\nu \rightarrow 0) \equiv \sigma_{DC} = 2.36 \times 10^{-4}$ S/cm. This value can be directly read off from the conductivity isotherms, which are shown in Figure 2 alongside with the Arrhenius plot of $\sigma_{DC}T$ vs. $1000/T$. For selected temperatures, viz. for 20, 100 and 200 °C the data are also shown using the representation according to Nyquist [29]. The conductivity isotherms shown here perfectly agree with those published earlier by our group, see Breuer et al. [27]. For a general discussion and interpretation of conductivity data we refer to the literature [29–31].

To evaluate the compatibility of the electrolyte with a range of current collector materials, the various metals were applied on both sides of the cylindrical pellets by sputtering. As the reaction of interest is supposed to occur at the working electrode, we took into account that the current flow at the working electrode should, in principle, never be limited by the current flow passing through the reference/counter electrode. In classical liquid-based electrochemistry, this condition is achieved by using a counter electrode with a much larger surface than that of the working electrode. This condition is much more difficult to achieve in the solid state. However, here we investigated the influence of the size of the working electrode and varied it from 2.5, 4, 6 to 8 mm; the latter diameter corresponds to the full size of the surface of the pellet.

Except for Cu, all electrode materials were sputtered with success and did not show any direct reaction with the electrolyte. However, in the case of the Cu electrode we noticed a silver colored surface directly after the sputtering process. Irrespective of this change in color, we took a pellet with a working electrode of 2.5 mm in diameter, which was subjected to CV. CV measurements resulted in a noisy signal due to contact problems, as it is shown in Figure A2a. At a potential E larger than 2 V we notice electrochemical reactions, at least at very low scan rates of 2 mV/s. The corresponding maximum current amplitude is relatively small and turned out to be in the order of 0.6 µA at $E = 4$ V. Additionally, inspection by light microscopy revealed a diffuse region with coppery color between the actual electrode and pure $La_{0.9}Ba_{0.1}F_{2.9}$, see Figure A2b.

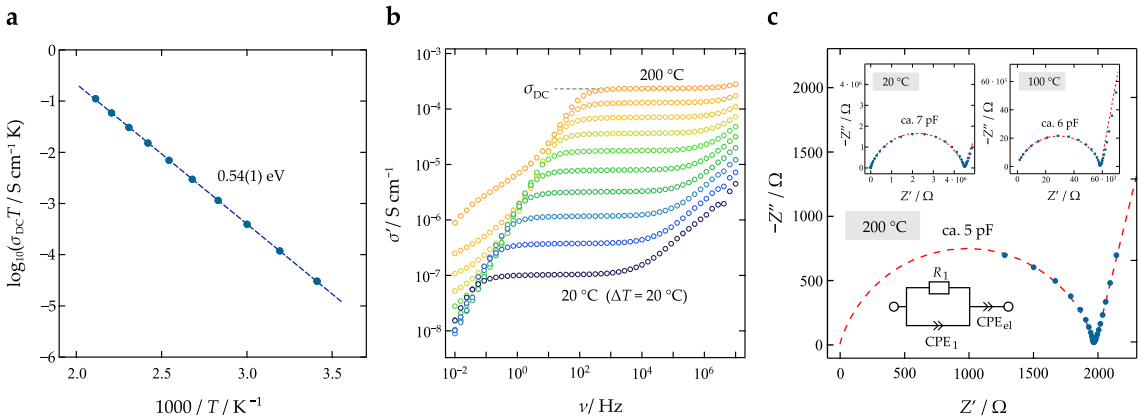

Figure 2. (**a**) Arrhenius Plot of the ionic conductivity σ_{DC} multiplied with absolute temperature T vs. $1000/T$ of nanocrystalline $La_{0.9}Ba_{0.1}F_{2.9}$ that was prepared by a mechanochemical approach. (**b**) Conductivity isotherms of $La_{0.9}Ba_{0.1}F_{2.9}$ starting from 20 °C and ending at 200 °C, which was the highest temperature where we measured conductivities. (**c**) Nyquist representation of the complex impedance data of $La_{0.9}Ba_{0.1}F_{2.9}$; the curve refers to a temperature of 200 °C and shows the imaginary part of the complex impedance $-Z''$ plotted vs. the real part Z'. The inset shows additionally the Nyquist representation at temperatures of 20 °C and 100 °C. The spike at low frequencies represents electrode polarization effects originating from the ion-blocking electrodes used. The whole location curve was parameterized with the equivalent circuit shown in the inset. It consists of a resistor R_1 connected in parallel to a constant phase element (CPE); this R_1-CPE_1 element represents the overall (bulk) semicircle and leads to an associated capacitance C [32,33] of ∼5 pF, which is a typical value for electrical relaxation taking place in the interior regions of the grains [29]. Another CPE element, connected in series, was used to approximate electrode polarization.

Similar results were found for the Ag electrode. From visual inspection the electrode appeared to have not reacted with the electrolyte; CV, however, points to irreversible changes, as is documented in Figure A2c. During cycling the electrode also suffered from contact issues and changed color from silvery to orange. Below $E = 4$ V the current amplitude did not exceed values above 5 µA; thus larger as in the case of the Cu electrode. Hence, we investigated the electrode and the surface of the electrolyte via light microscopy, SEM and EDX line scanning (see Figure 3). Changes in color at the Ag | $La_{0.9}Ba_{0.1}F_{2.9}$ interface are clearly visible in Figure 3, which shows SEM images of the surface before (Figure 3a) and after cycling (Figure 3d). SEM images taken in SE mode, see (Figure 3b) and (Figure 3e), indicate that the original clear border between the electrode and the ternary fluoride $La_{0.9}Ba_{0.1}F_{2.9}$ became more diffuse. Presumably, migration of Ag is responsible for this observation. To prove this assumption EDX linescans across the interface (as indicated by the horizontal bars in (Figure 3b) and (Figure 3e)) were performed. The results from before (Figure 3c) and after CV (Figure 3f) indeed reveal a trend in Ag distribution. While the concentration of Ag on the reference surface falls away sharply at the Ag | $La_{0.9}Ba_{0.1}F_{2.9}$ interface, after the CV measurements it does not. Therefore, we conclude that Ag migrates in the material, visibly over the surface during cycling. Ag migration leads to irreversible changes at this interface.

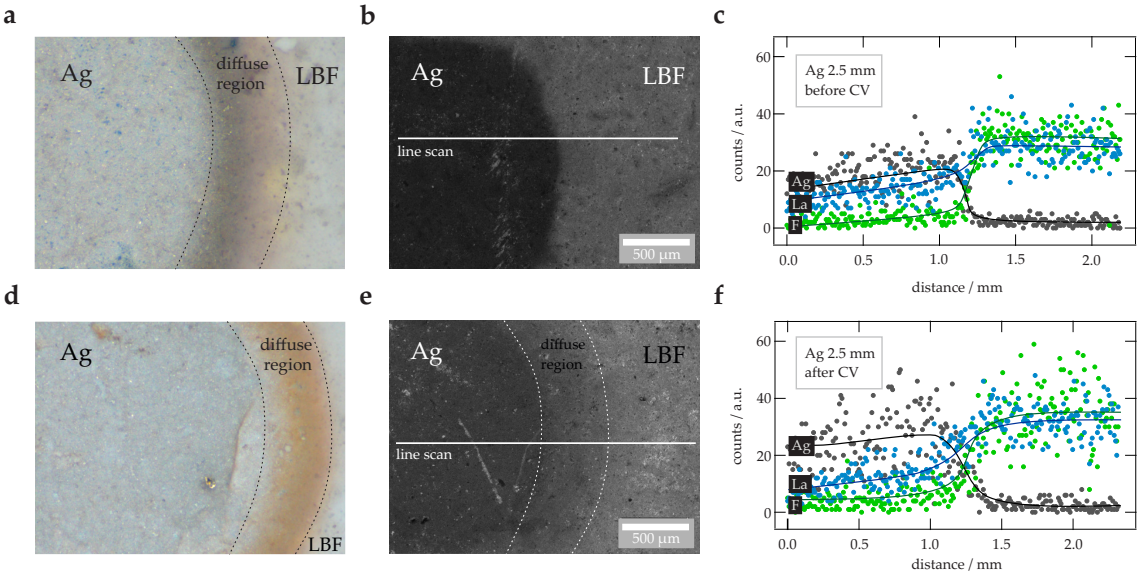

Figure 3. (**a**) Images acquired by digital light microscopy of a sample pellet with Ag as working electrode ($d = 2.5$ mm) *before* the cyclic voltammetry (CV) measurements have been carried out. (**b**) SEM image (secondary electron (SE) detector) of this pellet before CV. The horizontal line indicates the run of the energy dispersive X-ray spectroscopy (EDX) line scan. (**c**) EDX line scan across the surface of the pellet, as depicted in (**b**), for the elements F, Ag and La. The lines are only a guide for the eye. (**d**) Image obtained via digital light microscopy of a sample pellet with Ag working electrode *after* CV. (**e**) SEM image (SE detector) of the sample pellet with Ag as working electrode, the image was taken after the CV measurements. The horizontal line indicates the run of the (EDX) line scan. (**f**) EDX line scan across the surface of the pellet, as depicted in (b), for the elements F, Ag and La, respectively The lines are drawn to guide the eye.

In Figure 4a,b CVs of the symmetrical cell Au | $La_{0.9}Ba_{0.1}F_{2.9}$ | Au, recorded in a voltage window of -1 to 4 V and scan rates ranging from 2 mV/s to 0.1 V/s, are shown. The corresponding images from light microscopy are depicted in Figure 5. In the cyclic voltamogram with the WE having a size of 2.5 mm, see (a), distinct anodic and cathodic peaks are visible at a scan rate of 2 mV/s. Two anodic peaks (positive direction of scanning) are clearly visible and also two less apparent cathodic peaks show up in the negative direction of scanning. The main anodic peak at $E = 3$ V, whose counterpart is visible at a faster scan rate of 10 mV/s at ca. $E = 0.6$ V. Most likely, these peaks reveal the formation (and decomposition) of AuF_3 at the Au | $La_{0.9}Ba_{0.1}F_{2.9}$ interfaces. With increasing cycling, i.e., with increasing Au interdiffusion (see below), the shape of the CVs changes. At scan rates of 50 and 100 mV/s anodic and cathodic peaks at lower voltages appear indicating the irreversibly change of the interface on its electrochemical behavior. The maximum current amplitude that is reached at a scan rate of 100 mV/s is approximately 8 µA at ca. $E = 2.1$ V.

The first cycle of a pellet with a diameter of the working electrode of 8 mm is depicted in Figure 4f. When compared with the CV recorded using a disc with $d = 2.5$ mm, similarities can be seen. Again, two peaks in the positive direction occur. In contrast, no cathodic peaks are visible in this case. This trend continues when going to higher scan rates, see Figure 4e,f, as the curves do not reveal any peaks at E lower than 2 V but current responses as high as 3 µA when E reaches 3.5 V. CV's for WE diameters of 4 and 6 mm are shown for the sake of brevity in the Appendix A, see Figure A3a,d, as no major differences compared to a WE diameter of 2.5 mm are recognizable. If we take for example a look on Figure 4, where Au is used as electrode material, a small scan rate results in a small current for a WE diameter of 2.5 mm and the current is increasing with the scan rate. The opposite trend is, however, visible for a WE diameter of 8 mm; the corresponding current is decreasing with the scan rate. The difference in behavior between the 2.5 mm WE and the 8 mm WE can be traced back to the influence of the CE. As mentioned in the experimental section, the CE electrode is covering one entire

side of the pellet (8 mm in diameter) and only the diameter of the WE is varied. For a 2.5 mm WE with an 8 mm CE the ratio between the surface areas is higher than 1:10. A large surface area of the CE with respect to the WE is necessary whenever a 2-electrode cell configurations is used to ensure that the current through the cell is limited by the WE, then the influence of the CE would be small. This is, however, not the case when 8 mm working electrodes are used, the WE:CE surface area ratio is 1:1. Thus, in this case, the CE would show a significant influence on the current response of the cell, as seen in Figure 4.

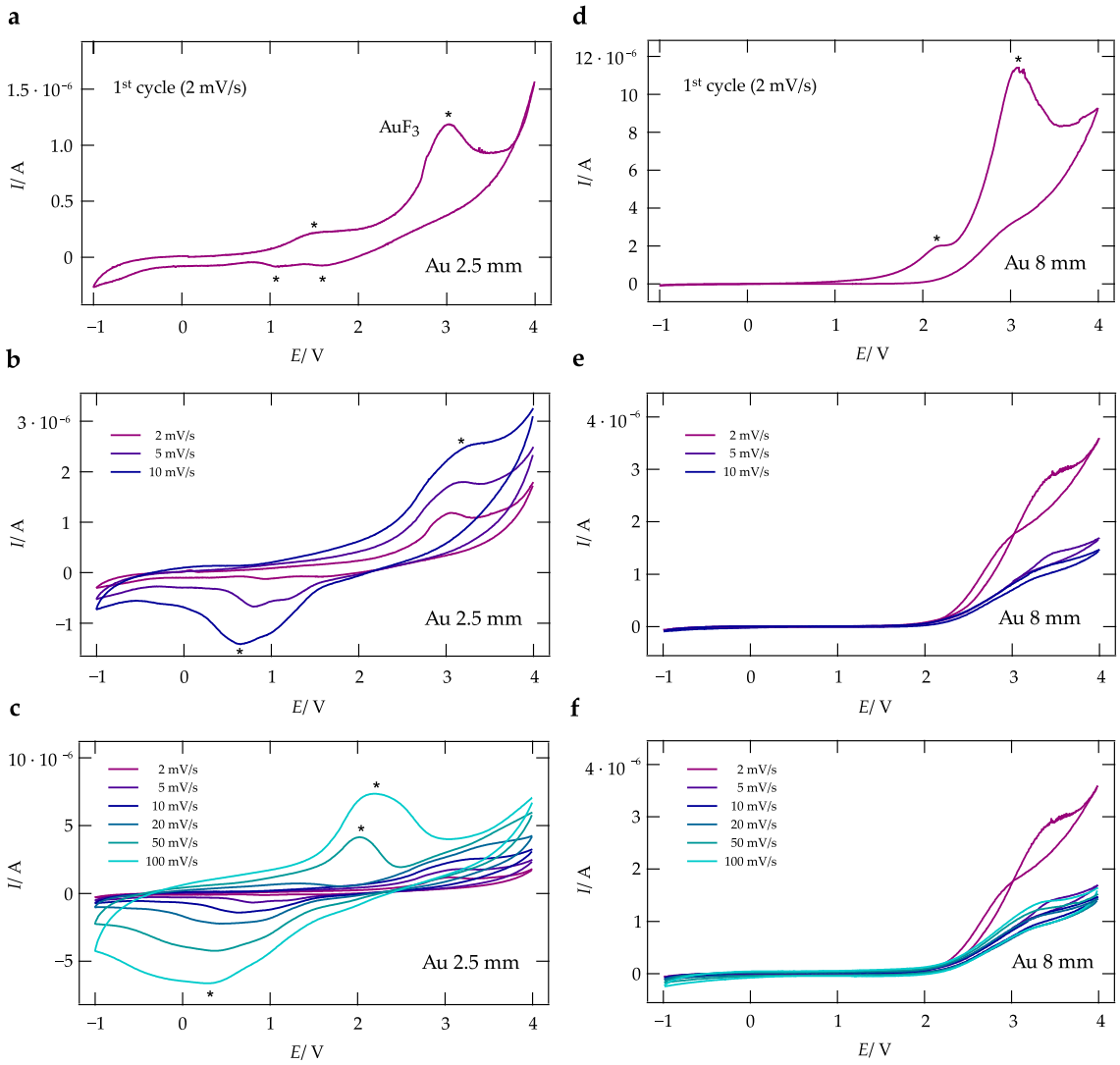

Figure 4. Cyclic voltamogram of cells with $La_{0.9}Ba_{0.1}F_{2.9}$ as solid electrolyte and Au working as electrode metal. The CVs were recorded at a temperature of 200 °C, with scan rates ranging from 2 mV/s up to 0.1 V/s; working electrode diameters are 2.5 mm (**a**–**c**) and 8 mm (**d**–**f**). The current response of the first cycles are shown in (**a**,**d**).

Similarly to our observations with Ag as electrode, investigations of the Au | $La_{0.9}Ba_{0.1}F_{2.9}$ interface by light microscopy revealed a color change at the border of the two phases (see Figure 5a,d). The change is seen after the CV measurements have been carried out, hence during cycling Au interdiffuses into the electrolyte phase. This observation is independent of the diameter of the working electrode used. Au interdiffusion is also supported by SEM images, using either the SE or the BSE detector. The originally clear border between the materials (Figure 5b) has become blurred (Figure 5e). EDX line scans across the border carried before and after cycling (Figure 5c,f) underpin our conclusion of Au migration as the distribution function of the elements changes from a step-like shape to a

sigmoid-like one. In particular, also the F concentration profile (and the La profile as well) smears out, which indicates the formation of binary Au-F compounds, possibly tysonite-type $La_{1-x}Au_xF_3$.

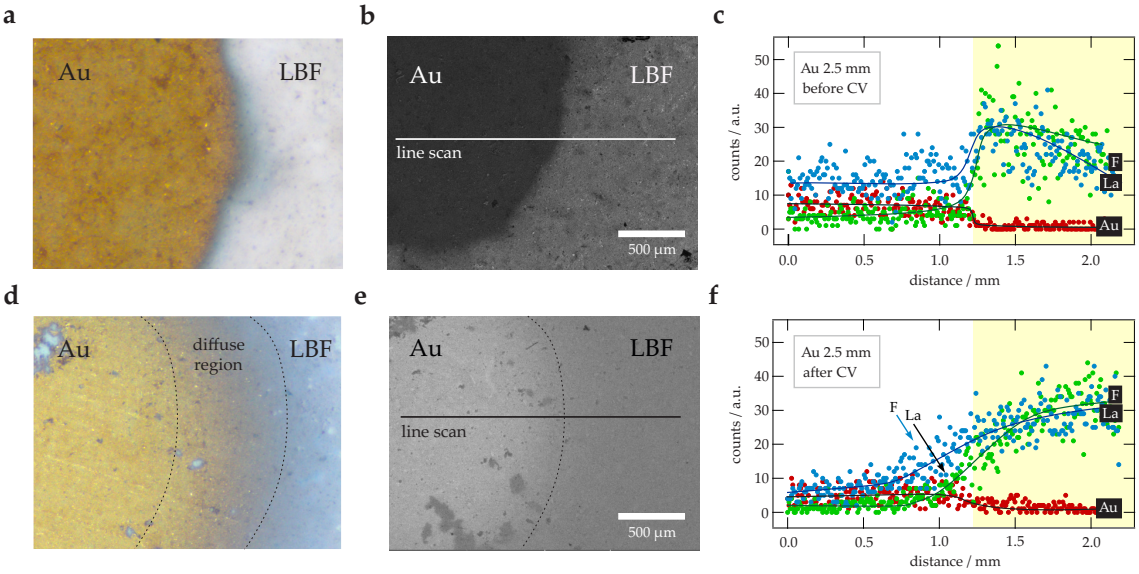

Figure 5. (**a**) Digital light microscopy image of a sample pellet with Au working electrode ($d = 2.5$ mm) before the CV measurements were carried out. (**b**) SEM image (SE detector) of the sample pellet with the Au working electrode *before* CV. The horizontal line indicates the run of the EDX line scan. (**c**) EDX line scan across the surface of the pellet, as depicted in (**b**), for the elements F, Au and La. The lines are only a guide to the eye. (**d**) Image taken by digital light microscopy of the cell *after* CV. (**e**) SEM image (backscattered electron (BSE) detector) of the cell with Au electrodes *after* the CV measurements. The horizontal line indicates the run of the EDX line scan. (**f**) EDX line scan across the surface of the pellet, as depicted in (e), for the elements F, Au and La. The lines serve as a guide to the eye.

The corresponding CVs of the sandwich cells with Ni as electrode material are shown in Figure 6. As evidenced by the slightly noisy signal, the measurements suffer a bit from contact issues.

The CV measurements on a cell with a 2.5 mm thick WE do not reveal any distinct current peaks. As in the case of the cells with Au electrodes, the diameter of the WE, see the curves obtained with cells equipped with a WE having a diameter of 8 mm, yields somewhat different results at high scan rates; for instance, we see that at a scan rate of 0.1 V/s a prominent current peak appears at 0.2 V, which is, however, absent for WEs with a diameter of only 2.5 mm. This peak is also seen at lower scan rates. Correspondingly, peaks with positive current and low intensity show up at ca. 3.4 V, at least at lower scan rates. The latter peak dominates the current response also during the first cycle (see Figure 6d,f). It has shoulders at 2.5 V and 1.2 V, respectively. Note that the current amplitude turned out to be much larger for the very first cycle, indicating irreversible reduction/oxidation processes taking place at the Ni | $La_{0.9}Ba_{0.1}F_{2.9}$ interface. The formation of NiF_2 passive films on the surface of Ni is known and it seems that such a layer is also forming here. Cells with WE having diameters of 4 and 6 mm, respectively, result in basically identical CVs as seen for the cells with a 2 mm WE. The corresponding responses are shown in Figure A3b,e.

Finally, in Figure 7, CVs of Pt | $La_{0.9}Ba_{0.1}F_{2.9}$ | Pt cells with a WE having a diameter of 2.5 mm (Figure 7a) or 8 mm (Figure 7b) are shown.

Again, scan rates were varied to range from 2 mV/s to 0.1 V/s. For cells with a WE having a diameter of 8 mm no distinct oxidation/reduction peaks are visible. This observation is in contrast to the situation of the cell with a 2.5 mm WE. Two shallow peaks with positive currents and at least one in the direction of negative current are seen. For the sake of completeness, the results from CV on cells with WE having diameters of 4 mm and 6 mm are shown in Figure A3c,f.

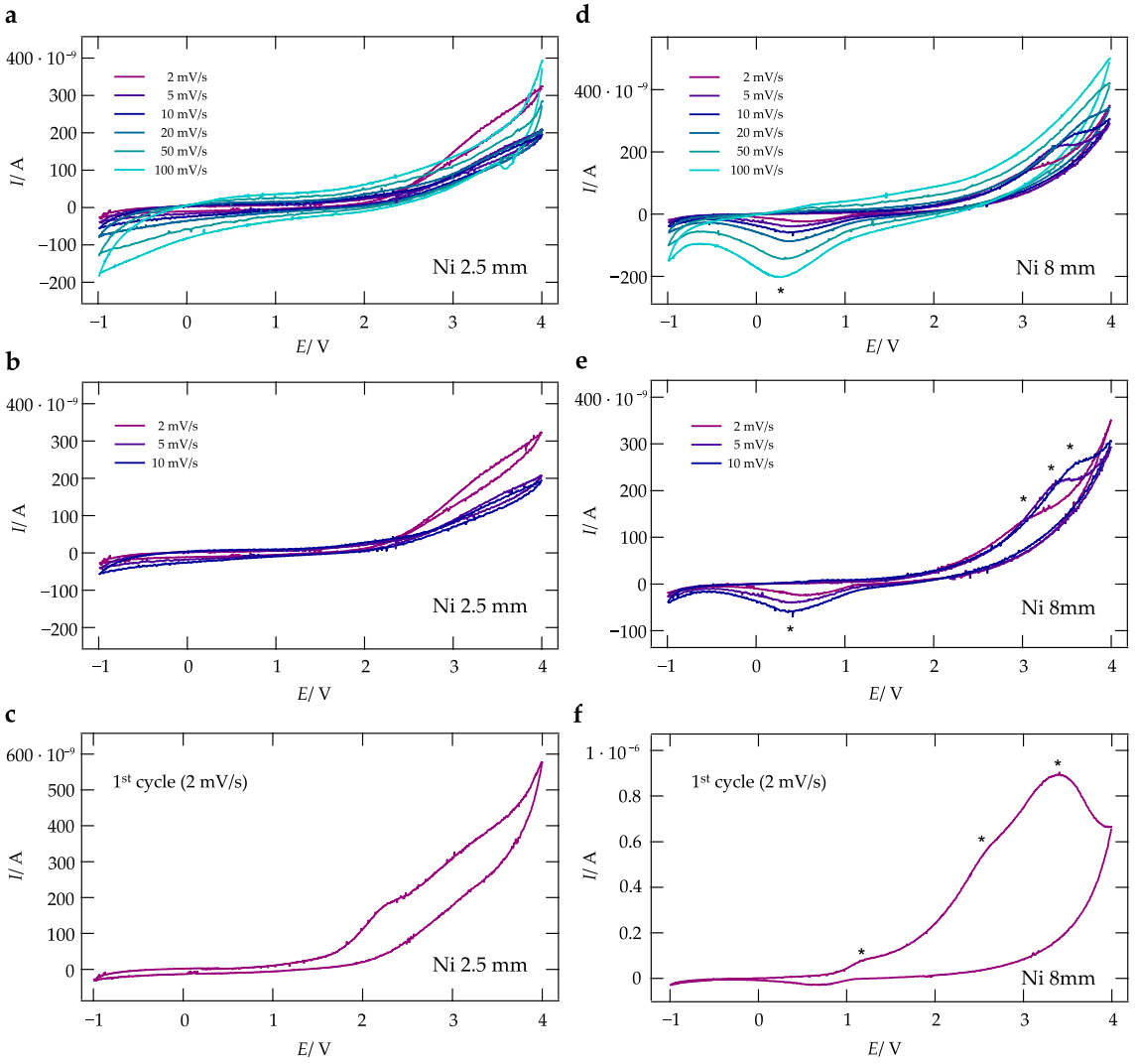

Figure 6. CVs of symmetrical cells with $La_{0.9}Ba_{0.1}F_{2.9}$ as electrolyte and Ni as electrode material. CVs were recorded at a temperature of 200 °C; scan rates ranged from 2 mV/s to to 0.1 V/s. The diameter of the working electrodes was either 2.5 mm (**a**–**c**) or 8 mm (**d**–**f**).

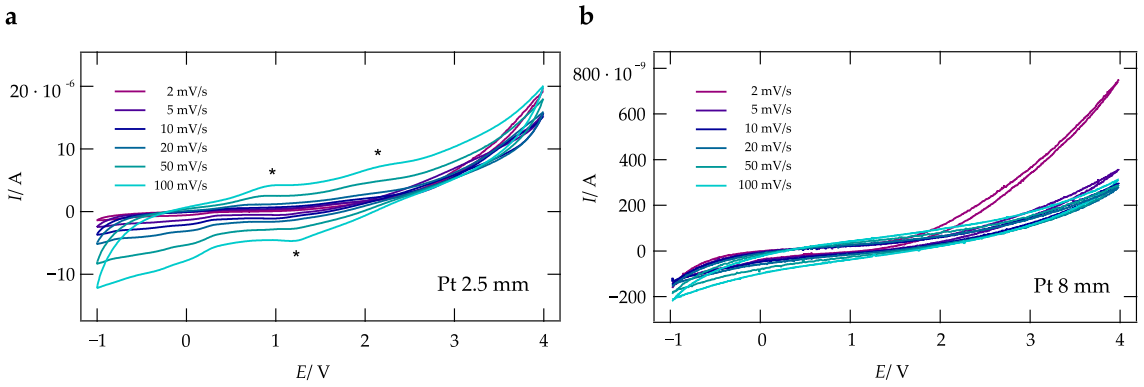

Figure 7. CVs of a $La_{0.9}Ba_{0.1}F_{2.9}$ cell with two Pt electrodes. The diameter of the WE was either 2.5 mm (**a**) or (**b**) 8 mm. CVs were recorded at scan rates ranging from 0.002 V/s to 0.1 V/s at 200 °C.

4. Conclusions and Outlook

We tested the electrochemical stability of several metal electrodes that might work as current collector materials in the first generation of fluorine-ion batteries. We see that most metals tested are

not in stable contact with the studied nanocrystalline ionic conductor $La_{0.9}Ba_{0.1}F_{2.9}$. While Cu reacts on contact, also Ag, Au, Pt and Ni undergo complex electrochemical reactions showing instabilities at the interface between the metal current collector and the ceramic electrolyte. In addition, we also see a significant migration of the metals. This diffusion processes point toward the necessity of developing and using diffusion barrier layers in prospective fluoride-ion systems. While all the systems undergo degradation upon subsequent cycles in CV experiments, we also see that Ni is very likely the most efficient metal that is able to form a passivating layer at the metal | electrolyte interface.

Author Contributions: Conceptualization, I.H. and H.M.R.W.; methodology, I.H.; formal analysis, M.G.; investigation, M.G. and V.P.; data curation, M.G.; writing—original draft preparation, M.G.; writing—review and editing, H.M.R.W. and I.H.; visualization, M.G.; supervision, H.M.R.W.; project administration, H.M.R.W. and I.H.; funding acquisition, H.M.R.W.

Funding: This research received funding by the FFG K-project 'safe battery'.

Acknowledgments: We thank our colleagues at the ICTM (TU Graz) for helpful discussions.

Conflicts of Interest: The authors declare no conflict of interest.

Abbreviations

The following abbreviations are used in this manuscript:

FIB	Fluorine Ion Battery
CV	Cyclic Voltammetry
EIS	Electrochemical Impedance Spectroscopy
SEM	Scanning Electron Microscopy
CE	Counter Electrode
WE	Working Electrode
EDX	Energy-Dispersive X-ray Spectroscopy
SE	Secondary Electrons
BSE	Backscattered Electrons

Appendix A

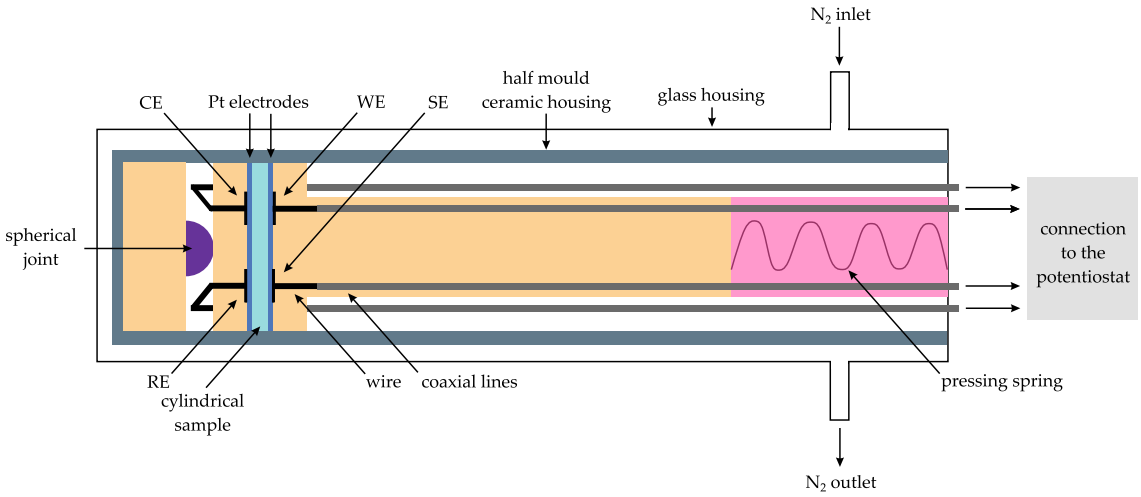

Figure A1. Scematic drawing of the cell set-up for conducting solid state Cyclic Voltammetry in a two-electrode set-up.

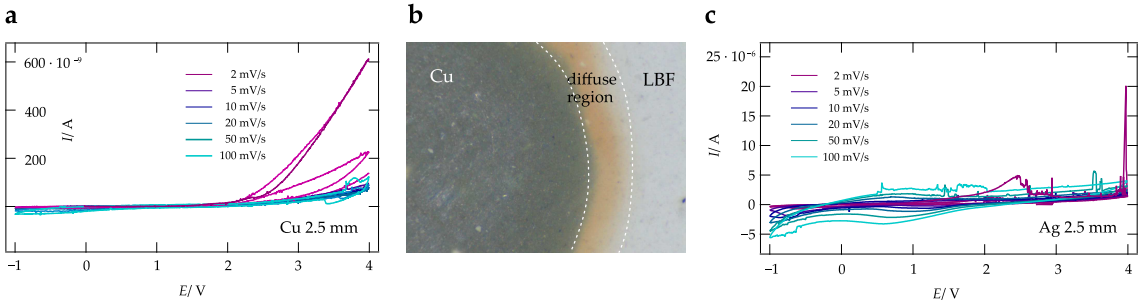

Figure A2. CV of a $La_{0.9}Ba_{0.1}F_{2.9}$ cell with Cu (**a**) and Ag (**c**) as electrode material (d = 2.5 mm, 0.002 V/s to 0.1 V/s, 200 °C). (**b**) Light microscopy image of a Cu cell (d = 2.5 mm) *after* CV. At the Cu | electrolyte interface a diffusive region with orange color appears.

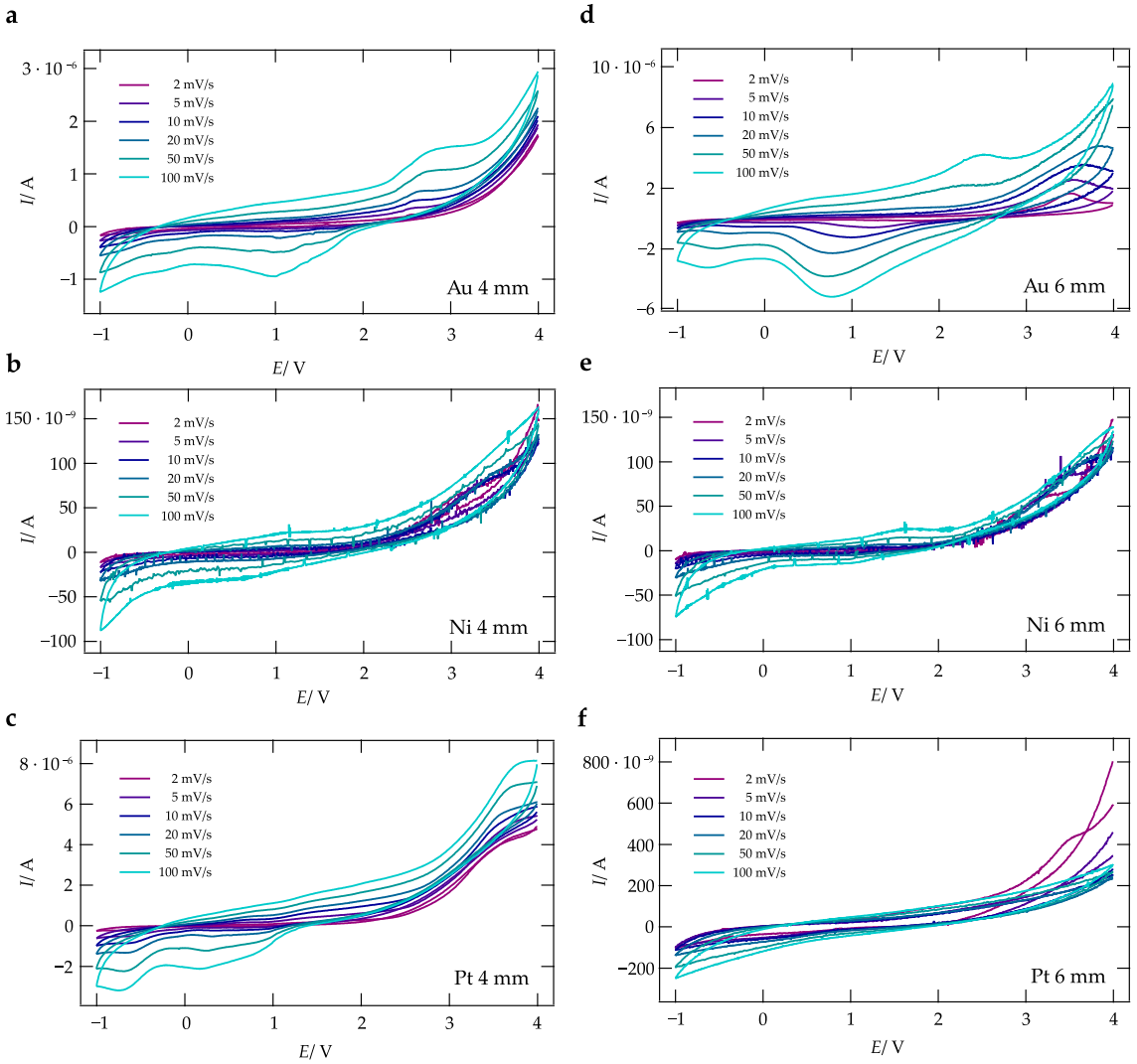

Figure A3. CVs for symmetric $La_{0.9}Ba_{0.1}F_{2.9}$ cells (0.002 V/s to 0.1 V/s, 200 °C) with Au electrodes (WE d = 4 mm and d = 6 mm see (**a**,**d**)), Ni electrodes (WE d = 4 mm and d = 6 mm see (**e**,**b**)), and Pt electrodes (WE d = 4 mm and d = 6 mm see (**c**,**f**)).

References

1. Turcheniuk, K.; Bondarev, D.; Singhal, V.; Yushin, G. Ten Years Left to Redesign Lithium-Ion Batteries. *Nature* **2018**, *559*, 467–470. [CrossRef] [PubMed]
2. Vaalma, C.; Buchholz, D.; Weil, M.; Passerini, S. A Cost and Resource Analysis of Sodium-Ion Batteries. *Nat. Rev. Chem.* **2018**, *3*, 18013. [CrossRef]

3. Faraday, M. *Experimental Researches in Electricity, Art. 1339*; Taylor and Francis: London, UK, 1893.
4. O'Keeffe, M. Phase Transitions and Translational Freedom in Solid Electrolytes. In *Superionic Conductors*; Springer: Boston, MA, USA, 1976; pp. 101–114.
5. Funke, K. Solid State Ionics: From Michael Faraday to green energy—The European dimension. *Sci. Technol. Adv. Mater.* **2013**, *14*, 043502. [CrossRef]
6. Takahashi, T. High Conductivity Solid Ionic Conductors: The Past and the Present. In *High Conductivity Solid Ionic Conductors*; World Scientific: Singapore, 1989; pp. 1–16.
7. Tubandt, C. Über Elektrizitätsleitung in festen kristallisierten Verbindungen. Zweite Mitteilung. Überführung und Wanderung der Ionen in einheitlichen festen Elektrolyten. *Z. Anorg. Allg. Chem.* **1921**, *115*, 105–126. [CrossRef]
8. Baukal, W. Ger. Offen. Galvanische Zelle mit dotiertem Calciumfluorid als Festelektrolyt. Germany Patent GWXXBX DE 2017128, 7 April 1977.
9. Kennedy, J.H.; Hunter, J.C. Thin-Film Galvanic Cell $Pb/PbF_2/PbF_2$,CuF_2/Cu. *J. Electrochem. Soc.* **1976**, *123*, 10–14. [CrossRef]
10. Schoonman, J. A Solid-State Galvanic Cell with Fluoride-Conducting Electrolytes. *J. Electrochem. Soc.* **1976**, *123*, 1772–1775. [CrossRef]
11. Schoonman, J.; Wapenaar, K.; Overluizen, G.; Dirksen, G. Fluoride-Conducting Solid Electrolytes in Galvanic Cells. *J. Electrochem. Soc.* **1979**, *126*, 709–713. [CrossRef]
12. Schoonman, J.; Wolfert, A. Solid-State Galvanic Cells with Fast Fluoride Conducting Electrolytes. *Solid State Ion.* **1981**, *3–4*, 373–379. [CrossRef]
13. Anji Reddy, M.; Fichtner, M. Batteries based on Fluoride Shuttle. *J. Mater. Chem.* **2011**, *21*, 17059–17062. [CrossRef]
14. Reddy, M.A.; Fichtner, M. Fluoride Cathodes for Secondary Batteries. In *Advanced Fluoride-Based Materials for Energy Conversion*; Nakajima, T.; Groult, H., Eds.; Elsevier: Amsterdam, The Netherlands, 2015; pp. 51–76.
15. Thieu, D.T.; Fawey, M.H.; Bhatia, H.; Diemant, T.; Chakravadhanula, V.S.K.; Behm, R.J.; Kübel, C.; Fichtner, M. CuF_2 as Reversible Cathode for Fluoride Ion Batteries. *Adv. Fuct. Mater.* **2017**, *27*, 1701051. [CrossRef]
16. Bhatia, H.; Thieu, D.T.; Pohl, A.H.; Chakravadhanula, V.S.K.; Fawey, M.H.; Kübel, C.; Fichtner, M. Conductivity Optimization of Tysonite-type $La_{1-x}Ba_xF_{3-x}$ Solid Electrolytes for Advanced Fluoride Ion Battery. *ACS Appl. Mater. Interfaces* **2017**, *9*, 23707–23715. [CrossRef] [PubMed]
17. Wapenaar, K.; Koesveld, J.V.; Schoonman, J. Conductivity Enhancement in Fluorite-Structured $Ba_{1-x}La_xF_{2+x}$ Solid Solutions. *Solid State Ion.* **1981**, *2*, 145–154. [CrossRef]
18. Gschwind, F.; Zao-Karger, Z.; Fichtner, M. A Fluoride-Doped PEG Matrix as an Electrolyte for Anion Transportation in a Room-Temperature Fluoride Ion Battery. *J. Mater. Chem. A* **2014**, *2*, 1214–1218. [CrossRef]
19. Davis, V.K.; Bates, C.M.; Omichi, K.; Savoie, B.M.; Momčilović, N.; Xu, Q.; Wolf, W.J.; Webb, M.A.; Billings, K.J.; Chou, N.H.; et al. Room-Temperature Cycling of Metal Fluoride Electrodes: Liquid Electrolytes for High-Energy Fluoride Ion Cells. *Science* **2018**, *362*, 1144–1148. [CrossRef] [PubMed]
20. Rongeat, C.; Anji Reddy, M.; Diemant, T.; Behm, R.J.; Fichtner, M. Development of New Anode Composite Materials for Fluoride Ion Batteries. *J. Mater. Chem. A* **2014**, *2*, 20861–20872. [CrossRef]
21. Zhang, L.; Reddy, M.A.; Fichtner, M. Electrochemical Performance of All-Solid-State Fluoride-Ion Batteries based on Thin-Film Electrolyte using Alternative Conductive Additives and Anodes. *J. Solid State Electrochem.* **2018**, *22*, 997–1006. [CrossRef]
22. Nowroozi, M.A.; Ivlev, S.; Rohrer, J.; Clemens, O. La_2CoO_4: A New Intercalation based Cathode Material for Fluoride Ion Batteries with Improved Cycling Stability. *J. Mater. Chem. A* **2018**, *6*, 4658–4669. [CrossRef]
23. Mohammad, I.; Chable, J.; Witter, R.; Fichtner, M.; Reddy, M.A. Synthesis of Fast Fluoride-Ion-Conductive Fluorite-Type $Ba_{1-x}Sb_xF_{2+x}$ ($0.1 < x < 0.4$): A Potential Solid Electrolyte for Fluoride-Ion Batteries. *ACS Appl. Mater. Interfaces* **2018**, *10*, 17249–17256.
24. Dieudonne, B.; Chable, J.; Body, M.; Legein, C.; Durand, E.; Mauvy, F.; Fourcade, S.; Leblanc, M.; Maisonneuve, V.; Demourgues, A. The Key Role of the Composition and Structural Features in Fluoride Ion Conductivity in Tysonite $Ce_{1-x}Sr_xF_{3-x}$ Solid Solutions. *Dalton Trans.* **2017**, *46*, 3761–3769. [CrossRef]
25. Dieudonne, B.; Chable, J.; Mauvy, F.; Fourcade, S.; Durand, E.; Lebraud, E.; Leblanc, M.; Legein, C.; Body, M.; Maisonneuve, V.; et al. Exploring the $Sm_{1-x}Ca_xF_{3-x}$ Tysonite Solid Solution as a Solid-State Electrolyte: Relationships between Structural Features and Fast Ionic Conductivity. *J. Phys. Chem. C* **2015**, *119*, 25170–25179. [CrossRef]

26. Raccichini, R.; Amores, M.; Hinds, G. Critical Review of the Use of Reference Electrodes in Li-Ion Batteries: A Diagnostic Perspective. *Batteries* **2019**, *5*, 12. [CrossRef]
27. Breuer, S.; Gombotz, M.; Pregartner, V.; Hanzu, I.; Wilkening, M. Heterogeneous F Anion Transport, Local Dynamics and Electrochemical Stability of Nanocrystalline $La_{1-x}Ba_xF_{3-x}$. *Energy Storage Mater.* **2019**, *16*, 481–490. [CrossRef]
28. Setup of The Impedance Measuring Cell (Novocontrol). Available online: https://www.novocontrol.de/brochures/BDS1200.pdf (accessed on 21 October 2019).
29. Irvine, J.T.S.; Sinclair, D.C.; West, A.R. Electroceramics: Characterization by Impedance Spectroscopy. *Adv. Mater.* **1990**, *2*, 132–138. [CrossRef]
30. Gombotz, M.; Lunghammer, S.; Breuer, S.; Hanzu, I.; Preishuber-Pflügl, F.; Wilkening, H.M.R. Spatial Confinement—Rapid 2D F^- Diffusion in Micro- and Nanocrystalline $RbSn_2F_5$. *Phys. Chem. Chem. Phys.* **2019**, *21*, 1872–1883. [CrossRef]
31. Preishuber-Pflügl, F.; Bottke, P.; Pregartner, V.; Bitschnau, B.; Wilkening, M. Correlated Fluorine Diffusion and Ionic conduction in the Nanocrystalline F^- Solid Electrolyte $Ba_{0.6}La_{0.4}F_{2.4}$ – ^{19}F $T_{1(\rho)}$ NMR Relaxation vs. Conductivity Measurements. *Phys. Chem. Chem. Phys.* **2014**, *16*, 9580–9590. [CrossRef]
32. Narayanan, S.; Epp, V.; Wilkening, M.; Thangadurai, V. Macroscopic and Microscopic Li^+ Transport Parameters in Cubic Garnet-Type "$Li_{6.5}La_{2.5}Ba_{0.5}ZrTaO_{12}$" as Probed by Impedance Spectroscopy and NMR. *RSC Adv.* **2012**, *2*, 2553–2561. [CrossRef]
33. Lunghammer, S.; Ma, Q.; Rettenwander, D.; Hanzu, I.; Tietz, F.; Wilkening, H. Bulk and Grain-Boundary Ionic Conductivity in Sodium Zirconophosphosilicate $Na_3Zr_2(SiO_4)_2PO_4$ (NASICON). *Chem. Phys. Lett.* **2018**, *701*, 147–150. [CrossRef]

5 Conclusion

Within this thesis a large variety of different characterisation techniques were applied to study the structure and diffusion in ion conducting materials. It was possible to find answers to the main questions defined in the introduction, which will be introduced in the following.

How does a present phase transition influence ion dynamics in the solid electrolyte Li_3YBr_6? And, is nanocrystalline Li_3YBr_6 a sustainable alternative to microcrystalline Li_3YBr_6 annealed at high temperatures?

The occurring phase transition is characterised by an occupation of the $8j$ site by Li^+ above 0°C [2]. We found that the occupation of this additional site comes along with enhanced ion diffusion in microcrystalline Li_3YBr_6 as seen by impedance spectroscopy. Relaxation rates, retrieved from NMR relaxation measurements, pointed towards comparable ion dynamics in micro- as well as nanocrystalline Li_3YBr_6. The latter one, only milled for 1 h (compared to 50 h of milling plus annealing for microcrystalline Li_3YBr_6), exhibits slightly lower conductivity values, which would not automatically disqualify it as solid electrolyte. The determined electronic conductivity of nanocrystalline Li_3YBr_6 is, however, significantly higher and makes short annealing periods indispensable.

Is the so far unknown lithium ion conductor $Li[In_xLi_y]Br_4$ a suitable material to be employed as solid electrolyte in LIB?

Within the scope of this study it became clear that the investigated Li^+ conductor is only suitable as electrolyte with reservations. Reaching only $4.9 \cdot 10^{-6}$ S cm^{-1} at room temperature it does not provide sufficiently high conductivity to be competitive with other known systems. Therefore, this electrolyte could be employed in cells operating at higher temperature, *e.g.* at 60°C, where a higher conductivity ($6 \cdot 10^{-5}$ S cm^{-1}) is reached, however, being accompanied by a high electronic conductivity ($3 \cdot 10^{-8}$ S cm^{-1}), which might trigger cell degradation.

Are ion dynamics in LiF enhanced if a certain amount of the insulator TiO_2 is added?

After synthesis and investigation of the phase purity of the composites $(1-x_v)$LiF:$x_v TiO_2$ (x = 0.1 - 0.5), their conductivity was measured by impedance spectroscopy. Compared to microcrystalline LiF an increase of nearly 4 orders of magnitude in conductivity was found for the sample with 40vol% TiO_2. Hence, the introduction of conductor | insulator interfaces drastically improves ion dynamics in this system. Via static ^{7}Li and ^{19}F NMR measurements, Li^+ was revealed to be the dominant mobile species in these composites.

Does the incorporation of H^+ upon degradation in the garnet material $Li_{6.4}La_3ZrTaO_{12}$ change the Li^+ dynamics and/or structure?

Neutron diffraction experiments of crystals immersed for 31 days in water showed that only a small amount of hydrogen, namely 0.4 pfu, are incorporated into the structure without changing it. NMR measurements were able to reveal that relatively rapid motion of H^+ takes place, while Li^+ dynamics are slowed down to only a small extent.

Can evidence be found with the aid of NMR and impedance spectroscopy that 2D F^- motion occurs in $RbSn_2F_5$?

Activation energies E_A were extracted from impedance spectroscopy as well as relaxation rates ($1/T_{1\rho}$). For the latter one a spectral density function introduced by P. M. Richards for 2D diffusion was used to approximate the data and extract E_A. Here, the activation energy matched the one from impedance spectroscopy, hence, clearly demonstrating that 2D ion motion prevails in $RbSn_2F_5$.

Under which conditions does the highly conductive α^* form of Ag_3SI transform into the β-phase?

It was found that the transformation from α^*- to β-Ag_3SI occurs within approximately 140 h at 30°C and 28 h at 60°C, hence, showing that the temperature has a strong influence on the stability of α^*-Ag_3SI. Furthermore, it was shown that intermediate cooling steps could not slow the transformation down.

Is $La_{0.9}Ba_{0.1}F_{2.9}$ electrochemically stable in combination with the most widely used electrode materials?

Every tested metal electrode (Ni, Cu, Ag, Au, Pt) reacted either immediately or during the electrochemical testing with $La_{0.9}Ba_{0.1}F_{2.9}$. Most likely, Ni is the only material forming passivating layers at the interface, highlighting the reactivity of F^- bearing electrolytes and the necessity of developing diffusion barrier layers within such systems.

A Experimental

Mechanochemical Syntheses

Mechanochemical syntheses were carried out either in 45 ml milling beakers made of ZrO_2 or tungstencarbide with 180 balls made of the same material and 5 mm in diameter. The educts were loaded in all cases inside a glovebox (O_2, $H_2O < 0.5$ ppm) and the syntheses itself were carried out in a planetary mill (Fritsch Pulverisette 7 premium line). The rotation speed as well as the milling time were adjusted to the corresponding educts and reaction, respectively. 15 minutes of milling were always followed by a rest period of 15 minutes to allow cooling of the beakers. Detailed milling parameters of each synthesis can be found in the according publications.

X-ray Powder Diffraction

A Bruker D8 Advance diffractometer or a Rigaku miniflex were used to obtain x-ray powder diffractograms under atmospheric pressure and ambient temperature. Diffractograms of air sensitive materials were carried out with special sample holders shielding the sample from air with Kapton foil. Both mentioned devices operate with Bragg Brentano gemotery and CuK_α radiation (1.5406 Å). The range was usually set from 10 to 100°2θ, whereas data points were collected with a stepsize of 0.01 to 0.1°2θ, measured for 0.1 to 1 sec each. If necessary, Rietveld Refinement was carried out with X-PertHighScorePlus (PANalytical).

Electrochemical Impedance Spectroscopy

For the determination of the overall conductivity of solid conductors, an appropriate amount of powdered sample (60 - 100 mg) was pressed to cylindrical pellets with a diameter of 5 mm using a hand press (0.5 t). Subsequently two ion blocking electrodes, typically made of Au, were applied by sputtering (for more details see Section Sputter devices).

Alternating current (AC) impedance spectroscopy was carried out with a broadband spectrometer (Novocontrol Concept 80) in conjunction with a ZGS interface and an active BDS 1200 cell. Usual measurements were performed in a frequency range between 10^{-2} and 10^{7} Hz, whereas it was possible with an Agilent high frequency analyser and a special sample holder (only for air insensitive materials), to reach frequencies of 1 MHz up to 3 GHz. The conductivity measurements were performed in a temperature range from -140°C to 260°C, whereat the temperature was regulated by a QUATRO cryosystem. During the whole measurement the sample chamber was continuously flushed with dry and freshly evaporated N_2 gas. In the case of air-sensitive materials a special sample holder made of Teflon was used, with the drawback of introducing inductance, resulting in not analysable Nyquist Plots. Conductivity isotherms however remained unaffected by the sample holder. Evaluation of the data was done with IGOR Pro (Wavemetrics) and ZView (Princeton Applied Research).

Sputter devices

To apply blocking electrodes made of various materials (Ni, Cu, Ag, Au, Pt or Cu), two different sputter devices were used. Electrodes onto air sensitive materials were sputtered with a Leica EM SCD050 sputter device, controlled by a LEICA EM QSG100 control system, placed in an argon filled glovebox (H_2O, $O_2 < 0.1$ ppm). A Leica EM ACE200 sputter device was used for air insensitive materials.

Polarisation

By impedance spectroscopy the overall conductivity is measured, whereby in particular cases the ratio of electric to ionic conductivity gains significance. Therefore, Hebb-Wagner-type polarisation measurements were used to determine the electric conductivity of solid samples. Therefore sample powder (100 - 140 mg) was pressed to cylindrical pellets with a diameter of 8 mm using a handpress by applying 0.5 t (100 MPa). Ion-blocking electrodes were sputtered on both sides (for more details see Section Sputter devices). The used potentiostat (Parstat MC, Princeton Applied Research) was equipped with a low current option. If slightly air insensitive samples were investigated, the sample chamber was continuously flushed with N_2. If high temperatures were necessary to ensure fast kinetics the sample was placed into a tube furnace (Reetz). Air sensitive materials were mounted in Swagelok-type cells and heated in a climate chamber.

Static Nuclear Magnetic Resonance Spectroscopy

Static measurements were carried out on a Bruker Avance III NMR spectrometer in combination with a shimmed Bruker Biospin Ultrashield 300 WB cryomagnet with a nominal magnetic field of 7.04 T. Measurements in the laboratory and rotating frame of reference were carried out on the isotopes listed in Table A.1. In the same table the nuclei spin, natural abundance and resulting frequency is listed of the investigated isotopes.
Details regarding pulse sequences and data evaluation can be found in the publications, see 3.4.6.

Table A.1: Investigated Nuclei on the Bruker Avance III 300 spectrometer

Isotop	**Spin**	**Natural abundance**	**NMR frequency at 7.04 T**
^{1}H	1/2	99.98 %	300 MHz
^{7}Li	3/2	97.158 %	116.59 MHz
^{19}F	1/2	100 %	282.231 MHz

Magic Angle Spinning Nuclear Magnetic Resonance Spectroscopy

A Bruker Avance III spectrometer in combination with a shimmed cryomagnet Bruker Biospin Ultrashield 500 WB Plus with a nominal magnetic field of 11.7 T was used to record Free Induction Decay's, which were Fourier transformed to the according MAS NMR spectra. In Table A.3 all nuclei, which were investigated throughout this study, are listed alongside with their spin, natural abundance and their characteristic Lamor frequency. Details regarding pulse sequences and data evaluation can be found in the publications, see 3.4.6.

Table A.3: Investigated Nuclei on the Bruker Avance III 500 spectrometer

Isotop	**Spin**	**Natural abundance**	**NMR frequency at 11.7 T**
^{1}H	1/2	99.98 %	500 MHz
^{6}Li	1	7.42 %	73.578 MHz
^{7}Li	3/2	92.58 %	194.317 MHz
^{19}F	1/2	100 %	470.385 MHz
^{23}Na	3/2	100 %	132.256 MHz
^{79}Br	3/2	50.54 %	125.267 MHz
^{87}Rb	3/2	27.85 %	163.606 MHz
^{109}Ag	1/2	48.18 %	23.260 MHz
^{119}Sn	1/2	8.58 %	186.362 MHz

Cyclic Voltammetry

Cyclic Voltammetry in the two-electrode set-up was performed with a Parstat MC potentiostat (Princton Applied Research) equipped with a low current option. Fluoride samples, pressed to cylindrical pellets, were equipped with several different metal electrodes (Pt, Au, Ag, Ni, Cu) by sputtering to obtain a sandwich-type configuration (*electrode* | *sample* | *electrode*). Thereafter the samples were mounted in the cell, for a description see Paper 4.6. The sample chamber was constantly purged with N_2 gas. The data was acquired with the program Versa Studio, analysis was carried out with IGOR Pro.

B Bibliography

[1] T. Asano, A. Sakai, S. Ouchi, M. Sakaida, A. Miyazaki, S. Hasegawa. Solid Halide Electrolytes with High Lithium-Ion Conductivity for Application in 4 V Class Bulk-Type All-Solid-State Batteries. *Advanced Materials* **30** (2018) 1803075. doi:10.1002/adma.201803075

[2] R. Schlem, A. Banik, S. Ohni, E. Suard, W. Zeier. Insights into the Lithium Substructure of the Superionic Conductors Li_3YCl_6 and Li_3YBr_6. *Chem. Mater.* **33** (2021) 327. doi:10.1021/acs.chemmater.0c04352

[3] R. Gross, A. Marx. *Festkörperphysik.* De Gruyter, 2nd Auflage, 2014

[4] A. R. West. *Solid State Chemistry and Its Applications.* John Wiley & Sons, Ltd, 2. Auflage, 2014

[5] E. Lifshin (Herausgeber). *X-ray Characterization of Materials.* Wiley-VCH Verlag GmbH&Co. KGaA, Weinheim, 1999

[6] A. Bravais. Les systemes formes par des pointes distribues regulierement sur un plan ou dans l'espace. *J.Ecole.Polytech.* (1850) 1

[7] V. K. Pecharsky, P. Y. Zavalij. *Fundamentals of Powder Diffraction and Structural Characterization of Materials.* Springer, 2. Auflage, 2009. doi:10.1007/978-0-387-09579-0

[8] W. Massa. *Crystal Structure Determination.* Springer-Verlag Berlin Heidelberg, 2000. doi:10.1007/978-3-662-04248-9

[9] Inorganic Crystal Structure Database (ICSD) (accessed on 2.2.2021 - 15:43) `https://icsd.fiz-karlsruhe.de/search/basic.xhtml;jsessionid=A27C54B7D574574AD4BD2C3155255F86`

[10] E. Zolotoyabko. *Basic Concepts of X-Ray Diffraction.* Wiley-VCH Verlag GmbH&Co. KGaA, Weinheim, 2014

[11] P. Scherrer. Bestimmung der Größe und der inneren Struktur von Kolloidteilchen mittels Röntgenstrahlen. *Nachrichten von der Gesellschaft der Wissenschaften zu Göttingen, Mathematisch-Physikalische Klasse* (1918) 98

[12] H. Mehrer. *Diffusion in Solids - Fundamentals, Methods, Materials, Diffusion-Controlled Processes (Springer Series in Solid-State Sciences 155)*. Springer-Verlag Berlin Heidelberg, Berlin Heidelberg, 2007

[13] R. J. D. Tilley. *Understanding Solids*. John Wiley & Sons, Ltd, 2005. doi:10.1002/0470020849

[14] P. Heitjans, S. Indris. Diffusion and ionic conduction in nanocrystalline ceramics. *Journal of Physics: Condensed Matter* **15** (2003) R1257. doi:10.1088/0953-8984/15/30/202

[15] R. J. D. Tilley. *Defects in Solids*. John Wiley & Sons, Inc., Hoboken, New Jersey, 2008

[16] A. D. McNaught, A. Wilkinson. IUPAC. Compendium of Chemical Terminology (the "Gold Book") 2nd ed. (accessed on 9.2.2021 - 10:32), 1997. doi:https://doi.org/10.1351/goldbook.MT07141 `http://goldbook.iupac.org/terms/view/MT07141`

[17] T. Friščić. Supramolecular concepts and new techniques in mechanochemistry: Cocrystals, cages, rotaxanes, open metal–organic frameworks. *Chemical Society Reviews* **41** (2012) 3493. doi:10.1039/c2cs15332g

[18] D. K. Bučar, S. Filip, M. Arhangelskis, G. O. Lloyd, W. Jones. Advantages of mechanochemical cocrystallisation in the solid-state chemistry of pigments: Colour-tuned fluorescein cocrystals. *CrystEngComm* **15** (2013) 6289. doi:10.1039/c3ce41013g

[19] L. Anderson, R. Boulatov. *Polymer Mechanochemistry: A New Frontier for Physical Organic Chemistry*, Band 52. Elsevier Ltd., 1 Auflage, 2018. doi:10.1016/bs.apoc.2018.08.001

[20] W. Jones, M. D. Eddleston. Introductory lecture: Mechanochemistry, a versatile synthesis strategy for new materials. *Faraday Discussions* **170** (2014) 9. doi:10.1039/c4fd00162a

[21] T. Friić, L. Fábián. Mechanochemical conversion of a metal oxide into coordination polymers and porous frameworks using liquid-assisted grinding (LAG).

CrystEngComm **11** (2009) 743.
doi:10.1039/b822934c

[22] M. Wilkening, A. Düvel, F. Preishuber-Pflügl, K. Da Silva, S. Breuer, V. Šepelák, P. Heitjans. Structure and ion dynamics of mechanosynthesized oxides and fluorides. *Zeitschrift fur Kristallographie - Crystalline Materials* **232** (2017) 107.
doi:10.1515/zkri-2016-1963

[23] F. Preishuber-Pflügl, M. Wilkening. Mechanochemically synthesized fluorides: Local structures and ion transport. *Dalton Transactions* **45** (2016) 8675.
doi:10.1039/c6dt00944a

[24] A. Düvel, J. Bednarcik, V. Šepelák, P. Heitjans. Mechanosynthesis of the fast fluoride ion conductor $Ba_{1-x}La_xF_{2+x}$: from the fluorite to the tysonite structure. *Journal of Physical Chemistry C* **118** (2014) 7117.
doi:10.1021/jp410018t

[25] S. Breuer, M. Gombotz, V. Pregartner, I. Hanzu, M. Wilkening. Heterogeneous F anion transport, local dynamics and electrochemical stability of nanocrystalline $La_{1-x}Ba_xF_{3-x}$. *Energy Storage Materials* **16** (2019) 481.
doi:10.1016/j.ensm.2018.10.010

[26] M. Gombotz, S. Lunghammer, S. Breuer, I. Hanzu, F. Preishuber-Pflügl, H. M. R. Wilkening. Spatial confinement rapid 2D F^- diffusion in micro- and nanocrystalline $RbSn_2F_5$. *Physical Chemistry Chemical Physics* **21** (2019) 1872.
doi:10.1039/c8cp07206j

[27] V. Epp, M. Wilkening. Motion of Li^+ in nanoengineered $LiBH_4$ and $LiBH_4$:Al_2O_3 comparison with the microcrystalline form. *ChemPhysChem* **14** (2013) 3706.
doi:10.1002/cphc.201300743

[28] V. Šepelák, D. Baabe, D. Mienert, D. Schultze, F. Krumeich, F. J. Litterst, K. D. Becker. Evolution of structure and magnetic properties with annealing temperature in nanoscale high-energy-milled nickel ferrite. *Journal of Magnetism and Magnetic Materials* **257** (2003) 377.
doi:10.1016/S0304-8853(02)01279-9

[29] P. Baláž, T. Ohtani, Z. Bastl, E. Boldižárová. Properties and Reactivity of Mechanochemically Synthesized Tin Sulfides. *Journal of Solid State Chemistry* **144** (1999) 1.
doi:10.1006/jssc.1998.7944

[30] P. Baláž, M. Achimovicová, M. Baláž, P. Billik, C. Z. Zara, J. M. Criado, F. Delogu, E. Dutková, E. Gaffet, F. J. Gotor, R. Kumar, I. Mitov, T. Rojac, M. Senna, A. Streletskii, W. C. Krystyna. Hallmarks of mechanochemistry: From nanoparticles to technology. *Chemical Society Reviews* **42** (2013) 7571.
doi:10.1039/c3cs35468g

[31] P. Baláž. *Mechanochemistry in nanoscience and minerals engineering.* Springer-Verlag Berlin Heidelberg, Berlin Heidelberg, 2008.
doi:10.1007/978-3-540-74855-7

[32] F. Bowden, A. Yoffe. *Initiation and Growth of Explosion in Liquids and Solids.* Cambridge University Press, Cambridge, 1952

[33] F. Bowden, A. Yoffe. *Fast Reactions in Solids.* London, Butterworths, 1958

[34] F. Bowden, D. Tabor. *The Friction and Lubrication of Solids.* Clarendon Press, Oxford, 1958

[35] P. A. Thiessen, K. Meyer, G. Heinicke. *Grundlagen der Tribochemie.* Akademie Verlag, Berlin, 1967

[36] L. Takacs, J. S. McHenry. Temperature of the milling balls in shaker and planetary mills. *Journal of Materials Science* **41** (2006) 5246.
doi:10.1007/s10853-006-0312-4

[37] Fritsch Planetenmühle Pulverisette 7 premium line - Zubehör (accessed on 8.01.2021 - 14:55)
`https://www.fritsch.de/probenaufbereitung/mahlen/planetenmuehlen/details/produkt/pulverisette-7-premium-line/zubehoer/`

[38] V. F. Lvovich. *Impedance Spectroscopy - Applications to Electrochemical and Dielectric Phenomena.* John Wiley & Sons, Inc., Hoboken, New Jersey, 2012

[39] E. Barsoukov, J. R. Macdonald. *Impedance Spectroscopy Theory, Experiment, and Applications.* John Wiley & Sons, Inc., Hoboken, New Jersey, 2nd Auflage, 2005

[40] ZView by scribner (accessed on 9.2.2021 - 17:28)
`http://www.scribner.com/software/68-general-electrochemistr376-zview-for-windows`

[41] J. T. S. Irvine, D. C. Sinclair, A. R. West. Electroceramics: Characterization by Impedance Spectroscopy. *Advanced Materials* **2** (1990) 132.
doi:10.1002/adma.19900020304

[42] J. C. Dyre, P. Maass, B. Roling, D. L. Sidebottom. Fundamental questions relating to ion conduction in disordered solids. *Reports on Progress in Physics* **72** (2009) 046501.
doi:10.1088/0034-4885/72/4/046501

[43] D. P. Almond, C. C. Hunter, A. R. West. The extraction of ionic conductivities and hopping rates from a.c. conductivity data. *Journal of Materials Science* **19** (1984) 3236.
doi:10.1007/BF00549810

[44] A. K. Jonscher. The ' universal ' dielectric response. *Nature* **267** (1977) 673

[45] D. L. Sidebottom. Dimensionality dependence of the conductivity dispersion in ionic materials. *Physical Review Letters* **83** (1999) 983.
doi:10.1103/PhysRevLett.83.983

[46] D. L. Sidebottom. Colloquium: Understanding ion motion in disordered solids from impedance spectroscopy scaling. *Reviews of Modern Physics* **81** (2009) 999.
doi:10.1103/RevModPhys.81.999

[47] E. Barsoukov, J. Macdonald. *Impedance Spectroscopy - Theory, Experiment, and Applications.* John Wiley & Sons, Inc., Hoboken, New Jersey, 2nd editio Auflage, 2005

[48] D. L. Sidebottom, B. Roling, K. Funke. Ionic conduction in solids: Comparing conductivity and modulus representations with regard to scaling properties. *Physical Review B - Condensed Matter and Materials Physics* **63** (2001) 1.
doi:10.1103/PhysRevB.63.024301

[49] K. L. Ngai, C. León. Relating macroscopic electrical relaxation to microscopic movements of the ions in ionically conducting materials by theory and experiment. *Physical Review B - Condensed Matter and Materials Physics* **60** (1999) 9396.
doi:10.1103/PhysRevB.60.9396

[50] D. P. Almond, A. R. West. Mechanical and Electrical Relaxation Characteristics of Ionic Conductors. *Journal of Non-Crystalline Solids* **88** (1986) 222.
doi:10.1016/S0022-3093(86)80024-2

[51] H. Friebolin. *Basic One- and Two-Dimensional NMR Spectroscopy.* Wiley-VCH Verlag GmbH&Co. KGaA, Weinheim, 5th editio Auflage, 2011

[52] M. Duer (Herausgeber). *Solid-State NMR Spectroscopy - Principles and Applications.* Blackwell Science Ltd, 2002

[53] D. Canet. *NMR - Konzepte und Methoden.* Springer-Verlag Berlin Heidelberg, Berlin Heidelberg, 1994.
doi:10.1007/978-3-642-79122-2

[54] J. Keeler. *Understanding NMR Spectroscopy.* John Wiley & Sons, Ltd, 2nd Auflage, 2011

[55] P. Heitjans, J. Kärger. *Diffusion in Condensed Matter.* Springer-Verlag Berlin Heidelberg, Berlin Heidelberg, 2005

[56] M. H. Levitt. *Spin Dynamics - Basics of Nuclear Magnetic Resonance.* John Wiley & Sons, Ltd, Chichester, 2nd Auflage, 2008

[57] Bruker - NMR frequency tables (accessed on 19.01.2021 - 17:41)
`http://kodu.ut.ee/{~}laurit/AK2/NMR{_}tables{_}Bruker2012.pdf`

[58] V. Epp, Ö. Gün, H. J. Deiseroth, M. Wilkening. Long-range Li^+ dynamics in the lithium argyrodite Li $_7PSe_6$ as probed by rotating-frame spin-lattice relaxation NMR. *Physical Chemistry Chemical Physics* **15** (2013) 7123.
doi:10.1039/c3cp44379e

[59] D. C. Ailion, C. P. Slichter. Observation of Ultra-Slow Translational Diffusion in Metallic Lithium by Magnetic Resonance. *Physical Review* **137** (1965) A235.
doi:10.1103/physrev.137.a235

[60] F. Bloch. Nuclear induction. *Physical Review* **70** (1946) 460.
doi:10.1103/PhysRev.70.460

[61] V. Epp, M. Wilkening. Li-ion Dynamics in Solids as Seen Via Relaxation NMR. *Handbook of Solid State Batteries* (Herausgeber N. J. Dudney, W. C. West, J. Nanda), Chapter: 5, S. 133–190. World Scientific, 2015.
doi:10.1142/9789814651905_0005

[62] D. Ailion, C. P. Slichter. Study of ultraslow atomic motions by magnetic resonance. *Physical Review Letters* **12** (1964) 168.
doi:10.1103/PhysRevLett.12.168

[63] D. A. Slichter, Charles P. Low-Field Relaxation and the Study of. *Physical Review* **135** (1964) A1099

[64] N. Bloembergen, E. M. Purcell, R. V. Pound. Relaxation effects in nuclear magnetic resonance absorption. *Physical Review* **73** (1948) 679.
doi:10.1103/PhysRev.73.679

[65] P. M. Richards. Magnetic Resonance in Superionic Conductors. *Physics of Superionic Conductors, Topics in Current Physics*, S. 141–174. Springer-Verlag Berlin Heidelberg, Berlin Heidelberg, 1979

[66] M. Gombotz, D. Rettenwander, H. M. R. Wilkening. Lithium-Ion Transport in Nanocrystalline Spinel-type $Li[In_xLi_y]Br_4$ as Seen by Conductivity Spectroscopy and NMR. *Frontiers in Chemistry* **8** (2020) 100.
doi:10.3389/fchem.2020.00100

[67] M. Gombotz, H. M. R. Wilkening. Fast Li Ion Dynamics in the Mechanosynthesized Nanostructured Form of the Solid Electrolyte Li_3YBr_6. *ACS Sustainable Chemistry and Engineering2* (2020).
doi:10.1021/acssuschemeng.0c06694

[68] 111 kHz CPMAS Bruker (accessed on 10.12.2020)
`https://www.bruker.com/products/mr/nmr/probes/probes/solids/very-fast-mas/07-mm.html`

[69] Bruker. Aeon 1GHz (accessed on 2.12.2020 - 13:16)
`https://www.bruker.com/products/mr/nmr/magnets/aeon-1ghz.html`

[70] G. Facey. What is a Magnet Quench? (accessed on 26.11.2020 - 09:24), 2008
`http://u-of-o-nmr-facility.blogspot.com/2008/02/what-is-magnet-quench.html`

[71] S. Breuer, V. Pregartner, S. Lunghammer, H. M. R. Wilkening. Dispersed Solid Conductors: Fast Interfacial Li-Ion Dynamics in Nanostrucutred LiF and LiF:gamma-Al_2O_3 Composites. *J. Phys. Chem. C* **123** (2019) 5222.
doi:10.1021/acs.jpcc.8b10978

[72] C. Galven, J. Dittmer, E. Suard, F. Le Berre, M.-P. Crosnier-Lopez. Instability of Lithium Garnets against Moisture. Structural Characterization and Dynamics of $Li_{7-x}H_xLa_3Sn_2O_{12}$ and $Li_{5-x}H_xLa_3Nb_2O_{12}$. *Chemistry of Materials* **24** (2012) 3335.
doi:10.1021/cm300964k

[73] Q. Liu, Z. Geng, C. Han, Y. Fu, S. Li, Y. bing He, F. Kang, B. Li. Challenges and perspectives of garnet solid electrolytes for all solid-state lithium batteries. *Journal of Power Sources* **389** (2018) 120.
doi:10.1016/j.jpowsour.2018.04.019

[74] R. Murugan, V. Thangadurai, W. Weppner. Fast lithium ion conduction in garnet-type $Li_7La_3Zr_2O_{12}$. *Angewandte Chemie - International Edition* **46** (2007)

7778.
doi:10.1002/anie.200701144

[75] L. Cheng, E. J. Crumlin, W. Chen, R. Qiao, H. Hou, S. Franz Lux, V. Zorba, R. Russo, R. Kostecki, Z. Liu, K. Persson, W. Yang, J. Cabana, T. Richardson, G. Chen, M. Doeff. The origin of high electrolyte-electrode interfacial resistances in lithium cells containing garnet type solid electrolytes. *Physical Chemistry Chemical Physics* **16** (2014) 18294.
doi:10.1039/c4cp02921f

[76] L. Cheng, M. Liu, A. Mehta, H. Xin, F. Lin, K. Persson, G. Chen, E. J. Crumlin, M. Doeff. Garnet Electrolyte Surface Degradation and Recovery. *ACS Applied Energy Materials* **1** (2018) 7244.
doi:10.1021/acsaem.8b01723

[77] C. Hiebl, D. Young, R. Wagner, H. M. Wilkening, G. J. Redhammer, D. Rettenwander. Proton Bulk Diffusion in Cubic $Li_7La_3Zr_2O_{12}$ Garnets as Probed by Single X-ray Diffraction. *Journal of Physical Chemistry C* **123** (2019) 1094.
doi:10.1021/acs.jpcc.8b10694

[78] B. Gadermaier, L. Resch, D. M. Pickup, I. Hanghofer, I. Hanzu, P. Heitjans, W. Sprengel, R. Würschum, A. V. Chadwick, H. M. Wilkening. Influence of defects on ionic transport in $LiTaO_3$ - A study using EXAFS and positron annihilation lifetime spectroscopy. *Solid State Ionics* **352** (2020) 115355.
doi:10.1016/j.ssi.2020.115355

[79] M. Brinek, C. Hiebl, H. M. R. Wilkening. Understanding the Origin of Enhanced Li-Ion Transport in Nanocrystalline Argyrodite-Type Li_6PS_5I. *Chem. Mater.* **32** (2020) 4754.
doi:10.1021/acs.chemmater.0c01367

[80] M. Gombotz, V. Pregartner, I. Hanzu, H. M. R. Wilkening. Fluoride-ion batteries: On the electrochemical stability of nanocrystalline $La_{0.9}Ba_{0.1}F_{2.9}$ against metal electrodes. *Nanomaterials* **9** (2019) 1.
doi:10.3390/nano9111517

[81] V. K. Davis, C. M. Bates, K. Omichi, B. M. Savoie, N. Momčilović, Q. Xu, W. J. Wolf, M. A. Webb, K. J. Billings, N. H. Chou, S. Alayoglu, R. K. McKenney, I. M. Darolles, N. G. Nair, A. Hightower, D. Rosenberg, M. Ahmed, C. J. Brooks, T. F. Miller, R. H. Grubbs, S. C. Jones. Room-temperature cycling of metal fluoride electrodes: Liquid electrolytes for high-energy

fluoride ion cells. *Science* **362** (2018) 1144.
doi:10.1126/science.aat7070

[82] N. I. Sorokin, B. P. Sobolev. Nonstoichiometric fluorides—Solid electrolytes for electrochemical devices: A review. *Crystallography Reports* **52** (2007) 842.
doi:10.1134/S1063774507050148

[83] F. Gschwind, G. Rodriguez-Garcia, D. J. S. Sandbeck, A. Gross, M. Weil, M. Fichtner, N. Hörmann. Fluoride ion batteries: Theoretical performance, safety, toxicity, and a combinatorial screening of new electrodes. *Journal of Fluorine Chemistry* **182** (2016) 76.
doi:10.1016/j.jfluchem.2015.12.002

[84] M. Faraday. *Experimental Researches in Electricity, Art. 1339.* Taylor and Francis, London, UK, 1893

[85] C. Tubandt. Uber Elektrizitatsleitung in festen kristallisierten Verbindungen . *Z. Anorg. Allg. CHem.* **115** (1923) 105.
doi:10.1002/zaac.19211150106

[86] J. H. Kennedy, J. C. Hunter. Thin-Film Galvanic Cell Pb / PbF_2 / PbF_2 , CuF_2 / Cu. *J. Electrochem. Soc.* **123** (1976) 10.
doi:10.1149/1.2132740

[87] J. Schoonman. A Solid-State Galvanic Cell with Fluoride-Conducting Electrolytes. *Journal of the Electrochemical Society* **123** (1976) 1772.
doi:10.1149/1.2132694

[88] W. Baukal. Galvanische Zelle mit dotiertem Calciumfluorid als Festelektrolyt, 1977

[89] M. Anji Reddy, M. Fichtner. Batteries based on fluoride shuttle. *Journal of Materials Chemistry* **21** (2011) 17059.
doi:10.1039/c1jm13535j

[90] C. Rongeat, M. Anji Reddy, T. Diemant, R. J. Behm, M. Fichtner. Development of new anode composite materials for fluoride ion batteries. *Journal of Materials Chemistry A* **2** (2014) 20861.
doi:10.1039/c4ta02840f

[91] D. T. Thieu, M. H. Fawey, H. Bhatia, T. Diemant, V. S. K. Chakravadhanula, R. J. Behm, C. Kübel, M. Fichtner. CuF_2 as Reversible Cathode for Fluoride Ion Batteries. *Advanced Functional Materials* **27** (2017) 1.
doi:10.1002/adfm.201701051

[92] H. Bhatia, D. T. Thieu, A. H. Pohl, V. S. K. Chakravadhanula, M. H. Fawey, C. Kübel, M. Fichtner. Conductivity Optimization of Tysonite-type $La_{1-x}Ba_xF_{3-x}$ Solid Electrolytes for Advanced Fluoride Ion Battery. *ACS Applied Materials and Interfaces* **9** (2017) 23707.
doi:10.1021/acsami.7b04936

[93] I. Mohammad, J. Chable, R. Witter, M. Fichtner, M. A. Reddy. Synthesis of Fast Fluoride-Ion-Conductive Fluorite-Type $Ba_{1-x}Sb_xF_{2+x}$ ($0.1 \leq x \leq 0.4$): A Potential Solid Electrolyte for Fluoride-Ion Batteries. *ACS Applied Materials and Interfaces* **10** (2018) 17249.
doi:10.1021/acsami.8b04108

[94] C. Rongeat, M. A. Reddy, R. Witter, M. Fichtner. Nanostructured Fluorite-type Fluorides as Electrolyte for Fluoride Ion Batteries. *The Journal of Physical Chemistry C* **117** (2013) 4943.
doi:10.1021/jp3117825

[95] M. A. Nowroozi, S. Ivlev, J. Rohrer, O. Clemens. La_2CoO_4: A new intercalation based cathode material for fluoride ion batteries with improved cycling stability. *Journal of Materials Chemistry A* **6** (2018) 4658.
doi:10.1039/c7ta09427b

[96] M. Hammad Fawey, V. S. K. Chakravadhanula, M. A. Reddy, C. Rongeat, T. Scherer, H. Hahn, M. Fichtner, C. Kübel. In situ TEM studies of micron-sized all-solid-state fluoride ion batteries: Preparation, prospects, and challenges. *Microscopy Research and Technique* **79** (2016) 615.
doi:10.1002/jemt.22675

[97] I. Mohammad, R. Witter, M. Fichtner, M. A. Reddy. Introducing Interlayer Electrolytes: Toward Room-Temperature High-Potential Solid-State Rechargeable Fluoride Ion Batteries. *ACS Applied Energy Materials* **2** (2019) 1553.
doi:10.1021/acsaem.8b02166

[98] L. Zhang, M. A. Reddy, M. Fichtner. Electrochemical performance of all solid-state fluoride-ion batteries based on thin-film electrolyte using alternative conductive additives and anodes. *Journal of Solid State Electrochemistry* **22** (2018) 997.
doi:10.1007/s10008-017-3838-2

[99] M. A. Nowroozi, K. Wissel, M. Donzelli, N. Hosseinpourkahvaz, S. Plana-Ruiz, U. Kolb, R. Schoch, M. Bauer, A. M. Malik, J. Rohrer, S. Ivlev, F. Kraus, O. Clemens. High cycle life all-solid-state fluoride ion battery with La_2NiO_{4+d} high voltage cathode. *Communications Materials* **1** (2020) 1.
doi:10.1038/s43246-020-0030-5

[100] B. Dieudonne, J. Chable, M. Body, C. Legein, E. Durand, F. Mauvy, S. Fourcade, M. Leblanc, V. Maisonneuve, A. Demourgues. The key role of the composition and structural features in fluoride ion conductivity in tysonite $Ce_{1-x}Sr_xF_{3-x}$ solid solutions. *Dalton Transactions* **46** (2017) 3761.
doi:10.1039/c6dt04714a

[101] B. Dieudonné, J. Chable, F. Mauvy, S. Fourcade, E. Durand, E. Lebraud, M. Leblanc, C. Legein, M. Body, V. Maisonneuve, A. Demourgues. Exploring the $Sm_{1-x}Ca_xF_{3-x}$ Tysonite Solid Solution as a Solid-State Electrolyte: Relationships between Structural Features and F^- - Ionic Conductivity. *Journal of Physical Chemistry C* **119** (2015) 25170.
doi:10.1021/acs.jpcc.5b05016

[102] I. Mohammad, R. Witter, M. Fichtner, M. Anji Reddy. Room-Temperature, Rechargeable Solid-State Fluoride-Ion Batteries. *ACS Applied Energy Materials* **1** (2018) 4766.
doi:10.1021/acsaem.8b00864

[103] F. Gschwind, Z. Zhao-Karger, M. Fichtner. Fluoride-doped PEG matrix as an electrolyte for anion transportation in a room-temperature fluoride ion battery. *Journal of Materials Chemistry A* **2** (2014) 1214.
doi:10.1039/C3TA13881J

[104] F. Gschwind, J. Bastien. Parametric investigation of room-temperature fluoride-ion batteries: Assessment of electrolytes, Mg-based anodes, and BiF_3-cathodes. *Journal of Materials Chemistry A* **3** (2015) 5628.
doi:10.1039/c4ta06625a

C Publications

C.1 Publications in Peer Reviewed Journals

Heterogeneous F anion transport, local dynamics and electrochemical stability of nanocrystalline $La_{1-x}Ba_xF_{3-x}$
S. Breuer, M. Gombotz, V. Pregartner, I. Hanzu, H. M. R. Wilkening
Energy Storage Materials, Vol. 16, 2018, p. 481-490
DOI: 10.1016/j.ensm.2018.10.010

Spatial confinement - Rapid 2D F^- diffusion in micro- and nanocrystalline $RbSn_2F_5$
M. Gombotz, S. Lunghammer, S. Breuer, I. Hanzu, F. Preishuber-Pflügl and H. M. R. Wilkening
PCCP, Vol. 21, 2019, p. 1872-1883
DOI: 10.1039/C8CP07206J

Fluoride-Ion Batteries: On the Electrochemical Stability of Nanocrystalline $La_{0.9}Ba_{0.1}F_{2.9}$ Against Metal Electrodes
M. Gombotz, V. Pregartner, I. Hanzu and H. M. R. Wilkening
Nanomaterials, Vol. 9, 2019, p. 151
DOI: 10.3390/nano9111517

Combined Effects of Anion Substitution and Nanoconfinement on the Ionic Conductivity of Li-Based Complex Hydrides
R. Zettl, L. de Kort, M. Gombotz, H. M. Wilkening, P. de Jongh and P. Ngene
J. Phys. Chem. C, Vol. 124, 2020, p. 2806-2816
DOI: 10.1021/acs.jpcc.9b10607

Lithium-Ion Transport in Nanocrystalline Spinel-type $Li[In_xLi_y]Br_4$ as Seen by Conductivity Spectroscopy and NMR
M. Gombotz, D. Rettenwander and H. M. R. Wilkening
Frontiers in Chemistry, Vol. 8, 2020, 100
DOI: 10.3389/fchem.2020.00100

Li-Ion Diffusion in Nanoconfined $LiBH_4$-LiI/Al_2O_3: From 2D Bulk Transport to 3D Long-Range Interfacial Dynamics
R. Zettl, M. Gombotz, D. Clarkson, S. Greenbaum, P. Ngene, P. de Jongh, H. M. R. Wilkening
ACS Applied Materials & Interfaces, Vol. 120, 2020, 34, p. 38570–38583
DOI: 10.1021/acsami.0c10361

Rapid Low-Dimensional Li^+ Ion Hopping Processes in Synthetic Hectorite-Type $Li_{0.5}[Mg_{2.5}Li_{0.5}]Si_4O_{10}F_2$
C. Hiebl, P. Loch, M. Brinek, M. Gombotz, B. Gadermaier, P. Heitjans, J. Breu, H. M. R. Wilkening
Chemistry of Materials, Vol. 32, 17, 2020, p. 7445–7457
DOI: 10.1021/acs.chemmater.0c02460

Fast Li ion dynamics in the mechanosynthesized nanostructured form of the solid electrolyte Li_3YBr_6
M. Gombotz and H. M. R. Wilkening
ACS, Vol. 9, 2, 2021, p. 743-755
DOI: 10.1021/acssuschemeng.0c06694

C.2 Oral Presentations

Fast anion dynamics in the layered ceramic $RbSn_2F_5$
M. Gombotz, S. Lunghammer, S. Breuer and M. Wilkening
AuCers Workshop "Keramik in Österreich", TU Vienna, 15.2.2018

Air sensitivity of $Li_7La_3Zr_2O_{12}$ garnets: A single crystal study
M. Gombotz, J. Alvarado, S. Ganschow, L. Cheng, S. Sainio, D. Nordlund, P. Posch, D. Rettenwander, M. M. Doeff, H. M. R. Wilkening
Doc Days Chemie 2019, TU and KFU Graz, 25.4.2019

C.3 Posters

Fast 2D diffusion in nano crystalline $RbSn_2F_5$ as seen by impedance and magnetic nuclear resonance measurements
M. Gombotz, S. Lunghammer, S. Breuer, F. Preishuber-Pflügl and M. Wilkening
Americas International Meeting on Electrochemistry and Solid State Science (AIMES), 30.9 - 4.10.2018, Cancun, Mexico

Air sensitivity of $Li_7La_3Zr_2O_{12}$ garnets: A single crystal study
M. Gombotz, J. Alvarado, S. Ganschow, L. Cheng, S. Sainio, D. Nordlund, P. Posch, D. Rettenwander, M. M. Doeff and H. M. R. Wilkening
22^{th} Conference on Solid State Ionics (SSI-22), 16.6 - 21.6.2018, PyeongChang, South Korea
Awarded with a Poster Price from the Journal PCCP, Royal Society of Chemistry

D Acknowledgement

Die Erarbeitung dieser Arbeit wäre mir alleine nicht möglich gewesen und ich möchte daher den folgenden Personen meinen Dank ausdrücken;

Univ.-Prof. Martin Wilkening
ICTM, TU Graz
nicht nur für die Möglichkeit meine Doktorarbeit in seiner Arbeitsgruppe zu verfassen, sondern auch dafür, dass ich mich im Rahmen meiner Arbeit sehr frei entfalten durfte. Ich möchte mich auch dafür bedanken, dass ich mich im Ausland auf Konferenzen und im Zuge meines Aufenthalts am LBNL weiterbilden durfte.

Univ.-Prof. Werner Sitte
Montanuniversität Leoben
für die Tatsache, dass er als Gutachter dieser Arbeit fungiert und für die damit aufgebrachte Zeit.

Dr. Ilie Hanzu
ICTM, TU Graz
für die Hilfe bei der experimentellen Arbeit und dem Verfassen der Publikation über die elektrochemische Stabilität von Fluorionenleitern. Darüber hinaus für sein offenes Ohr und die stete Hilfsbereitschaft, wann immer ich Probleme im Labor hatte.

Dr. Daniel Rettenwander
ICTM, TU Graz
für seine Hilfe bezüglich XRD und für die Herstellung des Kontaktes zum LBNL.

Marca Doeff, PhD. und Judith Alvarado, PhD.
Lawrence Berkeley National Laboratory (LBNL), USA
für ihre professionelle Unterstützung während meines Aufenthaltes im LBNL. Vor allem Judith Alvarado, die meinen wissenschaftlichen als auch privaten Horizont erweitert hat.

Dr. Marina Brinek, DI Caroline Hiebl and Dr. Roman Zettl
ICTM, TU Graz
dafür, dass sie mich schon seit dem Schreiben meiner Diplomarbeit unterhalten. Sie haben meine Erwartungen BürokollegInnen betreffend, in jedem Belangen weit übertroffen.

und all den aktuellen und vergangenen Mitgliedern der AG Wilkening für die interessanten Diskussionen, die Hilfe im Labor (hier v.a. Ing. **Veronika Pregartner**), und darüber hinaus dafür, dass sie meine Zeit als Dissertantin ungemein bereichert haben.

Ich kann mit Worten nicht ausdrücken, wie dankbar ich bin eine Familie zu haben, ohne die ich zweifelsohne, niemals auch nur annähernd so weit gekommen wäre. Meinen Großeltern Rosa und Franz, meinen Eltern Rosi und Gottfried sowie Lisi, einen besonderen Dank dafür, dass sie mir gezeigt haben, was im Leben am Ende doch am Wichtigsten bleibt und dafür, dass sie es geschafft haben mir zeitgleich Wurzeln und Flügel zu geben.

Das Erste, dass der Mensch im Leben vorfindet,
das Letzte, wonach der die Hand ausstreckt,
das Kostbarste, was er im Leben besitzt,
ist die Familie.
Adolf Kolping

Zuletzt möchte ich zum Ausdruck bringen, wie überaus dankbar und glücklich ich bin, Gregor an meiner Seite zu haben. Auf sein offenes Ohr und seine unermüdliche Unterstützung konnte bzw. kann ich mich nicht nur im privaten Sinne, sondern auch im fachlichen immer verlassen.

Es gibt nichts Schöneres als geliebt zu werden,
geliebt um seiner selbst willen oder viel mehr;
trotz seiner selbst.
Victor Hugo